AFRL-RB-WP-TR-2012-0040

NUMERICAL MODELING OF PULSED ELECTRICAL DISCHARGES FOR HIGH-SPEED FLOW CONTROL

Jonathan Poggie

Computational Aerophysics Branch
Aeronautical Sciences Division

FEBRUARY 2012
Interim Report

AIR FORCE RESEARCH LABORATORY
AIR VEHICLES DIRECTORATE
WRIGHT-PATTERSON AIR FORCE BASE, OH 45433-7542
AIR FORCE MATERIEL COMMAND
UNITED STATES AIR FORCE

NOTICE AND SIGNATURE PAGE

This report was cleared for public release by the USAF 88th Air Base Wing (88 ABW) Public Affairs Office (PAO) and is available to the general public, including foreign nationals. Copies may be obtained from the Defense Technical Information Center (DTIC) (http://www.dtic.mil).

AFRL-RB-WP-TR-2012-0040 HAS BEEN REVIEWED AND IS APPROVED FOR PUBLICATION IN ACCORDANCE WITH THE ASSIGNED DISTRIBUTION STATEMENT.

*//Signature//   //Signature//
_____   _____
JONATHAN POGGIE, Program Manager   CARL TILMANN, Branch Chief
Computational Applications Branch   Computational Applications Branch
Aeronautical Sciences Division   Aeronautical Sciences Division
Structures Division

//Signature//
_____
MICHAEL STANEK, Technical Advisor
Aeronautical Sciences Division
Air Vehicles Directorate

This report is published in the interest of scientific and technical information exchange, and its publication does not constitute the Government's approval or disapproval of its ideas or findings.

*Disseminated copies will show "//Signature//" stamped or typed above the signature blocks.

REPORT DOCUMENTATION PAGE

Form Approved
OMB No. 0704-0188

The public reporting burden for this collection of information is estimated to average 1 hour per response, including the time for reviewing instructions, searching existing data sources, gathering and maintaining the data needed, and completing and reviewing the collection of information. Send comments regarding this burden estimate or any other aspect of this collection of information, including suggestions for reducing this burden, to Department of Defense, Washington Headquarters Services, Directorate for Information Operations and Reports (0704-0188), 1215 Jefferson Davis Highway, Suite 1204, Arlington, VA 22202-4302. Respondents should be aware that notwithstanding any other provision of law, no person shall be subject to any penalty for failing to comply with a collection of information if it does not display a currently valid OMB control number. **PLEASE DO NOT RETURN YOUR FORM TO THE ABOVE ADDRESS.**

1. REPORT DATE *(DD-MM-YY)*	2. REPORT TYPE	3. DATES COVERED *(From - To)*
February 2012	Interim	01 January 2009 – 01 January 2012

4. TITLE AND SUBTITLE
NUMERICAL MODELING OF PULSED ELECTRICAL DISCHARGES FOR HIGH-SPEED FLOW CONTROL

5a. CONTRACT NUMBER
In-house

5b. GRANT NUMBER

5c. PROGRAM ELEMENT NUMBER
61102F

6. AUTHOR(S)
Jonathan Poggie

5d. PROJECT NUMBER
2307

5e. TASK NUMBER

5f. WORK UNIT NUMBER
A03S0C

7. PERFORMING ORGANIZATION NAME(S) AND ADDRESS(ES)
Computational Aerophysics Branch (AFRL/RBAC)
Aeronautical Sciences Division, Air Force Research Laboratory
Air Vehicles Directorate
Wright-Patterson Air Force Base, OH 45433-7542
Air Force Materiel Command, United States Air Force

8. PERFORMING ORGANIZATION REPORT NUMBER
AFRL-RB-WP-TR-2012-0040

9. SPONSORING/MONITORING AGENCY NAME(S) AND ADDRESS(ES)
Air Force Research Laboratory
Air Vehicles Directorate
Wright-Patterson Air Force Base, OH 45433-7542
Air Force Materiel Command
United States Air Force

10. SPONSORING/MONITORING AGENCY ACRONYM(S)
AFRL/RBAC

11. SPONSORING/MONITORING AGENCY REPORT NUMBER(S)
AFRL-RB-WP-TR-2012-0040

12. DISTRIBUTION/AVAILABILITY STATEMENT
Approved for public release; distribution unlimited.

13. SUPPLEMENTARY NOTES
PAO Case Number: 88ABW-2012-1466; Clearance Date: 15 Mar 2012. Report contains color.

14. ABSTRACT
This report describes work carried out on numerical modeling of flow control devices based on pulsed electrical discharges. Given the lack of flow control options in the high-speed regime, there is strong interest in developing such devices for control of laminar-turbulent transition, turbulence, engine unstart, and inlet shock train stability. Pulsed electrical discharge actuators offer the features of rapid actuation, low profile, and low mean power consumption. Under this project, work was carried out on improving both the physical models used to represent the actuators and the accuracy of the numerical schemes used to implement them. Initial work focused on demonstrating the use of high-order, compact difference methods for discharge modeling. These were initially demonstrated on canonical problems in one and two dimensions, and later on more complex problems. Subsequent work compared different physical models for pulsed discharges: one-moment (drift-diffusion with local equilibrium with the electric field), two-moment (drift-diffusion with energy equation), and five-moment (continuity, momentum, and energy equations for each species). The results were found to be sensitive to the model used for the electrons. Later stages of the project involved collaboration with The Ohio State University (OSU). Reduced chemical kinetic models for air were developed, and the importance of rapid thermalization reactions in pulsed discharges was explored. Three-dimensional fluid dynamics computations were carried out to investigate flow physics and control in a Mach 5 cylinder flow experiment carried out at OSU.

15. SUBJECT TERMS
computational fluid dynamics, CFD, computational, flow control, plasma, algorithms, hypersonics

16. SECURITY CLASSIFICATION OF:			17. LIMITATION OF ABSTRACT:	18. NUMBER OF PAGES	19a. NAME OF RESPONSIBLE PERSON (Monitor)
a. REPORT Unclassified	**b. ABSTRACT** Unclassified	**c. THIS PAGE** Unclassified	SAR	180	Jonathan Poggie
					19b. TELEPHONE NUMBER *(Include Area Code)* N/A

Standard Form 298 (Rev. 8-98)
Prescribed by ANSI Std. Z39-18

Table of Contents

List of Figures

Acknowledgements

1 Summary

This report describes work carried out on numerical modeling of flow control devices based on pulsed electrical discharges. Given the lack of flow control options in the high-speed regime, there is strong interest in developing such devices for control of laminar-turbulent transition, turbulence, engine unstart, and inlet shock train stability. Pulsed electrical discharge actuators offer the features of rapid actuation, low profile, and low mean power consumption. Under this project, work was carried out on improving both the physical models used to represent the actuators and the accuracy of the numerical schemes used to implement them.

Initial work focused on demonstrating the use of high-order, compact difference methods for discharge modeling. These were initially demonstrated on canonical problems in one and two dimensions, and later on more complex problems. Subsequent work compared different physical models for pulsed discharges: one-moment (drift-diffusion with local equilibrium with the electric field), two-moment (drift-diffusion with energy equation), and five-moment (continuity, momentum, and energy equations for each species). The results were found to be sensitive to the model used for the electrons. Later stages of the project involved collaboration with The Ohio State University (OSU). Reduced chemical kinetic models for air were developed, and the importance of rapid thermalization reactions in pulsed discharges was explored. Three-dimensional fluid dynamics computations were carried out to investigate flow physics and control in a Mach 5 cylinder flow experiment carried out at OSU. In ongoing work, the air plasma chemistry models are being combined with the different dynamics models (1-5 moments) in an attempt to further increase the fidelity of the physical model.

2 Introduction

Interest in plasma-based flow control dates to the mid-1950s, when magnetohydrodynamic (MHD) reentry heat shields were first investigated. Activity in the research area waned in the 1970s, with some work on drag reduction using corona discharges appearing in the 1980s. A resurgence in the field took place in the 1990s, with the introduction of dielectric barrier discharge (DBD) actuators, a revisit of reentry magnetohydrodynamics, and the disclosure of the AJAX hypersonic vehicle concept. In the fifteen years since this resurgence, plasma-based flow control techniques have been a topic of ongoing research, motivated by the possibility of extremely rapid actuation, a low-profile configuration, and the ability to operate in hostile environments.

In the high-speed regime, plasma-based flow control devices have suffered the drawbacks of either excessive weight or insufficient control authority. Pulsed discharge devices, based on either arc or glow discharges, seem to be a promising way around these difficulties. Nanosecond-scale pulsed glow discharges are efficient generators of both ions and electronically excited molecules because of the presence of an extremely high instantaneous reduced electric field. Through thermalization and electromagnetic force, the actuators can convert the input electrical energy into bulk fluid motion useful for flow control.

Despite considerable effort by the research community on modeling plasma actuators, efficient numerical modeling techniques have remained elusive because of the complex, nonlinear physics and disparate time scales that govern discharge behavior. To address this deficiency, this research program was to develop improved methods for modeling plasma discharges for flow control. This report describes efforts from 2009 to 2012 under the program.

2.1 Background

Research efforts under this project have focused on improving the physical models and numerical methods employed in computations of pulsed electrical discharges. The general approach is described below.

2.1.1 Physical Models

This research program has focused on nonequilibrium plasmadynamics. The aim of the work was to improve our capability for prediction by moving to more fundamental models, provided from the foundation of the field in statistical physics. A brief introduction to the theoretical framework is given here.

Approved for public release; distribution unlimited.

We begin our description of molecular motion by assuming that classical Newtonian mechanics holds, and that the particle acceleration is generated by gravity and the Lorentz force. The state of a particle can be specified by its position and velocity. In principal, the motion of a large group of particles can be predicted from Newton's laws, given all their positions and velocities at a certain time. This represents the molecular dynamics level of simulation, which has been explored extensively in the materials science field. In problems involving more than a moderate number of molecules (typically 10^3-10^6), however, molecular dynamics simulation is not possible because of computational cost and sensitivity to initial conditions. We are therefore driven to describe the physics statistically, predicting macroscopic quantities, averaged over a large number of particles.

The first level of statistical approximation is Direct Simulation Monte Carlo (DSMC). In this approach, the motion of representative molecules is determined by Newton's laws, with a statistical treatment of collisions. The resulting data are averaged to determine macroscopic properties. The DSMC approach has proved to be a very productive means for treating hypersonic rarefied gas flows and microscale flows.

An alternative approach is to employ the formalism of statistical mechanics. The fundamental dependent variable, from the statistical point of view, is the velocity distribution function for each species, which represents the probability of finding a particle in a particular small element of phase space (position-velocity space).

In the statistical mechanics treatment, the electric and magnetic fields are taken to be macroscopic fields, which are obtained by averaging over a volume large enough to contain a large number of particles, but still small compared to the length scale of macroscopic property variations. Particle trajectories are assumed to be governed by Newtonian mechanics and the macroscopic fields, except during collisions where the motion is governed by intermolecular forces (and where quantum mechanical effects may be significant). The gas is also assumed to be sufficiently dilute that these collisions can be considered as rare, discrete, short-duration events. This is assumption is generally valid for the Earth's atmosphere, but must be carefully evaluated in plasma applications. With these assumptions, and the restriction that a statistically significant number of particles be present in the small volume under consideration, the generalized Boltzmann equation, or equation of change of the probability density function, can be derived.

The generalized Boltzmann equation can be interpreted as stating that the number of particles observed, while following a selected initial group along their trajectories in phase space, is altered only by their sudden appearance or disappearance in local phase space through collisions. In a gas mixture, there is a Boltzmann equation for each species present; the species are coupled through the collision terms. If collision cross-section data are available for each collision process, the collision term can be evaluated through a convolution integral between each cross-section and the distribution functions of the

colliding species. Given a suitable collision model, the Boltzmann equation can be solved to find the time evolution of the distribution function.

Besides the distribution function, statistical quantities of interest include average values, which are more readily-measured, macroscopic properties.   Equations for the evolution of average values can be obtained from moments of the Boltzmann equation. The resulting equation of change is called the transport equation. Moments of interest include the mass, momentum, and translational kinetic energy of the particles. These equations include source terms that represent particle generation and destruction by chemical reactions, momentum exchange between fluid species, and kinetic energy exchange in collisions.

To address modes of internal energy, such as rotation, vibration, and electronic excitation, we consider each internal energy level as a separate species. In analogy to the procedure described above, we write the Boltzmann equation for each energy level, take the moment with the associated energy, and sum over all internal energy states. The resulting internal energy equation has a source term that represents the exchange of internal energy in collisions.

Adding the translational and internal energy equations for a given species gives an expression of total energy conservation for that species, with a source term that describes the exchange of total energy between species.

At this stage, standard definitions are introduced for the mean velocity, the kinetic pressure, translational temperature, thermal energy, viscous stress, and heat flux. With appropriate closure models, the resulting equation set forms a five-moment model for each species (mass, three momentum, and energy equations). Coupled with Maxwell's equations, this level of modeling has begun to show promise in describing the behavior of weakly-ionized, nonequilibrium plasmas, as well as fusion plasmas. Unlike conventional, simplified models for weakly-ionized plasmas, the five-moment formulation includes particle inertia, which is important in the nanosecond-pulse discharges now being used for plasma-based flow control. Further, the purpose of a plasma actuator is to add momentum and energy to the bulk, and solving for this quantities has an appealing directness. In order to more accurately treat pulsed discharges, we are employing this formulation in our ongoing research efforts, which are described later.

Simplifications are possible, however, if a degree of approximation is accepted. In the drift-diffusion formulation, the inertia and viscous terms are neglected in the momentum equation. This allows the equation to be solved algebraically, reducing the number of conservation laws by three. Further, under the local field equilibrium assumption, the electron temperature is assumed to be a unique function of the reduced electric field (field magnitude divided by total number density). This approximation eliminates the species energy equation. The drift-diffusion formulation and the local field equilibrium

approximation form the basis of the one- and two-moment models, which are also examined later in this report.

Considering the general conservation equations again, the conservation of mass, momentum, and total energy in collisions requires that the sum, over all species, of each of the corresponding collision source terms be zero. These properties can be used to relate the species conservation laws to the conservation laws for the gas as a whole. Summing the equations requires converting the definitions of pressure, temperature, and the flux terms to a reference frame corresponding to the mass-averaged velocity. Summing over all species, and introducing appropriate mass-weighted definitions of the total quantities, the global conservation laws for mass, momentum, and total energy are obtained.

All the collision source terms sum to zero, so that the global conservation contain no source terms except an electromagnetic body force and an electromagnetic energy deposition term. The resulting equation set forms the basis of the gasdynamics of neutral fluids, and, when coupled to a suitable form of Maxwell's equations, the one-species magnetohydrodynamic model for plasmadynamics.

We have employed each of these levels of modeling in some way in the work described here. Full mathematical details can be found in the Appendices.

2.1.2   Compact Difference Methods

In order to reduce the computational cost of modeling plasma discharges for high-speed flow control, new algorithms were developed, based on high-order, compact, spatial differences. This section will briefly describe compact differences, for a formulation of up to sixth order spatial accuracy.

Considering a one-dimensional, uniform mesh, the following central difference scheme with a 5-point stencil can be used to generate estimates of the first derivative $\phi' = \partial\phi/\partial x|_i$ with up to sixth-order accuracy:

$$\alpha\phi'_{i-1} + \phi'_i + \alpha\phi'_{i+1} = a\frac{\phi_{i+1} - \phi_{i-1}}{2\Delta x} + b\frac{\phi_{i+2} - \phi_{i-2}}{4\Delta x} \qquad (2.1)$$

where α, a, and b are constants that are used to alter the properties of the discrete approximation. Taylor series expansions can be used to derive a family of 2nd-6th order accurate schemes corresponding to this formalism.

Numerical stability was enforced using filtering, typically with a filter of two orders greater than the accuracy of the basic scheme. The form of the filtering scheme for interior points was as follows:

$$\alpha_f \overline{\phi}_{i-1} + \overline{\phi}_i + \alpha_f \overline{\phi}_{i+1} = \sum_{n=0}^{N} \frac{a_n}{2} \left(\phi_{i+n} + \phi_{i-n} \right) \qquad (2.2)$$

Careful treatment of the boundary conditions was necessary to maintain the spatial accuracy of the scheme.

2.2 Program Objectives

The main technical objective of this program is to develop accurate and efficient computation tools to enable the design of flow control actuators based on pulsed electrical discharges. These devices are an appealing flow control option for the high-speed regime because of their low profile, rapid actuation, and ability to operate in hostile environments.

2.3 Approach

The technical approach has been to attack two areas that contribute to the accuracy of a numerical model: the physical formulation and the numerical algorithm. An improved physical model may allow us to more accurately represent how a plasma actuator converts its electrical input into momentum and energy of the bulk flow for control. Higher-order numerical methods may allow us to achieve a given level of accuracy on coarser grid, for a net reduction in computational cost. The physical model has been addressed both in terms of the accuracy of the model of particle motion (different numbers of moments) and the fidelity of the chemical kinetics model (different numbers of species and reactions). The work on numerical algorithms has compared fourth-through sixth-order compact difference to conventional second-order upwind methods.

The personnel involved in this work were Dr. Jonathan Poggie and Dr. Nicholas Bisek of AFRL/RBAC, and Prof. Igor Adamovich and Dr. Munetake Nishihara of OSU.

2.4 Challenges

Although past efforts have been fairly successful in duplicating the basic behavior of electrical discharges in high-speed flow, the computational cost of such calculations remains extremely high. Relevant temporal scales vary by many orders of magnitude: for a discharge in 670 Pa nitrogen, electron impact ionization and dielectric relaxation have a characteristic time scale of 0.1 ns, whereas the ion diffusion time scale is on the order of 0.1 ms. With a typical time step of 1.0 ns obtained with a semi-implicit scheme, 10^5-10^6 steps are required to ensure time convergence.

Further, extremely accurate spatial resolution is required to accurately predict ionization rates, which, in conventional plasma models, depend exponentially on the electric field, a first derivative of the computed solution. Grid resolution studies have shown that very fine meshes are required for grid convergence using either second-order upwind spatial discretization or Sharfetter-Gummel exponential discretization.

Thus there is a strong motivation to develop new, more efficient numerical algorithms for these problems. Only when robust, efficient computer codes are available for discharge modeling will basic research efforts in this field pay off with a transition of the computational technology to industry.

3 Results and Discussion

The following subsections review the work that was done under this project to develop improved numerical models for electrical discharges. Additional details can be found in Appendices A-D. These efforts included work on improving numerical algorithms and on developing more detailed physical models. Starting in 2010, a collaboration was undertaken with the research group of Prof. Igor Adamovich at The Ohio State University. This led to an effort to analyze experiments on nanosecond-pulsed electrical discharges carried out by that group in a Mach 5 cylinder flow.

3.1 Compact Difference Methods

In previous work, second-order finite difference methods had been employed successfully in the modeling of glow discharges for high-speed flow control. Detailed grid resolution studies, however, revealed that very fine grid resolution was required for acceptable quantitative results. High-order compact difference methods offer a possible means of achieving high spatial accuracy on coarser grids, potentially leading to a significant reduction in the computational cost of an accurate solution. This portion of the project explored the feasibility of applying high-order, compact difference methods to the discharge modeling.

In initial work, one-dimensional compact difference calculations were carried out (Ref. [1], Appendix A). An initial formulation of a five-moment discharge model (continuity, momentum, and energy equations for each species) was developed. Sample compact difference calculations were carried out for one-dimensional test cases, and accuracy was compared to a standard second-order upwind scheme. Fourth-order accuracy was demonstrated with compact differencing for several problems. In particular, example calculations were carried out for the structure of a neutral gas shock, a transient low-density sheath, and a shock in an ionized gas.
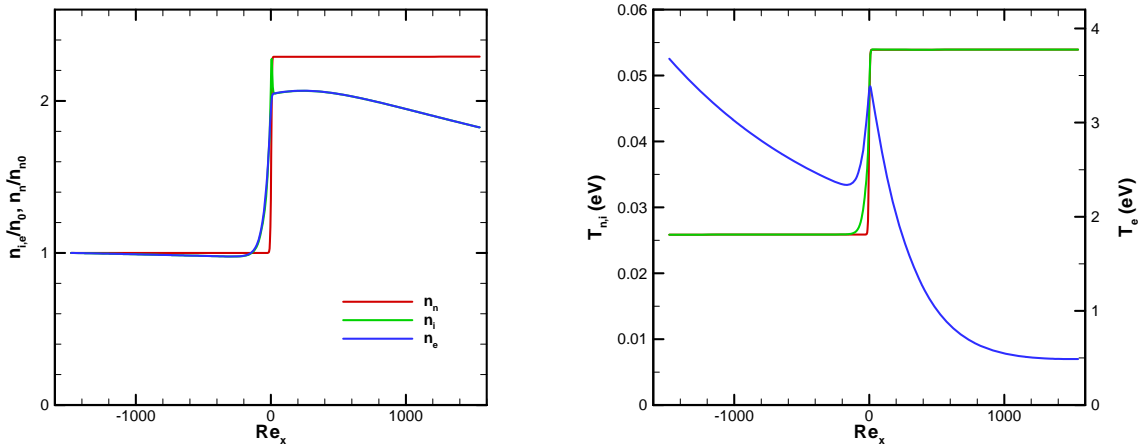
(a) Number densities.   **(b) Temperature.**

Figure 1: Three-species model of shock structure. Red lines: neutrals, green lines: ions, blue lines: electrons

Figure 1 shows sample results obtained for a three-species, five-moment model of the internal structure of a shock wave in argon. The continuity, momentum, and energy equations were solved for ions, electrons, and neutrals using a fourth-order compact difference scheme on a mesh of 1001 points. The upstream conditions for the neutrals were 645 m/s, 1.3 kPa, and 300K. The upstream fractional ionization was 10^{-6} and the electron temperature was 3.6 eV. The shock transition zone is seen to be substantially thicker for the charged particles than for the neutral gas. The large difference in mass between the ions and electrons leads to charge separation in the vicinity of the neutral gas jump, setting up an electric potential rise of a few volts across the shock. Recombination leads to a drop in charged particle density downstream of the shock.

Later, the work was extended to two dimensions (Ref. [2], Appendix A). Sample compact difference calculations were carried out for several test cases, including a Poisson equation solution, a compressible Couette flow problem, a hypersonic laminar boundary layer flow, and a transient plasma-sheath problem. Spatial convergence of second- through sixth-order compact schemes was investigated, and found to be comparable to the theoretical order of accuracy. In particular, compact difference methods of up to sixth order can successfully achieve their theoretical order of accuracy for the coupled Poisson and Euler equations with source terms. Further, a hybrid compact-difference / Roe scheme was implemented and successfully tested in a hypersonic laminar boundary layer problem.
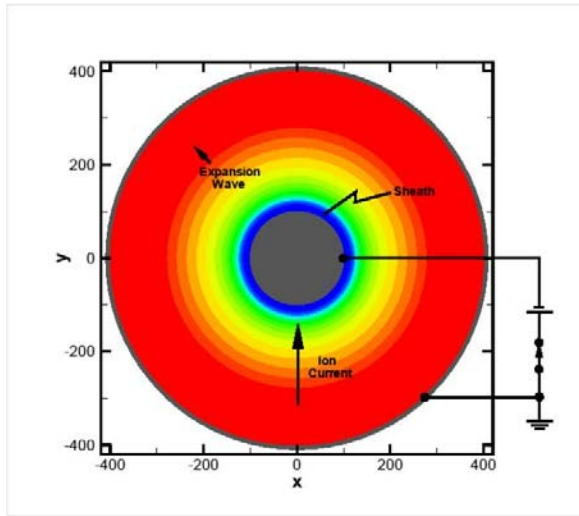
(a) Ion number density at t = 18.　　　　**(b) Spatial convergence study.**
Figure 2: Transient sheath test case.
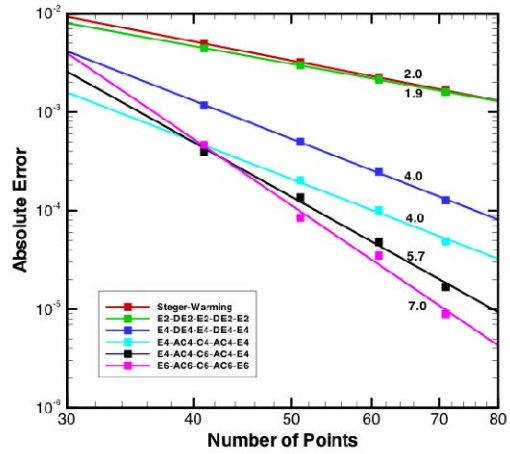
Figure 2 shows results from a two-dimensional transient sheath calculation used as a test of the coupled conservation equations and Poisson equation. In this annular electrode configuration, the outer electrode was grounded, and a potential of -50 V was suddenly applied at the inner electrode at $t = 0$. The working gas was argon at 0.07 Pa and 300 K. The electrons were assumed to be in Boltzmann equilibrium, and the neutral background gas was assumed to be uniform and at rest for these short time scales. For the baseline calculations, the ion conservation equations were solved on mesh of 101 by 101 points using a sixth-order compact difference scheme (Figure 2a).

The ionized gas has the following response to the change in boundary conditions. With the sudden application of a negative potential, the electrons are repelled from the electrode, forming a layer of positive charge. The relatively massive ions slowly respond to the changed conditions, forming an ion current into the electrode. As a result, the space charge diminishes, and the sheath expands. Ahead of the sheath, a quasi-neutral presheath propagates into the bulk plasma as an expansion wave.

As a gauge of the quality of the solution for different numerical schemes, the ion current at the inner electrode for a nondimensional time $t = 18$ was examined. The error in this quantity, relative to a reference solution of 101 by 101 points obtained using using the sixth-order compact difference scheme, is plotted versus grid size in Figure 2b for grids between 41 by 41 and 71 by 71 points. Each set of data was fit to a power law, and the curves are annotated with the corresponding exponent on the plot. The computed exponents are seen to follow the value for the order of the scheme. These results show that compact difference methods of up to sixth order can successfully achieve their theoretical order of accuracy for the coupled Poisson and Euler equations with source terms.

3.2   Physical Models for Particle Motion

After the initial development of the new compact difference code, additional work was carried out on the implementation of different physical models in the code (Ref. [3], Appendix B).   In order to investigate the role of inertia in pulsed electrical discharges, a five-moment model for charged particle motion (continuity, momentum, and energy equations) was compared to a two-moment model (continuity and energy equations). Three species were considered: ions, electrons, and neutrals. Either the two- or five-moment model was used for the ions and electrons, but the five-moment model was always employed for the neutrals. Ionization and excitation reactions were included in each model.

Two glow discharge test cases in 107 Pa argon were examined. A steady-state, one-dimensional discharge was considered first. For this case, relatively subtle differences in the velocities and temperatures in the cathode sheath led to significant differences between the predictions of the two models for ionization rates and number densities. A two-dimensional, transient discharge problem with an elliptical cathode was studied next. Relative to the two-moment model, the five-moment model predicted a slower response to the activation of the cathode, and lower electron velocities and temperatures in the later stages of the simulation. These differences can be attributed to particle inertia and to differences in the boundary conditions for the two models. Both models predicted that neutral gas velocities on the order of 1.3 m/s occurred within 1 µs, with a negligible rise in neutral temperature (~ 0.3 K). More rapid heating occurs in molecular gases, which are discussed later in this report.
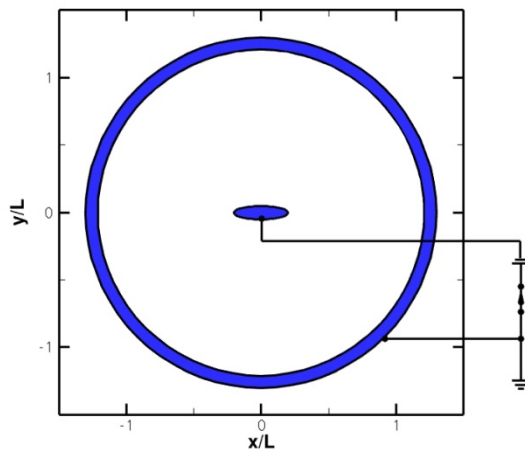
(a) Configuration.
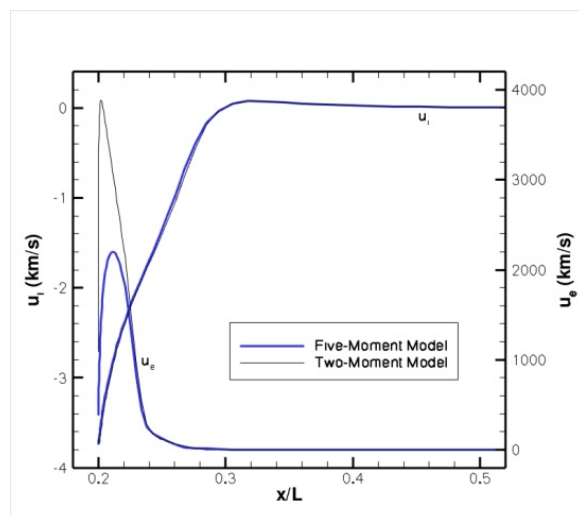
(b) Centerline, horizontal velocity at 1 µs for two- and five-moment models.

Approved for public release; distribution unlimited.
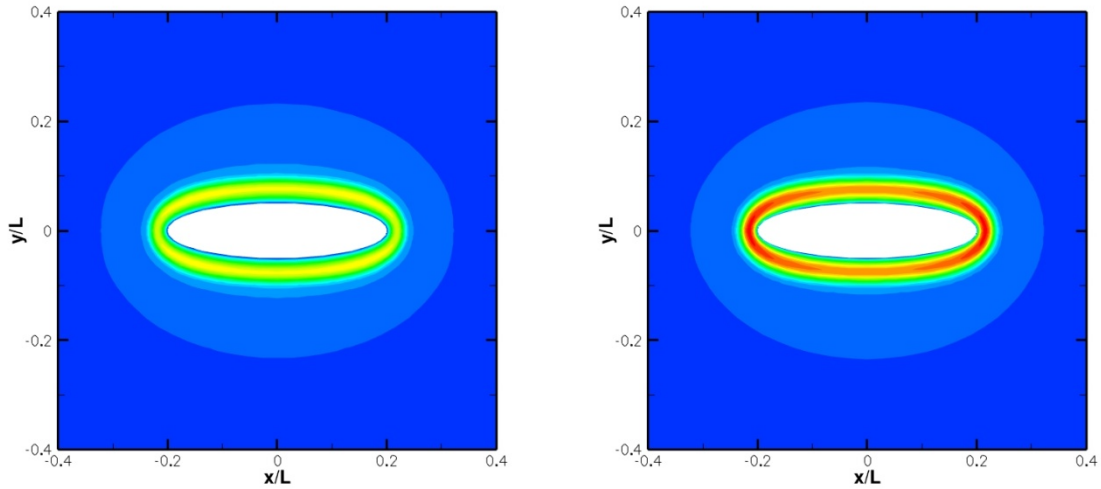
(c) Electron temperature, 1 μs, 5-moment model.

(d) Electron temperature, 1 μs, 2-moment model.

Figure 3: Transient Discharge with elliptical cathode.

Figure 3 shows results from a test case designed to highlight the differences between the two- and five-moment models. It is a two-dimensional, transient problem, where particle inertia, electric field strength, and charged particle heating could be expected to be significant. A schematic diagram of the problem is given in Figure 3a. The inner boundary is taken to be the cathode, which was brought suddenly to a potential of -120 V at t = 0. The shape of the cathode was a 4:1 ellipse, and the grounded anode formed the circular outer boundary.

The initial and boundary conditions were as follows. The background neutral gas was at initially at rest at 107 Pa and 323 K. A uniform plasma of number density 10^{15} m^{-3}, with an ion temperature of 323 K (0.03 eV) and an electron temperature of 11600 K (1 eV), was assumed to exist at t = 0 between the two electrodes. The secondary emission coefficient was 0.05, and the secondary emission temperature was 5800 K (0.5 eV).

Figure 3b compares the predictions of the two- and five-moment models for the horizontal velocity distribution on the centerline (y = 0) at a time of t = 1 μs. At this relatively late time, the predictions for the ion properties coincide closely for the two models, but the two-moment model predicts substantially higher electron velocities. This discrepancy also appears in electron temperature, as seen in Figure 3c and Figure 3d.

Calculations with the five-moment model were seen to be feasible, and may prove to be a useful tool in studying nanosecond-pulse discharges. The computational cost for the five-moment model is about twice that of the two-moment model, as based on timings of the two-dimensional calculations presented here. Since significant differences in the charged

particle behavior are observed between the two models, the increased generality of the five-moment model may be worth the additional computational cost.
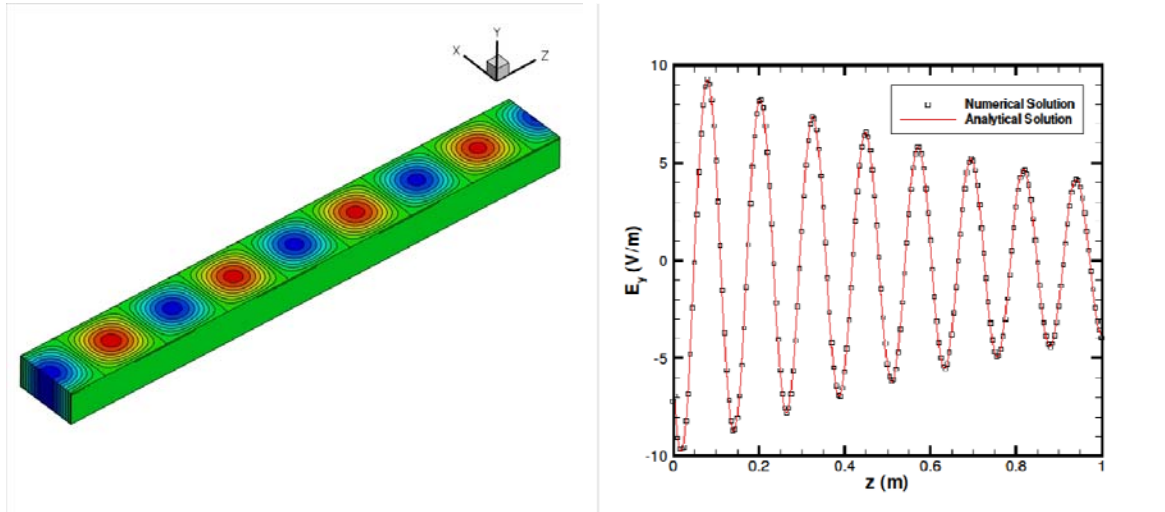
(a) Solution for rectangular waveguide.   (b) Transverse plasma waves.
Figure 4: Solutions of the full Maxwell's equations.

In subsequent work, the code was extended to three-dimensions (Ref. [4], Appendix B). The new computer code modeled the behavior of weakly-ionized gases through a three-species fluid model coupled to either the Poisson equation or the full set of Maxwell's equations. The three-dimensional numerical implementation involved compact spatial differences of up to sixth-order accuracy, driven by a fourth-order Runge-Kutta time marching scheme.

Sample calculations were carried out for three test cases: a DC discharge in one dimension, a three-dimensional rectangular waveguide problem, and a one-dimensional wave propagation problem in a warm, collisional plasma. In all cases, good agreement was obtained between the numerical solutions and either analytical solutions or previously-published numerical solutions. The physical model for the electron motion was found to have a strong influence on the solution. Boundary conditions and viscous effects were found to have a less significant effect. The solution for wave propagation in a plasma using the full Maxwell's equations represents a first step towards modeling microwave discharges, and toward incorporating wave effects in the modeling of nanosecond pulse discharges.

Sample results for the solution of the full Maxwell's equations are shown in Figure 4. The first test case (Figure 4a) was a rectangular wave guide. Hollow conducting pipes, or waveguides, are a commonly used technology for transmitting electromagnetic waves in the microwave regime (1-100 GHz frequency or 3-300 mm wavelength) with low attenuation. Waveguides of rectangular cross-section represent a good computational test

case, since analytical solutions are available, and rectangular waveguides of 2:1 aspect ratio are commonly used in applications. Calculations were carried out for a 43 mm by 86 mm rectangular waveguide, chosen to correspond to commercially-available configurations designed to transmit energy at 2.45 GHz. (The cutoff frequency for this configuration is about 1.7 GHz.) The basic computational mesh consisted of a uniform grid of 41 by 21 by 201 points, with the waveguide axis aligned with the z-direction. Four wavelengths were captured along this axis. Waves were excited by imposing an oscillating current sheet at z = 0. The numerical solutions agree closely with the corresponding analytical solution for the TE_{10} mode.
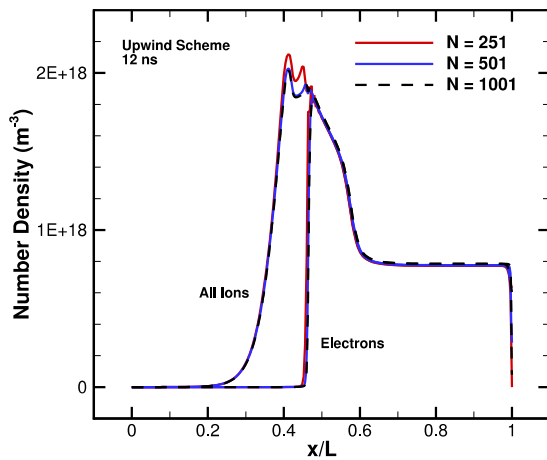
A second test case involved transverse waves in a warm, collisional plasma (Figure 4b). This problem forms a good test case because it couples the full Maxwell's equations to the five-moment fluid model for the electrons and an analytical solution is available. As with the waveguide calculations described previously, the waves were excited in the present case by imposing an oscillating current sheet at the station z = 0. Sample results are shown in the figure for a plasma frequency of 9.0 GHz and a collision frequency of 53 GHz, corresponding to a 1.33 kPa argon plasma with fractional ionization of $3x10^{-8}$ and electron temperature 11600 K. The numerical results are seen to be in good agreement with the analytical solution for an excitation frequency of 2.45 GHz.


3.3   Chemical Kinetics

The next phase of the project concentrated on developing an air plasma chemistry model suitable for reproducing the rapid thermalization effects observed in experiments. This work was carried out in collaboration with The Ohio State University. Numerical calculations were carried out to examine the physics of the operation of a nanosecond-pulse, single dielectric barrier discharge in a configuration with planar symmetry. This simplified configuration was chosen as a vehicle to develop a physics-based nanosecond discharge model, including realistic air plasma chemistry and compressible bulk gas flow. Discharge parameters (temperature, pressure, and input waveform) were selected to be representative of recent experiments on bow shock control with a nanosecond discharge in a Mach 5 cylinder flow carried out at The Ohio State University.

In the first phase of the work, a four-species formulation was employed, including neutrals, ions, electrons, and a representative excited molecular species (Ref. [5], Appendix C). The following models were employed to predict particle motion: a drift-diffusion formulation for the charged particles, a diffusion equation for the excited molecules, and a five-moment fluid formulation for the neutrals. The Poisson equation was solved for the electric potential. During a 20 kV Gaussian input pulse lasting approximately 120 ns, an average energy density of about 40 J/m^3 was stored in excited molecular states. Quenching reactions released this stored energy within about 10 μs, converting it into translational energy of the neutrals and forming weak shock waves. The maximum neutral gas temperature rise predicted by the model was about 40 K.
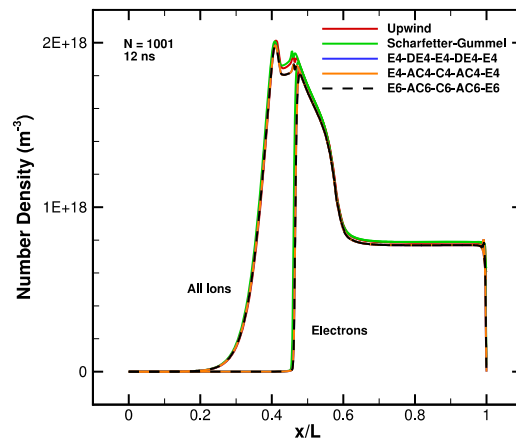
(a) Grid resolution study.   (b) Results with different numerical schemes.

Figure 5: Numerical accuracy in nanosecond-pulse discharge calculations.
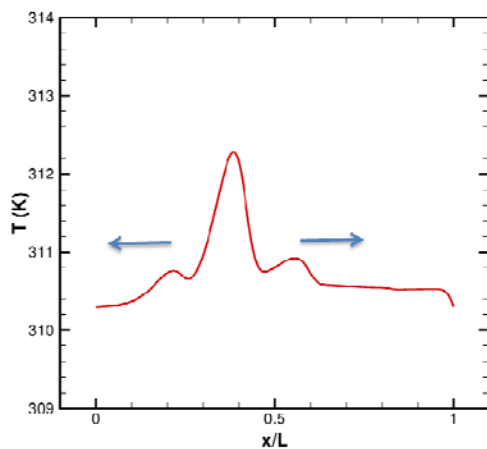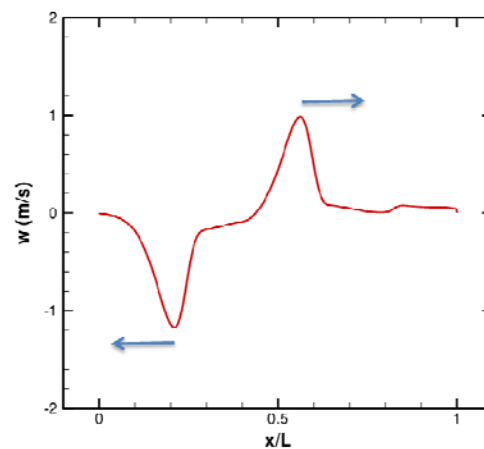
(a) Temperature.   (b) Velocity.

Figure 6: Bulk gas properties at 1.1 μs.

In the second phase of the work, more detailed model was developed (Ref. [6], Appendix C). First, a reduced plasma kinetic model (15 species and 42 processes) was developed by carrying out a sensitivity analysis of zero-dimensional plasma computations with an extended chemical kinetic model (46 species and 395 processes). Transient, one-dimensional discharge computations were then carried out using the reduced kinetic model, incorporating a drift-diffusion formulation for each species, a self-consistent

computation of the electric potential using the Poisson equation, and a mass-averaged gas dynamic formulation for the bulk gas motion.

A careful grid resolution study was carried out as part of the project (Figure 5a). A grid spacing of 4 μm is required for strict grid convergence. Since a variety of numerical schemes has been implemented in the code as part of the numerical algorithm efforts described above, calculations were carried out to compare the different schemes (Figure 5b). The numerical schemes included the Scharfetter-Gummel scheme, a second-order upwind scheme, and fourth-sixth order compact differencing. For the fine grid employed here agreed well, except near the sheath edge. There the additional dissipation in the lower order schemes led to a slightly different result.

The computational results qualitatively reproduced many of the features observed in the experiments, including the rapid thermalization of the input electrical energy and the consequent formation of a weak shock wave. At breakdown, input electrical energy was rapidly transformed (over roughly 1 ns) into ionization products, dissociation products, and electronically excited particles, with subsequent thermalization over a relatively longer time-scale (roughly 10 μs). Figure 6 shows the changes in bulk gas temperature and velocity that occur with the discharge. The rapid thermalization of the input electrical power leads to a sharp rise in temperature near the sheath edge, and the consequent formation of weak waves traveling away from this location.

The motivation for this work was modeling nanosecond-pulse, dielectric barrier discharges for applications in high-speed flow control. The effectiveness of such devices as flow control actuators depends crucially on the rapid thermalization of the input electrical energy, and in particular on the rate of quenching of excited electronic states of nitrogen molecules and oxygen atoms and on the rate of electron-ion recombination. In ongoing work, we are attempting to further increase the fidelity of the physical modeling by combining the two- and five-moment models of particle motion with the relatively detailed chemical kinetic models described in the present here.

3.4   Fluid Dynamics and Three-Dimensionality

The computational cost of a high-fidelity plasma model precludes its application to complex, three-dimensional configurations. Therefore, computational studies were carried out with a reduced-order plasma model in order to explore the three-dimensional fluid dynamics of The Ohio State University Mach 5 cylinder flow experiments (Ref. [7], Appendix D).

In the experiments, a Mach 5 air flow over a cylinder with a flush-mounted dielectric barrier discharge actuator was studied. The actuator was pulsed at nanosecond time scales, which rapidly added energy to the flow, thereby creating a shock wave that traveled away from the pulse source. As the shock wave traveled upstream, it interacted

with the standing bow-shock and momentarily increased the bow-shock standoff distance. These phenomenon were observed experimentally using phase-locked schlieren imaging.

The focus of this project was to numerically reproduce the flow phenomena observed in the experiment in order to provide additional insight into the shock-shock interaction, to examine the effect the dielectric barrier discharge pulse had on the surface properties of the cylinder, and to develop a reduced-order phenomenological model representative of the nanosecond pulse discharge system. The nanosecond pulse dielectric barrier discharge plasma actuators are known to operate with relatively low temperatures. This work explores the possibility that the induced compression wave is generated by rapid thermalization of the discharge which results in a local temperature rise occurring on longer time scales.

Two-dimensional simulations were performed, provided many useful details about the discharge event, and showed reasonable agreement with experiment. However, the simulations indicated the experiment experienced significant three-dimensional effects, thus requiring a three-dimensional simulation of the entire experiment to accurately capture the complex cylinder / tunnel-sidewall interaction and replicate the resultant flow.

Three-dimensional results of the discharge event revealed that the discharge pulse produced a compression wave that interacted with the standing bow-shock and that the momentary increase in the bow-shock standoff distance was not due to the interaction the three-dimensional compression wave had with the cylinder/tunnel-sidewall boundary layer.

(a) Temperature Distribution.

(b) Comparison of shock standoff to experiment.
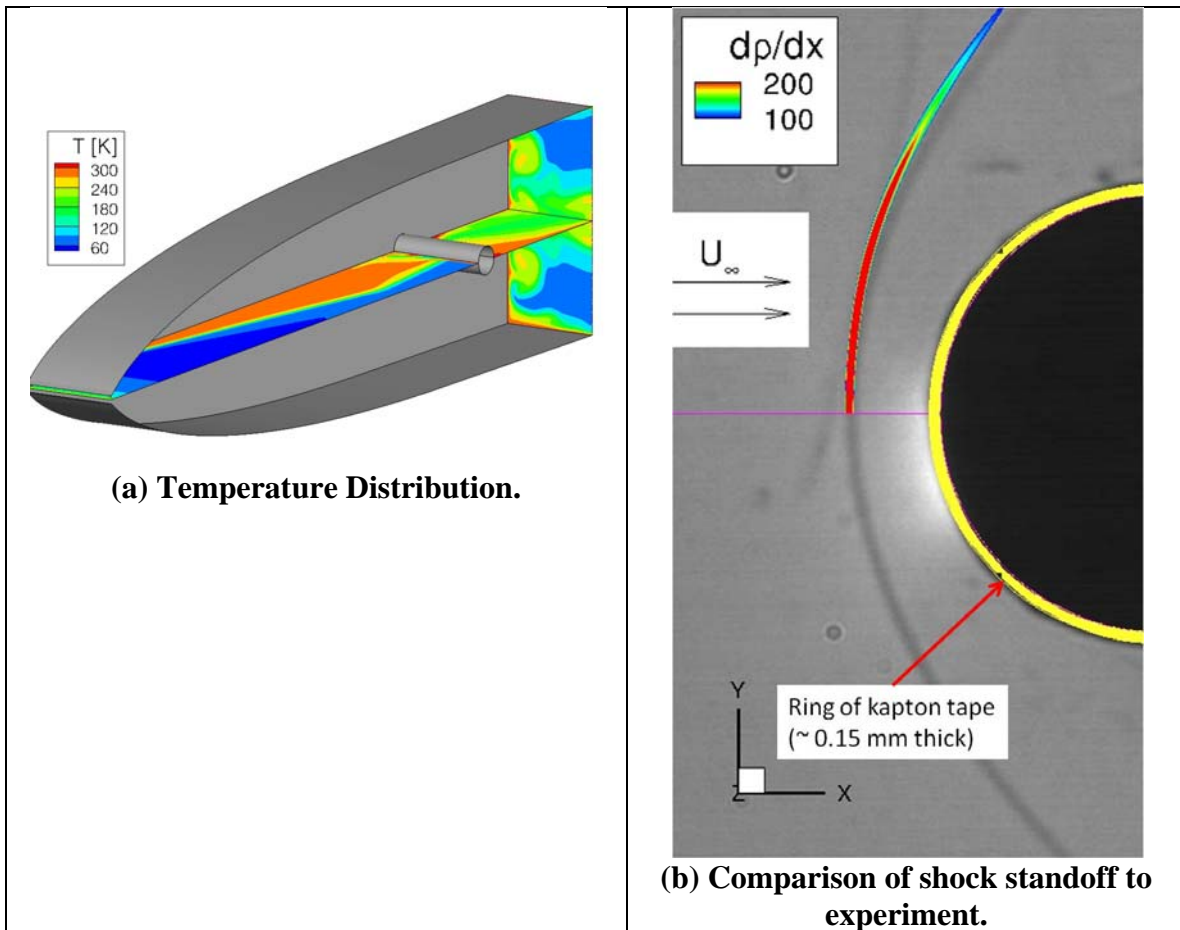
Figure 7: Results of three-dimensional computations of Mach 5 cylinder flow.

Selected results from the computations of the baseline flow (no control applied) are shown in Figure 7. The temperature distribution in selected planes (Figure 7a) illustrates the complexity and three-dimensionality of the flow. With the use of a well-resolved computational mesh (about 15 million cells), excellent agreement with experiment was obtained (Figure 7b).

4 Conclusions

This project focused on numerical modeling of flow control devices based on pulsed electrical discharges. Work was carried out both on improving both the physical models used to represent the actuators and on improving the accuracy of the numerical schemes used to implement them. High-order, compact difference methods were initially demonstrated on canonical problems in one and two dimensions, and later on more complex problems. Compact difference schemes appear to be a promising numerical approach for modeling plasma actuators for high-speed flow control. Several different physical models for charged particle dynamics pulsed discharges were implemented and evaluated. The results were found to be sensitive to the model used for the electrons, whereas boundary conditions and viscous effects were found to have a less significant effect. Reduced chemical kinetic models for air were developed, and the importance of rapid thermalization reactions in pulsed discharges was demonstrated. In ongoing work, the air plasma chemistry models are being combined with the different particle dynamics models. The flow in the Ohio State University Mach 5 wind tunnel flow was found to be highly three-dimensional with the cylinder model in place. Nevertheless, three-dimensional computations were able to replicate experiment fairly accurately, and illustrate how discharge heat release forms a weak shock wave that can act to perturb the bow shock.

References

[1] J. Poggie, "High-Order Compact Difference Methods for Glow Discharge Modeling," AIAA Paper 2009-1047, American Institute of Aeronautics and Astronautics, January 2009.

[2] J. Poggie, "Compact Difference Methods for Discharge Modeling in Aerodynamics," AIAA Paper 2009-3908, American Institute of Aeronautics and Astronautics, June 2009.

[3] J. Poggie, "Role of Charged Particle Inertia in Pulsed Electrical Discharges," AIAA Paper 2010-1195, American Institute of Aeronautics and Astronautics, January 2010.

[4] J. Poggie, "High-Order Numerical Methods for Electrical Discharge Modeling," AIAA Paper 2010-4632, American Institute of Aeronautics and Astronautics, June 2010.

[5] J. Poggie, N. Bisek, I. V. Adamovich, and M. Nishihara, "High-Speed Flow Control with Electrical Discharges," AIAA Paper 2011-3104, American Institute of Aeronautics and Astronautics, June 2011.

[6] J. Poggie, N. Bisek, I. V. Adamovich, and M. Nishihara, "Numerical Simulation of Nanosecond-Pulse Electrical Discharges," AIAA Paper 2012-1025, American Institute of Aeronautics and Astronautics, January 2012.

[7] N. Bisek, J. Poggie, M. Nishihara, and I. Adamovich, "Computational and Experimental Analysis of Mach 5 Air Flow over a Cylinder with a Nanosecond Pulse Discharge," AIAA Paper 2012-0186, American Institute of Aeronautics and Astronautics, January 2012.

Appendix A

Compact Difference Methods for Electrical Discharge Modeling

47th AIAA Aerospace Sciences Meeting Including The New Horizons Forum and Aerospace Exposition
5 - 8 January 2009, Orlando, Florida

AIAA 2009-1047

High-Order Compact Difference Methods
for Glow Discharge Modeling

Jonathan Poggie[*]

Air Force Research Laboratory, Wright-Patterson AFB, Ohio 45433-7512 USA

This paper explores the feasibility of applying high-order, compact difference methods to the modeling of glow discharges for high-speed flow control. Previous papers (AIAA 2007-0632, 2008-1357) have successfully applied second-order finite difference methods to glow discharge modeling. Detailed grid resolution studies, however, have revealed that very fine grid resolution is required for acceptable quantitative results. High-order compact difference methods offer a possible means of achieving high spatial accuracy on coarser grids, potentially leading to a significant reduction in the computational cost of an accurate solution. Sample compact difference calculations are presented here for one-dimensional test cases, and accuracy is compared to a standard second-order upwind scheme. In particular, fourth order accuracy is demonstrated with compact differencing for several problems involving the internal structure of weak shocks and the plasma-sheath transition. Future work will focus on applying the compact difference method to problems of interest in plasma aerodynamics.

I.   Introduction

Since the mid-1990s, there has been considerable research interest in plasma-based flow control techniques for aerospace applications. Because of their favorable weight and power consumption properties, small-scale actuators based on glow and arc discharges have become increasingly popular, and much effort has been put toward numerical modeling of actuator behavior.[1–3]

Toward this end, the author has developed a second-order accurate, finite-difference code capable of modeling the region of finite space-charge present in the vicinity of electrode surfaces in the electric discharges used for flow control.[3–5] The physical model includes the fluid conservation laws for the bulk gas flow, a model for charged particle motion, and a self-consistent computation of the electric potential. This code has been successfully applied to a variety of discharge problems, including low-density plasma-sheath problems, DC glow discharges, and RF glow discharges. Comparisons among different numerical methods have been carried out, and a central difference scheme, an upwind scheme, and a finite difference implementation of the Sharfetter-Gummel scheme have all been found to give very similar results.

Recently, an investigation was carried out on spatial resolution issues in modeling DC glow discharges.[4,5] A detailed grid resolution study was carried out, and very fine grid resolution was found to be required for acceptable quantitative results. Coarse grids led to underestimates of number density, temperature, and current density and to overestimates of the lateral extent of the discharge column.

High-order compact difference methods[6,7] offer a possible means of achieving high spatial accuracy on coarser grids, potentially leading to a significant reduction in computational cost. This paper presents a preliminary, one-dimensional implementation of a compact difference scheme for plasma discharge problems. Sample calculations are presented here for several test problems, including shock internal structure and the plasma-sheath transition.

II.   Methods

The physical model and the numerical methods are described in this section. The physical model includes the fluid conservation laws for the motion of each species and a self-consistent computation of the electric potential. The numerical implementation involves compact spatial differences of up to sixth order accuracy, driven by a low-storage, fourth-order Runge-Kutta time marching scheme.

---

[*]Senior Aerospace Engineer, Computational Sciences Branch, AFRL/RBAC, 2210 Eighth St., Associate Fellow AIAA.
Cleared for public release, distribution unlimited (88ABW-2008-1309).

American Institute of Aeronautics and Astronautics

22

A. Physical Model

Continuum methods, based on moments of the Boltzmann equation, have been a popular and productive means of modeling electrical discharges. One-dimensional modeling of direct-current glow discharges was carried out as early as the late 1950s,[8,9] and two-dimensional simulations were first carried out in the late 1980s.[10,11] By the early 1990s, two dimensional simulations of radio-frequency glow discharges[12,13] and transient low-density discharges[14,15] were done. Three-dimensional simulations have appeared more recently.[3,16]

A variety of physical models have been employed in such work. One of the most common models is drift-diffusion, assuming local equilibrium with the electric field, so all coefficients are a function of the local reduced field E/N.[9–11] The next step up in generality is to solve the electron energy equation as well, and use the local electron temperature T_e instead of the local E/N to determine the transport and ionization coefficients.[17,18]

Some studies have used continuity-momentum equations in place of the drift-diffusion model, thus including the effects of particle momentum. The role of inertia in DC and RF discharges has been examined, including the momentum of the electrons,[19] the heavy particles,[20] or both.[21,22] Ion inertia is important in the transient sheath that appears in plasma-source ion implantation,[23] and in modeling the low-density plasma-sheath transition.[24,25]

One aim of this ongoing project is to determine limits of the moment method in modeling electrical discharges, specifically whether a three-moment model for each species can be accurate and computationally tractable. A relatively general formulation of the conservation equations for electrical discharges is outlined below, based on standard references.[26–28] Briefly, the conservation laws can be derived from moments of the Boltzmann equation, with closure models utilized for the inelastic collision source terms,[26] the elastic collision source terms,[26,29] and the flux terms.[27,30,31] In this preliminary work, a one-dimensional form of these equations is used, suitable for the test problems of shock internal structure and the plasma-sheath transition investigated in this paper.

1. Governing Equations

The focus of this paper is on one-dimensional shock and sheath structure in ionized argon. Gravity is neglected, and the absence of an applied magnetic field is assumed. The conservation equations for each species are:

$$\frac{\partial}{\partial t}(m_s n_s) + \frac{\partial}{\partial x}(m_s n_s u_s) = S_s$$

$$\frac{\partial}{\partial t}(m_s n_s u_s) + \frac{\partial}{\partial x}(m_s n_s u_s^2 + n_s k_B T_s) = \frac{\partial}{\partial x}\left[\tfrac{4}{3}\mu_{vs}\frac{\partial u_s}{\partial x}\right] + q_s n_s E + A_s$$

$$\frac{\partial}{\partial t}\left[n_s\left(H_s + \frac{k_B T_s}{\gamma_s - 1} + \tfrac{1}{2}m_s u_s^2\right)\right] + \frac{\partial}{\partial x}\left[n_s u_s\left(H_s + \frac{\gamma_s k_B T_s}{\gamma_s - 1} + \tfrac{1}{2}m_s u_s^2\right)\right] =$$
$$\frac{\partial}{\partial x}\left[\tfrac{4}{3}\mu_{vs} u_s \frac{\partial u_s}{\partial x} + k_s \frac{\partial T_s}{\partial x}\right] + q_s n_s u_s E + M_s \tag{1}$$

where the notation $s = n, i, e$ indicates the neutrals, ions, and electrons, respectively.

The mass per particle of each species is denoted as m_s, and the corresponding charge per particle is $q_n = 0$, $q_i = +e$, and $q_e = -e$. The number density is n_s, the velocity is u_s, and the translational temperature is T_s. The viscosity and thermal conductivity of each species are denoted as μ_{vs} and k_s, respectively. The electric field is E, and the symbol k_B indicates the Boltzmann constant. The internal energy per particle is assumed to have the form $m_s \epsilon_s = H_s + k_B T_s/(\gamma_s - 1)$, where $\gamma_s = 5/3$ is the ratio of specific heats. The heat of formation is $H_n = H_e = 0$ and $H_i = \mathcal{H}$, where $\mathcal{H} = 15.7$ eV for argon ionization.

It assumed that the gas is weakly ionized, so that the primary elastic collisions are with neutral particles. For the inelastic collisions, it is assumed that the species appear or disappear with the average momentum and energy of their peers, except for the electrons, which lose energy $\mathcal{H}$ in each inelastic collision.

Consider the reaction pair $\mathrm{Ar} + \mathrm{e}^- \rightleftharpoons \mathrm{Ar}^+ + 2\mathrm{e}^-$ and let ω be the production rate of charged particles. The species source terms become:

$$S_i = m_i \omega$$
$$S_e = m_e \omega \tag{2}$$
$$S_n = -m_n \omega$$

The momentum source terms are:

$$A_i = \omega m_i u_i - n_i m_{in} \nu_{in}(u_i - u_n)$$
$$A_e = \omega m_e u_e - n_e m_{en} \nu_{en}(u_e - u_n) \tag{3}$$
$$A_n = -(A_i + A_e)$$

American Institute of Aeronautics and Astronautics

The energy source terms are:

$$M_i = \omega \left(\mathcal{H} + \frac{k_B T_i}{\gamma_i - 1} + \tfrac{1}{2} m_i u_i^2 \right) - \frac{n_i m_{in} \nu_{in}}{m_i + m_n} \left[3 k_B (T_i - T_n) + (u_i - u_n)(m_i u_i + m_n u_n) \right]$$

$$M_e = -\omega \mathcal{H} + \omega \left(\frac{k_B T_e}{\gamma_e - 1} + \tfrac{1}{2} m_e u_e^2 \right) - \frac{n_e m_{en} \nu_{en}}{m_e + m_n} \left[3 k_B (T_e - T_n) + (u_e - u_n)(m_e u_e + m_n u_n) \right] \qquad (4)$$

$$M_n = -(M_i + M_e)$$

To complete the physical model, the electric field must be found from a consistent solution of Maxwell's equations. For the present work, the Poisson equation is solved for the electric potential:

$$\frac{\partial^2 \phi}{\partial x^2} = -\frac{1}{\epsilon_0} \sum_s q_s n_s \qquad (5)$$

and the electric field is found from $E = -\partial \phi / \partial x$.

Some calculations were carried out with the full model (1)-(5), but for the work presented in this paper, Boltzmann equilibrium was assumed for the electrons in order to reduce the computational cost of carrying out many runs for convergence studies. Under this the assumption, the electron temperature is held fixed, and the electron number density is computed from:

$$n_e = n_o \exp \left(\frac{e\phi}{k_B T_e} \right) \qquad (6)$$

where n_0 is a reference number density, corresponding to the potential $\phi = 0$.

2. Transport Properties and Reaction Rates

The collision frequency between the charged and neutral species ν_{sn} was estimated from mobility data, with the correlations for ion and electron mobility in argon taken from Ward.[8]

For the ionization rates, two models were considered. One had the form $\omega = z n_e$, where the ionization rate z is an eigenvalue of the problem, the production rate necessary to maintain a steady state. Alternatively, ionization and recombination coefficients were taken from the correlations of Adamovich et al.[32]

Standard correlations were used for the viscosity and thermal conductivity of the neutral particles.[33] The viscosity and thermal conductivity of the charged particles were neglected for the present work. A reasonable estimate of their magnitudes[21,30] can be found by assuming that the ions have the same transport coefficients as the neutrals, and that the electron transport coefficients can be found by assuming a Lewis number of unity and a Prandtl number of $2/3$.

3. Nondimensionalization

The equations were solved in non-dimensional form. For brevity, only an outline of the nondimensionalization procedure is given here. Global reference quantities were chosen for length L_R, velocity u_R, number density n_R, potential ϕ_R, collision rate ν_R, viscosity μ_{vR}, and thermal conductivity k_R. For each species, however, there was a different reference density $\rho_{Rs} = m_s n_R$, temperature $T_{Rs} = m_s u_R^2 / k_B$, and pressure $p_{Rs} = m_s n_R u_R^2$. Space charge was normalized by the electron charge e, and heat of formation was normalized by $m_s u_R^2$.

The nondimensionalized equations have much the same form as (1)-(5). In addition to a Reynolds number and Prandtl number for each species, the following nondimensional parameters appeared as a consequence of this form of nondimensionalization:

$$\Phi_s = \frac{e\phi_R}{m_s u_R^2} \quad C = \frac{\nu_R L_R}{u_R} \quad a = L_R \sqrt{\frac{e n_R}{\epsilon_0 \phi_R}}$$

The nondimensional parameters are, respectively, a relative field strength, a nondimensional collision frequency parameter, and a non-neutrality parameter.

B. Numerical Methods

The governing equations (1)-(4) were solved using a fourth-order accurate, low-storage Runge-Kutta time marching scheme combined with either a second-order Steger-Warming scheme or a compact spatial scheme of up to sixth order accuracy. For the compact scheme, stability was enforced by filtering, typically with a filter of two orders greater than the accuracy of the basic scheme. The Poisson equation (5) was solved by an iterative scheme (described below),

American Institute of Aeronautics and Astronautics

with either second-order central or compact spatial differences. The Poisson solution was not filtered. For the present examples, a one-dimensional, uniform mesh was employed, but an extension of the method to multi-dimensional, curvilinear grids is planned for future work.

1. Governing Equations

The conservation laws (1) can be written in the form:

$$\frac{\partial U}{\partial t} + \frac{\partial E}{\partial x} = \frac{\partial E_v}{\partial x} + S \tag{7}$$

where U is the vector of conserved variables, E is the inviscid flux vector, E_v is the viscous flux vector, and S represents the source terms. A standard, low-storage, fourth-order Runge-Kutta scheme[34] was used for time integration of Eq. (7). Two different schemes were used to evaluate the spatial differences: either a compact difference scheme of up to sixth-order accuracy (described below), or a second-order Steger-Warming scheme, which used third-order MUSCL extrapolation[35] for the inviscid fluxes and second-order central differencing for the viscous terms.

The Poisson equation (5) was solved at the end of each stage of the Runge-Kutta time-integration. It can be written in the form:

$$\frac{\partial^2 \phi}{\partial x^2} = S_\phi \tag{8}$$

An iteration procedure was introduced such that the potential at step m was $\phi^{m+1} = \phi^m + \Delta\phi$. With a linear expansion about the solution from the previous iteration, the discretized equation has the form:

$$\left[1 - \Delta\tau \delta_x^2 + \Delta\tau \frac{\partial S_\phi}{\partial \phi} \right] \Delta\phi = \omega \Delta\tau \left[\delta_x^2 \phi^m - S_\phi^m \right] \tag{9}$$

with iteration driving $\Delta\phi$ to zero. Here τ is a time-like variable introduced to motivate the iteration process, and ω is an over-relaxation factor. Discretizing the left-hand side using second order central differences in space, a tridiagonal system of equations is obtained. (Since iteration drives $\Delta\phi$ to zero, the form of the discretization of the left-hand-side does not affect the order of spatial accuracy of the converged solution.) Either central or compact difference schemes were used to evaluate the spatial differences present on the right hand side of Eq. (9), and the system was solved using the Thomas tridiagonal algorithm.[36] Iteration was continued until the change in potential $\Delta\phi$ was less than a small tolerance.

2. Compact Differences

Considering a one-dimensional, uniform mesh, the following central difference scheme[6,7] with a 5-point stencil can be used to generate estimates of the first derivative $\phi' = \partial\phi/\partial x|_i$ with up to sixth-order accuracy:

$$\alpha\phi'_{i-1} + \phi'_i + \alpha\phi'_{i+1} = a\frac{\phi_{i+1} - \phi_{i-1}}{2\,\Delta x} + b\frac{\phi_{i+2} - \phi_{i-2}}{4\,\Delta x} \tag{10}$$

Here α, a, and b are constants that are used to alter the properties of the scheme, and $\phi(x)$ is a generic function, not to be confused with the electric potential. Taylor series expansions can be used to derive a family of second to sixth order accurate schemes employing this template.[6,7] Table 1 gives selected coefficients for internal points using Eq. (10) for different orders of accuracy. Note that the implicit form of the scheme ($\alpha \neq 0$) results in a narrower stencil for a given order of accuracy that for an explicit form ($\alpha = 0$). Modified schemes[7] were used near boundaries, where the interior stencil would protrude outside of the domain.

Table 2 shows the forms of the compact difference scheme that were examined in this project, using the notation of Gaitonde and Visbal. To evaluate the derivative at each point, the appropriate form of Eq. (10) was solved using the Thomas tridiagonal algorithm.[36] Second derivatives were evaluated by applying the differencing scheme twice.

Figure 1 illustrates the accuracy of each of the schemes (see Table 2) in computing the derivative of the function $f(x) = \sin x$ in the range $0 \leq x \leq \pi$. The L_2-norm for the full domain is shown in Fig. 1a. With this metric of solution quality, the accuracy is seen to be constrained by the lower order stencil used near the boundaries. If points near the boundary are omitted from the norm (Fig. 1b), the convergence rate is seen to improve, and the accuracy of the scheme E4-AC4-C6-AC4-E4 is seen to lie between that of pure fourth- and sixth-order schemes.

American Institute of Aeronautics and Astronautics

Numerical stability was enforced using filtering, typically with a filter of two orders greater than the accuracy of the basic scheme. The form of the filtering scheme[7] for interior points was as follows:

$$\alpha_f \overline{\overline{\phi}}_{i-1} + \overline{\overline{\phi}}_i + \alpha_f \overline{\overline{\phi}}_{i+1} = \sum_{n=0}^{N} \frac{a_n}{2}(\phi_{i+n} + \phi_{i-n}) \tag{11}$$

where $\overline{\phi}_i$ is the filtered value of ϕ_i, and $N + 1$ is the order of the filter. A table of coefficients for interior-point filters of second to eighth order is given in Table 3. Modified filters were used near the boundaries; the various options are shown in Table 2. (In the table, F0 indicates that no filter was applied to the boundary points.) The filter was applied to each primitive variable at the end of a time step, and the boundary conditions were updated so that the boundary points were consistent with the filtered interior points. For the cases labeled Filter A in Table 2, the filter's free parameter was set to $\alpha = 0.40$, whereas for Filter B, the value was varied between $\alpha = 0.49$ at the boundary and $\alpha = 0.40$ for the interior points.

Careful treatment of the boundary conditions was necessary to maintain the spatial accuracy of the scheme. Unless otherwise noted, both extrapolation and derivative (Neumann) boundary conditions were handled with a scheme of spatial order corresponding to that of the boundary scheme.

III.   Results

Several test problems were examined in order to evaluate the accuracy of the compact scheme relative to the second-order Steger-Warming scheme. The focus was on one-dimensional shock and sheath structure in ionized argon.

A.   Neutral-Gas Shock

As a test of the code's ability to solve electrically-neutral, viscous gasdynamics problems, a calculation was carried out of the internal structure of a weak shock in argon. The following notation will be used: the subscript 1 indicates the state upstream of the shock, 2 indicates the downstream state, m indicates an average of the upstream and downstream states, and $x_{1/2}$ indicates the position corresponding to $u = u_m$. The upstream Mach number was $M_1 = 1.2$. The dimensional upstream conditions were: $p_1 = 42.2$ kPa, $T_1 = 125$ K, $u_1 = 125$ m/s. Downstream conditions were computed using the ideal gas jump conditions.[37] The computational domain was $L = 5$ μm in width.

A reference computation was carried out with 401 points using the E4-AC4-C6-AC4-E4 compact difference scheme. Figure 2a shows the basic shock structure, with the independent variables normalized using the conditions upstream of the shock. Pressure, temperature, and density increase monotonically through the shock, whereas velocity decreases to satisfy continuity. Because of the effects of heat conduction, entropy has the characteristic maximum typical of shock structure (See Zel'dovich and Raizer,[38] pp. 473–475). The total enthalpy, $H = e + p/\rho + u^2/2$, has a slight variation through the shock, and the upstream and downstream values are equal: $H_1 = H_2$.

As a qualitative verification of code accuracy, the reference solution is compared to the approximate analytical solution of G. I. Taylor in Fig. 2b. (See Thompson,[39] pp. 361-368, for a full discussion of the Taylor weak shock theory. In the figure, $A = (\gamma + 1)/[8/3 + 2(\gamma - 1)/\mathrm{Pr}] \approx 4/7$.) Although the analytical solution cannot be used for a quantitative verification of the code because of its approximate nature, the agreement between the numerical and analytical solutions is seen to be quite good. In particular, the shock thickness is predicted accurately.

The shock thickness based on the total enthalpy profile was chosen as a parameter for studying the convergence of the scheme. This thickness was defined as: $\Delta_H = \int_{-\infty}^{\infty}(H - H_1)/H_1 \, dx$. Since the total enthalpy upstream and downstream of the shock are equal in the present problem, the integrand is zero at the boundaries of the domain. Integration was carried out using Eq. (13), below. Grid convergence was studied using this parameter for two numerical schemes: the E4-AC4-C6-AC4-E4 compact difference scheme and the second-order accurate Steger-Warming scheme. Figure 2c shows the percentage error in the total enthalpy thickness, with the reference solution used as the baseline. The remarkable accuracy of the compact scheme relative to the Steger-Warming scheme is apparent in the plot. Note the difference in accuracy between the two filters used with the compact scheme.

B.   Transient Sheath Problem

As a test of the coupled potential and moment equations, this section investigates the effect of a suddenly-applied voltage on an initially-uniform, low-density plasma. This transient sheath problem was used as a test case in previous papers.[40,41]

American Institute of Aeronautics and Astronautics

A two-moment model was considered for the this problem. The ion and electron temperatures were held fixed at $T_i = 293$ K and $T_e = 11600$ K, respectively, and the electron number density was computed by assuming Boltzmann equilibrium, Eq. (6). Viscous forces and collisions with neutrals were neglected for the ions. This restricted model was implemented in the code by turning off selected terms in the full model.

The initial condition was taken to be a stationary, uniform plasma of number density $n_0 = 1 \times 10^{14}$ m^{-3}, and a potential of $\phi = -50$ V was suddenly applied at the left electrode ($x = 0$) at time $t = 0$. The potential at the right boundary of the computational domain was held fixed at zero.

The characteristic scales in this problem are the ion plasma frequency $f_p = \sqrt{n_o e^2/(4\pi^2 \epsilon_0 m_i)}$, the Bohm velocity $u_B = \sqrt{k_B T_e/m_i}$, and the electron Debye length $\lambda_D = \sqrt{\epsilon_0 k_B T_e/(n_0 e^2)}$. The computational domain was taken to be $L = 200\lambda_{De}$ wide. The ion properties at $x = 0$ were found by extrapolation (with an order of accuracy corresponding to that of the numerical scheme at the boundary), and the properties at $x = L$ of the computational domain were held fixed at $n_i = n_0$ and $u_i = 0$.

Figure 3a shows the distribution of ion and electron number densities at selected times for a reference calculation with the E4-AC4-C6-AC4-E4 compact difference scheme with a grid of 401 points and a nondimensional time step of $f_p \Delta t = 0.01$. With the sudden application of a negative potential, the electrons are repelled from the electrode, forming a layer of positive charge. The relatively massive ions slowly respond to the changed conditions, forming an ion current into the electrode. As a result, the space charge diminishes, and the sheath expands. Ahead of the sheath, a quasi-neutral presheath propagates into the bulk plasma.

The time-evolution of the ion current density $j_i = e n_i |u_i|$ at the electrode is shown in Fig. 3b. The inset shows the long-time behavior on an expanded time scale. There is an initial surge in current as the transient sheath forms, followed by a gradual relaxation to constant current density at large times. In this asymptotic state, the current to the electrode is balanced by ions uncovered by the expanding rarefaction wave. The presheath accelerates the ions up to approximately the Bohm velocity, supporting a quasi-steady sheath.

The transient sheath problem was studied analytically by Lieberman,[42] who developed approximate expressions for the time-evolution of the ion current density at the cathode. Lieberman used a matrix sheath model for the short-time behavior, and a Child law sheath model for the long-time solution. Qualitative agreement between the numerical solution and Lieberman's theory is seen in Fig. 3b. (This is the level of agreement seen by Lieberman as well.)

As a gauge of the quality of the solution for different numerical schemes, the ion current at $x = 0$ and $f_p t = 24$ was examined. The error in this quantity, relative to the reference solution, is plotted versus grid size in Fig. 3c. The Steger-Warming scheme and the E4-AC4-C6-AC4-E4 compact scheme with Filter A appear to converge, respectively, with the expected second and fourth order accuracy. The compact scheme with Filter B has a high absolute accuracy, but the slope does not have the expected value.

C. Steady-State Sheath

As a somewhat more complex test case, the problem of an ionized gas confined between a pair of planar electrodes fixed at a distance of $2L$ apart was considered. The electrodes were assumed to be maintained at a constant negative potential, and to draw a current that was maintained by 'direct' ionization.

In order to exercise more features of the code, a three-moment model of ion motion was considered, along with constant temperature, Boltzmann electrons and a uniform, neutral background gas at rest. Viscous forces on the ions were neglected. The ionization rate was taken to have the form $\omega = z n_e$. As in the previous case, this restricted model was implemented in the code by turning off selected terms in the full model.

The ion properties at $x = 0$ were found by extrapolation, whereas the following conditions were imposed at the symmetry plane ($x = L$): $n_i = n_0$, $\partial u_i/\partial x = z$, and $\partial T_i/\partial x = 0$. (The boundary conditions were imposed with an order of accuracy corresponding to that of the numerical scheme at the boundary.) The centerline boundary condition on the velocity follows from applying the symmetry conditions, and has been found to be more stable than directly imposing $u_i = 0$. The boundary conditions on the electric potential were $\phi(0) = -50$ V and $\phi(L) = 0$.

The temperatures of the neutral gas and the electrons were taken to be $T_n = 293$ K and $T_e = 11600$ K, respectively. The centerline number density was $n_0 = 1 \times 10^{14}$ m^{-3}. The neutral gas pressure was taken to be $p_n = 50$ mPa.

A procedure based on the integral form of the ion continuity equation was used to estimate, at each time step, the ionization frequency z required to achieve a steady state. Assuming a steady state, and integrating the ion continuity equation (1a) from the wall at $x = 0$ to the center at $x = L$, the following formula is obtained for the ionization rate:

$$z = \frac{-n_i u_i|_{x=0}}{\int_0^L n_e\ dx} \tag{12}$$

A new value of z was computed at the end of each time step from Eq. (12). In order to make the order of accuracy of the integration in Eq. (12) consistent with compact difference schemes of up to sixth order accuracy, the following integration formula was employed:

$$
\int_{x_0}^{x_n} f(x)\,dx = h\left\{\sum_{i=0}^{n} f_i - \frac{f_0 + f_n}{2}\right.
$$
$$
- \frac{23681 f_0 - 55688 f_1 + 66109 f_2 - 57024 f_3 + 31523 f_4 - 9976 f_5 + 1375 f_6}{120960}
$$
$$
\left. - \frac{23681 f_n - 55688 f_{n-1} + 66109 f_{n-2} - 57024 f_{n-3} + 31523 f_{n-4} - 9976 f_{n-5} + 1375 f_{n-6}}{120960}\right\} \tag{13}
$$

This is an eight-order accurate integration scheme, exact for a seventh order polynomial. (The author would like to thank Dr. Michael D. White of the Ohio Aerospace Institute for providing this formula.) The calculations were marched in time until the change of the ionization frequency and the independent variables with each time step had reached a minimum.

The computational domain was taken to be $L = 100\lambda_D$ in width, and a reference computation was carried out with a grid of 401 points using the E4-AC4-C6-AC4-E4 compact difference scheme. Figure 4a shows the ion and electron number densities and the ion temperature. The quasi-neutral presheath (where $n_i \approx n_e$) is apparent near the centerline, and the sheath (where $n_e \approx 0$) is visible near the electrode on the left. The ion temperature rises near the electrode due to the dissipative effects of elastic ion-neutral collisions (see Eq. 4a).

The electric potential and ion velocity are shown in Fig. 4b. The majority of the potential drop occurs in the sheath, with only a slight change in the presheath. Despite the collisional drag with the neutrals, the ions are seen to be strongly accelerated toward the electrode by the electric field in the sheath.

The error in the ionization rate z, relative to the reference solution, was chosen as a figure of merit for spatial convergence. The results of the convergence study are shown in Fig. 4c. The convergence behavior of the two schemes is seen to be similar to that observed in the previous examples.

D. Shock Structure with Three-Species Model

As a final test, a computation involving a three-species model of a shock in a weakly-ionized, nonequilibrium plasma was carried out. The flow conditions were chosen to be similar to those examined by Adamovich et al.[32] The upstream conditions for the neutrals were $u_1 = 645$ m/s, $p_1 = 1.3$ kPa, and $T_1 = 300$ K. The electron temperature was taken to be $T_e = 3.6$ eV, and the fractional ionization in the incoming flow was $n_{i,e}/n_n = 1 \times 10^{-6}$. The electric potential was set to zero at the upstream boundary, and extrapolation was used for all quantities at the downstream boundary. Ideal gas jump relations were used for the initial conditions.

As with the previous problems, the electrons were assumed to be in Boltzmann equilibrium. Ionization and recombination rates were chosen to match those of Adamovich et al.

The computational domain was $L = 5$ mm wide, and a grid of 1001 points was employed. The E4-AC4-C6-AC4-E4 compact difference scheme was used. For stability, Filter B was employed, and second-order extrapolation was used for the outlet boundary condition.

The results of the computations are shown in Fig. 5. Figure 5a shows the number density for each species and the electric potential. The velocity for each species is shown in Fig. 5b, and the corresponding temperatures in Fig. 5c. The shock transition zone is seen to be substantially thicker for the charged particles than for the neutral gas. The large difference in mass between the ions and electrons leads to charge separation in the vicinity of the neutral gas jump, setting up an electric potential rise of a few volts across the shock.

IV. Summary and Conclusions

This paper has explored the feasibility of applying high-order, compact difference methods to the modeling of glow discharges for high-speed flow control. High-order compact difference methods offer a possible means of achieving high spatial accuracy on coarser grids, potentially leading to a significant reduction in the computational cost of an accurate solution. Sample calculations were presented for shock and sheath problems in ionized argon, and the compact difference methods were shown to be superior in both absolute accuracy and rate of spatial convergence. Future work will focus on applying the compact difference method to problems of interest in plasma aerodynamics.

Acknowledgments

References

[1] Surzhikov, S. T. and Shang, J. S., "Two-Component Plasma Model for Two-Dimensional Glow Discharge in Magnetic Field," *Journal of Computational Physics*, Vol. 199, 2004, pp. 437–464.

[2] Mahadevan, S. and Raja, L. L., "Simulations of Glow Discharge Phenomena in Air for High-Speed Flow Control," AIAA Paper 2008-1093, American Institute of Aeronautics and Astronautics, Reston VA, January 2008.

[3] Poggie, J., "Numerical Simulation of Direct Current Glow Discharges for High-Speed Flow Control," *Journal of Propulsion and Power*, Vol. 24, No. 5, 2008, pp. 916–922.

[4] Poggie, J., "Numerical Simulation of DC and RF Glow Discharges," AIAA Paper 2007-0632, American Institute of Aeronautics and Astronautics, Reston VA, January 2007.

[5] Poggie, J., "Discharge Modeling for Flow Control Applications," AIAA Paper 2008-1357, American Institute of Aeronautics and Astronautics, Reston VA, January 2008.

[6] Lele, S. K., "Compact Finite Difference Schemes with Spectral-Like Resolution," *Journal of Computational Physics*, Vol. 103, 1992, pp. 16–42.

[7] Gaitonde, D. V. and Visbal, M. R., "High-Order Schemes for Navier-Stokes Equations: Algorithm and Implementation in FDL3D," AFRL Technical Report AFRL-VA-WP-TR-1998-3060, Air Force Research Laboratory, Wright-Patterson Air Force Base, Ohio, 1998.

[8] Ward, A. L., "Calculations of Cathode-Fall Characteristics," *Journal of Applied Physics*, Vol. 33, No. 9, 1962, pp. 2789–2794.

[9] Ward, A. L., "Effect of Space Charge in Cold-Cathode Gas Discharges," *Physical Review*, Vol. 112, No. 6, 1958, pp. 1852–1857.

[10] Boeuf, J.-P., "A Two-Dimensional Model of DC Glow Discharges," *Journal of Applied Physics*, Vol. 63, No. 5, 1988, pp. 1342–1349.

[11] Raizer, Y. P. and Surzhikov, S. T., "Two-Dimensional Structure in a Normal Glow Discharge and Diffusion Effects in Cathode and Anode Spot Formation," *High Temperature*, Vol. 26, No. 3, 1988, pp. 304–311.

[12] Passchier, J. D. P. and Goedheer, W. J., "A Two-Dimensional Fluid Model for an Argon RF Discharge," *Journal of Applied Physics*, Vol. 74, No. 6, 1993, pp. 3744–3751.

[13] Young, F. F., "Two-Dimensional, Self-Consistent, Three-Moment Simulation of RF Glow Discharges," *IEEE Transactions on Plasma Science*, Vol. 21, No. 3, 1993, pp. 312–321.

[14] Hong, M. and Emmert, G. A., "Two-Dimensional Fluid Modeling of Time-Dependent Plasma Sheath," *Journal of Vacuum Science and Technology*, Vol. 12, No. 2, 1994, pp. 889–896.

[15] Sheridan, T. E. and Alport, M. J., "Two-Dimensional Model of Ion Dynamics During Plasma Source Ion Implantation," *Applied Physics Letters*, Vol. 64, No. 14, 1994, pp. 1783–1785.

[16] Georghiou, G. E., Papadakis, A. P., Morrow, R., and Metaxas, A. C., "Numerical Modelling of Atmospheric Pressure Gas Discharges Leading to Plasma Production," *Journal of Physics D: Applied Physics*, Vol. 38, 2005, pp. R303–R328.

[17] Graves, D. B. and Jensen, K. F., "A Continuum Model of DC and RF Discharges," *IEEE Transactions on Plasma Science*, Vol. PS-14, No. 2, 1986, pp. 78–91.

[18] Richards, A. D., Thompson, B. E., and Sawin, H. H., "Continuum Modeling of Argon Radio Frequency Glow Discharges," *Applied Physics Letters*, Vol. 50, No. 9, 1987, pp. 492–494.

[19] Barnes, M. S., Cotler, T. J., and Elta, M. E., "A Staggered-Mesh Finite-Difference Numerical Method for Solving the Transport Equations in Low Pressure RF Glow Discharges," *Journal of Computational Physics*, Vol. 77, 1988, pp. 53–72.

[20] Hammond, E. P., Mahesh, K., and Moin, P., "A Numerical Method to Simulate Radio-Frequency Plasma Discharges," *Journal of Computational Physics*, Vol. 176, 2002, pp. 402–429.

[21] Meyyappan, M. and Kreskovsky, J. P., "Glow Discharge Simulation Through Solutions to the Moments of the Boltzmann Transport Equation," *Journal of Applied Physics*, Vol. 68, No. 4, 1990, pp. 1506–1512.

[22] Meyyappan, M., "A Continuum Model for Low-Pressure Radio-Frequency Discharges," *Journal of Applied Physics*, Vol. 69, No. 12, 1991, pp. 8047–8051.

[23] Widner, M., Alexeff, I., Jones, W. D., and Lonngren, K. E., "Ion Acoustic Wave Excitation and Ion Sheath Evolution," *The Physics of Fluids*, Vol. 13, No. 10, 1970, pp. 2532–2540.

[24] Sternberg, N. and Poggie, J., "Plasma-Sheath Transition in the Magnetized Plasma-Wall Problem for Collisionless Ions," *IEEE Transactions on Plasma Science*, Vol. 32, No. 6, 2004, pp. 2217–2226.

[25] Poggie, J. and Sternberg, N., "Transition from the Constant Ion Mobility Regime to the Ion-Atom Charge-Exchange Regime for Bounded Collisional Plasmas," *Physics of Plasmas*, Vol. 12, No. 2, 2005, pp. 023502–1–023502–9.

[26] Burgers, J. M., *Flow Equations for Composite Gases*, Academic Press, New York, 1969.

[27] Appleton, J. P. and Bray, K. N. C., "The Conservation Equations for a Non-Equilibrium Plasma," *Journal of Fluid Mechanics*, Vol. 20, No. 4, 1964, pp. 659–672.

[28] Chapman, S. and Cowling, T. G., *The Mathematical Theory of Non-Uniform Gases*, Cambridge University Press, 2nd ed., 1952.

[29] Morse, T. F., "Energy and Momentum Exchange between Nonequipartition Gases," *The Physics of Fluids*, Vol. 6, No. 10, 1963, pp. 1420–1427.

[30] Yuan, X. and Raja, L. L., "Computational Study of Capacitively Coupled High-Pressure Glow Discharges in Helium," *IEEE Transactions on Plasma Science*, Vol. 31, No. 4, 2003, pp. 495–503.

[31] Lister, G. G., "Low-Pressure Gas Discharge Modelling," *Journal of Physics D*, Vol. 25, No. 12, 1992, pp. 1649–1680.

[32]Adamovich, I. V., Subramaniam, V. V., Rich, J. W., and Macheret, S. O., "Phenomenological Analysis of Shock-Wave Propagation in Weakly Ionized Plasmas," *AIAA Journal*, Vol. 36, No. 5, 1998, pp. 816–822.

[33]White, F. M., *Viscous Fluid Flow*, McGraw-Hill, New York, 2nd ed., 1991.

[34]Hoffmann, K. A. and Chiang, S. T., *Computational Fluid Dynamics*, Engineering Educational System, Wichita KS, 4th ed., 2000.

[35]Anderson, W. K., Thomas, J. L., and van Leer, B., "A Comparison of Finite Volume Flux Vector Splittings for the Euler Equations," AIAA Paper 85-0122, American Institute of Aeronautics and Astronautics, Reston VA, January 1985.

[36]Cheney, W. and Kincaid, D., *Numerical Mathematics and Computing*, Brooks/Cole Publishing, Pacific Grove, California, 3rd ed., 1994.

[37]White, F. M., *Fluid Mechanics*, McGraw-Hill, New York, 1986.

[38]Zel'dovich, Y. B. and Raizer, Y. P., *Physics of Shock Waves and High-Temperature Hydrodynamic Phenomena*, Dover, Mineola NY, 2002, Reprint of 1967 translation, with corrections.

[39]Thompson, P. A., *Compressible-Fluid Dynamics*, McGraw-Hill, New York, 1972, Reprinted by author, 1988.

[40]Poggie, J. and Gaitonde, D. V., "Electrode Boundary Conditions in Magnetogasdynamic Flow Control," AIAA Paper 2002-0199, American Institute of Aeronautics and Astronautics, Reston VA, January 2002.

[41]Poggie, J., Gaitonde, D. V., and Sternberg, N., "Numerical Simulation of Plasma Sheaths in Aerodynamic Applications," AIAA Paper 2002-2166, American Institute of Aeronautics and Astronautics, Reston VA, May 2002.

[42]Lieberman, M. A., "Model of Plasma Immersion Ion Implantation," *Journal of Applied Physics*, Vol. 66, No. 7, 1989, pp. 2926–2929.

Scheme	α	a	b	Stencil	Order
E2	0	1	0	3	2
E4	0	4/3	-1/3	5	4
C4	1/4	3/2	0	3	4
C6	1/3	14/9	1/9	5	6

Table 1. Coefficients for compact difference schemes at interior points. Adapted from Gaitonde and Visbal.[7]

Scheme	Filter A	Filter B
E2-DE2-E2-DE2-E2	F0-FB$_{2,4}$-F4-FB$_{2,4}$-F0	F0-F2-F4-F2-F0
E4-DE4-E4-DE4-E4	F0-FB$_{2,6}$-FB$_{3,6}$-F6-FB$_{3,6}$-FB$_{2,6}$-F0	F0-F2-F4-F6-F4-F2-F0
E4-AC4-C4-AC4-E4	F0-FB$_{2,6}$-FB$_{3,6}$-F6-FB$_{3,6}$-FB$_{2,6}$-F0	F0-F2-F4-F6-F4-F2-F0
E4-AC4-C6-AC4-E4	F0-FB$_{2,6}$-FB$_{3,8}$-FB$_{4,8}$-F8-FB$_{4,8}$-FB$_{3,8}$-FB$_{2,6}$-F0	F0-F2-F4-F6-F8-F6-F4-F2-F0
E6-AC6-C6-AC6-E6	–	–

Table 2. Compact difference schemes and corresponding filters. Notation of Gaitonde and Visbal.[7]
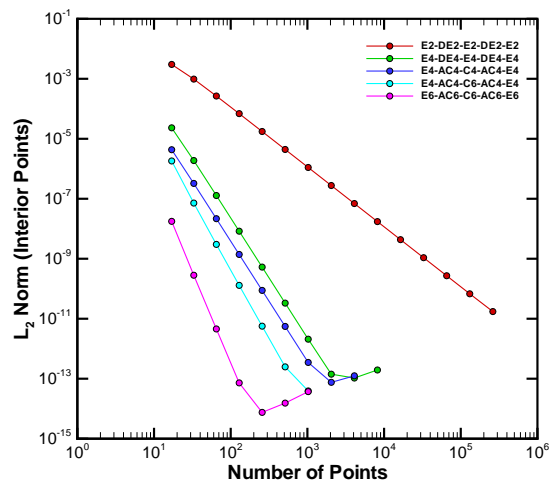
Scheme	a_0	a_1	a_2	$a3$	a_4	Order
F2	$\frac{1+2\alpha_f}{2}$	$\frac{1+2\alpha_f}{2}$	0	0	0	2
F4	$\frac{5+6\alpha_f}{8}$	$\frac{1+2\alpha_f}{2}$	$\frac{-1+2\alpha_f}{8}$	0	0	4
F6	$\frac{11+10\alpha_f}{16}$	$\frac{15+34\alpha_f}{32}$	$\frac{-3+6\alpha_f}{16}$	$\frac{1-2\alpha_f}{32}$	0	6
F8	$\frac{93+70\alpha_f}{128}$	$\frac{7+18\alpha_f}{16}$	$\frac{-7+14\alpha_f}{32}$	$\frac{1-2\alpha_f}{16}$	$\frac{-1+2\alpha_f}{128}$	8

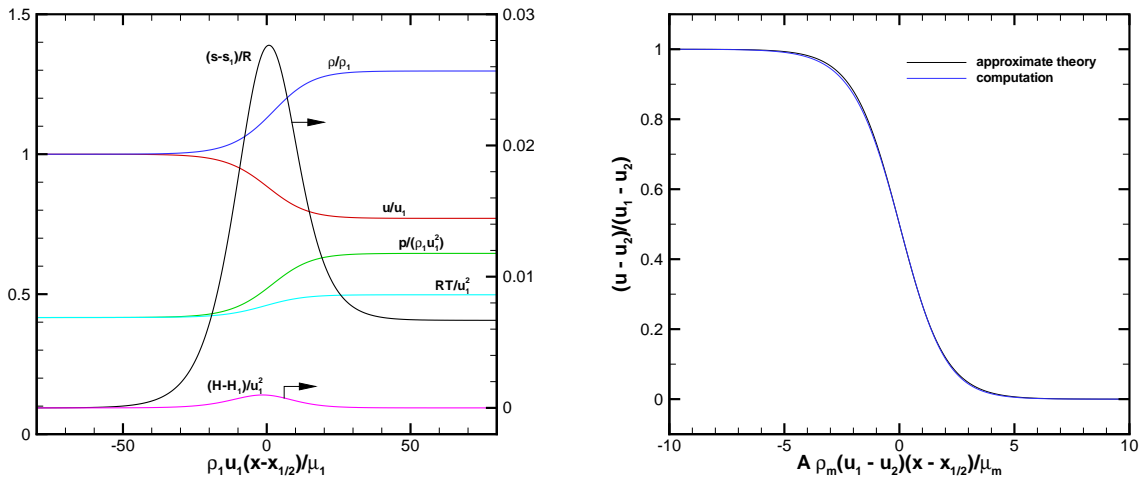**Table 3. Coefficients for filter schemes at interior points. Adapted from Gaitonde and Visbal.[7]**
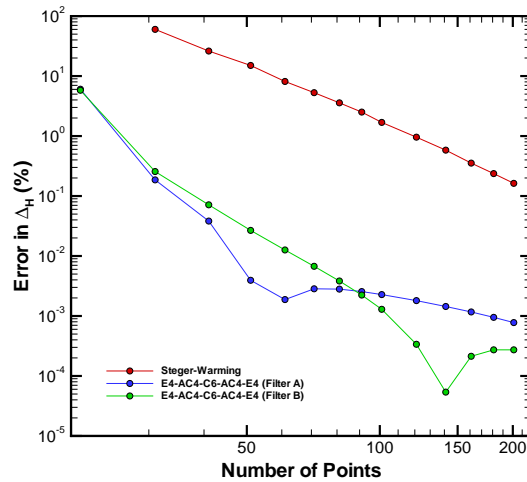
(a) L$_2$-norm for full domain.

(b) L$_2$-norm for interior points only.

Figure 1. Accuracy of $(\sin x)'$ with various compact difference schemes (see Table 2).
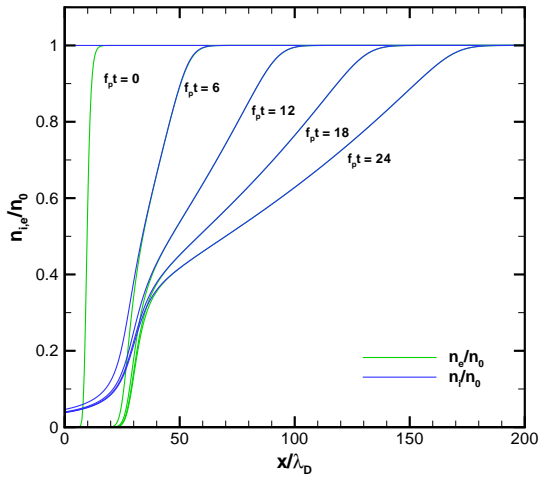
31

(a) Basic shock structure, computed with E4-AC4-C6-AC4-E4 scheme.

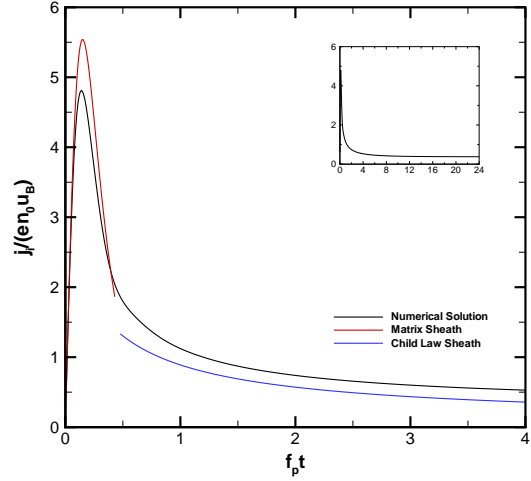(b) Comparison of approximate theory to computation with E4-AC4-C6-AC4-E4 scheme.

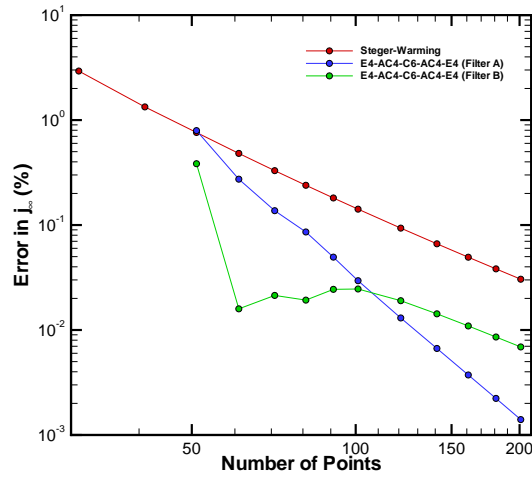(c) Spatial convergence for two numerical schemes.

Figure 2. Shock structure in argon at Mach 1.2.
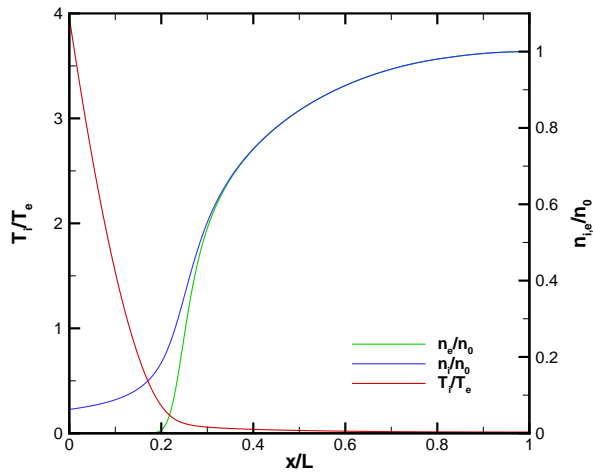
(a) Ion and electron number densities at selected times, E4-AC4-C6-AC4-E4 scheme.

(b) Time-history of ion current at negative electrode, numerical results with E4-AC4-C6-AC4-E4 scheme.

(c) Convergence of asymptotic ion current at electrode, $j(x = 0, t = 24)$.

Figure 3. Evolution of transient sheath.

(a) Ion and electron number densities, ion temperature.
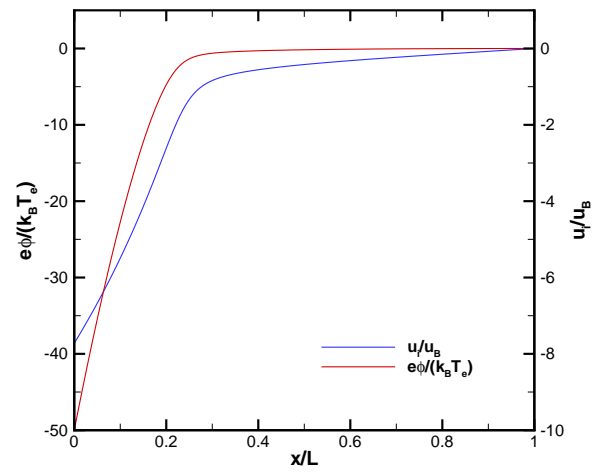
(b) Electric potential and ion velocity.
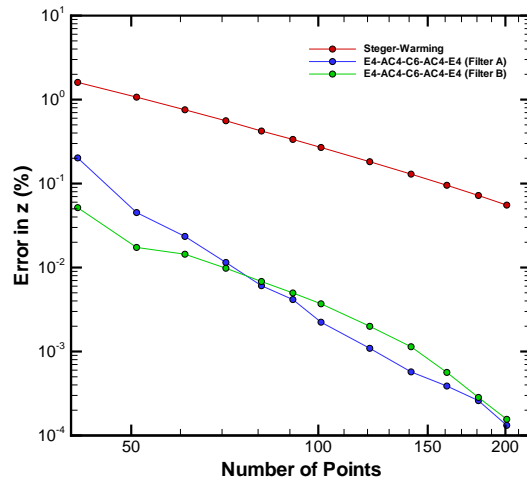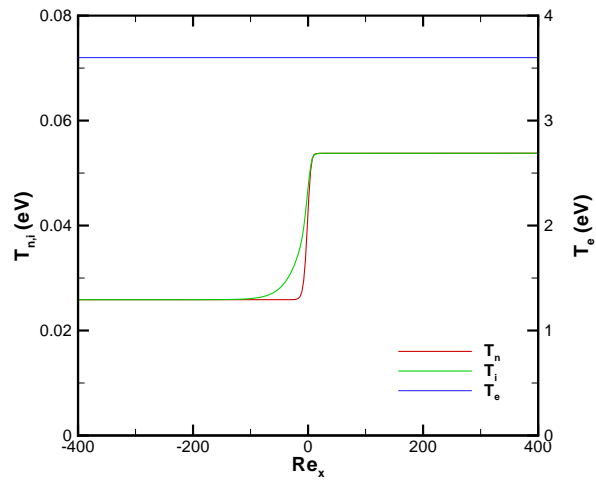

(c) Convergence of ionization rate.

Figure 4. Steady-state plasma-sheath problem.

American Institute of Aeronautics and Astronautics
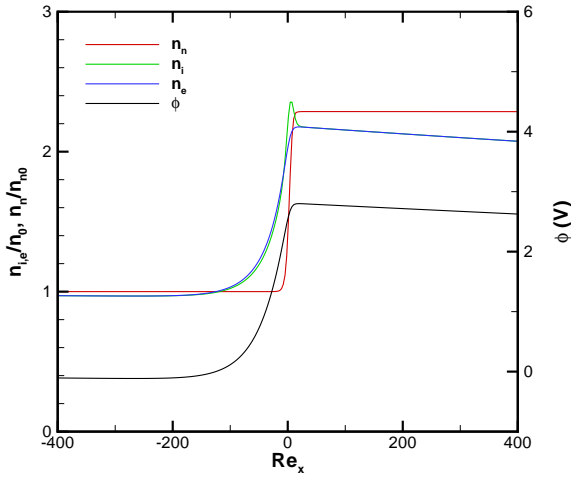
(a) Number densities and electric potential.
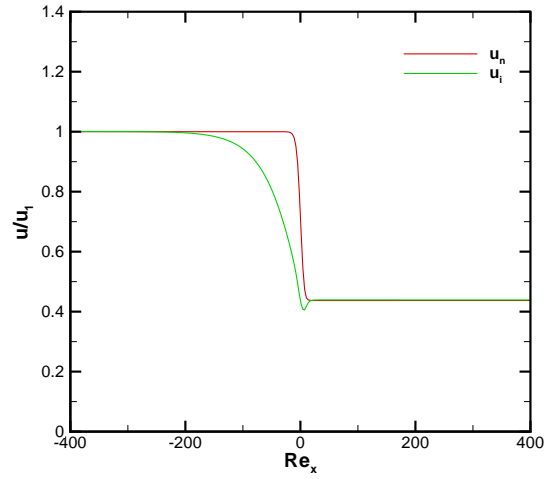
(b) Velocity.

(c) Temperature.

Figure 5. Three-species model of shock structure.

Compact Difference Methods
for Discharge Modeling in Aerodynamics

Jonathan Poggie*

Air Force Research Laboratory, Wright-Patterson AFB, Ohio 45433-7512 USA

   This paper explores the feasibility of applying high-order, compact difference methods to the modeling of glow discharges for high-speed flow control. Previous papers (AIAA 2008-1357) have successfully applied second-order finite difference methods to glow discharge modeling. Detailed grid resolution studies, however, have revealed that very fine grid resolution is required for acceptable quantitative results. High-order compact difference methods offer a possible means of achieving high spatial accuracy on coarser grids, potentially leading to a significant reduction in the computational cost of an accurate solution. In previous work (AIAA 2009-1047), preliminary, one-dimensional compact difference calculations were carried out for glow discharge problems. Here the work is extended to two dimensions. Sample compact difference calculations are presented for several test cases, including a Poisson equation solution, a compressible Couette flow problem, a hypersonic laminar boundary layer flow, and a transient plasma-sheath problem. Spatial convergence of second- through sixth-order compact schemes was investigated, and found to be comparable to the theoretical order of accuracy. In particular, compact difference methods of up to sixth order can successfully achieve their theoretical order of accuracy for the coupled Poisson and Euler equations with source terms. Compact difference schemes appear to be a promising numerical approach for modeling plasma actuators for high-speed flow control.

I.   Introduction

   Since the mid-1990s, there has been considerable research interest in plasma-based flow control techniques for aerospace applications. Because of their favorable weight and power consumption properties, small-scale actuators based on glow and arc discharges have become increasingly popular, and much effort has been invested in numerical modeling of actuator behavior.[1–3]

   Toward this end, the author has developed a second-order accurate, finite-difference code capable of modeling the region of finite space-charge present in the vicinity of electrode surfaces in the electric discharges used for flow control.[3–5] The physical model includes the fluid conservation laws for the bulk gas flow, a model for charged particle motion, and a self-consistent computation of the electric potential. This code has been successfully applied to a variety of discharge problems, including low-density plasma-sheath problems, DC glow discharges, and RF glow discharges. Comparisons among different numerical methods have been carried out, and a central difference scheme, an upwind scheme, and a finite difference implementation of the Sharfetter-Gummel scheme have all been found to give very similar results.

   Recently, an investigation was carried out on spatial resolution issues in modeling DC glow discharges.[4,5] A detailed grid resolution study was carried out, and very fine grid resolution was found to be required for acceptable quantitative results. Coarse grids led to underestimates of number density, temperature, and current density and to overestimates of the lateral extent of the discharge column.

   High-order compact difference methods[6,7] offer a possible means of achieving high spatial accuracy on coarser grids, potentially leading to a significant reduction in computational cost. In previous work,[8] preliminary, one-dimensional compact difference calculations were carried out for glow discharge problems. Here the work is extended to two dimensions. Sample compact difference calculations are presented here for several test cases, including a Poisson equation solution, a compressible Couette flow problem, a hypersonic laminar

---

   *Senior Aerospace Engineer, Computational Sciences Branch, AFRL/RBAC, 2210 Eighth St., Associate Fellow AIAA.
Cleared for public release, distribution unlimited (88ABW-2009-2441).

boundary layer flow, and a transient plasma-sheath problem. Accuracy is evaluated for second- through sixth-order compact schemes, and compared to standard second-order upwind schemes.

II.   Methods

The physical model and the numerical methods are described in this section. The physical model includes the fluid conservation laws for the motion of each species and a self-consistent computation of the electric potential. The baseline numerical implementation involves compact spatial differences of up to sixth order accuracy, driven by a low-storage, fourth-order Runge-Kutta time marching scheme.

A.   Physical Model

Continuum methods, based on moments of the Boltzmann equation, have been a popular and productive means of modeling electrical discharges. One-dimensional modeling of direct-current glow discharges was carried out as early as the late 1950s,[9,10] and two-dimensional simulations were first carried out in the late 1980s.[11,12] By the early 1990s, two dimensional simulations of radio-frequency glow discharges[13,14] and transient low-density discharges[15,16] had been performed. Three-dimensional simulations have appeared more recently.[3,17]

A variety of physical models have been employed in such work. One of the most common models is drift-diffusion, assuming local equilibrium with the electric field, so that the transport and ionization coefficients are a function of the local reduced field E/N.[9,11,12] The next step up in generality is to solve the electron energy equation as well, and use the local electron temperature T_e instead of the local E/N to determine the coefficients.[18,19]

Some studies have used continuity-momentum equations in place of the drift-diffusion model, thus including the effects of particle momentum. The role of inertia in DC and RF discharges has been examined, including the momentum of the electrons,[20] the heavy particles,[21] or both.[22,23] Ion inertia is important in the transient sheath that appears in plasma-source ion implantation,[24] and in modeling the low-density plasma-sheath transition.[25,26]

One aim of this ongoing project is to determine limits of the moment method in modeling electrical discharges, specifically whether a three-moment model for each species can be accurate and computationally tractable. A relatively general formulation of the conservation equations for electrical discharges is outlined below, based on standard references.[27–29] Briefly, the conservation laws can be derived from moments of the Boltzmann equation, with closure models utilized for the inelastic collision source terms,[29] the elastic collision source terms,[29,30] and the flux terms.[28,31,32]

1.   Governing Equations

The problem of sheath structure in ionized argon was used as a test case in the current project. Gravity is neglected, and the absence of an applied magnetic field is assumed. The conservation equations for each species are:

$$\frac{\partial}{\partial t}(m_s n_s) + \nabla \cdot (m_s n_s \mathbf{v}_s) = S_s$$

$$\frac{\partial}{\partial t}(m_s n_s \mathbf{v}_s) + \nabla \cdot (m_s n_s \mathbf{v}_s \mathbf{v}_s + p_s \mathbf{I}) = \nabla \cdot \tau_s + q_s n_s \mathbf{E} + \mathbf{A}_s \tag{1}$$

$$\frac{\partial}{\partial t}\left[m_s n_s \left(\epsilon_s + \tfrac{1}{2}v_s^2\right)\right] + \nabla \cdot \left[m_s n_s \mathbf{v}_s \left(\epsilon_s + \tfrac{1}{2}v_s^2\right) + p_s \mathbf{v}_s\right] = \nabla \cdot [\tau_s \cdot \mathbf{v}_s - \mathbf{Q}_s] + q_s n_s \mathbf{v}_s \cdot \mathbf{E} + M_s$$

where the notation $s = n, i, e$ indicates the neutrals, ions, and electrons, respectively.

The mass per particle of each species is denoted as m_s, and the corresponding charge per particle is $q_n = 0$, $q_i = +e$, and $q_e = -e$. The number density is n_s, the velocity is $\mathbf{v}_s$, and the translational temperature is T_s. The electric field is $\mathbf{E}$, and the symbol k_B indicates the Boltzmann constant. The pressure is found from $p_s = n_s k_B T_s$, and the internal energy per particle is assumed to have the form $m_s \epsilon_s = H_s + k_B T_s/(\gamma_s - 1)$, where $\gamma_s = 5/3$ is the ratio of specific heats. The heat of formation is $H_n = H_e = 0$ and $H_i = \mathcal{H}$, where $\mathcal{H} = 15.7$ eV for argon ionization.

It assumed that the gas is weakly ionized, so that the primary elastic collisions are with neutral particles. For the inelastic collisions, it is assumed that the species appear or disappear with the average momentum and energy of their peers, except for the electrons, which lose energy $\mathcal{H}$ in each inelastic collision.

The net production rate ω of charged particles in argon gas was given by:

$$\omega = k_f n_n n_e - k_b n_i n_e$$

$$k_f = \sigma_T \sqrt{\frac{8k_B T_e}{\pi m_e}} \left(1 + \frac{E_i}{k_B T_e}\right) \exp\left(-\frac{E_i}{k_B T_e}\right) \tag{2}$$

with $\sigma_T = 2 \times 10^{-12}$ m^2, $E_i = 15.7$ eV, $k_b = 3.5 \times 10^{-14}$ m^3/s. The ionization rate is from Meyyappan and Kreskovsky[22] and the recombination rate is from Adamovich et al.[33] The species source terms become:

$$S_i = m_i \omega$$
$$S_e = m_e \omega \tag{3}$$
$$S_n = -m_n \omega$$

The momentum source terms are:

$$\mathbf{A}_i = \omega m_i \mathbf{v}_i - n_i m_{in} \nu_{in}(\mathbf{v}_i - \mathbf{v}_n)$$
$$\mathbf{A}_e = \omega m_e \mathbf{v}_e - n_e m_{en} \nu_{en}(\mathbf{v}_e - \mathbf{v}_n) \tag{4}$$
$$\mathbf{A}_n = -(\mathbf{A}_i + \mathbf{A}_e)$$

The collision frequency between the charged and neutral species ν_{sn} was estimated from mobility data, with the correlations for ion and electron mobility in argon taken from Ward.[10] The energy source terms are:

$$M_i = \omega\left(\mathcal{H} + \frac{k_B T_i}{\gamma_i - 1} + \tfrac{1}{2}m_i v_i^2\right) - \frac{n_i m_{in} \nu_{in}}{m_i + m_n}\left[3k_B(T_i - T_n) + (\mathbf{v}_i - \mathbf{v}_n)\cdot(m_i \mathbf{v}_i + m_n \mathbf{v}_n)\right]$$

$$M_e = \omega\left(-\mathcal{H} + \frac{k_B T_e}{\gamma_e - 1} + \tfrac{1}{2}m_e v_e^2\right) - \frac{n_e m_{en} \nu_{en}}{m_e + m_n}\left[3k_B(T_e - T_n) + (\mathbf{v}_e - \mathbf{v}_n)\cdot(m_e \mathbf{v}_e + m_n \mathbf{v}_n)\right] \tag{5}$$

$$M_n = -(M_i + M_e)$$

For the neutral particles, it was assumed that the viscous term had a Newtonian form, with Stokes hypothesis applied, and that the heat flux followed Fourier's law:[34]

$$\tau_n = \mu_{vn}\left[(\nabla \mathbf{v}_n) + (\nabla \mathbf{v}_n)^T - \tfrac{2}{3}\nabla \cdot \mathbf{v}_n \mathbf{I}\right]$$
$$\mathbf{Q}_n = -k_n \nabla T_n \tag{6}$$

where μ_{vn} is the viscosity and k_n is the thermal conductivity for the neutral particles. The viscosity and thermal conductivity of the charged particles were neglected for the present work.

To complete the physical model, the electric field must be found from a consistent solution of Maxwell's equations. For the present work, the Poisson equation was solved for the electric potential:

$$\nabla^2 \phi = -\frac{e}{\epsilon_0}(n_i - n_e) \tag{7}$$

and the electric field was found from $E = -\nabla \phi$.

2. Nondimensionalization

The equations were solved in non-dimensional form. For brevity, only an outline of the nondimensionalization procedure is given here. Global reference quantities were chosen for length L_R, velocity u_R, number density n_R, potential ϕ_R, collision rate ν_R, viscosity μ_{vR}, and thermal conductivity k_R. For each species, however, there was a different reference density $\rho_{Rs} = m_s n_R$, temperature $T_{Rs} = m_s u_R^2/k_B$, and pressure $p_{Rs} = m_s n_R u_R^2$. Space charge was normalized by the electron charge e, and heat of formation was normalized by $m_s u_R^2$.

The nondimensionalized equations have much the same form as (1)-(7). In addition to a Reynolds number and Prandtl number for each species, the following nondimensional parameters appeared as a consequence of this form of nondimensionalization:

$$\Phi_s = \frac{e\phi_R}{m_s u_R^2} \quad C = \frac{\nu_R L_R}{u_R} \quad a = L_R\sqrt{\frac{en_R}{\epsilon_0 \phi_R}}$$

The nondimensional parameters are, respectively, a relative field strength, a nondimensional collision frequency parameter, and a non-neutrality parameter.

B. Numerical Methods

The governing equations (1)-(6) were solved using a fourth-order accurate, low-storage Runge-Kutta time marching scheme combined with either a compact spatial difference scheme, Steger-Warming flux splitting, or Roe flux difference splitting. The compact formalism was evaluated with second- through sixth-order accurate differencing, whereas the upwind schemes employed third-order upwind biased differencing in the MUSCL formalism. For the compact scheme, stability was enforced by filtering, typically with a filter of two orders greater than the accuracy of the basic scheme. The Poisson equation (7) was solved by an iterative scheme (described below), with either central or compact spatial differences. The Poisson solution was not filtered. The metric terms were evaluated with central or compact differencing of an order corresponding to the basic scheme.

1. Governing Equations

In transformed coordinates, the conservation laws (1) can be written in the form:

$$\frac{\partial U}{\partial t} + \frac{\partial E}{\partial \xi} + \frac{\partial F}{\partial \eta} = \frac{\partial E_v}{\partial \xi} + \frac{\partial F_v}{\partial \eta} + S \tag{8}$$

where U is the vector of conserved variables, E and F are the inviscid flux vectors, E_v and F_v are the viscous flux vectors, and S represents the source terms. A standard, low-storage, fourth-order Runge-Kutta scheme[35] was used for time integration of Eq. (8). Three different schemes were used to evaluate the spatial differences: either a compact difference scheme of up to sixth-order accuracy (described below), the Steger-Warming flux split scheme, or the Roe flux difference split scheme. The upwind schemes used third-order MUSCL extrapolation[36] for the inviscid fluxes and second-order central differencing for the viscous terms.

The Poisson equation (7) was solved at the end of each stage of the Runge-Kutta time-integration. It can be written in the following form in transformed coordinates:

$$\frac{\partial E}{\partial \xi} + \frac{\partial F}{\partial \eta} = S_\phi \tag{9}$$

An iteration procedure was introduced such that the potential at iteration step m was $\phi^{m+1} = \phi^m + \Delta\phi$. With a linear expansion about the solution from the previous iteration, and approximate factoring of the implicit terms, the discretized equation has the form:

$$[1 - \Delta\tau(\delta_\xi A\delta_\xi - D)]\,[1 - \Delta\tau\delta_\eta B\delta_\eta]\,\Delta\phi = \omega\Delta\tau\left[\frac{\partial E^m}{\partial \xi} + \frac{\partial F^m}{\partial \eta} - S_\phi^m\right] \tag{10}$$

with iteration driving $\Delta\phi$ to zero. Here A and B are flux Jacobians, D is the source Jacobian, τ is a time-like variable introduced to motivate the iteration process, and ω is an over-relaxation factor. Discretizing the left-hand side using second order central differences in space, a tridiagonal system of equations is obtained. (Since iteration drives $\Delta\phi$ to zero, the form of the discretization of the left-hand-side does not affect the order of spatial accuracy of the converged solution.) Either central or compact difference schemes were used to evaluate the spatial differences present on the right hand side of Eq. (10), and the system was solved using the Thomas tridiagonal algorithm.[37] The pseudo-time-step $\Delta\tau$ was varied cyclically to accelerate convergence, and iteration was continued until the change in potential $\Delta\phi$ had dropped below a specified tolerance.

2. Compact Differences

Considering a one-dimensional, uniform mesh, the following central difference scheme[6,7] with a 5-point stencil can be used to generate estimates of the first derivative $\phi_i' = \partial \phi / \partial x|_{x_i}$ with up to sixth-order accuracy:

$$\alpha \phi_{i-1}' + \phi_i' + \alpha \phi_{i+1}' = a \frac{\phi_{i+1} - \phi_{i-1}}{2\,\Delta x} + b \frac{\phi_{i+2} - \phi_{i-2}}{4\,\Delta x} \tag{11}$$

Here α, a, and b are constants that are used to alter the properties of the scheme, and $\phi(x)$ is a generic function, not to be confused with the electric potential. Taylor series expansions can be used to derive a family of second- to sixth-order accurate schemes employing this template.[6,7] Table 1 gives selected coefficients for internal points using Eq. (11) for different orders of accuracy. Note that the implicit form of the scheme ($\alpha \neq 0$) results in a narrower stencil for a given order of accuracy than for an explicit form ($\alpha = 0$). Modified schemes[7] were used near boundaries, where the interior stencil would protrude outside of the domain.

Table 2 shows the forms of the compact difference scheme that were examined in this project, using the notation of Gaitonde and Visbal. To evaluate the derivative at each point, the appropriate form of Eq. (11) was solved using the Thomas tridiagonal algorithm.[37] Second derivatives were evaluated by applying the differencing scheme twice.

Numerical stability was enforced using filtering, typically with a filter of two orders greater than the accuracy of the basic scheme. The form of the filtering scheme[7] for interior points was as follows:

$$\alpha_f \overline{\phi}_{i-1} + \overline{\phi}_i + \alpha_f \overline{\phi}_{i+1} = \sum_{n=0}^{N} \frac{a_n}{2} (\phi_{i+n} + \phi_{i-n}) \tag{12}$$

where $\overline{\phi}_i$ is the filtered value of ϕ_i, and $N+1$ is the order of the filter. A table of coefficients for interior-point filters of second to eighth order is given in Table 3. Modified filters were used near the boundaries; the various options are shown in Table 2. (In the table, F0 indicates that no filter was applied to the boundary points.) The filter was applied to the conserved variables at the end of a time step, and the boundary conditions were updated so that the boundary points were consistent with the filtered interior points. For the cases labeled Filter A in Table 2, the filter's free parameter was set to $\alpha = 0.40$, whereas for Filter B, the value was varied between $\alpha = 0.495$ at the boundary and $\alpha = 0.400$ for the interior points.

III. Results

Sample compact difference calculations are presented here for several test cases, including a Poisson equation solution, a compressible Couette flow problem, a hypersonic laminar boundary layer flow, and a transient plasma-sheath problem. Accuracy is evaluated for second- through sixth-order compact schemes, and compared to standard second-order upwind schemes.

A. Poisson Solver Test

To verify the correct implementation of the Poisson solver, the code was tested against the following problem:

$$\frac{\partial^2 \phi}{\partial x^2} + \frac{\partial^2 \phi}{\partial y^2} = xe^y \tag{13}$$

with $\phi = xe^y$ imposed on the boundary of the domain. The analytical solution for this problem is $\phi(x, y) = xe^y$.

Calculations were carried out with the compact difference schemes 1-5 in Table 2, and compared to calculations using a second-order central difference scheme. For each case, the solver was run for 10^5 iterations to ensure convergence to machine precision.

Sample results are shown in Fig. 1 for a 31×31 computational mesh (see Fig. 1a). The mesh is deliberately distorted to test the correct implementation of the metric terms. The solution obtained with Compact Scheme 5 is shown in Fig. 1b. The value of the potential rises smoothly from zero at the origin to about 2.7 at the upper right corner of the domain. The absolute error is shown, respectively, for the compact and central difference schemes in Figs. 1c-d. The maximum absolute error for the compact scheme was 6.3×10^{-6}, whereas the corresponding error for the central scheme was 1.3×10^{-2}.

40

The iterative convergence rate of of the two schemes is examined in Fig. 2a. The maximum change in the potential is plotted as a function of iteration number. Oscillations appear in the plots because of the cyclic variation of the pseudo-time parameter. The envelope of the curves drops almost linearly on these semi-log plots. Eventually, the limit of machine precision is reached, and the value levels off. The solution converged more slowly with the compact scheme, probably because the left-hand-side of Eq. (10) was evaluated using a second-order central difference framework. This issue will be addressed in future work.

Figure 2b shows the maximum error for each numerical scheme as a function of mesh size for grids between 11×11 and 161×161. The slope of the lines on the log-log plot follows the expected value for the order of the scheme. (Each curve is a power-law fit to the points, and is annotated with the absolute value of its exponent.) Generally, the compact schemes show better absolute accuracy than corresponding explicit numerical schemes of the same order. The second-order scheme in the compact formalism has higher absolute accuracy than the conventional central scheme. The difference between these two cases lies in the manner in which the second derivative is evaluated (conventional vs. first derivative applied twice).

B.   Compressible Couette Flow

As a test of the diffusion terms in the conservation laws, computations were carried out for a compressible Couette flow problem. A single species of neutral gas was assumed. This problem has a similar nature to the Poisson solver test, but includes the effects of variable transport properties, so is weakly non-linear. Further, the steady-state solution is obtained through time-marching, rather than iteration.

The problem consists of a thin layer of gas between two walls, one moving and one stationary, which are separated by a distance H. The lower wall ($y = 0$) is labeled 1, and the upper wall ($y = H$) is labeled 2. The boundary conditions are:

$$
\begin{aligned}
u(x,0) &= 0 & T(x,0) &= T_1 \\
u(x,H) &= u_2 & T(x,H) &= T_2
\end{aligned}
\tag{14}
$$

with $\partial/\partial x = 0$. The Prandtl number was assumed to be Pr = 0.72 and the viscosity was assumed to vary linearly with temperature. This problem has the following analytical solution:

$$
y^* = \frac{2u^* \left[T_1^* + \frac{1}{2} \left(1 - T_1^* \right) u^* + \mathrm{Pr} \frac{\gamma-1}{2} M^2 \left(\frac{1}{2} u^* - \frac{1}{3} u^{*2} \right) \right]}{1 + T_1^* + Pr \frac{\gamma-1}{6} M^2}
\tag{15}
$$

$$
T^* = T_1^* + \left(1 - T_1^* \right) u^* + \mathrm{Pr} \frac{\gamma - 1}{2} M^2 \left(u^* - u^{*2} \right)
$$

where $M = u_2/a_2$, $y^* = y/H$, $u^* = u/u_2$, and $T^* = T/T_2$.

Sample calculations were carried out for $M = 2$ and $T_1/T_2 = 2$, exercising only the neutral-gas module in the computer code. Filter A of Table 2 was used for these computations. Solution profiles are shown in Fig. 3a, where the analytical solution is compared to the numerical solution with Compact Scheme 5 on a 9×11 point mesh. The results computed with this high-order scheme are seen to match the analytical solution closely even for this course mesh. For the incompressible case ($M = 0$), both profiles would be linear; see Eq. (15). A moderate temperature rise due to dissipation is evident for this Mach 2 flow, and there is a corresponding distortion of the velocity profile.

The results of a grid convergence study are shown in Fig. 3b for each of the spatial differencing schemes of Table 2. Grids of 11, 21, 41, and 81 points in the y-direction were employed. Each of the schemes is seen to converge at rate close to its theoretical order of accuracy. (Each curve is annotated with the exponent of the power-law curve fit.) Interestingly, the mixed fourth and sixth order scheme is almost as accurate as the full sixth-order scheme for this problem. This high accuracy is probably a consequence of the mesh clustering near the boundaries that was employed for these test cases.

C.   Hypersonic Boundary Layer

As a full test of the basic fluid solver, computations were carried out for a Mach 6, laminar boundary layer flow in air. The thermophysical properties of air were taken from White,[34] and the modules for the Poisson equation and charged particle motion were turned off in the code. The Reynolds number, based on plate length, was $\mathrm{Re}_L = 1.8 \times 10^5$. An adiabatic wall boundary condition was chosen in order to introduce a strong hypersonic interaction effect.

The computational grid consisted of 101×101 points, with clustering near the wall and leading edge. Three numerical schemes were employed: Roe, Steger-Warming, and a mixed scheme with fourth-order compact differencing used in smooth regions and the Roe scheme employed where a shock was detected. Filter B of Table 2 was used for these computations.

The procedure for handling shocks with the compact scheme was largely based on the work of Visbal and Gaitonde.[38] Briefly, a simple, thresholded pressure-field smoothness switch was used to identify certain cells as containing a shock. The pressure field is shown in Fig. 4a, and the shock locations identified by the pressure switch are shown in Fig. 4b. The filter scheme was smoothly blended between no filtering at a shock, and full sixth-order filtering in regions of smooth solution away from shocks. Analogously, the scheme was blended between the Roe scheme at the shock and the full fourth-order compact scheme in smooth regions.

Velocity and temperature profiles obtained with each scheme are compared to a similarity solution corresponding to the local edge Mach number in Fig. 5a. Because of the streamwise pressure gradient caused by the hypersonic leading edge interaction effect, exact similarity does not exist for this flow. Nevertheless, reasonable agreement is obtained between the numerical results and the similarity solution. The three numerical schemes are seen to agree fairly closely.

Skin friction and recovery factor profiles provide a more challenging test of the accuracy of the numerical scheme, as shown in Fig. 5b. All three schemes agree closely for the recovery factor. The Roe and mixed compact schemes agree closely for the skin friction, but the highly dissipative (unmodified) Steger-Warming scheme does not accurately capture this property.

D. Transient Sheath

As a test of the coupled moment equations and Poisson equation, a two-dimensional transient sheath problem was considered, investigating the effect of a suddenly-applied voltage on an initially-uniform, low-density plasma in an annular domain. A similar transient sheath problem has been used as a one-dimensional test case in previous papers.[39, 40]

A three-moment model was considered for this problem. The ion properties were computed using the conservation laws (1), whereas the electron temperature was held fixed at $T_e = 11600$ K and the electron number density was computed by assuming Boltzmann equilibrium: $n_e = n_0 \exp(e\phi/k_B T_e)$. Both inelastic and elastic collisions were included in the computation, but ionization was negligible for the conditions examined here. The neutral background gas was assumed to be at rest with a temperature of 300 K and a pressure of 0.07 Pa.

A sample 101×101 computational mesh is shown in Fig. 6a. The spatial coordinates are nondimensionalized by the electron Debye length $\lambda_D = \sqrt{\epsilon_0 k_B T_e/(n_0 e^2)}$. An O-type mesh was employed, with 5 points of overlap in the circumferential direction.

The initial condition was taken to be a stationary, uniform plasma of number density $n_0 = 1 \times 10^{14}$ m^{-3} and temperature $T_i = 300$ K, and a potential of $\phi = -50$ V was suddenly applied at the inner electrode $(r = 100\lambda_D)$ at time $t = 0$. The potential at the outer boundary of the computational domain was held fixed at zero. Ion properties at the outer boundary were held fixed, while extrapolation consistent with each numerical scheme and supersonic ion outflow was used at the inner boundary.

The ionized gas has the following response to the change in boundary conditions. With the sudden application of a negative potential, the electrons are repelled from the electrode, forming a layer of positive charge. The relatively massive ions slowly respond to the changed conditions, forming an ion current into the electrode. As a result, the space charge diminishes, and the sheath expands. Ahead of the sheath, a quasi-neutral presheath propagates into the bulk plasma as an expansion wave.

Figure 6b shows the distribution of ion number density at $\omega_{pi}t = 18$, where $\omega_{pi} = \sqrt{n_o e^2/(\epsilon_0 m_i)}$. Corresponding radial profiles are shown in Figs. 7a-b, and the time-history of the ion current density at the inner electrode is shown in Fig. 7c. Here, number density is nondimensionalized by the initial plasma density n_0, the velocity is nondimensionalized by the the Bohm velocity $u_B = \sqrt{k_B T_e/m_i}$, and the temperature is nondimensionalized by the electron temperature T_e.

The space charge layer is evident for the approximate range $100 \leq r \leq 130$, and a large corresponding potential drop is evident (Fig. 7a). The large electric field there leads to high ion velocities, and high ion temperatures brought about by the dissipative effects of elastic ion-neutral collisions (Fig. 7b).

The time-evolution of the ion current density $j_i = e n_i |u_i|$ at the inner electrode is shown in Fig. 7c. The time-axis is shown on a logarithmic scale to illustrate the solution details more clearly. There is an initial surge in current as the transient sheath forms, followed by a gradual relaxation to constant current density

at large times. In this asymptotic state, the current to the electrode is balanced by ions uncovered by the expanding rarefaction wave. The presheath accelerates the ions up to approximately the Bohm velocity, supporting a quasi-steady sheath.

As a gauge of the quality of the solution for different numerical schemes, the ion current at the inner electrode for $\omega_{pi}t = 18$ was examined. The error in this quantity, relative to a reference solution of 101×101 points using Compact Scheme 5, is plotted versus grid size in Fig. 7d for grids between 41×41 and 71×71 points. Again, each power-law curve fit is annotated with its exponent, and the slope of the lines on the log-log plot follows the expected value for the order of the scheme. These results show that compact difference methods of up to sixth order can successfully achieve their theoretical order of accuracy for the coupled Poisson and Euler equations with source terms. It should be noted that spatial convergence tends to degenerate to second order if the Poisson solution is not tightly converged for each time step.

IV.   Summary and Conclusions

This paper has explored the feasibility of applying high-order, compact difference methods to the modeling of glow discharges for high-speed flow control. High-order compact difference methods offer a possible means of achieving high spatial accuracy on coarser grids, potentially leading to a significant reduction in computational cost. Two-dimensional compact difference calculations were carried out for several test cases, including a Poisson equation solution, a compressible Couette flow problem, a hypersonic laminar boundary layer flow, and a transient plasma-sheath problem. Spatial convergence of second- through sixth-order compact schemes was investigated, and found to be comparable to the theoretical order of accuracy. In particular, compact difference methods of up to sixth order can successfully achieve their theoretical order of accuracy for the coupled Poisson and Euler equations with source terms. Compact difference schemes appear to be a promising numerical approach for modeling plasma actuators for high-speed flow control. Future work will focus on shock capturing and on more complex discharge problems.

Acknowledgments

References

[1]Surzhikov, S. T. and Shang, J. S., "Two-Component Plasma Model for Two-Dimensional Glow Discharge in Magnetic Field," *Journal of Computational Physics*, Vol. 199, 2004, pp. 437–464.

[2]Mahadevan, S. and Raja, L. L., "Simulations of Glow Discharge Phenomena in Air for High-Speed Flow Control," AIAA Paper 2008-1093, American Institute of Aeronautics and Astronautics, Reston VA, January 2008.

[3]Poggie, J., "Numerical Simulation of Direct Current Glow Discharges for High-Speed Flow Control," *Journal of Propulsion and Power*, Vol. 24, No. 5, 2008, pp. 916–922.

[4]Poggie, J., "Numerical Simulation of DC and RF Glow Discharges," AIAA Paper 2007-0632, American Institute of Aeronautics and Astronautics, Reston VA, January 2007.

[5]Poggie, J., "Discharge Modeling for Flow Control Applications," AIAA Paper 2008-1357, American Institute of Aeronautics and Astronautics, Reston VA, January 2008.

[6]Lele, S. K., "Compact Finite Difference Schemes with Spectral-Like Resolution," *Journal of Computational Physics*, Vol. 103, 1992, pp. 16–42.

[7]Gaitonde, D. V. and Visbal, M. R., "High-Order Schemes for Navier-Stokes Equations: Algorithm and Implementation in FDL3D," AFRL Technical Report AFRL-VA-WP-TR-1998-3060, Air Force Research Laboratory, Wright-Patterson Air Force Base, Ohio, 1998.

[8]Poggie, J., "High-Order Compact Difference Methods for Glow Discharge Modeling," AIAA Paper 2009-1047, American Institute of Aeronautics and Astronautics, Reston VA, January 2009.

[9]Ward, A. L., "Effect of Space Charge in Cold-Cathode Gas Discharges," *Physical Review*, Vol. 112, No. 6, 1958, pp. 1852–1857.

[10]Ward, A. L., "Calculations of Cathode-Fall Characteristics," *Journal of Applied Physics*, Vol. 33, No. 9, 1962, pp. 2789–2794.

[11]Boeuf, J.-P., "A Two-Dimensional Model of DC Glow Discharges," *Journal of Applied Physics*, Vol. 63, No. 5, 1988, pp. 1342–1349.

[12]Raizer, Y. P. and Surzhikov, S. T., "Two-Dimensional Structure in a Normal Glow Discharge and Diffusion Effects in Cathode and Anode Spot Formation," *High Temperature*, Vol. 26, No. 3, 1988, pp. 304–311.

[13]Passchier, J. D. P. and Goedheer, W. J., "A Two-Dimensional Fluid Model for an Argon RF Discharge," *Journal of Applied Physics*, Vol. 74, No. 6, 1993, pp. 3744–3751.

[14]Young, F. F., "Two-Dimensional, Self-Consistent, Three-Moment Simulation of RF Glow Discharges," *IEEE Transactions on Plasma Science*, Vol. 21, No. 3, 1993, pp. 312–321.

[15]Hong, M. and Emmert, G. A., "Two-Dimensional Fluid Modeling of Time-Dependent Plasma Sheath," *Journal of Vacuum Science and Technology*, Vol. 12, No. 2, 1994, pp. 889–896.

[16]Sheridan, T. E. and Alport, M. J., "Two-Dimensional Model of Ion Dynamics During Plasma Source Ion Implantation," *Applied Physics Letters*, Vol. 64, No. 14, 1994, pp. 1783–1785.

[17]Georghiou, G. E., Papadakis, A. P., Morrow, R., and Metaxas, A. C., "Numerical Modelling of Atmospheric Pressure Gas Discharges Leading to Plasma Production," *Journal of Physics D: Applied Physics*, Vol. 38, 2005, pp. R303–R328.

[18]Graves, D. B. and Jensen, K. F., "A Continuum Model of DC and RF Discharges," *IEEE Transactions on Plasma Science*, Vol. PS-14, No. 2, 1986, pp. 78–91.

[19]Richards, A. D., Thompson, B. E., and Sawin, H. H., "Continuum Modeling of Argon Radio Frequency Glow Discharges," *Applied Physics Letters*, Vol. 50, No. 9, 1987, pp. 492–494.

[20]Barnes, M. S., Cotler, T. J., and Elta, M. E., "A Staggered-Mesh Finite-Difference Numerical Method for Solving the Transport Equations in Low Pressure RF Glow Discharges," *Journal of Computational Physics*, Vol. 77, 1988, pp. 53–72.

[21]Hammond, E. P., Mahesh, K., and Moin, P., "A Numerical Method to Simulate Radio-Frequency Plasma Discharges," *Journal of Computational Physics*, Vol. 176, 2002, pp. 402–429.

[22]Meyyappan, M. and Kreskovsky, J. P., "Glow Discharge Simulation Through Solutions to the Moments of the Boltzmann Transport Equation," *Journal of Applied Physics*, Vol. 68, No. 4, 1990, pp. 1506–1512.

[23]Meyyappan, M., "A Continuum Model for Low-Pressure Radio-Frequency Discharges," *Journal of Applied Physics*, Vol. 69, No. 12, 1991, pp. 8047–8051.

[24]Widner, M., Alexeff, I., Jones, W. D., and Lonngren, K. E., "Ion Acoustic Wave Excitation and Ion Sheath Evolution," *The Physics of Fluids*, Vol. 13, No. 10, 1970, pp. 2532–2540.

[25]Sternberg, N. and Poggie, J., "Plasma-Sheath Transition in the Magnetized Plasma-Wall Problem for Collisionless Ions," *IEEE Transactions on Plasma Science*, Vol. 32, No. 6, 2004, pp. 2217–2226.

[26]Poggie, J. and Sternberg, N., "Transition from the Constant Ion Mobility Regime to the Ion-Atom Charge-Exchange Regime for Bounded Collisional Plasmas," *Physics of Plasmas*, Vol. 12, No. 2, 2005, pp. 023502–1–023502–9.

[27]Chapman, S. and Cowling, T. G., *The Mathematical Theory of Non-Uniform Gases*, Cambridge University Press, 2nd ed., 1952.

[28]Appleton, J. P. and Bray, K. N. C., "The Conservation Equations for a Non-Equilibrium Plasma," *Journal of Fluid Mechanics*, Vol. 20, No. 4, 1964, pp. 659–672.

[29]Burgers, J. M., *Flow Equations for Composite Gases*, Academic Press, New York, 1969.

[30]Morse, T. F., "Energy and Momentum Exchange between Nonequipartition Gases," *The Physics of Fluids*, Vol. 6, No. 10, 1963, pp. 1420–1427.

[31]Lister, G. G., "Low-Pressure Gas Discharge Modelling," *Journal of Physics D*, Vol. 25, No. 12, 1992, pp. 1649–1680.

[32]Yuan, X. and Raja, L. L., "Computational Study of Capacitively Coupled High-Pressure Glow Discharges in Helium," *IEEE Transactions on Plasma Science*, Vol. 31, No. 4, 2003, pp. 495–503.

[33]Adamovich, I. V., Subramaniam, V. V., Rich, J. W., and Macheret, S. O., "Phenomenological Analysis of Shock-Wave Propagation in Weakly Ionized Plasmas," *AIAA Journal*, Vol. 36, No. 5, 1998, pp. 816–822.

[34]White, F. M., *Viscous Fluid Flow*, McGraw-Hill, New York, 2nd ed., 1991.

[35]Hoffmann, K. A. and Chiang, S. T., *Computational Fluid Dynamics*, Engineering Educational System, Wichita KS, 4th ed., 2000.

[36]Anderson, W. K., Thomas, J. L., and van Leer, B., "A Comparison of Finite Volume Flux Vector Splittings for the Euler Equations," AIAA Paper 85-0122, American Institute of Aeronautics and Astronautics, Reston VA, January 1985.

[37]Cheney, W. and Kincaid, D., *Numerical Mathematics and Computing*, Brooks/Cole Publishing, Pacific Grove, California, 3rd ed., 1994.

[38]Visbal, M. R. and Gaitonde, D. V., "Shock Capturing Using Compact-Differencing-Based Methods," AIAA Paper 2005-1265, American Institute of Aeronautics and Astronautics, Reston VA, January 2005.

[39]Poggie, J. and Gaitonde, D. V., "Electrode Boundary Conditions in Magnetogasdynamic Flow Control," AIAA Paper 2002-0199, American Institute of Aeronautics and Astronautics, Reston VA, January 2002.

[40]Poggie, J., Gaitonde, D. V., and Sternberg, N., "Numerical Simulation of Plasma Sheaths in Aerodynamic Applications," AIAA Paper 2002-2166, American Institute of Aeronautics and Astronautics, Reston VA, May 2002.

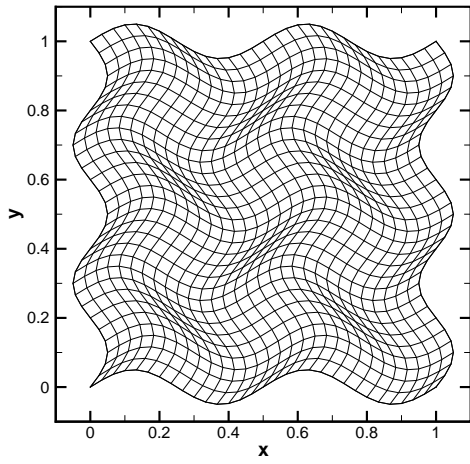| Scheme	α	a	b	Stencil	Order
E2	0	1	0	3	2
E4	0	4/3	-1/3	5	4
C4	1/4	3/2	0	3	4
C6	1/3	14/9	1/9	5	6

Table 1. Coefficients for compact difference schemes at interior points. Adapted from Gaitonde and Visbal.[7]

	Scheme	Filter A	Filter B
0	Conventional Central	F0-FB$_{2,4}$-F4-FB$_{2,4}$-F0	F0-F2-F4-F2-F0
1	E2-DE2-E2-DE2-E2	F0-FB$_{2,4}$-F4-FB$_{2,4}$-F0	F0-F2-F4-F2-F0
2	E4-DE4-E4-DE4-E4	F0-FB$_{2,6}$-FB$_{3,6}$-F6-FB$_{3,6}$-FB$_{2,6}$-F0	F0-F2-F4-F6-F4-F2-F0
3	E4-AC4-C4-AC4-E4	F0-FB$_{2,6}$-FB$_{3,6}$-F6-FB$_{3,6}$-FB$_{2,6}$-F0	F0-F2-F4-F6-F4-F2-F0
4	E4-AC4-C6-AC4-E4	F0-FB$_{2,6}$-FB$_{3,8}$-FB$_{4,8}$-F8-FB$_{4,8}$-FB$_{3,8}$-FB$_{2,6}$-F0	F0-F2-F4-F6-F8-F6-F4-F2-F0
5	E6-AC6-C6-AC6-E6	F0-FB$_{2,8}$-FB$_{3,8}$-FB$_{4,8}$-F8-FB$_{4,8}$-FB$_{3,8}$-FB$_{2,8}$-F0	F0-F2-F4-F6-F8-F6-F4-F2-F0

Table 2. Compact difference schemes and corresponding filters. Notation of Gaitonde and Visbal.[7]

Scheme	a_0	a_1	a_2	$a3$	a_4	Order
F2	$\frac{1+2\alpha_f}{2}$	$\frac{1+2\alpha_f}{2}$	0	0	0	2
F4	$\frac{5+6\alpha_f}{8}$	$\frac{1+2\alpha_f}{2}$	$\frac{-1+2\alpha_f}{8}$	0	0	4
F6	$\frac{11+10\alpha_f}{16}$	$\frac{15+34\alpha_f}{32}$	$\frac{-3+6\alpha_f}{16}$	$\frac{1-2\alpha_f}{32}$	0	6
F8	$\frac{93+70\alpha_f}{128}$	$\frac{7+18\alpha_f}{16}$	$\frac{-7+14\alpha_f}{32}$	$\frac{1-2\alpha_f}{16}$	$\frac{-1+2\alpha_f}{128}$	8

Table 3. Coefficients for filter schemes at interior points. Adapted from Gaitonde and Visbal.[7]

(a) Computational mesh.
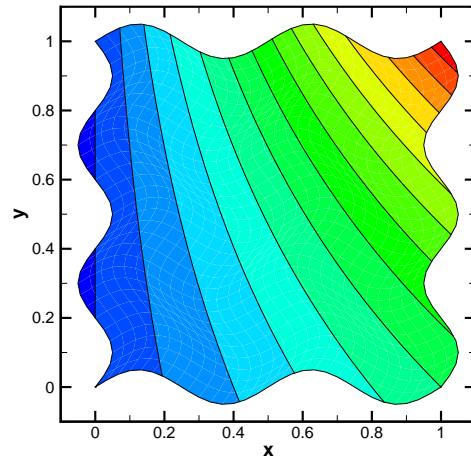
(b) Solution computed with Compact Scheme 5.
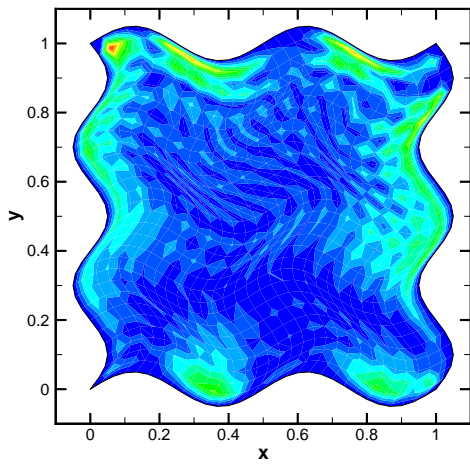
(c) Absolute error, Compact Scheme 5 (contour 1×10^{-6}).
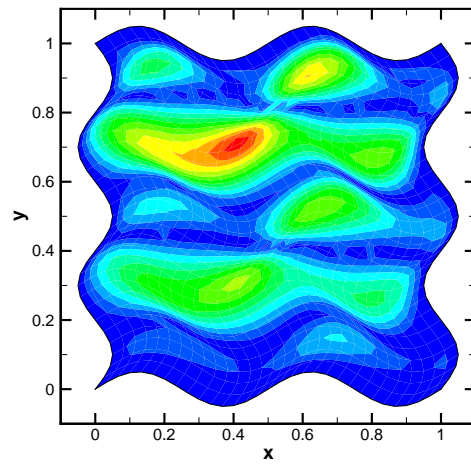
(d) Absolute error, central scheme (contour 1×10^{-3}).

Figure 1. Test of Poisson solver, 31×31 **grid.**
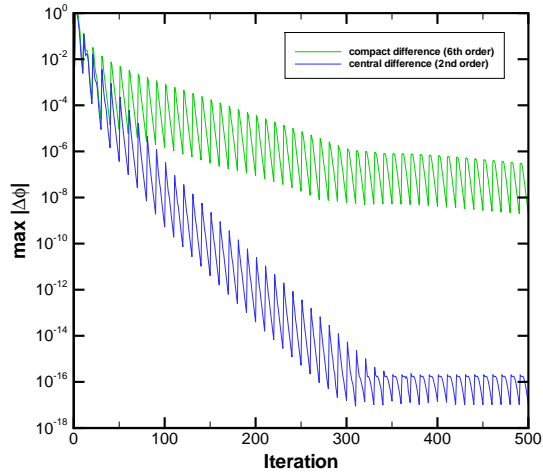
(a) Iterative convergence, 31×31 grid.
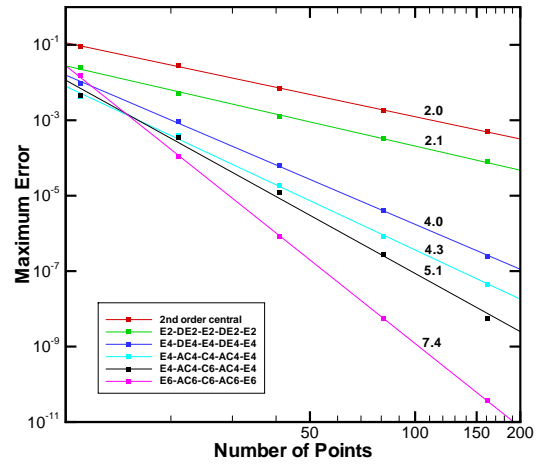
(b) Spatial convergence. Annotated with exponent of power law fit.
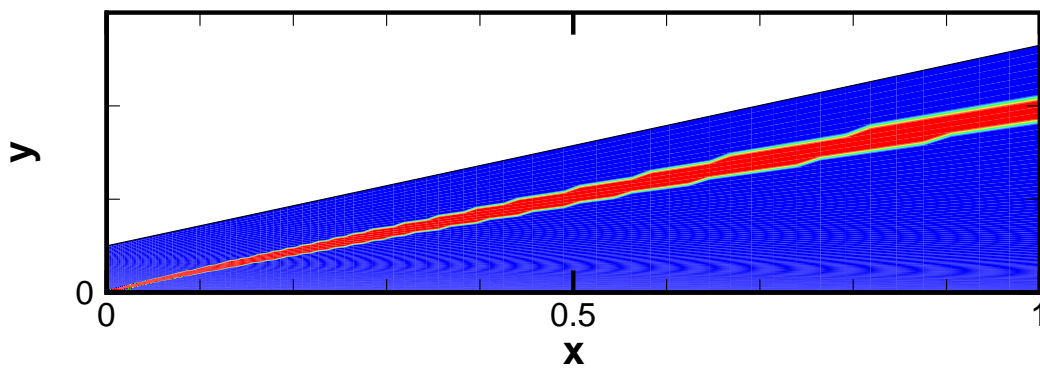
Figure 2. Convergence of Poisson solution.
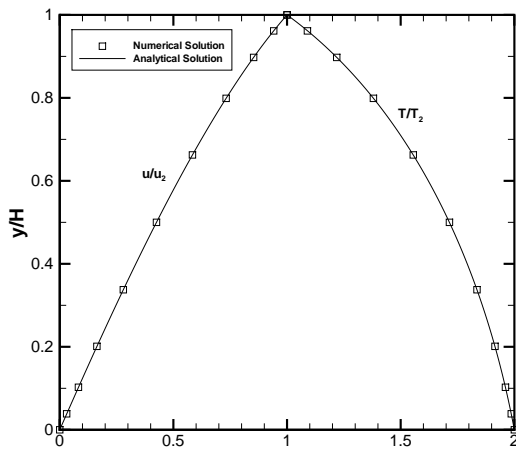
(a) Velocity and temperature profiles (Compact Scheme 5, 9×11 point mesh).
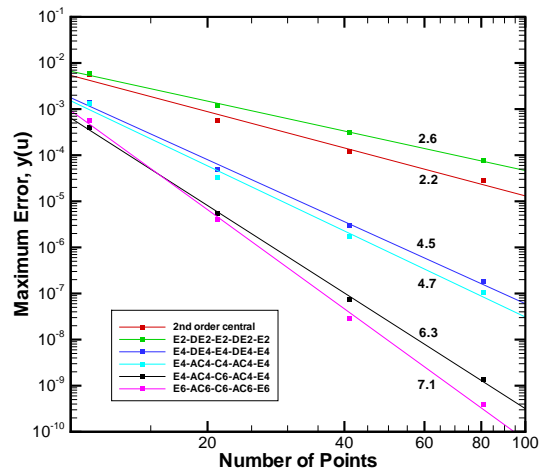
(b) Spatial convergence, refinement in y-direction. Annotated with exponent of power law fit.

Figure 3. Compressible Couette flow test case ($M = 2$, $T_1/T_2 = 2$).

(b) Shock location.

Figure 4. Shock detection for laminar, Mach 6 boundary layer solution.
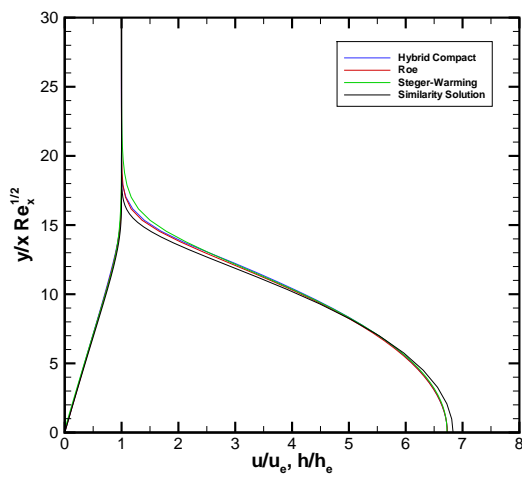
(a) Boundary layer profiles ($M_e = 5.9$).
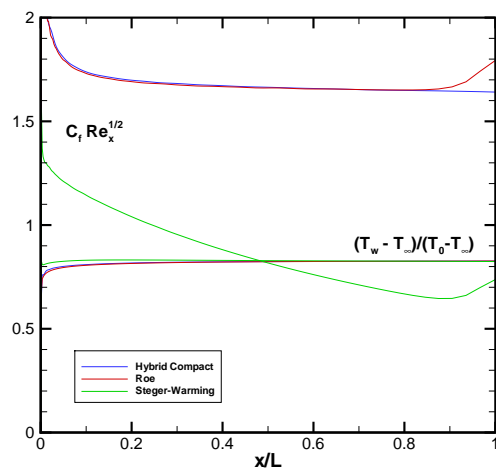
(b) Skin friction and recovery factor profiles.

Figure 5. Laminar, Mach 6 boundary layer solution.
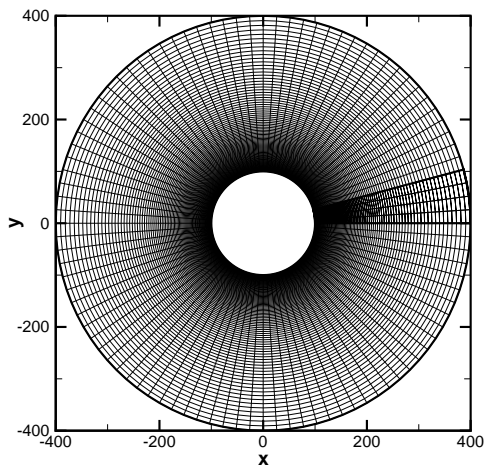
(a) Computational mesh (101 × 101 points).
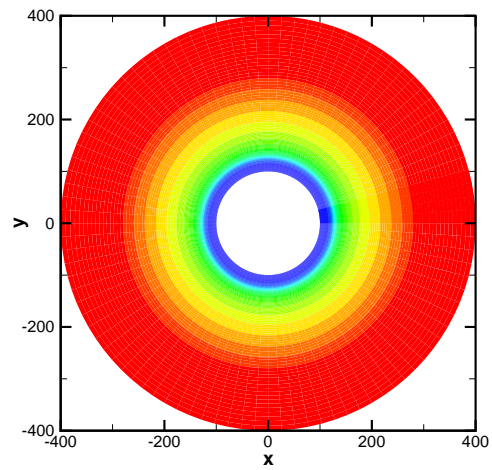
(b) Ion number density, $\omega_{pi}t = 18$, Compact Scheme 5.

Figure 6. Transient sheath test case.
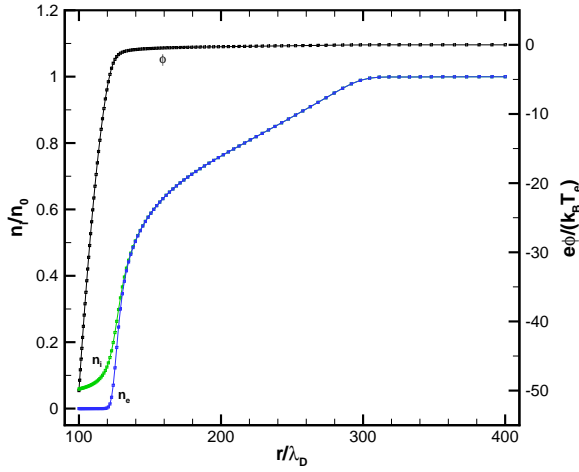
(a) Radial profile, $\omega_{pi}t = 18$, Compact Scheme 5.
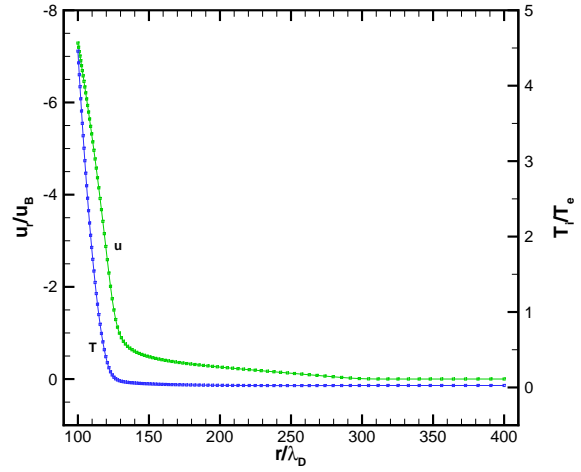
(b) Radial profile, $\omega_{pi}t = 18$, Compact Scheme 5.
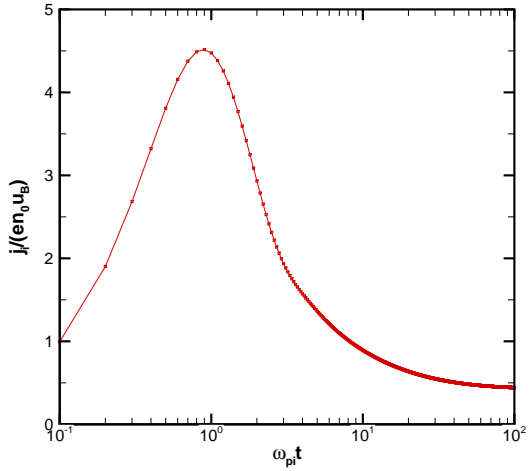
(c) Ion current, $r/\lambda_D = 100$, Compact Scheme 5.
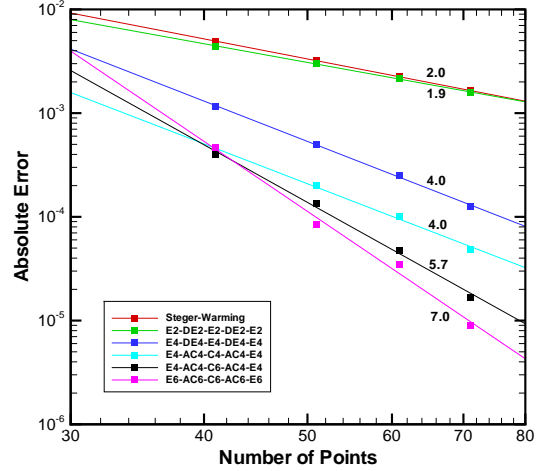
(d) Spatial convergence. Annotated with exponent of power law fit.

Figure 7. Transient sheath test case.

Appendix B

Physical Models for Particle Motion in Electrical Discharges

48th AIAA Aerospace Sciences Meeting Including the New Horizons Forum and Aerospace Exposition
4 - 7 January 2010, Orlando, Florida

AIAA 2010-1195

Role of Charged Particle Inertia
in Pulsed Electrical Discharges

Jonathan Poggie[*]

Air Force Research Laboratory, Wright-Patterson AFB, Ohio

In order to investigate the role of inertia in pulsed electrical discharges, this paper compares a five-moment model (continuity, momentum, and energy equations) to a two-moment model (continuity and energy equations) for charged particle motion. Three species were considered: ions, electrons, and neutrals. Either the two- or five-moment model was used for the ions and electrons, but the five-moment model was always employed for the neutrals. Ionization and excitation reactions were included in each model. Two glow discharge test cases in 107 Pa (0.8 Torr) argon were examined. A steady-state, one-dimensional discharge was considered first. For this case, relatively subtle differences in the velocities and temperatures in the cathode sheath led to significant differences between the predictions of the two models for ionization rates and number densities. A two-dimensional, transient discharge problem with an elliptical cathode was studied next. Relative to the two-moment model, the five-moment model predicted a slower response to the activation of the cathode, and lower electron velocities and temperatures in the later stages of the simulation. These differences can be attributed to particle inertia and to differences in the boundary conditions for the two models. Both models predicted that neutral gas velocities on the order of 1.3 m/s occurred within 1000 ns, with a negligible rise in neutral temperature (~ 0.3 K). More rapid heating is expected to occur in molecular gases, which will be the subject of future work.

I. Introduction

This paper examines the role of charged particle inertia in pulsed electrical discharges. Repetitive, short-pulse discharges are a well-known and appealing method for generating ionization and high instantaneous electric fields.[1,2] In aerospace applications, nanosecond-pulse discharges are an emerging tool for plasma-based flow control actuators,[3–5] and have been used as a source of ionization for nonequilibrium magnetohydrodynamic devices.[6,7]

Numerical studies of these discharges are motivated by the need to understand and optimize them. Particle methods, although they provide valuable insight and encompass the greatest portion of the relevant physics, are too computationally costly for practical discharge computations at relatively high pressures.[8] Direct solutions to the Boltzmann equation are also prohibitively costly. The only viable alternatives are continuum models, based on moments of the Boltzmann equation.

Traditional continuum modeling of electrical discharges employs a one-moment model, the continuity equation, with particle transport properties and ionization rates taken as a function of the reduced electric field.[9–11] More recent studies have extended this model by substituting an electron energy equation in place of the reduced electric field dependence.[12–14] Only a few studies have considered particle inertia; these typically have assumed constant ion temperature.[15–18]

Even though traditional continuum discharge models are useful for predicting particle densities in industrial plasma processing applications,[1,2] they may not be suitable for discharges used for aerospace applications, where the intent is to transfer momentum and energy from the charged particles to the neutrals in order to modify the flow. Further, many of the assumptions typically employed in these models may not be suitable for pulsed discharges.

1

In particular, the full set of Maxwell's Equations may have to be solved, charged particle inertia may be a significant effect, and local charged particle temperatures may not reflect a local equilibrium with the electric field. This paper addresses the latter two issues, comparing a five-moment model for the charged particles to a two-moment model. (It should be noted that coupling of fluid models to the full Maxwell's Equations has been treated by other researchers,[19, 20] and that that two-fluid, five-moment models have been employed in the fusion plasma community,[21] but typically for a weakly-collisional regime.)

Here the temperature variation of ions, electrons, and neutrals is considered, and a model incorporating continuity, momentum, and energy equations for each species is compared to one that replaces the momentum equation with the drift-diffusion approximation. The simpler model will be called the two-moment model (continuity and energy). Although the calculations presented here are at most two-dimensional, the more general model will be called the five-moment model (continuity, three momentum components, and energy) for consistency with the literature.

II.   Physical Model

This section will outline the two physical models employed in this work. Both are based on moments of the Boltzmann equation, and an outline of their derivation is given in Appendix A. The working gas was taken to be argon for all the test cases considered in this paper.

A.   Five-Moment Model

First we discuss the five-moment model, which includes particle inertia. The conservation equations for each species are:

$$\frac{\partial}{\partial t}(m_s n_s) + \nabla \cdot (m_s n_s \mathbf{v}_s) = S_s$$

$$\frac{\partial}{\partial t}(m_s n_s \mathbf{v}_s) + \nabla \cdot (m_s n_s \mathbf{v}_s \mathbf{v}_s + p_s \mathbf{I}) = \nabla \cdot \tau_s + q_s n_s \mathbf{E} + \mathbf{A}_s \tag{1}$$

$$\frac{\partial}{\partial t}\left[m_s n_s \left(\epsilon_s + \tfrac{1}{2}v_s^2\right)\right] + \nabla \cdot \left[m_s n_s \mathbf{v}_s \left(\epsilon_s + \tfrac{1}{2}v_s^2\right) + p_s \mathbf{v}_s\right] = \nabla \cdot [\tau_s \cdot \mathbf{v}_s - \mathbf{Q}_s] + q_s n_s \mathbf{v}_s \cdot \mathbf{E} + M_s$$

where the notation $s = i, e, n$ indicates the ions, electrons, and neutrals, respectively.

The mass per particle of each species is denoted as m_s, and the corresponding charge per particle is $q_{i,e} = \pm e$ and $q_n = 0$. The number density is n_s, the velocity is $\mathbf{v}_s$, and the translational temperature is T_s. The electric field is $\mathbf{E}$. The pressure is found from $p_s = n_s k_B T_s$, where k_B is the Boltzmann constant. The internal energy per particle is assumed to have the form $m_s \epsilon_s = H_s + k_B T_s / (\gamma_s - 1)$, where $\gamma_s = 5/3$ is the ratio of specific heats and H_s is the heat of formation per particle of species-s.

In order to close the equation set (1), models are needed for the collision source terms S_s, $\mathbf{A}_s$, and M_s, the viscous stress tensor τ_s, and the heat flux vector $\mathbf{Q}_s$. For the inelastic collision terms, the following ionization and excitation reactions were considered:

$$\mathrm{Ar} + \mathrm{e} \rightarrow \mathrm{Ar}^+ + 2\mathrm{e}$$

$$\mathrm{Ar} + \mathrm{e} \rightarrow \mathrm{Ar}^* + \mathrm{e}$$
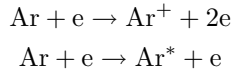
The reaction rates were taken from Park and Economou,[22] with the form $\omega_I = k_I n_e n_n$ for the ionization rate, and $\omega_X = k_X n_e n_n$ for the excitation rate. A more complete model would include conservation equations for the excited atoms, but for simplicity, the only effect of excitation considered in the present model was an energy loss from the electrons. Recombination reactions are neglected in the present work.

The inelastic collision components of the collision source terms have the form:

$$\begin{aligned}
S_i &= m_i \omega_I & \mathbf{A}_i &= m_i \omega_I \mathbf{v}_i & M_i &= m_i \omega_I (\epsilon_i + \tfrac{1}{2}v_i^2) \\
S_e &= m_e \omega_I & \mathbf{A}_e &= m_e \omega_I \mathbf{v}_e & M_e &= m_e \omega_I (\epsilon_e + \tfrac{1}{2}v_e^2) - \omega_I \mathcal{H}_I - \omega_X \mathcal{H}_X \\
S_n &= -m_n \omega_I & \mathbf{A}_n &= -m_n \omega_I \mathbf{v}_n & M_n &= -m_n \omega_I (\epsilon_n + \tfrac{1}{2}v_n^2)
\end{aligned} \tag{2}$$

where $\mathcal{H}_I$ is the energy lost by electrons in ionizing collisions, and $\mathcal{H}_X$ is the corresponding energy lost in excitation collisions. For this model, the ions are assumed to appear out of ionizing collisions with the average momentum and energy of their peers. Similarly, the neutrals that are lost to ionization are assumed

2

to have the same average momentum and energy as the other neutral particles. The electrons, however, lose additional energy because only the most energetic electrons initiate the collisions that cause ionization and excitation. A discussion of the form of the inelastic collision source terms is given in Appendix B.

The momentum and energy source terms also have an elastic collision component. Because the gas is assumed to be weakly ionized, the primary elastic collisions are with neutral particles. The form of the elastic collision term is taken from Burgers,[23] and is discussed in Appendix C. In this model, the momentum and energy source terms due to elastic collisions have the form:

$$\mathbf{A}_i = -n_i m_{in} \nu_{in}(\mathbf{v}_i - \mathbf{v}_n) \qquad M_i = -\frac{n_i m_{in} \nu_{in}}{m_i + m_n} \left[3k_B(T_i - T_n) + (\mathbf{v}_i - \mathbf{v}_n)\cdot(m_i\mathbf{v}_i + m_n\mathbf{v}_n) \right]$$

$$\mathbf{A}_e = -n_e m_{en} \nu_{en}(\mathbf{v}_e - \mathbf{v}_n) \qquad M_e = -\frac{n_e m_{en} \nu_{en}}{m_e + m_n} \left[3k_B(T_e - T_n) + (\mathbf{v}_e - \mathbf{v}_n)\cdot(m_e\mathbf{v}_e + m_n\mathbf{v}_n) \right] \qquad (3)$$

$$\mathbf{A}_n = -(\mathbf{A}_i + \mathbf{A}_e) \qquad M_n = -(M_i + M_e)$$

where $m_{sn} = m_s m_n/(m_s + m_n)$ is the reduced mass, with $s = i, e$. The collision frequency between the charged and neutral species ν_{sn} was estimated from mobility data, with the correlations for ion and electron mobility in argon taken from Ward.[9] The overall collision source terms are the sum of the inelastic collision component, Eq. (2), and the elastic collision component, Eq. (3).

For the flux terms, it was assumed that the viscous term had a Newtonian form, with Stokes hypothesis applied, and that the heat flux followed Fourier's law:

$$\tau_s = \mu_{vn} \left[(\nabla\mathbf{v}_s) + (\nabla\mathbf{v}_s)^T - \tfrac{2}{3}\nabla\cdot\mathbf{v}_s\mathbf{I} \right]$$

$$\mathbf{Q}_s = -k_s \nabla T_s \qquad (4)$$

where μ_{vs} is the viscosity and k_s is the thermal conductivity for species-s. The properties of the neutrals were taken from standard correlations for argon.[24] The charged particle transport properties were derived from mobility data, assuming a Lewis number of $\mathrm{Le}_s = m_s n_s C_{ps} D_s/k_s = 1$ and a Prandtl number of $\mathrm{Pr}_s = \mu_{vs} C_{ps}/k_s = 2/3$, where D_s is the species diffusion coefficient and $C_{ps} = 5k_B/(2m_s)$ is the specific heat at constant pressure. The results are:

$$D_s = \frac{k_B T_s}{|q_s|}\mu_s$$

$$\mu_{vs} = \tfrac{2}{3}n_s m_s D_s \qquad (5)$$

$$k_s = \tfrac{5}{2}k_B n_s D_s$$

where $\mu_s = |q_s|/(m_{sn}\nu_{sn})$ is the species mobility. Note that these transport coefficients are proportional to number density, so the electron transport properties become small for the low electron number densities in the cathode sheath.

B. Two-Moment Model

Next we discuss the two-moment model, or drift-diffusion formulation. This model neglects the acceleration terms in the momentum equation, and also neglects all viscous terms. The governing equations are reduced to:

$$\frac{\partial}{\partial t}(m_s n_s) + \nabla\cdot(m_s n_s \mathbf{v}_s) = S_s$$

$$n_s \mathbf{v}_s = n_s \mathbf{v}_n \pm n_s \mu_s \mathbf{E} - \frac{D_s}{k_B T_s}\nabla p_s \qquad (6)$$

$$\frac{\partial}{\partial t}(m_s n_s \epsilon_s) + \nabla\cdot(m_s n_s \mathbf{v}_s \epsilon_s) = -\nabla\cdot\mathbf{Q}_s - p_s\nabla\cdot\mathbf{v}_s + \tilde{M}_s$$

where the value of the species mobility μ_s was taken from Ward.[9] Note that here we solve the thermal energy equation, obtained by subtracting the mechanical energy equation, the scalar product of $\mathbf{v}_s$ and Eq. (1b), from the total energy equation (1c). The energy source terms are thus slightly different from those in Eqs. (2)-(3), and have the form:

$$\tilde{M}_i = m_i \omega_I \epsilon_i + \frac{n_i|q_i|}{(m_i + m_n)\mu_i}\left[-3k_B(T_i - T_n) + m_n|\mathbf{v}_i - \mathbf{v}_n|^2 \right]$$

$$\tilde{M}_e = m_e \omega_I \epsilon_e - \omega_I \mathcal{H}_I - \omega_X \mathcal{H}_X + \frac{n_e|q_e|}{(m_e + m_n)\mu_e}\left[-3k_B(T_e - T_n) + m_n|\mathbf{v}_e - \mathbf{v}_n|^2 \right] \qquad (7)$$

3

Note that the velocity difference terms due to elastic collisions are always positive. They have a dissipative nature, always tending to increase the thermal energy.

This two-moment formulation was only used for the charged particles; the neutrals were handled using Eq. (1).

C. One-Moment Model

For completeness, we derive the one-moment model that that corresponds to the formulation used in this paper. The one-moment model employs the continuity equation for each species, along with the drift-diffusion approximation for the particle fluxes. The particle transport properties and ionization rates are taken as a function of the reduced electric field.

The required relation between the electron temperature and reduced electric field can be found by assuming a homogeneous discharge. Considering the electron thermal energy equation (6)c, and neglecting all the terms in that involve gradients of the discharge properties, we obtain $\tilde{M}_e = 0$. Introducing the drift approximation for the electron velocity, and simplifying, we obtain:

$$\left(\frac{E}{n_n}\right)^2 = \frac{3k_B(T_e - T_n)}{m_n(\mu_e n_n)^2} + \frac{k_I \mathcal{H}_I + k_X \mathcal{H}_X}{e(\mu_e n_n)} \tag{8}$$

Given the form of the scaled electron mobility $\mu_e n_n$, the ionization rate k_I, and the excitation rate k_X, this equation provides an implicit relation between the reduced electric field and the electron temperature: $f(E/n_n, T_e) = 0$.

The corresponding model for the ions can be found by setting $\tilde{M}_i = 0$. The resulting equation for the rise in ion temperature is:

$$T_i - T_n = \frac{m_n}{3k_B}(\mu_i n_n)^2\left(\frac{E}{n_n}\right)^2 \tag{9}$$

D. Poisson Equation

To complete the physical model, the electric field must be found from a consistent solution of Maxwell's equations. For the present work, the Poisson equation was solved for the electric potential:

$$\nabla^2 \phi = -\frac{e}{\epsilon_0}(n_i - n_e) \tag{10}$$

and the electric field was found from $E = -\nabla \phi$.

III. Numerical Methods

This section briefly outlines the structure of the flow solver, and goes on to discuss the physical and numerical boundary conditions.

A. Flow Solver

In transformed coordinates, the two-dimensional forms of the conservation laws (1) and (6) can be written in the form:

$$\frac{\partial U}{\partial t} + \frac{\partial E}{\partial \xi} + \frac{\partial F}{\partial \eta} = \frac{\partial E_v}{\partial \xi} + \frac{\partial F_v}{\partial \eta} + S \tag{11}$$

where U is the vector of conserved variables, E and F are the inviscid flux vectors, E_v and F_v are the viscous flux vectors, and S represents the source terms. A standard, low-storage, fourth-order Runge-Kutta scheme[25] was used for time integration of Eq. (11).

Spatial differencing was carried out with the Steger-Warming flux splitting scheme for the five-moment model, and with a simple scalar upwind scheme for the two-moment model. The code employed third-order MUSCL extrapolation[26] for the inviscid fluxes and second-order central differencing for the viscous terms. A harmonic limiter was employed.

4

The Poisson equation (10) was solved at the end of each stage of the Runge-Kutta time-integration. It can be written in the following form in transformed coordinates:

$$\frac{\partial E}{\partial \xi} + \frac{\partial F}{\partial \eta} = S_\phi \tag{12}$$

An iteration procedure was introduced such that the potential at iteration step m was $\phi^{m+1} = \phi^m + \Delta\phi$. With a linear expansion about the solution from the previous iteration, and approximate factoring of the implicit terms, the discretized equation has the form:

$$[1 - \Delta\tau(\delta_\xi A \delta_\xi - D)][1 - \Delta\tau\delta_\eta B\delta_\eta]\Delta\phi = \omega\Delta\tau\left[\frac{\partial E^m}{\partial \xi} + \frac{\partial F^m}{\partial \eta} - S_\phi^m\right] \tag{13}$$

with iteration driving $\Delta\phi$ to zero. Here A and B are flux Jacobians, D is the source Jacobian, τ is a time-like variable introduced to motivate the iteration process, and ω is an over-relaxation factor. Discretizing the left-hand side using second order central differences in space, a tridiagonal system of equations is obtained. A second-order central difference scheme was also used to evaluate the spatial differences present on the right hand side of Eq. (13), and the system was solved using the Thomas tridiagonal algorithm.[27] The pseudo-time-step $\Delta\tau$ was varied cyclically to accelerate convergence, and iteration was continued until the change in potential $\Delta\phi$ had dropped below a specified tolerance.

B.   Boundary Conditions

For the neutral particles, boundary conditions of no-slip ($\mathbf{v}_n = 0$) and no temperature jump ($T_n = T_\infty$) were imposed at solid boundaries. The boundary conditions for the charged particles were based on those of Graves[28] and Wilcoxson and Manousiouthakis,[18] and are summarized for the two physical models in Fig. 1.

The boundary condition on the electron flux at an electrode is set by a balance between recombination and secondary emission: $n_e v_e^\perp = n_e k_r - \gamma_E n_i v_i^+$. Here we use the notation $v^\perp = \mathbf{v}\cdot\mathbf{n}$, where $\mathbf{n}$ is the outward normal, and $v_i^+ = \max(v_i^\perp, 0)$. The symbol γ_E represents the secondary emission coefficient, and k_r is a recombination coefficient with dimensions of velocity. Ion emission is prohibited, and the ion recombination rate at the boundary is assumed to be sufficiently fast to absorb any flux of ions.

For the two-moment model, the flux boundary conditions are imposed by using Eq. (6b) to set the particle pressure to match the boundary condition (Fig. 1c-d). For the five-moment model, the flux boundary conditions are imposed through the velocity, with the restriction that electron emission is limited to sonic speed (Fig. 1a-b). Where an additional boundary condition is required mathematically, the tangential component of velocity ($\mathbf{v}^\parallel = \mathbf{v} - v^\perp\mathbf{n}$) is set to zero.

Electron temperature at the boundary reflects a balance between the population of electrons flowing toward the wall and recombining, and the population emitted from the wall through secondary emission. As a rough model of this process, electron temperature is found from a flux-weighted average of the secondary emission temperature T_{es} and the temperature of the recombining particles T_{ea}:

$$\text{avg}(T_{ea}, T_{es}) = \frac{n_e k_r\, T_{ea} + \gamma_E n_i v_i^+\, T_{es}}{n_e k_r + \gamma_E n_i v_i^+}$$

Here the recombination temperature is estimated from the simplified energy equation $\frac{5}{2}k_B \nabla T_{ea}\cdot\mathbf{n} = -e\mathbf{E}\cdot\mathbf{n}$. The electron recombination rate is evaluated as the thermal speed at the temperature of the wall-directed population: $k_r = \sqrt{k_B T_{ea}/(2\pi m_e)}$.

Where an ion temperature boundary condition was required, it was set to the ambient temperature T_∞. To distinguish between inflow and outflow before applying the boundary conditions, extrapolation of the velocity field was used. (All extrapolation employed second-order accuracy.) The limit of sonic electron emission was enforced as a check after applying the subsonic boundary conditions.

IV.   Results

Two test cases were considered. The first was a basic, one-dimensional, DC discharge problem used to verify that the algorithms were implemented correctly. The second was a two-dimensional transient problem, designed to emphasize the differences between to two models.

A. DC Discharge in One Dimension

As a first test case, calculations were carried out with both models for a DC glow discharge in one dimension. The conditions were chosen to be similar to those used by Meyyappan and Kreskovsky.[15] (Those calculations did not include an excitation reaction, viscous terms, or ion temperature variation, so the present calculations are slightly different.)

The background neutral gas (argon) was assumed to be at rest, with a pressure of 107 Pa (0.8 Torr) and temperature of 323 K. The imposed potential was 120 V and the discharge gap was 35.25 mm. The initial condition was taken to be a uniform plasma of number density $n = 10^{15}$ m^{-3}, with temperatures $T_i = 323$ K (0.03 eV) and $T_e = 11600$ K (1 eV). The secondary emission coefficient was $\gamma_E = 0.05$, and the secondary emission temperature was $T_{es} = 5800$ K (0.5 eV). A total of 151 points were used across the discharge gap in the calculations, which were marched in time to 1.0 ms. (It should be noted here that poor grid resolution in the region of peak ionization can lead to run-away ionization for this problem.)

The basic discharge results are shown in Fig. 2. The data are nondimensionalized by the following reference values: $n_0 = 10^{16}$ m^{-3}, $u_R = 1$ km/s, and $L = 35.25$ mm. Number densities and electric potential are shown in Fig. 2a, temperatures in Fig. 2b, velocities in Fig. 2c, and ionization rate in Fig. 2d.

The product of pressure and gap width is $pL = 3.8$ m-Pa (2.8 cm-Torr). The normal cathode fall thickness for argon is given as $pd \approx 0.3$ cm-Torr by Lieberman and Lichtenberg[1] (p. 462), so the cathode layer thickness of $d \sim 0.15L$ seen in Fig. 2a is on the right order.

The electrons emitted from the cathode are initially accelerated by the strong electric field, reaching remarkably high peak velocities ($\sim 10^6$ m/s). Their directed energy is randomized in collision with neutrals, leading to a reduced mean velocity and increased electron temperatures, up to ~ 12 eV. High temperature leads to higher ionization rates, the energy cost of which brings the electron temperature back down to 1-2 eV in the positive column. Electrons are absorbed at the anode.

Ions generated in the center of the domain are absorbed at both boundaries. Ion velocities are substantially higher at the cathode (~ 2 km/s), and collisions with neutrals in that region lead to an order of magnitude increase in ion temperature there (up to ~ 0.5 eV).

The five-moment model and the drift-diffusion model predict similar temperatures (Fig. 2b) and velocities (Fig. 2c) under these conditions. Subtle differences in the results for the two models are magnified, however, by the extreme sensitivity of the ionization rate, leading to greater ionization rates (Fig. 2d) and plasma densities (Fig. 2a) for the two-moment model.

The relative magnitudes of the electron heating terms of Eq. (7b) are shown in Fig. 3. The terms are nondimensionalized in the plot by dividing by $m_n n_0 u_R^3 / L$. The terms are labelled as follows:

$$
\begin{array}{ll}
\text{Ionization Cost:} & -\omega_I \mathcal{H}_I \\
\text{Excitation Cost:} & -\omega_X \mathcal{H}_X \\
\text{Temperature Equilibration:} & -\frac{n_e |q_e|}{(m_e + m_n)\mu_e} 3k_B(T_e - T_n) \\
\text{Frictional Dissipation:} & \frac{n_e |q_e|}{(m_e + m_n)\mu_e} m_n |\mathbf{v}_e - \mathbf{v}_n|^2
\end{array}
$$

with their sum labeled 'Total Heating.'

Although there are quantitative differences between the predictions of the two models, the results are qualitatively the same. The frictional dissipation term adds heat to the system, and is balanced by the other terms, which represent thermal energy losses. The double-peaked profile of ionization cost mirrors the ionization profiles shown in Fig. 2d. The excitation cost also shows a double-peaked profile, with the relative magnitudes of the two peaks reversed relative to the ionization term. The temperature equilibration term is not significant in the cathode layer, but plays an important role in limiting electron temperatures in the positive column.

The corresponding ion heating terms of Eq. (7a) reflect a close balance between the frictional dissipation and the temperature equilibration terms, for a moderate net heating rate. (The corresponding plots are omitted for brevity.) Peak values of these terms occur near the cathode.

The results obtained here are qualitatively similar to those of Meyyappan and Kreskovsky[15] for the same conditions. (The present model includes viscous terms, ion temperature variation, and excitation reactions, which were omitted by Meyyappan and Kreskovsky.) Those authors observed similar number density distributions, although with very low densities in the cathode layer. They also obtained a similar ionization profile, with two peaks, the larger being the closer to the cathode. Their electron temperature and velocity profiles also showed large peaks in the cathode layer.

B. Transient Discharge with Elliptical Cathode

The second test case was designed to highlight the differences between the two- and five-moment models. It is a two-dimensional, transient problem, where particle inertia, electric field strength, and charged particle heating could be expected to be significant.

A schematic diagram of the problem is given in Fig. 4a. The inner boundary is taken to be the cathode, which is brought suddenly to a potential of $\phi = -120$ V at $t = 0$. The shape of the cathode is a 4:1 ellipse, and the grounded anode forms the circular outer boundary.

The 101×101 point computational grid is shown in Fig. 4b. It is an O-grid, with five-point overlap at the cut on the positive x-axis. (The overlap region is indicated by red lines in the figure.) An initial grid was generated algebraically, with clustering near the tips of the ellipse and at the inner and outer boundaries. This grid was then smoothed and made close to orthogonal using the commercial grid manipulation program Gridgen, from Pointwise, Inc. The minimum gap between the inner and outer electrodes was taken to be 35.25 mm to match the previous test case.

The initial and boundary conditions were also similar to those used in the previous test case. The background neutral gas was at initially at rest at 107 Pa and 323 K. A uniform plasma of number density $n = 10^{15}$ m^{-3}, with temperatures $T_i = 323$ K (0.03 eV) and $T_e = 11600$ K (1 eV), was assumed to exist at $t = 0$ between the two electrodes. Again, the secondary emission coefficient was $\gamma_E = 0.05$, and the secondary emission temperature was $T_{es} = 5800$ K (0.5 eV).

To highlight the initial evolution of the cathode sheath, Figs. 5-8 show the region around the right tip of the cathode for times of 1, 10, 100, and 1000 ns. In the number density distributions shown in Figs. 5a, 6a, 7a, and 8a, the sheath is seen to gradually thicken and the number densities to increase rapidly due to ionization. Looking at the electric potential distribution as a function of time, we see the rapid development of a strong electric field near the cathode (compare Figs. 5b, 6b, 7b, and 8b).

There is a corresponding increase in ion and electron temperature near the cathode (Figs. 5c, 6c, 7c, and 8c). Note the local maximum in electron temperature between $0.2L \leq x \leq 0.22L$; it is starting to form at $t = 1$ ns and is quite prominent at $t = 10$ ns. This peak grows rapidly with time. Ion temperature is seen to peak at the cathode surface.

The distributions of the horizontal component of velocity have an analogous form: the ion velocity peaks at the cathode, whereas the electron velocity has a local maximum some distance away from the wall. It is interesting to note that the electrons initially flow into the cathode, where they are absorbed through recombination (Fig. 5d), but as the ion bombardment of the cathode increases, the secondary emission rate exceeds the recombination rate and there is a net outflow of electrons as (Fig. 6d).

Corresponding results for the neutral particles are shown in Fig. 9. The neutrals are slower to respond to initiation of the discharge. At $t = 10$ ns, the neutral velocity is about 0.05 m/s, directed toward the cathode tip, and the neutral temperature is essentially unchanged. By $t = 1000$ ns, the neutral velocity has increased to about 1.3 m/s, and the neutral temperature has risen very slightly (about 0.3 K). For the neutral gas properties, the predictions of the two physical models are essentially the same. (Recall that the five-moment model was always used for the neutrals in this work; only the model for the charged particles was changed.)

Significant differences, however, are observed between the predictions of the two models for the charged particles in the initial stages of the development of the cathode sheath (Figs. 5-8). Although the results have qualitative similarity, the response of the five-moment model to the suddenly-applied potential is slower than that of the two-moment model. In particular, the local maxima in electron temperature and velocity are lower for the five-moment model than for the two-moment model, as are the corresponding maxima for the ions at the cathode surface. By $t = 1000$ ns, the predicted ion properties are very close for the two models, but significant differences remain for the electrons (Fig. 7).

Although it is difficult to represent in printed form, the results from the five-moment model, observed in flowfield movies, show acoustic waves propagating through the domain during the initial transient. These waves are not captured with the two-moment model.

Figures 10-11 show the two-dimensional property fields at $t = 1000$ ns for the five- and two-moment models, respectively. Particle number densities are shown in Figs. 10a and 11a, where the color contours represent the ions and the black lines the electrons. The electron-free sheath is apparent in the plots, as is a ring of high plasma density just outside the sheath.

Figures 10b-f and 11b-f show a field of view close in around the cathode. The potential distribution illustrates the strong electric field and large potential drop in the cathode sheath (Figs. 10b and 11b). Peak ion temperatures occur at the tips of the cathode (Figs. 10c and 11c), whereas the peak electron temperature

appears as a ring around the cathode (Figs. 10d and 11d). Peak charged particle speed is also seen to occur at the tips of the cathode (Figs. 10e-f and 11e-f).

As mentioned above, the results of the five-moment model tend to lag those of the the two-moment model because of the effects of inertia. Thus the temperatures and velocities are generally lower for the five-moment model (Fig. 10) than for the two-moment model (Fig. 11).

Corresponding results for the neutral particles are shown in Fig. 12. The features of the neutral particle fields are similar to those for the ions, with peak temperatures near the cathode tips, and significant inflow velocity there. These results reflect elastic collisions between ions and neutrals.

V.   Summary and Conclusions

In order to investigate the role of inertia in pulsed electrical discharges, this paper compared a five-moment model (continuity, momentum, and energy equations) to a two-moment model (continuity and energy equations) for charged particle motion. Three species were considered: ions, electrons, and neutrals. Either the two- or five-moment model was used for the ions and electrons, but the five-moment model was always employed for the neutrals. Ionization and excitation reactions were included in each model.

Two glow discharge test cases in 107 Pa argon were examined. The first was a basic, one-dimensional, DC discharge problem used to verify that the algorithms were implemented correctly. The basic results were found to be in qualitative agreement with those of Meyyappan and Kreskovsky.[15] Electron temperature and velocity profiles showed large local maxima in the cathode layer, whereas the corresponding ion properties peaked at the cathode. Two peaks were observed in the ionization profile, with the larger closer to the cathode. Fine grid resolution was required near these peaks to obtain acceptable numerical solutions. Comparing the results from the two- and five-moment models, it was observed that subtle differences in the velocities and temperatures in the cathode sheath led to significant differences between the predictions of the two models for ionization rates and number densities.

The second test case was a two-dimensional transient problem with an elliptical cathode, designed to emphasize the differences between the two models. Relative to the two-moment model, the five-moment model predicted a slower response to the activation of the cathode, and predicted acoustic waves propagating through the domain. In particular, the development of the charged particle temperature and velocity distributions for the five-moment model lagged that for the two-moment model. By 1000 ns, the ion properties had nearly caught up, but substantial differences remained for the electron properties. These differences can be attributed to the effects of particle inertia and to differences in the boundary conditions for the two models.

The evolution of the properties of the neutrals was also studied for this problem. Both models predicted that neutral gas velocities on the order of 1.3 m/s occurred within 1000 ns, with a negligible rise in neutral temperature (~ 0.3 K). The slow temperature rise may be a feature of the monatomic gas, argon, considered in this study. In molecular gases, the fastest energy transfer path from the electrons to the neutrals is molecular dissociation into high-energy products through electron impact.[3] For pulsed discharges in air on the order of 10 ns in duration, an overheating on the order of 100 K has been obtained experimentally[3] within 1000 ns. To study flow control actuators, therefore, it will be necessary to move to a reasonably realistic model for air; discharges in molecular gases are a topic of ongoing work.

In summary, calculations with the five-moment model are seen to be feasible, and may prove to be a useful tool in studying nanosecond-pulse discharges. The computational cost for the five-moment model is about twice that of the two-moment model, as based on timings of the two-dimensional calculations presented here. Since significant differences in the charged particle behavior are observed between the two models, the increased generality of the five-moment model may be worth the additional computational cost.

Appendix A: A Short Derivation of the Moment Equations

A brief discussion is presented here on the derivation of the conservation laws as moments of the Boltzmann equation. Useful references for additional details include Chapman and Cowling,[29] Seshadri,[30] and Olejniczak and Candler.[31]

Starting from the molecular dynamics viewpoint, classical Newtonian mechanics is assumed to hold, and

8

the particle acceleration $\mathbf{a}$ is assumed to be generated by gravity and the Lorentz force:

$$m_s \mathbf{a} = m_s \mathbf{g} + q_s \left(\mathbf{E} + \mathbf{u} \times \mathbf{B} \right) \tag{14}$$

Here m_s is the mass per particle, $\mathbf{g}$ is the acceleration due to gravity, q_s is the electric charge per particle, $\mathbf{u}$ is the particle velocity, $\mathbf{E}$ is the electric field, and $\mathbf{B}$ is the magnetic field.

The state of a particle can be specified by its position and velocity, the phase-space coordinates $(\mathbf{x}, \mathbf{u})$. In principal, the motion of a large group of particles can be predicted from Eq. (14), given all their positions and velocities at a certain time. In practice, this is not possible because of computational cost and sensitivity to initial conditions. Therefore, we are driven to describe the physics statistically, predicting macroscopic quantities, averaged over a large number of particles.

The fundamental dependent variable from the statistical point of view is the velocity distribution function for species-s, $f_s(\mathbf{x}, \mathbf{u}, t)$, which represents the probability of finding a particle in a particular small element of phase space. Here it is normalized so that the integral over all velocity space is unity:

$$\int f_s(\mathbf{x}, \mathbf{u}, t)\, d^3u = 1 \tag{15}$$

This definition requires that the distribution function tend to zero as the velocity components become large.

In the statistical treatment that follows, the electric and magnetic fields in Eq. (14) are taken to be macroscopic fields, obtained by averaging over a volume large enough to contain a large number of particles, but small compared to the length scale of macroscopic property variations. Particle trajectories are assumed to be governed by Eq. (14), except during collisions where the motion is governed by intermolecular forces (and where quantum mechanical effects may be significant). The gas is also assumed to be sufficiently dilute that these collisions can be considered as rare, discrete, short-duration events.

With these assumptions, and the restriction that a statistically significant number of particles be present in the small volume under consideration, the generalized Boltzmann equation, or equation of change of the probability density function, can be written as:

$$\frac{\partial}{\partial t}(n_s f_s) + \mathbf{u} \cdot \nabla (n_s f_s) + \mathbf{a} \cdot \nabla_u (n_s f_s) = \omega_s \tag{16}$$

The independent variables are particle velocity $\mathbf{u}$, position $\mathbf{x}$, and time t. Here n_s is the number density and ω_s represents the particle production rate due to collisions. (A derivation of the Boltzmann equation from the Liouville Theorem can be found in Ch. 7 of Hirschfelder, Curtis, and Bird.[32])

Equation (16) can be interpreted as stating that the number of particles observed, while following a selected initial group along their trajectories in phase space, is altered only by their sudden appearance or disappearance in local phase space through collisions. Given a suitable collision model, it can be solved to find the time-evolution of the distribution function. In a gas mixture, there is a Boltzmann equation for each species present; they are coupled through the collision term ω_s.

Other statistical quantities of interest are average values, which are more readily-measured, macroscopic properties. Considering a quantity $\phi(\mathbf{u})$ associated with each particle, an average value is defined as:

$$\langle \phi \rangle_s(\mathbf{x}, t) = \int \phi(\mathbf{u}) f_s(\mathbf{x}, \mathbf{u}, t)\, d^3u \tag{17}$$

where the integral is over all velocity space. Equations for the evolution of average values can be obtained from moments of the Boltzmann equation.

To obtain a moment equation, Eq. (16) is multiplied by ϕ, and integrated over all velocity space. It is assumed that, as the magnitude of the velocity approaches infinity, the velocity distribution function approaches zero sufficiently rapidly that the required moments of the velocity converge. The resulting equation of change of $\langle \phi \rangle_s$, or the transport equation, is:

$$\frac{\partial}{\partial t}\left(n_s \langle \phi \rangle_s\right) + \nabla \cdot (n_s \langle \mathbf{u} \phi \rangle_s) = n_s \langle \mathbf{a} \cdot \nabla_u \phi \rangle_s + \int \phi\, \omega_s\, d^3u \tag{18}$$

where the relation $\nabla_u \cdot \mathbf{a} = 0$, which follows from Eq. (14), has been used. (Detailed algebra for the derivation of Eq. (18) is presented by Seshadri.[30])

9

Moments of interest include the mass $\phi = m_s$, momentum $\phi = m_s\mathbf{u}$, and translational kinetic energy $\phi = \frac{1}{2}m_s u^2$ of the particles. Introducing these definitions into Eq. (18), the resulting mass, momentum, and translational energy conservation equations are:

$$\frac{\partial}{\partial t}(n_s m_s) + \nabla\cdot(n_s m_s \langle \mathbf{u}\rangle_s) = S_s$$

$$\frac{\partial}{\partial t}(n_s m_s \langle \mathbf{u}\rangle_s) + \nabla\cdot(n_s m_s \langle \mathbf{uu}\rangle_s) = n_s m_s \langle \mathbf{a}\rangle_s + \mathbf{A}_s \tag{19}$$

$$\frac{\partial}{\partial t}\left(\tfrac{1}{2}n_s m_s \langle u^2\rangle_s\right) + \nabla\cdot\left(\tfrac{1}{2}n_s m_s \langle \mathbf{u}u^2\rangle_s\right) = n_s m_s \langle \mathbf{a}\cdot\mathbf{u}\rangle_s + M'_s$$

where the source terms due to collisions are:

$$S_s = m_s \int \omega_s \, d^3 u$$

$$\mathbf{A}_s = m_s \int \mathbf{u}\,\omega_s \, d^3 u \tag{20}$$

$$M'_s = \tfrac{1}{2}m_s \int u^2 \,\omega_s \, d^3 u$$

These source terms represent particle generation and destruction by chemical reactions, momentum exchange between fluid species, and kinetic energy exchange in collisions.

Treatment of modes of internal energy, such as rotation, vibration, and electronic excitation, requires some additional work. Let the velocity distribution function associated with particles having internal energy level $\psi_{s\alpha}$ be $f_{s\alpha}$, where the subscript s indicates the species and α indicates the energy level. (The variable α simply represents an enumeration of energy states, and can represent one or more quantum numbers and grouped or ungrouped energy levels.) Define the average over the distribution $f_{s\alpha}$ as $\langle\phi\rangle_{s\alpha} = \int \phi f_{s\alpha}\, d^3 u$. The internal energy levels are assumed to be independent of the particle velocity in the sense that $\langle\psi_{s\alpha}\rangle_{s\alpha} = \psi_{s\alpha}$. In analogy to the procedure described above, write the Boltzmann equation for $f_{s\alpha}$, take the moment with $\psi_{s\alpha}$, and sum over all internal energy states. The resulting internal energy equation for species-s is:

$$\frac{\partial}{\partial t}\sum_\alpha n_{s\alpha}\psi_{s\alpha} + \nabla\cdot\sum_\alpha n_{s\alpha}\psi_{s\alpha}\langle\mathbf{u}\rangle_{s\alpha} = M''_s \tag{21}$$

where

$$M''_s = \sum_\alpha \psi_{s\alpha} \int \omega_{s\alpha}\, d^3 u \tag{22}$$

Here $n_{s\alpha}$ is the number density of particles having internal energy level $\psi_{s\alpha}$, and $\omega_{s\alpha}$ represents the production rate of particles of internal energy level $\psi_{s\alpha}$ in collisions. Note that $n_s = \sum_\alpha n_{s\alpha}$, $f_s = \sum_\alpha f_{s\alpha} n_{s\alpha}/n_s$, and that the ratio $n_{s\alpha}/n_s$ represents a distribution function for the particles over the possible discrete energy levels. Further, the sum of production rates of particles in each energy state is equal to the production rate for the species as a whole: $\omega_s = \sum_\alpha \omega_{s\alpha}$.

Adding the energy equations (19c) and (21) gives:

$$\frac{\partial}{\partial t}\left[\sum_\alpha n_{s\alpha}\psi_{s\alpha} + \tfrac{1}{2}n_s m_s \langle u^2\rangle_s\right]$$

$$+\nabla\cdot\left[\sum_\alpha n_{s\alpha}\psi_{s\alpha}\langle\mathbf{u}\rangle_{s\alpha} + \tfrac{1}{2}n_s m_s \langle \mathbf{u}u^2\rangle_s\right] = n_s m_s \langle\mathbf{a}\cdot\mathbf{u}\rangle_s + M_s \tag{23}$$

Equation (23) is an expression of total energy conservation, and the source term $M_s = M'_s + M''_s$ describes the exchange of total energy between fluid species.

A number of definitions are now introduced to describe the moment terms. The mean velocity is defined

as $\mathbf{v}_s = \langle \mathbf{u} \rangle_s$ and the peculiar velocity as $\mathbf{V}_s = \mathbf{u} - \mathbf{v}_s$. (Note that $\langle \mathbf{V}_s \rangle_s = 0$.) Also defined are the:

$$\text{Kinetic pressure: } p_s = \tfrac{1}{3} n_s m_s \langle V_s^2 \rangle_s$$
$$\text{Translational temperature: } T_s = \tfrac{1}{3} m_s \langle V_s^2 \rangle_s / k_B$$
$$\text{Thermal energy: } \epsilon_s = \sum_\alpha n_{s\alpha} \psi_{s\alpha} / (n_s m_s) + \tfrac{1}{2} \langle V_s^2 \rangle_s \tag{24}$$
$$\text{Viscous stress: } \tau_s = -n_s m_s [\langle \mathbf{V}_s \mathbf{V}_s \rangle_s - \tfrac{1}{3} \langle V_s^2 \rangle_s \mathbf{I}]$$
$$\text{Heat flux: } \mathbf{Q}_s = \tfrac{1}{2} n_s m_s \langle \mathbf{V}_s V_s^2 \rangle_s + \sum_\alpha n_{s\alpha} \psi_{s\alpha} \langle \mathbf{V}_s \rangle_{s\alpha}$$

Pressure and temperature are proportional to the average translational kinetic energy of the molecules. Total thermal energy contains a component due to internal energy states as well as translational kinetic energy. Viscous stress is related to the anisotropic component of the velocity correlation, representing transport of momentum by random molecular motions. Similarly, the heat flux represents transport of thermal energy by random molecular motion. Note the additional component of heat flux that arises when particles of a given species in different energy states have different velocity distribution functions.

Using these definitions in Eqs. (19a), (19b), and (23), and introducing the averaged form of (14), the the mass, momentum, and energy conservation equations for species-s become:

$$\frac{\partial \rho_s}{\partial t} + \nabla \cdot (\rho_s \mathbf{v}_s) = S_s$$
$$\frac{\partial}{\partial t}(\rho_s \mathbf{v}_s) + \nabla \cdot (\rho_s \mathbf{v}_s \mathbf{v}_s + p_s \mathbf{I}) = \nabla \cdot \tau_s + \rho_s \mathbf{g} + \zeta_s (\mathbf{E} + \mathbf{v}_s \times \mathbf{B}) + \mathbf{A}_s \tag{25}$$
$$\frac{\partial}{\partial t} \left[\rho_s \left(\epsilon_s + \tfrac{1}{2} v_s^2 \right) \right] + \nabla \cdot \left[\rho_s \mathbf{v}_s \left(\epsilon_s + \tfrac{1}{2} v_s^2 \right) + p_s \mathbf{v}_s \right] =$$
$$\nabla \cdot [\tau_s \cdot \mathbf{v}_s - \mathbf{Q}_s] + \rho_s \mathbf{v}_s \cdot \mathbf{g} + \zeta_s \mathbf{v}_s \cdot \mathbf{E} + M_s$$

where the mass density has been defined as $\rho_s = n_s m_s$ and the charge density as $\zeta_s = n_s q_s$. Note that the magnetic body force does not appear in Eq. (25c) because $\mathbf{u} \cdot (\mathbf{u} \times \mathbf{B}) = 0$.

Appendix B: Inelastic Collisions

A brief discussion of the form of the inelastic collision source terms is presented here. An alternative treatment is presented in Ch. 7 of Burgers.[23]

For inelastic collisions, the collision term on the right hand side of Eq. (16) can be written in the form:

$$\omega_s = \sum_r R_{rs} \hat{f}_{rs} \tag{26}$$

where R_{rs} is the rate of production or destruction of species-s in the class of inelastic collisions represented by reaction-r, and $\hat{f}_{rs}$ is the distribution function for the subset of particles of species-s participating in reaction-r. Equation (26) is an expression of particle accounting: the rate of generation of particles times the fraction that have a certain velocity gives the rate of change in number of particles in that velocity band.

The reaction rate R_{rs} is a signed quantity, and forward and backward reactions are considered separately. For binary collisions, the particle generation rate has the typical form $R_{rs} = \pm k_r n_a n_b$, where k_r is the rate constant for reaction-r, and n_a and n_b are the number densities of the colliding species.

The distribution function of reacting particles ($\hat{f}_{rs}$) is different from that of the species as a whole (f_s) because only a subset of particles are able to participate in reactions. For example, many reactions have an activation energy threshold, and only particles more energetic than that threshold can react. Similarly, the particles just born in reactions can have a different distribution function from the other members of their species.

Consequently, the reacting particles will have a different mean velocity and a different thermal energy than the species as a whole. Define the average of a property ϕ, with respect to the distribution function

$\hat{f}_{rs}$, as $\langle \phi \rangle_{rs} = \int \phi \hat{f}_{rs} \, d^3u$, and introduce Eq. (26) into Eqs. (20). The following source terms are obtained:

$$S_s = m_s \sum_r R_{rs}$$

$$\mathbf{A}_s = m_s \sum_r R_{rs} \langle \mathbf{u} \rangle_{rs} \tag{27}$$

$$M'_s = \tfrac{1}{2} m_s \sum_r R_{rs} \langle u^2 \rangle_{rs}$$

This is again simply particle accounting: the source terms are sums of the particle generation (destruction) rate of species-s times the average mass, momentum, or translational energy the particles appear (disappear) with.

Analogously, let $\omega_{s\alpha} = \sum_r R_{rs\alpha} \hat{f}_{rs\alpha}$, and substitute into Eq. (22). (Note that $R_{rs} = \sum_\alpha R_{rs\alpha}$.) The result is:

$$M''_s = \sum_r \sum_\alpha R_{rs\alpha} \psi_{s\alpha} \tag{28}$$

This source term is a double summation, over all reactions and internal energy levels, of the rate in reaction-r at which species-s appears in energy level-α times the value of that energy level. Defining $\psi_{rs} = \sum_\alpha R_{rs\alpha} \psi_{s\alpha} / R_{rs}$, indicating how the internal energy of species-s born in reaction-r is distributed over internal energy levels-α, and using (27c) and (28), the total energy source term $M_s = M'_s + M''_s$ can be written as:

$$M_s = \sum_r R_{rs} \left[\psi_{rs} + \tfrac{1}{2} m_s \langle u^2 \rangle_{rs} \right] \tag{29}$$

For the subset of particles-s participating in reaction-r, let $\mathbf{c}_{rs} = \langle \mathbf{u} \rangle_{rs} - \mathbf{v}_s = \langle \mathbf{V}_s \rangle_{rs}$ be the mean velocity relative to the mean flow velocity of all particles of species-s. Similarly, let the difference in internal energy between the reacting particles and the species as a whole be $H_{rs} = \psi_{rs} + \tfrac{1}{2} m_s \langle V_s^2 \rangle_{rs} - m_s \epsilon_s$. Since both $\mathbf{c}_{rs}$ and H_{rs} are zero if $\hat{f}_{rs} = \hat{f}_{rs\alpha} = f_s$, $\mathbf{c}_{rs}$ will be called the excess velocity and H_{rs} the excess internal energy. Using these definitions in Eqs. (27b) and (29), the inelastic momentum and energy source terms can be rewritten as:

$$\mathbf{A}_s = m_s \sum_r R_{rs} \mathbf{c}_{rs} + S_s \mathbf{v}_s$$

$$M_s = \sum_r R_{rs} H_{rs} + m_s \mathbf{v}_s \cdot \sum_r R_{rs} \mathbf{c}_{rs} + S_s \left(\epsilon_s + \tfrac{1}{2} v_s^2 \right) \tag{30}$$

Note that a minimal, consistent model for the inelastic momentum and energy sources must include at the least the terms proportional to S_s in Eq. (30). Writing the equations in nonconservative form, it becomes apparent that the absence of these terms causes the form of the momentum equation and the thermal energy equation to depend on reference frame, in violation of the principles of classical dynamics and thermodynamics.[33] (The terms containing the excess velocity are invariant because it is a velocity difference.)

Empirical data on reaction rates allow the evaluation of the term S_s in (27a). A precise model of the momentum and energy terms in (30) would require specific information on the distribution functions of the reacting particles. Some reasonable assumptions, however, can be made to create a closure model for these terms: the excess velocity will be assumed to be negligible ($\mathbf{c}_{rs} \approx 0$), and the excess internal energy H_{rs} of the reacting species will be approximated by the equilibrium heat of reaction per particle.

Using $\mathbf{c}_{rs} \approx 0$, the inelastic collision source terms for each species-s of charged particle are:

$$S_s = m_s \sum_r R_{rs}$$

$$\mathbf{A}_s = S_s \mathbf{v}_s \tag{31}$$

$$M_s = \sum_r R_{rs} H_{rs} + S_s \left(\epsilon_s + \tfrac{1}{2} v_s^2 \right)$$

Empirical data can be used for the reaction rates and the heat of reaction. The error incurred in the momentum term by neglecting the excess velocity may be mitigated by an appropriately chosen collision frequency, taken from experimental data, in the elastic collision terms.

12

Appendix C: Elastic Collisions

A more complete theoretical treatment is available for the elastic collisions,[23] based on the BGK model.[34] The model used for the term ω_s has the same form as Eq. (26), but in the form of paired interactions. All particles entering collisions are assumed to participate equally, so those particles have the same distribution function f_s as the species as a whole. Particles coming out of collisions are assumed to have completely randomized velocities, and have a distribution f_{st}^* with local mean velocity $\mathbf{v}_{st}$ and temperature T_{st}. (This notation represents particles of species-s coming out of collisions with species-t.) The form of the Boltzmann equation source term is then:

$$\omega_s = \sum_t k_{st} n_s n_t (f_{st}^* - f_s) \tag{32}$$

where the sum includes the case $t = s$, and the rate parameter k_{st} is taken to be independent of particle velocity. The resulting moment equation source terms, analogous to Eq. (27), are:

$$S_s = 0$$
$$\mathbf{A}_s = m_s n_s \sum_t k_{st} n_t (\mathbf{v}_{st} - \mathbf{v}_s) \tag{33}$$
$$M_s' = \tfrac{1}{2} m_s n_s \sum_t k_{st} n_t \left[\frac{3k_B}{m_s}(T_{st} - T_s) + v_{st}^2 - v_s^2 \right]$$

where the relations $\langle \mathbf{u} \rangle_{st} = \mathbf{v}_{st}$ and $\langle u^2 \rangle_{st} = v_{st}^2 + 3k_B T_{st}/m_s$ have been used.

The variables $\mathbf{v}_{st}$ and T_{st} must now be related to the other flow variables. To do this, we use the fact that mass, momentum, and kinetic energy are conserved in an elastic collision. We assume that particle velocities are fully randomized in collisions, so there is no preferential direction for the particles exiting a collision, and the particle velocities entering and leaving the collision are all uncorrelated. The mean velocity coming out of a collision is then:

$$\mathbf{v}_{st} = \frac{m_s \mathbf{v}_s + m_t \mathbf{v}_t}{m_s + m_t} \tag{34}$$

and the corresponding mean thermal energy is:

$$\tfrac{3}{2} k_B T_{st} = \tfrac{3}{2} k_B T_s + \frac{m_{st}}{m_s + m_t} \left[3k_B (T_t - T_s) + \tfrac{1}{2} m_t |\mathbf{v}_t - \mathbf{v}_s|^2 \right] \tag{35}$$

where $m_{st} = m_s m_t/(m_s + m_t)$ is the reduced mass. Introducing Eqs. (34) and (35) into Eqs. (33), and simplifying, we arrive at the model used here for momentum and energy exchange in elastic collisions:

$$\mathbf{A}_s = -n_s \sum_t m_{st} \nu_{st} (\mathbf{v}_s - \mathbf{v}_t)$$
$$M_s = -n_s \sum_t \frac{m_{st} \nu_{st}}{m_s + m_t} \left[3k_B (T_s - T_t) + (\mathbf{v}_s - \mathbf{v}_t) \cdot (m_s \mathbf{v}_s + m_t \mathbf{v}_t) \right] \tag{36}$$

Here $\nu_{st} = k_{st} n_t$ is the average momentum transfer collision frequency between particles of types s and t.

Acknowledgments

References

[1] Lieberman, M. A. and Lichtenberg, A. J., *Principles of Plasma Discharges and Materials Processing*, J. Wiley, New York, 1994.

[2] Fridman, A. and Kennedy, L. A., *Plasma Physics and Engineering*, Taylor and Francis, New York, 2004.

[3] Roupassov, D. V., Nikipelov, A. A., Nudnova, M. M., and Starikovskii, A. Y., "Flow Separation Control by Plasma Actuator with Nanosecond Pulsed-Periodic Discharge," *AIAA Journal*, Vol. 47, No. 1, 2009, pp. 168–185.

[4]Bredan, D. and Raja, L. L., "Simulations of Nanosecond Pulsed Plasmas in Supersonic Flow," AIAA Paper 2009-3594, June 2009.

[5]Likhanskii, A. V., Semak, V. V., Shneider, M. N., Opaits, D. F., Miles, R. B., and Macheret, S. O., "The Role of the Photoionization in the Numerical Modeling of the DBD Plasma Actuator," AIAA Paper 2009-841, January 2009.

[6]Murray, R. C., Zaidi, S. H., Carraro, M. R., Vasilyak, L. M., Macheret, S. O., Shneider, M. N., and Miles, R. B., "Magnetohydrodynamic Power Generation Using Externally Ionized, Cold, Supersonic Air as Working Fluid," *AIAA Journal*, Vol. 44, No. 1, 2006, pp. 119–127.

[7]Adamovich, I. V., Lempert, W. R., Nishihara, M., Rich, J. W., and Utkin, Y. G., "Repetitively Pulsed Nonequilibrium Plasmas for Magnetohydrodynamic Flow Control and Plasma-Assisted Combustion," *Journal of Propulsion and Power*, Vol. 24, No. 6, 2008, pp. 1198–1215.

[8]Font, G. I., "Boundary-Layer Control with Atmospheric Plasma Discharges," *AIAA Journal*, Vol. 44, No. 7, 2006, pp. 1572–1578.

[9]Ward, A. L., "Calculations of Cathode-Fall Characteristics," *Journal of Applied Physics*, Vol. 33, No. 9, 1962, pp. 2789–2794.

[10]Boeuf, J.-P., "A Two-Dimensional Model of DC Glow Discharges," *Journal of Applied Physics*, Vol. 63, No. 5, 1988, pp. 1342–1349.

[11]Raizer, Y. P. and Surzhikov, S. T., "Two-Dimensional Structure in a Normal Glow Discharge and Diffusion Effects in Cathode and Anode Spot Formation," *High Temperature*, Vol. 26, No. 3, 1988, pp. 304–311.

[12]Graves, D. B. and Jensen, K. F., "A Continuum Model of DC and RF Discharges," *IEEE Transactions on Plasma Science*, Vol. PS-14, No. 2, 1986, pp. 78–91.

[13]Passchier, J. D. P. and Goedheer, W. J., "A Two-Dimensional Fluid Model for an Argon RF Discharge," *Journal of Applied Physics*, Vol. 74, No. 6, 1993, pp. 3744–3751.

[14]Young, F. F., "Two-Dimensional, Self-Consistent, Three-Moment Simulation of RF Glow Discharges," *IEEE Transactions on Plasma Science*, Vol. 21, No. 3, 1993, pp. 312–321.

[15]Meyyappan, M. and Kreskovsky, J. P., "Glow Discharge Simulation Through Solutions to the Moments of the Boltzmann Transport Equation," *Journal of Applied Physics*, Vol. 68, No. 4, 1990, pp. 1506–1512.

[16]Meyyappan, M., "A Continuum Model for Low-Pressure Radio-Frequency Discharges," *Journal of Applied Physics*, Vol. 69, No. 12, 1991, pp. 8047–8051.

[17]Meyyappan, M. and Govindan, T. R., "Two-Dimensional Analysis of Radio Frequency Discharges," *IEEE Transactions on Plasma Science*, Vol. 24, No. 1, 1996, pp. 119–120.

[18]Wilcoxson, M. H. and Manousiouthakis, V. I., "Simulation of a Three-Moment Fluid Model of a Two-Dimensional Radio Frequency Discharge," *Chemical Engineering Science*, Vol. 51, No. 7, 1996, pp. 1089–1106.

[19]D'Ambrosio, D. and Giordano, D., "Electromagnetic Fluid Dynamics for Aerospace Applications," *Journal of Thermophysics and Heat Transfer*, Vol. 21, No. 2, 2007, pp. 284–302.

[20]MacCormack, R. W., "Solution of Maxwell's Equations Coupled to the Navier-Stokes Equations," AIAA Paper 2009-3911, June 2009.

[21]Hakim, A. and Shumlak, U., "Two-Fluid Physics and Field-Reversed Configurations," *Physics of Plasmas*, Vol. 14, No. 5, 2007, pp. 055911–1 – 055911–11.

[22]Park, S.-K. and Economou, D. J., "Analysis of Low Pressure RF Glow Discharges Using Continuum Model," *Journal of Applied Physics*, Vol. 68, No. 8, 1990, pp. 3904–3915.

[23]Burgers, J. M., *Flow Equations for Composite Gases*, Academic Press, New York, 1969.

[24]White, F. M., *Viscous Fluid Flow*, McGraw-Hill, New York, 2nd ed., 1991.

[25]Hoffmann, K. A. and Chiang, S. T., *Computational Fluid Dynamics*, Engineering Educational System, Wichita KS, 4th ed., 2000.

[26]Anderson, W. K., Thomas, J. L., and van Leer, B., "A Comparison of Finite Volume Flux Vector Splittings for the Euler Equations," AIAA Paper 85-0122, January 1985.

[27]Cheney, W. and Kincaid, D., *Numerical Mathematics and Computing*, Brooks/Cole Publishing, Pacific Grove, California, 3rd ed., 1994.

[28]Graves, D. B., "Fluid Model Simulations of a 13.56-MHz RF Discharge: Time and Space Dependence of Rates of Electron Impact Ionization," *Journal of Applied Physics*, Vol. 62, No. 1, 1987, pp. 88–94.

[29]Chapman, S. and Cowling, T. G., *The Mathematical Theory of Non-Uniform Gases*, Cambridge University Press, 2nd ed., 1952.

[30]Seshadri, S. R., *Fundamentals of Plasma Physics*, Elsevier, New York, 1973.

[31]Olejniczak, J. and Candler, G. V., "Vibrational Energy Conservation with Vibration-Dissociation Coupling: General Theory and Numerical Studies," *Physics of Fluids*, Vol. 7, No. 7, 1995, pp. 1764–1774.

[32]Hirschfelder, J. O., Curtis, C. F., and Bird, R. B., *Molecular Theory of Gases and Liquids*, J. Wiley, New York, 1954.

[33]Lam, S. H., "MAE 558: Plasmadynamics Notes," Department of Mechanical and Aerospace Engineering, Princeton University, Princeton NJ 08544. URL: http://www.princeton.edu/~lam/SHL/Plasma.pdf [accessed 3 June 2008].

[34]Bhatnagar, P. L., Gross, E. P., and Krook, M., "A Model for Collision Processes in Gasses. I. Small Amplitude Processes in Charged and Neutral One-Component Systems," *Physical Review*, Vol. 94, No. 3, 1954, pp. 511–525.

	Inflow ($v_e^\perp < 0$)	Outflow ($v_e^\perp > 0$)
Subsonic ($|v_e^\perp| < a_e$)	extrapolate n_e	extrapolate n_e
	$v_e^\perp = k_r - \gamma_E \Gamma_i^+/n_e$	$v_e^\perp = k_r - \gamma_E \Gamma_i^+/n_e$
	$\mathbf{v}_e^\parallel = 0$	extrapolate $\mathbf{v}_e^\parallel$
	$T_e = \text{avg}(T_{ea}, T_{es})$	$T_e = \text{avg}(T_{ea}, T_{es})$
Supersonic ($|v_e^\perp| \geq a_e$)	$n_e = \gamma_E \Gamma_i^+/a_e$	extrapolate n_e
	$v_e^\perp = -a_e$	extrapolate $\mathbf{v}_e$
	$\mathbf{v}_e^\parallel = 0$	extrapolate T_e
	$T_e = T_{es}$	

(a) Electrons, five-moment model.

Inflow ($v_i^\perp < 0$)	Outflow ($v_i^\perp > 0$)
extrapolate n_i	extrapolate n_i
$v_i^\perp = 0$	extrapolate $\mathbf{v}_i$
extrapolate $\mathbf{v}_i^\parallel$	extrapolate T_i
$T_i = T_\infty$	

(b) Ions, five-moment model.

Inflow/Outflow
$n_e v_e^\perp = n_e k_r - \gamma_E n_i v_i^+$
$T_e = \text{avg}(T_{ea}, T_{es})$

(c) Electrons, two-moment model.

Inflow ($v_i^\perp < 0$)	Outflow ($v_i^\perp > 0$)
$v_i^\perp = 0$	extrapolate n_i
$T_i = T_\infty$	extrapolate T_i

(d) Ions, two-moment model.

Figure 1. Boundary conditions for charged particles.
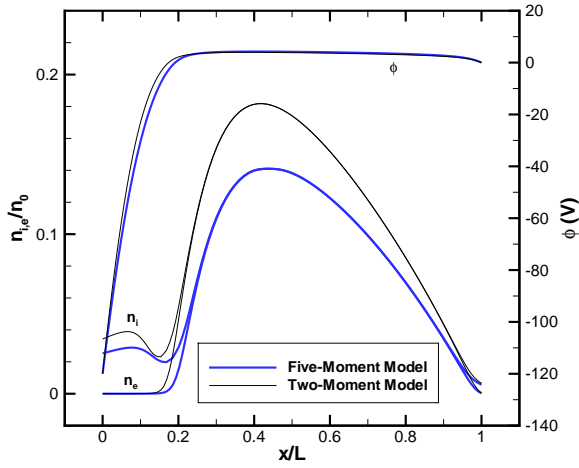
(a) Number densities and potential.
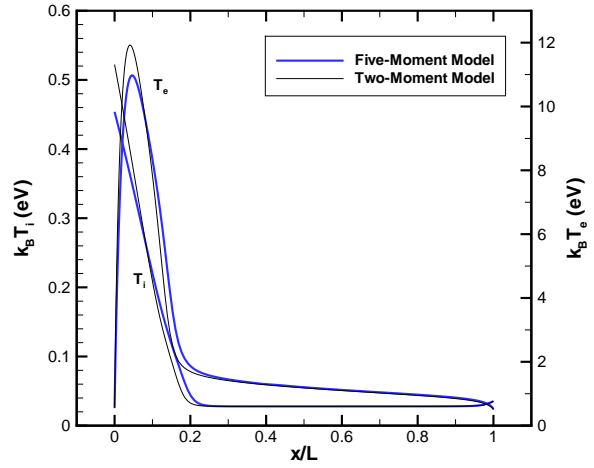
(b) Temperatures.
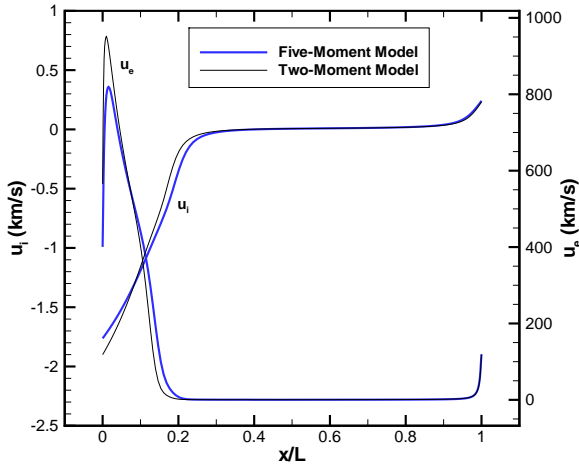
(c) Velocities.
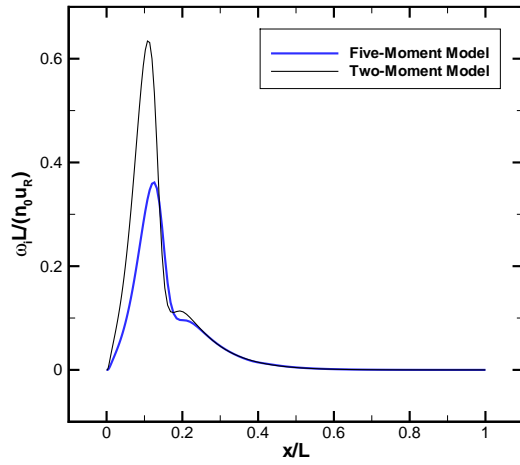
(d) Ionization rate.

Figure 2. Comparison of two-moment and five-moment models for one-dimensional, DC discharge.
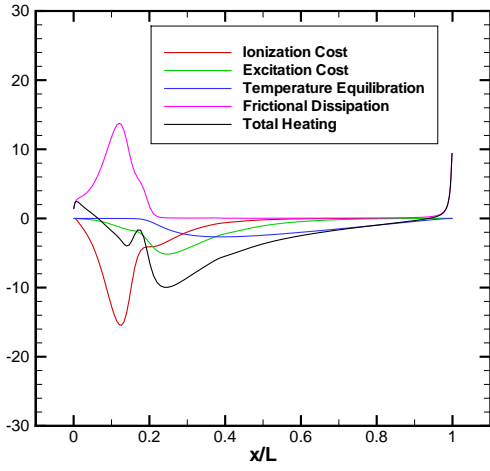
16
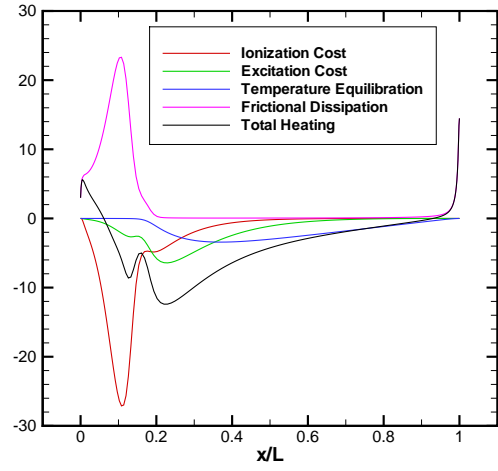
(a) Five-moment model.

(b) Two-moment model.

Figure 3. Electron heating terms for one-dimensional, DC discharge.
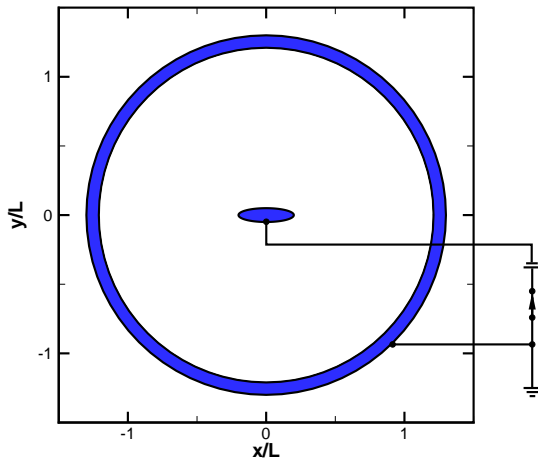
(a) Schematic diagram.
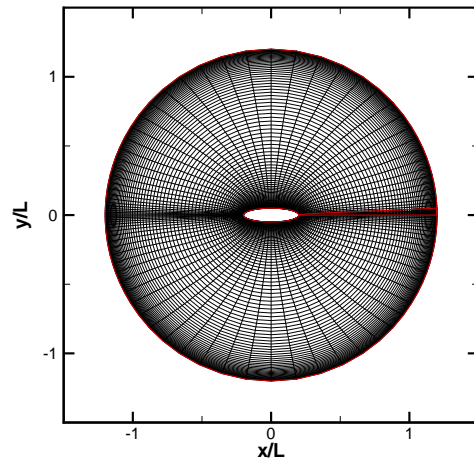
(b) Computational mesh.

Figure 4. Transient discharge problem with elliptical cathode.
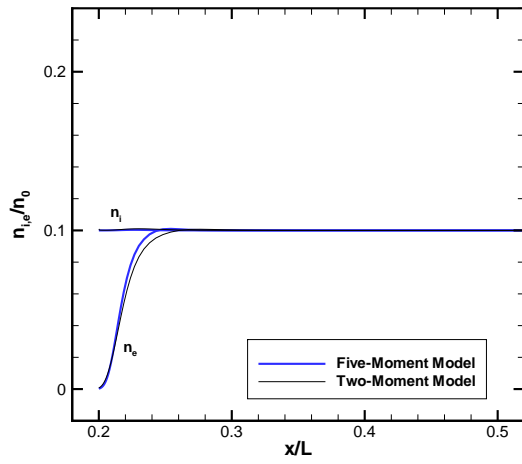
(a) Number density.
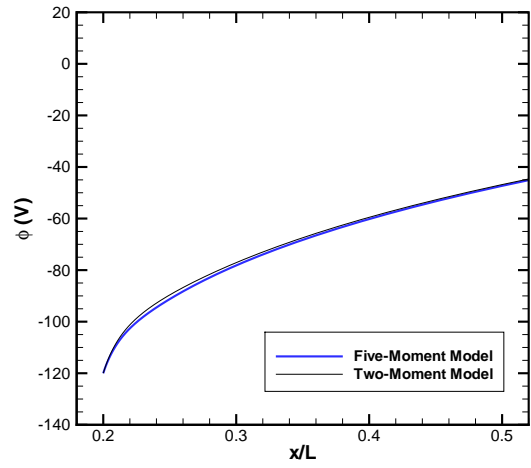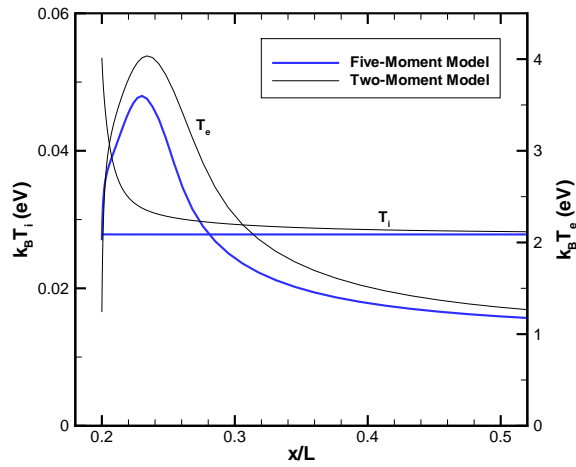
(b) Potential.
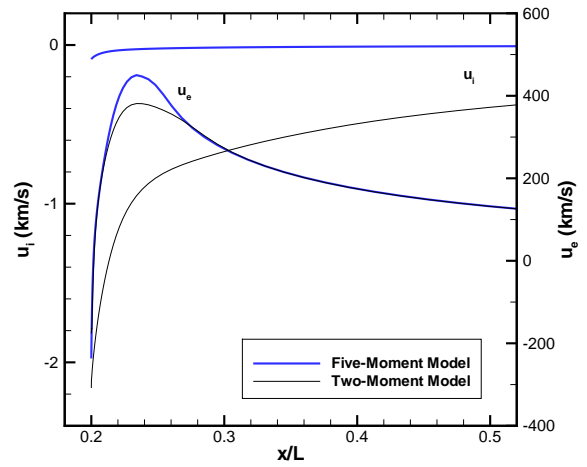
(c) Temperature.

(d) Horizontal velocity component.

Figure 5. Cathode sheath evolution in transient discharge (1 ns).
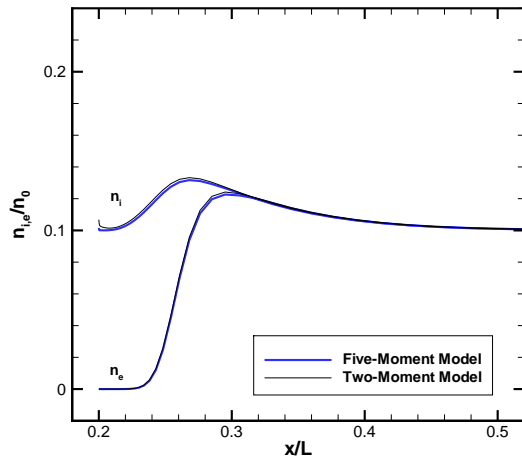
(a) Number density.
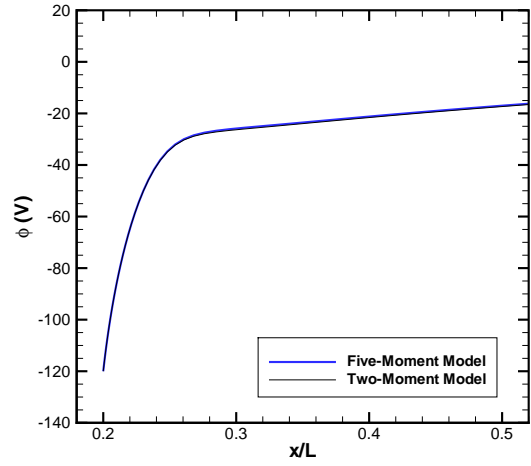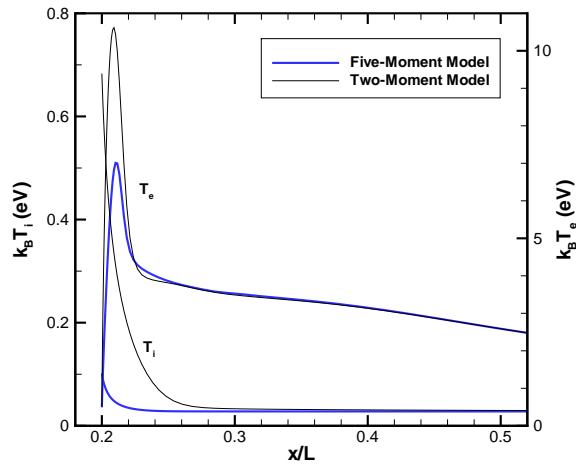
(b) Potential.
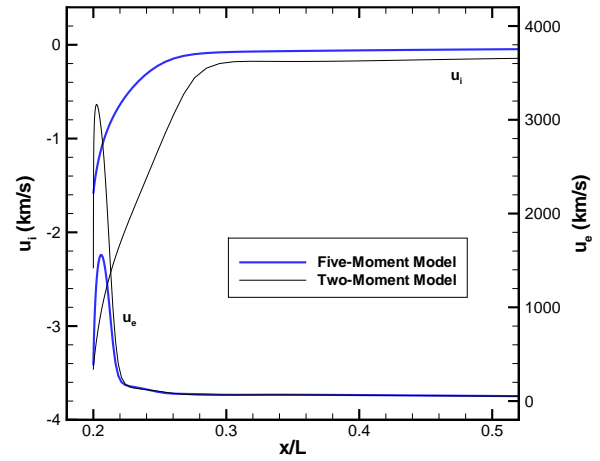
(c) Temperature.

(d) Horizontal velocity component.

Figure 6. Cathode sheath evolution in transient discharge (10 ns).
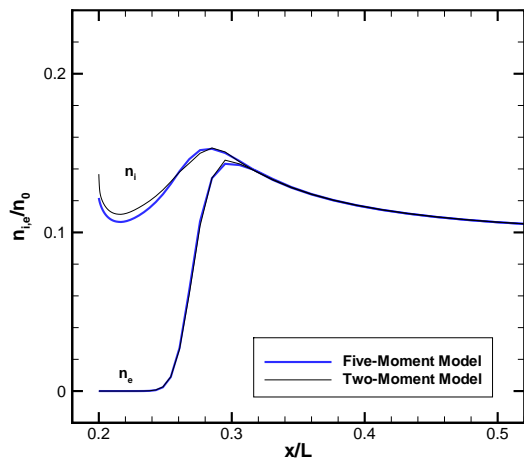
(a) Number density.
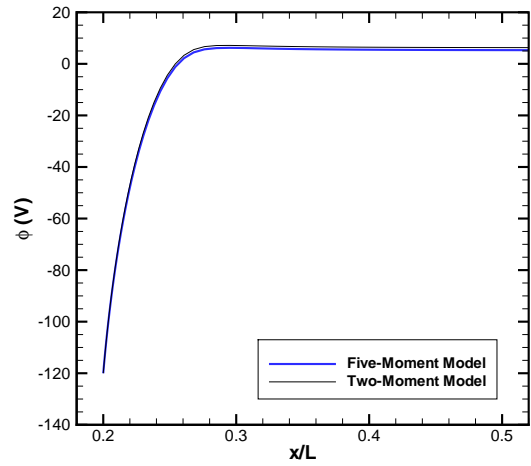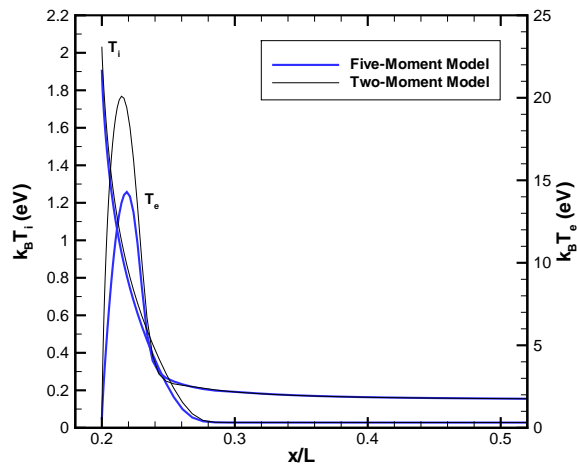
(b) Potential.
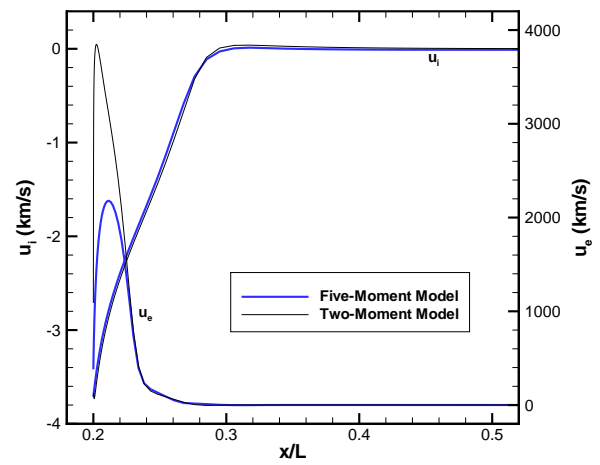
(c) Temperature.

(d) Horizontal velocity component.

Figure 7. Cathode sheath evolution in transient discharge (100 ns).

20
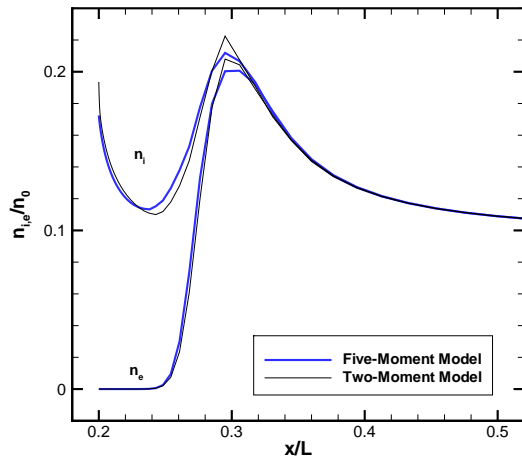
(a) Number density.
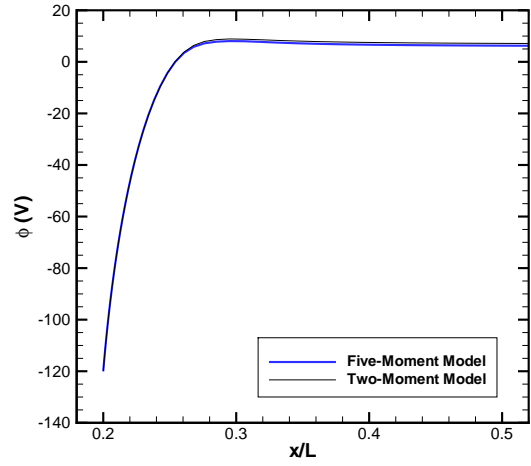
(b) Potential.
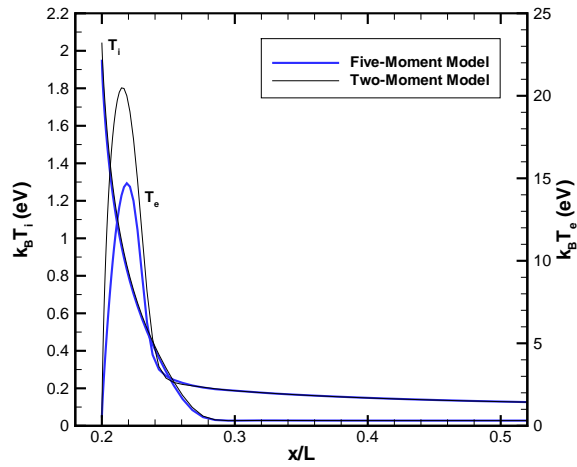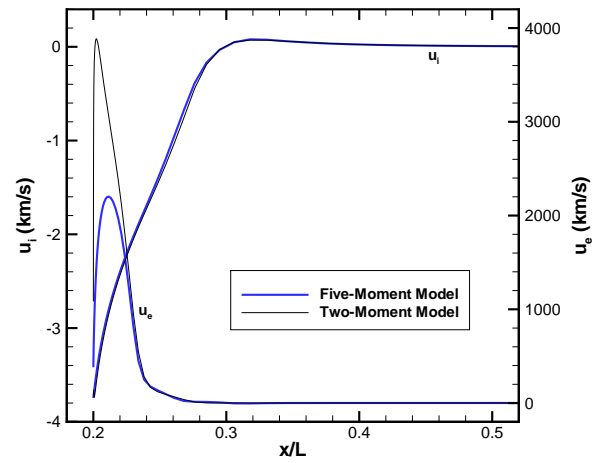
(c) Temperature.

(d) Horizontal velocity component.

Figure 8. Cathode sheath evolution in transient discharge (1000 ns).

21
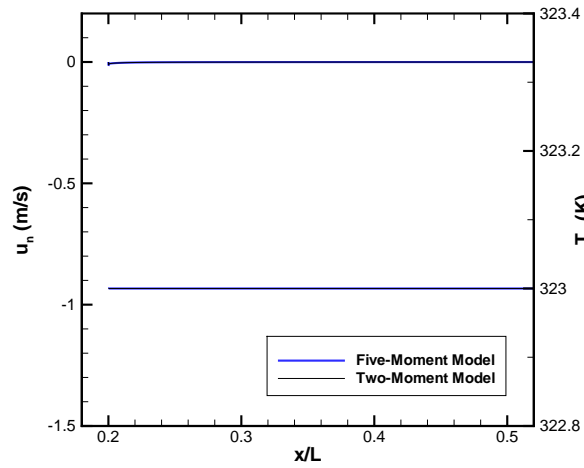
(a) 1 ns.
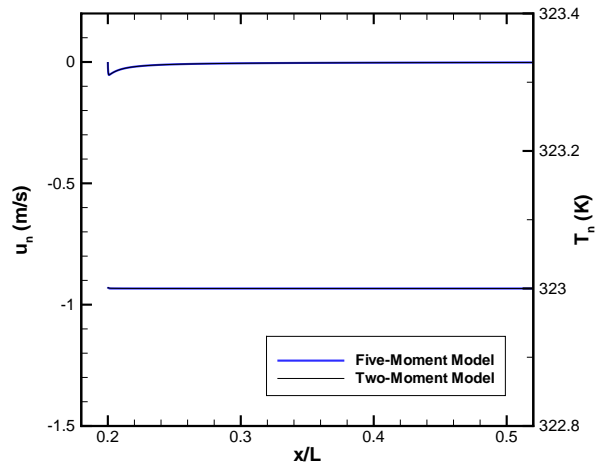
(b) 10 ns.
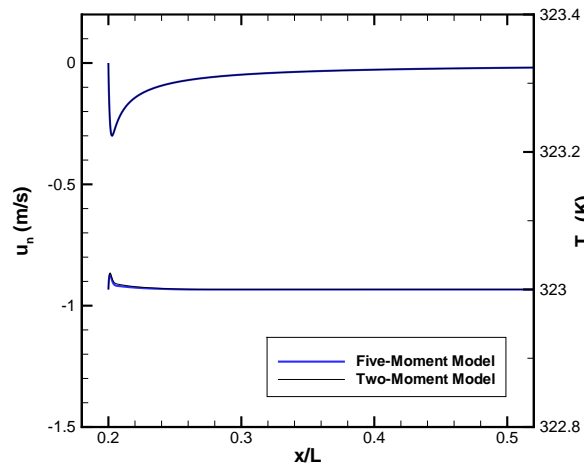
(c) 100 ns.
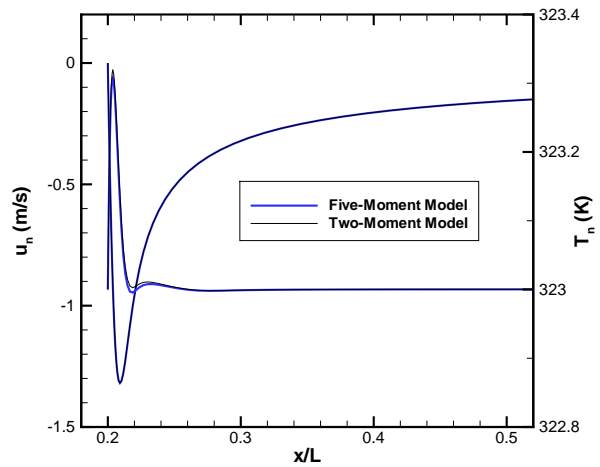
(d) 1000 ns.

Figure 9. Horizontal velocity component and temperature for neutral particles.
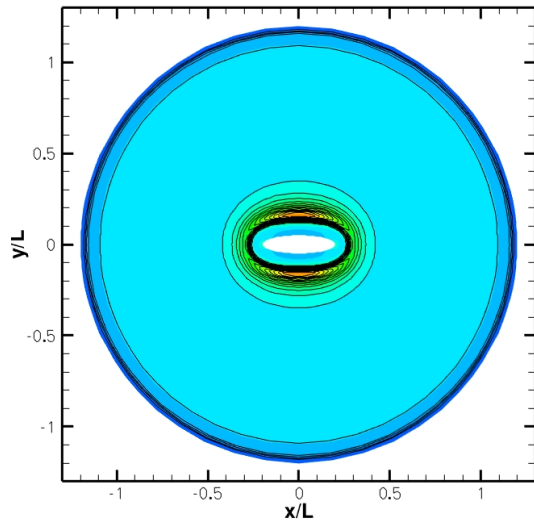
22

(a) Number densities (contour 2×10^{13} m^{-3}).

(b) Potential (contour 10 V).

(c) Ion temperature (contour 0.1 eV).

(d) Electron temperature (contour 1 eV).

(e) Ion speed (contour 0.5 km/s).

(f) Electron speed (contour 500 km/s).

Figure 10. Results for transient elliptic cathode problem, five-moment model (1000 ns).
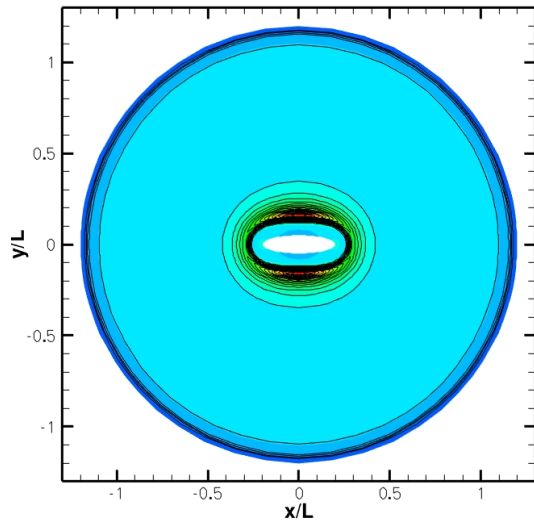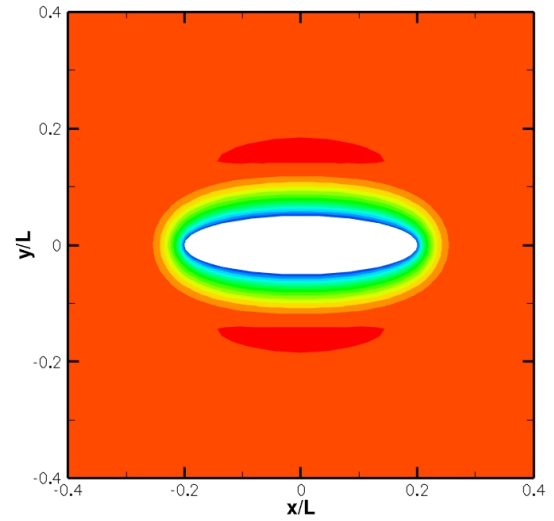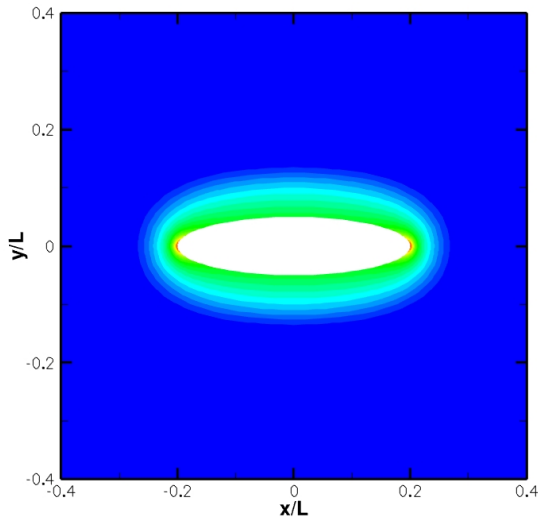
23

(a) Number densities (contour 2×10^{13} m^{-3}).

(b) Potential (contour 10 V).

(c) Ion temperature (contour 0.1 eV).
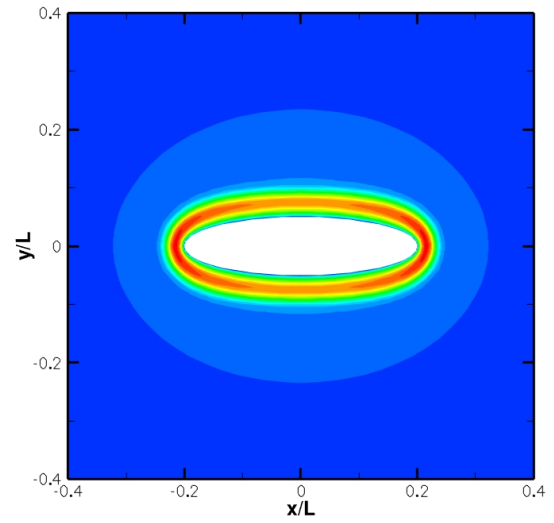
(d) Electron temperature (contour 1 eV).
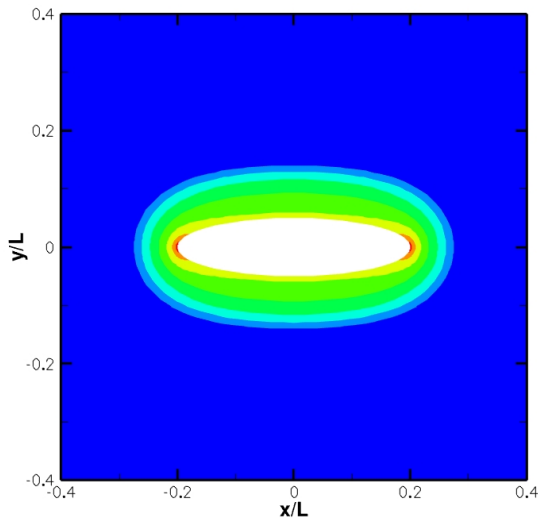
(e) Ion speed (contour 0.5 km/s).
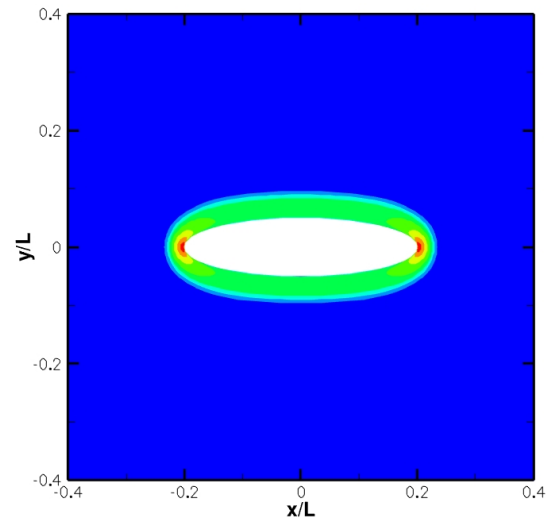
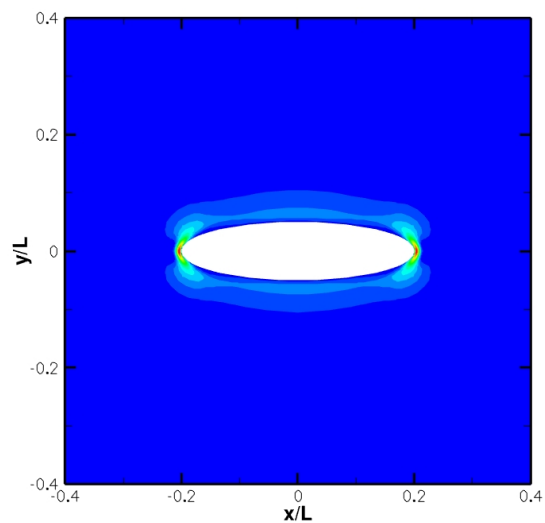(f) Electron speed (contour 500 km/s).

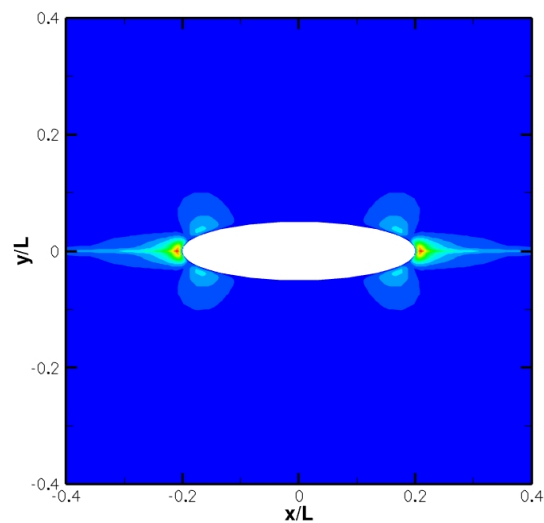**Figure 11. Results for transient elliptic cathode problem, two-moment model (1000 ns).**

24
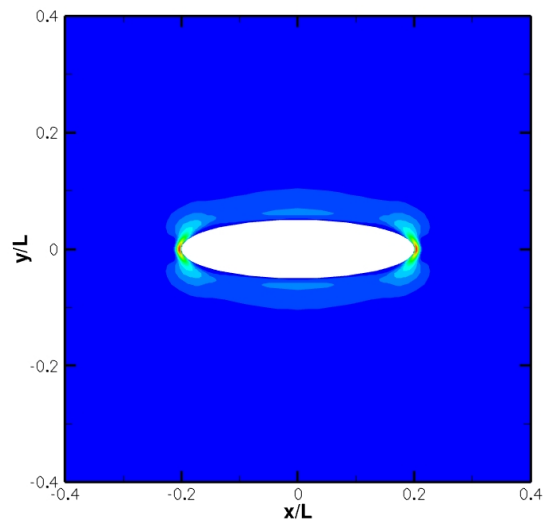
(a) Neutral temperature, 5-moment model (contour 0.02 K).
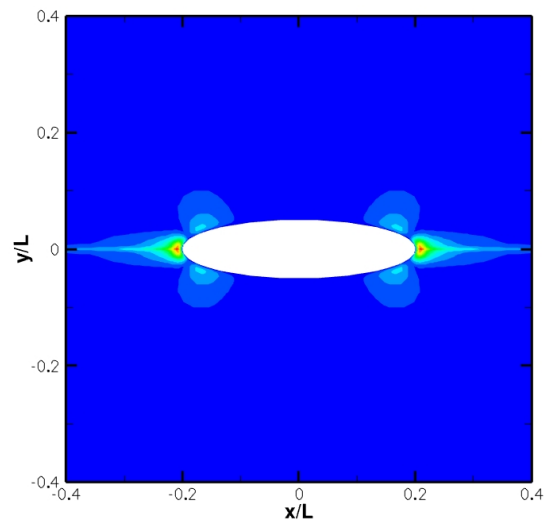
(b) Neutral speed, 5-moment model (contour 0.1 m/s).

(c) Neutral temperature, 2-moment model (contour 0.02 K).

(d) Neutral speed, 2-moment model (contour 0.1 m/s).

Figure 12. Neutral particle properties in transient elliptic cathode problem (1000 ns).

High-Order Numerical Methods
for Electrical Discharge Modeling

Jonathan Poggie[*]

Air Force Research Laboratory, Wright-Patterson AFB, Ohio 45433-7512 USA

A new computer code has been developed to model the behavior of weakly-ionized gases through a three-species fluid model coupled to either the Poisson equation or the full set of Maxwell's equations. The three-dimensional numerical implementation involves compact spatial differences of up to sixth order accuracy, driven by a fourth-order Runge-Kutta time marching scheme. Sample calculations are presented here for three test cases: a DC discharge in one dimension, a three-dimensional rectangular waveguide problem, and a one-dimensional wave propagation problem in a warm, collisional plasma. In all cases, good agreement was obtained between the numerical solutions and either analytical solutions or previously-published numerical solutions.

I.   Introduction

Over the past fifteen years, plasma-based flow control techniques have been a topic of strong research interest, motivated by the possibility of extremely rapid actuation, low-profile configuration, and the ability to operate in hostile environments. Numerical studies of these discharges are motivated by the need to understand and optimize them for aerodynamic applications. Particle methods, although they provide valuable insight and encompass the greatest portion of the relevant physics, are too computationally costly at present for practical discharge computations at relatively high pressures.[1] Direct solutions to the Boltzmann equation are also prohibitively costly. The only viable alternatives are continuum models, based on moments of the Boltzmann equation.

Traditional continuum modeling of electrical discharges employs a one-moment model, the continuity equation, with particle transport properties and ionization rates taken as a function of the reduced electric field.[2–4] More recent studies have extended this model by substituting an electron energy equation in place of the reduced electric field dependence.[5–7] Only a few studies have considered particle inertia; these typically have assumed constant ion temperature,[8–12] although some studies of shock structure have employed more general models.[13]

For low-frequency applications, the Poisson equation for the electric potential is assumed to govern the electromagnetic effects. For high frequencies and for pulsed discharges, the full set of Maxwell's equations may have to be solved for the electromagnetic fields. The coupling of a fluid-plasma model with Maxwell's equations has been investigated for applications in microwave cavity plasma reactors,[14,15] and for simulation of the hypersonic radio blackout problem.[16] These computations generally neglect ion motion and assume quasi-neutrality. More recently, numerical solutions of coupled fluid-electromagnetic equations have been investigated in the aerospace community[17,18] and in the fusion plasma community.[19] In such applications, ion motion and space charge may be important.

The present paper explores the possibility of solving a more general model, including three species of particles (ions, electrons, and neutrals), with continuity, momentum, and energy equations for each species (i.e., a five-moment model for each species). Results obtained with a five-moment model for each species are compared to a more conventional two-moment model. The electromagnetic fields are computed using either the Poisson equation or the full set of Maxwell's equations. The baseline numerical implementation involves compact spatial differences of up to sixth-order accuracy, driven by a fourth-order Runge-Kutta

---

American Institute of Aeronautics and Astronautics

time marching scheme. Sample calculations are presented here for several test cases, including a basic glow discharge, a waveguide, and a plasma wave propagation problem.

II.   Physical Model

A basic model for a discharge in a weakly-ionized gas is described here. Either two- or five-moment models are employed for the particle motion. To compute the electromagnetic fields, either the Poisson equation or the full Maxwell's equations are employed. An outline of the derivation of these physical models was presented in a previous paper.[20]

A.   Five-Moment Model

First we discuss the five-moment model, which includes particle inertia. The conservation equations for mass, momentum, and total energy of each species are:

$$\frac{\partial}{\partial t}(m_s n_s) + \nabla \cdot (m_s n_s \mathbf{v}_s) = S_s$$
$$\frac{\partial}{\partial t}(m_s n_s \mathbf{v}_s) + \nabla \cdot (m_s n_s \mathbf{v}_s \mathbf{v}_s + p_s \mathbf{I}) =$$
$$\nabla \cdot \tau_s + m_s n_s \mathbf{g} + q_s n_s (\mathbf{E} + \mathbf{v}_s \times \mathbf{B}) + \mathbf{A}_s \tag{1}$$
$$\frac{\partial}{\partial t}\left[m_s n_s \left(\epsilon_s + \tfrac{1}{2}v_s^2\right)\right] + \nabla \cdot \left[m_s n_s \mathbf{v}_s \left(\epsilon_s + \tfrac{1}{2}v_s^2\right) + p_s \mathbf{v}_s\right] =$$
$$\nabla \cdot [\tau_s \cdot \mathbf{v}_s - \mathbf{Q}_s] + m_s n_s \mathbf{v}_s \cdot \mathbf{g} + q_s n_s \mathbf{v}_s \cdot \mathbf{E} + M_s$$

where the notation $s = i, e, n$ indicates the ions, electrons, and neutrals, respectively.

The mass per particle of each species is denoted as m_s, and the corresponding charge per particle is q_s. The species number density is n_s, the mass density is $\rho_s = m_s n_s$, the charge density is $\zeta_s = q_s n_s$, and the current density is $\mathbf{j}_s = q_s n_s \mathbf{v}_s$. The velocity is $\mathbf{v}_s$ and the translational temperature is T_s. The electric field is $\mathbf{E}$, the magnetic field is $\mathbf{B}$, and the gravitational field is $\mathbf{g}$. (Gravity is neglected for the present test cases, but buoyancy effects may be important for discharges in low-speed flow.) The pressure is found from $p_s = n_s k_B T_s$, where k_B is the Boltzmann constant. The internal energy per particle is assumed to have the form $m_s \epsilon_s = \mathcal{H}_s + k_B T_s/(\gamma_s - 1)$, where $\gamma_s = 5/3$ is the ratio of specific heats and $\mathcal{H}_s$ is the heat of formation per particle of species-s.

In order to close the equation set (1), models are needed for the collision source terms S_s, $\mathbf{A}_s$, and M_s, the viscous stress tensor τ_s, and the heat flux vector $\mathbf{Q}_s$. The inelastic components of the collision source terms have the form:

$$S_s = m_s \sum_r R_{rs}$$
$$\mathbf{A}_s = S_s \mathbf{v}_s \tag{2}$$
$$M_s = S_s \left(\epsilon_s + \tfrac{1}{2}v_s^2\right) + \sum_r R_{rs} H_{rs}$$

Here R_{rs} is the rate of production of species-s in reaction-r, H_{rs} is the corresponding energy gain for species-s, and the summation is over all reactions. For this model, the particles are assumed to appear out of collisions with the average momentum of their peers. A analogous form is used for the energy term, but with provision for an additional energy loss or gain, because only the most energetic particles participate in inelastic collisions.

The momentum and energy source terms also have an elastic collision component. Because the gas is assumed to be weakly ionized, the primary elastic collisions are with neutral particles. The following models[21] are used for the elastic components of the collision source terms for the charged particles:

$$\mathbf{A}_s = -n_s m_{sn} \nu_{sn} (\mathbf{v}_s - \mathbf{v}_n)$$
$$M_s = -n_s \frac{m_{sn}\nu_{sn}}{m_s + m_n} [3k_B(T_s - T_n) + (\mathbf{v}_s - \mathbf{v}_n)\cdot(m_s \mathbf{v}_s + m_n \mathbf{v}_n)] \tag{3}$$

where $m_{sn} = m_s m_n/(m_s + m_n)$ is the reduced mass, with $s = i, e$. The corresponding elastic source terms

American Institute of Aeronautics and Astronautics

for the neutrals are taken to be:

$$\mathbf{A}_n = -\sum_{t\neq n} \mathbf{A}_t$$

$$M_n = -\sum_{t\neq n} M_t$$

(4)

because overall momentum and energy is conserved in collisions. The overall collision source terms are the sum of the inelastic collision component, Eq. (2), and the elastic collision component, Eq. (3)-(4).

For the flux terms, it is assumed that the viscous term has a Newtonian form, with Stokes hypothesis applied, and that the heat flux follows Fourier's law:

$$\tau_s = \mu_{vs} \left[(\nabla\mathbf{v}_s) + (\nabla\mathbf{v}_s)^T - \tfrac{2}{3}\nabla\cdot\mathbf{v}_s\mathbf{I} \right]$$

$$\mathbf{Q}_s = -k_s\nabla T_s$$

(5)

where μ_{vs} is the viscosity and k_s is the thermal conductivity for species-s.

B. Two-Moment Model

Next we discuss the two-moment model, or drift-diffusion formulation. This model neglects the acceleration terms in the momentum equation, and also neglects all viscous terms. Neglecting viscous, gravitational, and inertia terms, the momentum equation can be solved for the species velocity:

$$n_s\mathbf{v}_s = n_s\mathbf{v}_n + s_s n_s \mu_s \mathbf{N}_s \cdot (\mathbf{E} + \mathbf{v}_n \times \mathbf{B}) - \frac{D_s}{k_B T_s}\mathbf{N}_s\cdot\nabla p_s$$

$$N_{(s)ij} = \frac{1}{1+\mu_s^2 B^2}\left(\delta_{ij} + \mu_s^2 B_i B_j + s_s\mu_s\epsilon_{ijk}B_k\right)$$

(6)

where the product is on the second index of $\mathbf{N}_s$. Here, the sign of the particle charge is $s_s = q_s/|q_s|$, the mobility is defined as $\mu_s = |q_s|/(m_{sn}\nu_{sn})$, and the diffusion coefficient as $D_s = \mu_s k_B T_s/|q_s|$.

With the drift-diffusion form, it is preferable to solve the thermal, rather than total, energy equation. This equation is obtained by subtracting the mechanical energy equation, the scalar product of the velocity with the momentum equation, from the total energy equation. Thus the conservation equations in the two-moment formulation are:

$$\frac{\partial}{\partial t}(m_s n_s) + \nabla\cdot(m_s n_s \mathbf{v}_s) = S_s$$

$$\frac{\partial}{\partial t}(m_s n_s \epsilon_s) + \nabla\cdot(m_s n_s \mathbf{v}_s \epsilon_s) = -\nabla\cdot\mathbf{Q}_s - p_s\nabla\cdot\mathbf{v}_s + \tilde{M}_s$$

(7)

where viscous dissipation $\tau_s : \nabla\mathbf{v}_s$ has been neglected on the right-hand-side of the energy equation in order to be consistent with the formulation for the momentum equation.

The energy source terms are slightly different from those in the total energy equation and have the form:

$$\tilde{M}_s = S_s\epsilon_s + \sum_r R_{rs}H_{rs} + \frac{n_s|q_s|}{(m_s+m_n)\mu_s}\left[-3k_B(T_s - T_n) + m_n|\mathbf{v}_s - \mathbf{v}_n|^2\right]$$

(8)

Note that the velocity difference terms due to elastic collisions are always positive. They have a dissipative nature, always tending to increase the thermal energy.

C. Gas Properties

The working gas was argon for the computations carried out for this paper. The following ionization and excitation reactions were considered:

$$\mathrm{Ar} + \mathrm{e} \rightarrow \mathrm{Ar}^+ + 2\mathrm{e}$$

$$\mathrm{Ar} + \mathrm{e} \rightarrow \mathrm{Ar}^* + \mathrm{e}$$
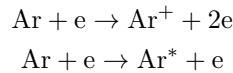
The reaction rates were taken from Park and Economou.[22] A more complete model would include conservation equations for the excited atoms. The only effect of excitation considered in the present model, however, was an energy loss from the electron fluid. Recombination reactions are neglected in the present work.

With these assumptions, the inelastic collision source terms have the form:

$$\sum_r R_{re} = \sum_r R_{ri} = -\sum_r R_{rn} = \omega_I$$

$$\sum_r R_{re} H_{re} = -\omega_I \mathcal{H}_I - \omega_X \mathcal{H}_X$$

(9)

with the form $\omega_I = k_I n_e n_n$ for the ionization rate, and $\omega_X = k_X n_e n_n$ for the excitation rate. Here $\mathcal{H}_I$ is the energy lost by electrons in ionizing collisions, and $\mathcal{H}_X$ is the corresponding energy lost in excitation collisions.

The transport properties of the neutrals were taken from standard correlations. The charged particle transport properties were derived from collision rates based on mobility data, and the assumption of a species Lewis number of unity and a species Prandtl number of two-thirds: $\mu_{vs} = \frac{2}{3} n_s m_s D_s$ and $k_s = \frac{5}{2} k_B n_s D_s$. Note that the charged particle transport coefficients are proportional to number density, so the electron transport properties become small for the low electron number densities in the cathode sheath.

D. Electromagnetics

To complete the physical model, the electric field must be found from a consistent solution of Maxwell's equations. Maxwell's equations can be written as follows:

$$\frac{\partial \mathbf{B}}{\partial t} + \nabla \times \mathbf{E} = 0$$

$$\frac{\partial \mathbf{E}}{\partial t} - c^2 \nabla \times \mathbf{B} = -\mathbf{j}/\epsilon_0$$

$$\nabla \cdot \mathbf{E} = \zeta/\epsilon_0$$

$$\nabla \cdot \mathbf{B} = 0$$

(10)

These are Faraday's law, the Ampère-Maxwell law, Gauss's law, and conservation of magnetic flux, respectively. The net space charge is $\zeta = \sum_s q_s n_s$ and the total current density is $\mathbf{j} = \sum_s q_s n_s \mathbf{v}_s$.

In the low-frequency limit, the Poisson equation is employed to compute the electric potential, and a similar equation is used for the vector potential:

$$\nabla^2 \phi = -\zeta/\epsilon_0$$

$$\nabla^2 \mathbf{A} = \mu_0 \mathbf{j}$$

(11)

with $\mathbf{E} = -\nabla \phi$ and $\mathbf{B} = \nabla \times \mathbf{A}$. Only the Poisson equation was solved for the examples in the low-frequency limit discussed here; the magnetic field was zero for these cases.

III.   Numerical Methods

In the baseline numerical implementation, the governing equations were solved using a fourth-order accurate, Runge-Kutta time marching scheme combined with second- through sixth-order accurate compact spatial difference schemes. Stability was enforced by filtering, typically with a filter of two orders greater than the accuracy of the basic scheme.

A. Conservation Equations

In transformed coordinates, the conservation laws (1) and (7) can be written in the form:

$$\frac{\partial U}{\partial t} + \frac{\partial E}{\partial \xi} + \frac{\partial F}{\partial \eta} + \frac{\partial G}{\partial \zeta} = \frac{\partial E_v}{\partial \xi} + \frac{\partial F_v}{\partial \eta} + \frac{\partial G_v}{\partial \zeta} + S$$

(12)

where U is the vector of conserved variables, E, F, and G are the inviscid flux vectors, E_v, F_v, and G_v are the viscous flux vectors, and S represents the source terms. A standard, fourth-order Runge-Kutta scheme was used for time integration of Eq. (12), and spatial differences were evaluated using a compact difference scheme of up to sixth-order accuracy (described below).

B. Maxwell's Equations

In order to solve Eq. (10), the present work employs the Purely Hyperbolic Maxwell Equations (PHME) formulation developed by Munz and coworkers.[23,24] This formulation is an alternative to projection methods; error correction potentials are propagated as waves, rather than being applied as a correction step. The approach has been successfully employed by Hakim et al.[25] for the solution of two-fluid magnetohydrodynamic problems.

The PHME formulation modifies Eq. (10) to include error correction potentials, which can be viewed as Lagrange multipliers[24] that couple the two constraint equations (10c)-(10d) to the time-evolution equations (10a)-(10b). The formulation can be written as:

$$
\frac{\partial \mathbf{B}}{\partial t} + \nabla \times \mathbf{E} + \gamma \nabla \Psi = 0
$$

$$
\frac{\partial \mathbf{E}}{\partial t} - c^2 \nabla \times \mathbf{B} + \chi c^2 \nabla \Phi = -\mathbf{j}/\epsilon_0
$$

$$
\frac{\partial \Phi}{\partial t} + \chi \nabla \cdot \mathbf{E} = \chi \zeta / \epsilon_0
$$

$$
\frac{\partial \Psi}{\partial t} + \gamma c^2 \nabla \cdot \mathbf{B} = 0
$$

(13)

The error correction potentials are Φ and Ψ; these have the dimensions of magnetic field and electric field, respectively. The parameters χ and γ are dimensionless, and the error correction potentials travel at speeds of χc and γc, respectively. If charge conservation and the divergence conditions on the fields are satisfied exactly, the PHME formulation (13) reduces to the conventional Maxwell's equations (10).

In the present work, the PHME are cast in the form of Eq. (12), and solved in a manner analogous to the fluid equations, using compact spatial differences and conventional fourth-order Runge-Kutta time-marching. The compact difference formulation is similar to that of Shang[26] and White and Visbal[27] for the conventional Maxwell's equations.

C. Poisson Equation

In the low-frequency formulation, the Poisson equation (11a) was solved at the end of each stage of the Runge-Kutta time-integration. It can be written in the following form in transformed coordinates:

$$
\frac{\partial E}{\partial \xi} + \frac{\partial F}{\partial \eta} + \frac{\partial G}{\partial \zeta} = S_\phi
$$

(14)

An iteration procedure was introduced, based on the approach of Holst,[28] such that the potential at iteration step m was $\phi^{m+1} = \phi^m + \Delta\phi$. With a linear expansion about the solution from the previous iteration, and approximate factoring of the implicit terms, the discretized equation has the form:

$$
[1 - \Delta\tau(\delta_\xi A \delta_\xi - D)][1 - \Delta\tau \delta_\eta B \delta_\eta][1 - \Delta\tau \delta_\zeta C \delta_\zeta] \Delta\phi = \omega \Delta\tau \left[\frac{\partial E^m}{\partial \xi} + \frac{\partial F^m}{\partial \eta} + \frac{\partial G^m}{\partial \zeta} - S_\phi^m \right]
$$

(15)

with iteration driving $\Delta\phi$ to zero. Here A, B, and C are flux Jacobians, D is the source Jacobian, τ is a time-like variable introduced to motivate the iteration process, and ω is an over-relaxation factor. Discretizing the left-hand side using second order central differences in space, a tridiagonal system of equations is obtained. A compact difference scheme was also used to evaluate the spatial differences present on the right hand side of Eq. (15), and the system was solved using the Thomas tridiagonal algorithm.[29] The pseudo-time-step $\Delta\tau$ was varied cyclically to accelerate convergence, and iteration was continued until the change in potential $\Delta\phi$ had dropped below a specified tolerance.

D. Compact Differences

Considering a one-dimensional, uniform mesh, the following central difference scheme[30,31] with a five-point stencil can be used to generate estimates of the first derivative $\phi' = \partial\phi/\partial x|_i$ with up to sixth-order accuracy:

$$
\alpha \phi'_{i-1} + \phi'_i + \alpha \phi'_{i+1} = a \frac{\phi_{i+1} - \phi_{i-1}}{2\,\Delta x} + b \frac{\phi_{i+2} - \phi_{i-2}}{4\,\Delta x}
$$

(16)

Here α, a, and b are constants that are used to alter the properties of the scheme, and $\phi(x)$ is a generic function, not to be confused with the electric potential. Taylor series expansions can be used to derive a family of second to sixth order accurate schemes employing this template.[30,31] Modified schemes[31] were used near boundaries, where the interior stencil would protrude outside of the domain.

To evaluate the derivative at each point, the appropriate form of Eq. (16) was solved using the Thomas tridiagonal algorithm.[29] Second derivatives were evaluated by applying the differencing scheme twice.

Numerical stability was enforced using filtering, typically with a filter of two orders greater than the accuracy of the basic scheme. The form of the filtering scheme[31] for interior points was as follows:

$$\alpha_f \overline{\phi}_{i-1} + \overline{\phi}_i + \alpha_f \overline{\phi}_{i+1} = \sum_{n=0}^{N} \frac{a_n}{2}(\phi_{i+n} + \phi_{i-n}) \tag{17}$$

where $\overline{\phi}_i$ is the filtered value of ϕ_i, and $N + 1$ is the order of the filter. Modified filters were used near the boundaries. The filter was applied to each primitive variable at the end of a time step, and the boundary conditions were updated so that the boundary points were consistent with the filtered interior points.

IV. Results

Sample calculations are presented here for three test cases: a DC discharge in one dimension, a three-dimensional rectangular waveguide problem, and a one-dimensional wave propagation problem in a warm, collisional plasma. The first problem exercises both the two- and five-moment formulations of the species conservation equations, coupled to the Poisson equation for the electric potential. The waveguide problem illustrates the use of the PHME formulation to solve a standard problem in computational electromagnetics. The plasma wave propagation problem tests a case where the PHME are coupled to the five-moment fluid model.

A. DC Discharge in One Dimension

As a first test case, calculations were carried out for a DC glow discharge in one dimension, using the Poisson equation coupled to either the two- or five-moment model. The conditions were chosen to be similar to those used by Meyyappan and Kreskovsky.[8]

The background neutral gas (argon) was assumed to be at rest, with a pressure of 107 Pa (0.8 Torr) and temperature of 323 K. The imposed potential was 120 V and the discharge gap was 35.25 mm. The initial condition was taken to be a uniform plasma of number density $n = 10^{15}$ m^{-3}, with temperatures $T_i = 323$ K (0.03 eV) and $T_e = 11600$ K (1 eV). The secondary emission coefficient was $\gamma_E = 0.05$, and the secondary emission temperature was $T_{es} = 5800$ K (0.5 eV). A total of 151 points were used across the discharge gap in the calculations, which were marched in time to 1.0 ms. The boundary conditions employed at the electrodes are given in detail in Fig. 1.

Calculations were carried out for this case using two numerical schemes. The first set of calculations employed an upwind scheme, using third-order MUSCL extrapolation of the inviscid fluxes and a harmonic limiter. (This methodology was described in a previous paper.[20]) Selected calculations were then repeated using the compact difference scheme described previously. Since the difference between the results obtained with the two methods was small, only the results obtained with the upwind method are presented here.

The basic discharge results are shown in Fig. 2. The data are nondimensionalized by the following reference values: $n_0 = 10^{16}$ m^{-3}, $u_R = 1$ km/s, and $L = 35.25$ mm. Number densities and electric potential are shown in Fig. 2a, temperatures in Fig. 2b, velocities in Fig. 2c, and ionization rate in Fig. 2d.

The product of pressure and gap width is $pL = 3.8$ m-Pa (2.8 cm-Torr). The computed cathode layer thickness of $d \sim 0.15L$ seen in Fig. 2a is consistent with the experimental value for argon of $pd \approx 0.3$ cm-Torr.[32]

The electrons emitted from the cathode are initially accelerated by the strong electric field, reaching remarkably high peak velocities ($\sim 10^6$ m/s). Their directed energy is randomized in collision with neutrals, leading to a reduced mean velocity and increased electron temperatures, up to ~ 12 eV. Temperatures are limited by the energy cost of ionization, and the electron temperature drops to 1-2 eV in the positive column. Electrons are absorbed at the anode.

American Institute of Aeronautics and Astronautics

Ions generated in the center of the domain are absorbed at both boundaries. Ion velocities are substantially higher at the cathode ($\sim$2 km/s), and collisions with neutrals in that region lead to an order of magnitude increase in ion temperature there (up to $\sim$0.5 eV).

The five-moment model and the drift-diffusion model predict similar temperatures (Fig. 2b) and velocities (Fig. 2c) under these conditions. Subtle differences in the results for the two models are magnified, however, by the extreme sensitivity of the ionization rate, leading to greater ionization rates (Fig. 2d) and plasma densities (Fig. 2a) for the two-moment model.

The relative magnitudes of the electron heating terms of Eq. (8) are shown in Fig. 3. The terms are nondimensionalized in the plot by dividing by $m_n n_0 u_R^3 / L$. The terms are labelled as follows:

$$
\begin{array}{ll}
\text{Ionization Cost:} & -\omega_I \mathcal{H}_I \\
\text{Excitation Cost:} & -\omega_X \mathcal{H}_X \\
\text{Temperature Equilibration:} & -\frac{n_e |q_e|}{(m_e + m_n)\mu_e} 3 k_B (T_e - T_n) \\
\text{Frictional Dissipation:} & \frac{n_e |q_e|}{(m_e + m_n)\mu_e} m_n |\mathbf{v}_e - \mathbf{v}_n|^2
\end{array}
$$

with their sum labeled 'Total Heating.'

Although there are quantitative differences between the predictions of the two models, the results are qualitatively the same. The frictional dissipation term adds heat to the system, and is balanced by the other terms, which represent thermal energy losses. The double-peaked profile of ionization cost mirrors the ionization profiles shown in Fig. 2d. The excitation cost also shows a double-peaked profile, with the relative magnitudes of the two peaks reversed relative to the ionization term. The temperature equilibration term is not significant in the cathode layer, but plays an important role in limiting electron temperatures in the positive column.

The corresponding plots for the ions are given in Fig. 4. The ion heating terms of reflect a close balance between the frictional dissipation and the temperature equilibration terms, for a moderate net heating rate. Peak values of these terms occur near the cathode.

The results obtained here are qualitatively similar to those of Meyyappan and Kreskovsky[8] for the same conditions. (The present model includes viscous terms, ion temperature variation, and excitation reactions, which were omitted by Meyyappan and Kreskovsky.) Those authors observed similar number density distributions, although with very low densities in the cathode layer. They also obtained a similar ionization profile, with two peaks, the larger being the closer to the cathode. Their electron temperature and velocity profiles also showed large peaks in the cathode layer.

A comparison shows that subtle differences in the velocities and temperatures in the cathode sheath lead to significant differences between the predictions of the two- and five-moment models for ionization rates and number densities. Two main physical phenomena are neglected in the two-moment model: viscous terms and the inertia terms. Here we investigate the effects of including or neglecting these terms.

Additional calculations were run in order to compare the four possible combinations of two- and five-moment models for ions and electrons. Figure 5a shows the results: switching from the two- to the five-moment model has little effect for the ions, but a profound effect for the electrons. Thus the discrepancy between the predictions of the models is a result of neglecting either the electron inertia terms or electron viscous terms in the two-moment model.

Figure 5b compares the results obtained with the two-moment model, the five-moment model, and the five-moment model with the electron viscosity set to zero. The results show that neglecting electron viscosity drives the five-moment model farther from, rather than closer to, the two-moment model. Thus the difference in the predictions of the two models must be due to the electron inertia terms, not the electron viscous terms.

The baseline boundary conditions employed in this paper limit the electron emission velocity to sonic (Fig. 1). The effect of relaxing this restriction and allowing the electrons to be emitted supersonically is shown in Fig. 6. It is seen that the ionization rate is increased slightly for supersonic emission, with a corresponding increase in the charged particle densities.

B. Rectangular Waveguide

Hollow conducting pipes, or waveguides, are a commonly used technology for transmitting electromagnetic waves in the microwave regime (1-100 GHz frequency or 3-300 mm wavelength) with low attenuation. Waveguides of rectangular cross-section represent a good computational test case, since analytical solutions are available,[33] and rectangular waveguides of 2:1 aspect ratio are commonly used in applications.

Calculations were carried out for a 43 mm by 86 mm rectangular waveguide, chosen to correspond to commercially-available configurations designed to transmit energy at 2.45 GHz. (The cutoff frequency for this configuration is about $f_c = 1.7$ GHz.) The basic computational mesh consisted of a uniform grid of $41 \times 21 \times 201$ points, with the waveguide axis aligned with the z-direction. Four wavelengths were captured along this axis.

Because the waveguide configuration very effectively confines wave propagation to the z-direction, careful attention must be given to the end boundary conditions to avoid spurious reflections that may contaminate the solution. Thus additional stretched mesh layers (stretching ratio 1.2) of 22 points were added to each end of the basic mesh in order to implement the wave absorption scheme of White and Visbal.[34] The boundary condition of Mur[35] was applied at the endpoints: $(\partial/\partial t \pm v\,\partial/\partial x)W = 0$, where W is an electromagnetic field component, and $v = c$, χc, or γc as appropriate. The walls of the channel were assumed to be perfect conductors: the the normal component of the magnetic field and the tangential component of the electric field were taken to be zero at these boundaries.

Waves were generated by imposing a current sheet at the $z = 0$ plane. This sheet was periodic in time, uniform in the x- and y-directions, and had a Gaussian form in the z-direction with a length scale of about two grid points. Calculations were carried out with fourth-order spatial and temporal accuracy, and the calculations were run for 600 cycles of the forcing frequency.

Figure 7 shows the electric field obtained numerically for forcing at 2.45 GHz. (The absorbing boundary points are omitted in this figure for clarity.) Contours of the y-component of the electric field on the surface of the computational mesh are shown in Fig. 7a, and the corresponding data along the channel centerline are shown in Fig. 7b. The position of the imposed current sheet at $z = 0$ is evident in both plots as a slight defect in the solution.

A particular feature of the 2:1 rectangular wave guide is that the TE_{10}-mode is the only propagating mode for the frequency range $f_c \leq f \leq 2f_c$. Thus, the uniform current sheet excites only that mode, and the numerical results were found to coincide closely with the analytical solution for the TE_{10}-mode, as seen in the line plot in Fig. 7b.

Additional calculations (omitted for brevity) were carried out for the TE_{11} mode at 5.80 GHz and for TEM modes in a coaxial wave guide. Good agreement with the corresponding analytical solutions was also obtained for these cases.

C. Transverse Waves in a Warm, Collisional Plasma

An analytical solution is available for the case of transverse electromagnetic waves in a warm, collisional electron plasma,[36,37] and this problem forms a good test case that couples the full Maxwell's equations to the five-moment fluid model.

For the analytical solution, the neutrals and ions are assumed to form a uniform, stationary background gas. The electrons are assumed to move as a small perturbation from a uniform state. Ionization, viscous, and heat conduction terms are neglected. Linearization for small disturbances of the form $n = n_0 + n_1$ leads to the following equations for the electron motion and field evolution:

$$
\begin{aligned}
\frac{\partial n_1}{\partial t} + n_0 \nabla \cdot \mathbf{v}_1 &= 0 \\
n_0 \frac{\partial \mathbf{v}_1}{\partial t} &= -a_0^2 \nabla n_1 - \frac{e}{m} n_0 \mathbf{E}_1 - n_0 \nu \mathbf{v}_1 \\
\frac{\partial \mathbf{B}_1}{\partial t} + \nabla \times \mathbf{E}_1 &= 0 \\
\frac{\partial \mathbf{E}_1}{\partial t} - c^2 \nabla \times \mathbf{B}_1 &= \frac{e}{\epsilon_0} n_0 \mathbf{v}_1 \\
\nabla \cdot \mathbf{E}_1 &= -\frac{e}{\epsilon_0} n_1 \\
\nabla \cdot \mathbf{B}_1 &= 0
\end{aligned}
\tag{18}
$$

where the fluid variables are those of the electrons alone, ν is the electron-neutral collision frequency, and $a_0 = \sqrt{\gamma_e k_B T_e / m_e}$ is the electron sound speed. These equations admit transverse wave solutions of the

form:

$$\begin{bmatrix} E_x \\ E_y \end{bmatrix} \exp[i(kz - \omega t)]$$

$$\begin{bmatrix} B_x \\ B_y \end{bmatrix} = \frac{k}{\omega} \begin{bmatrix} -E_y \\ E_x \end{bmatrix} \exp[i(kz - \omega t)] \tag{19}$$

$$\begin{bmatrix} v_x \\ v_y \end{bmatrix} = i \frac{e}{m} \frac{c^2 k^2 - \omega^2}{\omega^2 \omega_p^2} \begin{bmatrix} E_x \\ E_y \end{bmatrix} \exp[i(kz - \omega t)]$$

where $\omega_p = \sqrt{e^2 n_0/(m_e \epsilon_0)}$ is the electron plasma frequency. If the temporal frequency is assumed to be real, the complex wave number has the form:

$$k = \pm \frac{1}{c} \sqrt{\omega^2 - \omega_p^2/(1 + i\nu/\omega)} \tag{20}$$

Computations were carried out for comparison to the analytical solution. As with the waveguide calculations described previously, the waves were excited by imposing a current sheet at the station $z = 0$. Sample results are shown in Fig. 8 for a plasma frequency of $\omega_p/2\pi = 9.0$ GHz and a collision frequency of $\nu = 53$ GHz, corresponding to a 1330 Pa argon plasma with fractional ionization of 3×10^{-8} and electron temperature 11600 K. The numerical results are seen to be in good agreement with the analytical solution for excitation frequencies of $\omega/2\pi = 434$ MHz and $\omega/2\pi = 2.45$ GHz.

V.   Summary and Conclusions

This paper reports on a project to improve the fidelity of continuum electrical discharge computations through the use of more detailed physical models. To this end, a new computer code has been developed that incorporates a three-species fluid model coupled to either the Poisson equation or the full set of Maxwell's equations. The three-dimensional numerical implementation involves compact spatial differences of up to sixth-order accuracy, driven by a fourth-order Runge-Kutta time marching scheme. Sample calculations were presented here for three test cases.

The first test case involved a one-dimensional DC discharge in argon at 107 Pa pressure. This problem exercised both the two- and five-moment formulations of the species conservation equations, coupled to the Poisson equation for the electric potential. The basic results were in qualitative agreement with similar published calculations.

The thermal energy budget for the electron fluid was found to represent primarily a balance between dissipative frictional heating and the energy cost of ionization, although the temperature equilibration terms and the cost of excitation collisions were also significant. The corresponding ion heating terms reflected a close balance between the frictional dissipation and the temperature equilibration terms, for a moderate net heating rate. Comparing the five-moment model to the two-moment model, it was found that the five-moment model predicted lower ionization rates and charged particle densities. Comparing various combinations of the models and included terms, it was found that the primary reason for the differences in the predictions of the five-moment and two-moment models lies in electron inertia effects in the cathode layer.

Given the differences between the predictions of the two-models, further exploration of multi-moment discharge modeling is warranted. Very little research has been done in this area, and only one other direct comparison between different levels of model appears to have been published previously.[12]

The second test case illustrated the application of the Maxwell's equations solver to a standard problem in computational electromagnetics. This problem involved the excitation of the TE_{10}-mode in a 2:1 rectangular wave guide using a uniform current sheet placed in the center of the computational domain. The numerical results corresponded closely to the analytical solution for this case, and illustrate the feasibility of implementing the Purely Hyperbolic Maxwell Equations formulation using compact difference techniques.

For the final test case, a current sheet was used to excite transverse waves in a warm, collisional electron plasma, demonstrating a case where Maxwell's equations were coupled to the five-moment fluid model. The numerical results again showed good agreement with the available analytical solution.

Acknowledgments

References

[1]Font, G. I., "Boundary-Layer Control with Atmospheric Plasma Discharges," *AIAA Journal*, Vol. 44, No. 7, 2006, pp. 1572–1578.

[2]Ward, A. L., "Calculations of Cathode-Fall Characteristics," *Journal of Applied Physics*, Vol. 33, No. 9, 1962, pp. 2789–2794.

[3]Boeuf, J.-P., "A Two-Dimensional Model of DC Glow Discharges," *Journal of Applied Physics*, Vol. 63, No. 5, 1988, pp. 1342–1349.

[4]Raizer, Y. P. and Surzhikov, S. T., "Two-Dimensional Structure in a Normal Glow Discharge and Diffusion Effects in Cathode and Anode Spot Formation," *High Temperature*, Vol. 26, No. 3, 1988, pp. 304–311.

[5]Graves, D. B. and Jensen, K. F., "A Continuum Model of DC and RF Discharges," *IEEE Transactions on Plasma Science*, Vol. PS-14, No. 2, 1986, pp. 78–91.

[6]Passchier, J. D. P. and Goedheer, W. J., "A Two-Dimensional Fluid Model for an Argon RF Discharge," *Journal of Applied Physics*, Vol. 74, No. 6, 1993, pp. 3744–3751.

[7]Young, F. F., "Two-Dimensional, Self-Consistent, Three-Moment Simulation of RF Glow Discharges," *IEEE Transactions on Plasma Science*, Vol. 21, No. 3, 1993, pp. 312–321.

[8]Meyyappan, M. and Kreskovsky, J. P., "Glow Discharge Simulation Through Solutions to the Moments of the Boltzmann Transport Equation," *Journal of Applied Physics*, Vol. 68, No. 4, 1990, pp. 1506–1512.

[9]Meyyappan, M., "A Continuum Model for Low-Pressure Radio-Frequency Discharges," *Journal of Applied Physics*, Vol. 69, No. 12, 1991, pp. 8047–8051.

[10]Meyyappan, M. and Govindan, T. R., "Two-Dimensional Analysis of Radio Frequency Discharges," *IEEE Transactions on Plasma Science*, Vol. 24, No. 1, 1996, pp. 119–120.

[11]Wilcoxson, M. H. and Manousiouthakis, V. I., "Simulation of a Three-Moment Fluid Model of a Two-Dimensional Radio Frequency Discharge," *Chemical Engineering Science*, Vol. 51, No. 7, 1996, pp. 1089–1106.

[12]Chen, G. and Raja, L. L., "Fluid Modeling of Electron Heating in Low-Pressure, High-Frequency Capacitively Coupled Plasma Discharges," *Journal of Applied Physics*, Vol. 96, No. 11, 2004, pp. 6073–6081.

[13]Adamovich, I. V. and Rich, J. W., "Emission and Shock Visualization in Nonequilibrium Nitrogen Afterglow Plasma," *Journal of Applied Physics*, Vol. 102, 083303, 2007.

[14]Tan, W. and Grotjohn, T. A., "Modeling the Electromagnetic Excitation of a Microwave Cavity Plasma Reactor," *Journal of Vacuum Science and Technology A*, Vol. 12, No. 4, 1994, pp. 1216–1220.

[15]Lebedev, Y. A., Tatarinov, A. V., and Epstein, I. L., "Modeling of the Electrode Microwave Discharge in Nitrogen," *Plasma Sources Science and Technology*, Vol. 16, No. 4, 2007, pp. 726–733.

[16]White, M. D., "Communication Through a Non-Equilibrium Hypersonic Boundary Layer for Re-entry Vehicles," AIAA Paper 2007-1438.

[17]D'Ambrosio, D. and Giordano, D., "Electromagnetic Fluid Dynamics for Aerospace Applications," *Journal of Thermophysics and Heat Transfer*, Vol. 21, No. 2, 2007, pp. 284–302.

[18]MacCormack, R. W., "Solution of Maxwell's Equations Coupled to the Navier-Stokes Equations," AIAA Paper 2009-3911.

[19]Hakim, A. and Shumlak, U., "Two-Fluid Physics and Field-Reversed Configurations," *Physics of Plasmas*, Vol. 14, 055911, 2007.

[20]Poggie, J., "Role of Charged Particle Inertia in Pulsed Electrical Discharges," AIAA Paper 2010-1195.

[21]Burgers, J. M., *Flow Equations for Composite Gases*, Academic Press, New York, 1969.

[22]Park, S.-K. and Economou, D. J., "Analysis of Low Pressure RF Glow Discharges Using Continuum Model," *Journal of Applied Physics*, Vol. 68, No. 8, 1990, pp. 3904–3915.

[23]Munz, C.-D., Ommes, P., and Schneider, R., "A Three-Dimensional Finite-Volume Solver for the Maxwell Equations with Divergence Cleaning on Unstructured Meshes," *Computer Physics Communications*, Vol. 130, No. 2, 2000, pp. 83–117.

[24]Munz, C.-D., Ommes, P., Schneider, R., Sonnendrücker, E., and Voß, U., "Divergence Correction Techniques for Maxwell Solvers Based on a Hyperbolic Model," *Journal of Computational Physics*, Vol. 161, No. 2, 2000, pp. 484–511.

[25]Hakim, A., Loverich, J., and Shumlak, U., "A High-Resolution Wave Propagation Scheme for Ideal Two-Fluid Plasma Equations," *Journal of Computational Physics*, Vol. 219, No. 1, 2006, pp. 418–442.

[26]Shang, J. S., "High-Order Compact Difference Schemes for Time-Dependent Maxwell Equations," *Journal of Computational Physics*, Vol. 153, No. 2, 1999, pp. 312–333.

[27]White, M. D. and Visbal, M. R., "Implicit High-Order Generalized Coordinate Solution of Maxwell's Equations," *IEEE Antennas and Propagation Society International Symposium*, Vol. 3, 2002, pp. 256–259.

[28]Holst, T. L., "Transonic Flow Computations Using Nonlinear Potential Methods," *Progress in Aerospace Sciences*, Vol. 36, 2000, pp. 1–61.

[29]Cheney, W. and Kincaid, D., *Numerical Mathematics and Computing*, Brooks/Cole Publishing, Pacific Grove, California, 1994.

[30]Lele, S. K., "Compact Finite Difference Schemes with Spectral-Like Resolution," *Journal of Computational Physics*, Vol. 103, 1992, pp. 16–42.

[31]Gaitonde, D. V. and Visbal, M. R., "High-Order Schemes for Navier-Stokes Equations: Algorithm and Implementation in FDL3D," AFRL Technical Report AFRL-VA-WP-TR-1998-3060, Air Force Research Laboratory, Wright-Patterson Air Force Base, Ohio, 1998.

[32]Lieberman, M. A. and Lichtenberg, A. J., *Principles of Plasma Discharges and Materials Processing*, J. Wiley, New York, 1994.

[33]Elmore, W. C. and Heald, M. A., *Physics of Waves*, McGraw-Hill, New York, 1969, reprinted by Dover, New York, 1985.

[34]White, M. D. and Visbal, M. R., "Using Filters to Design Absorbing Boundary Conditions for High-Order CEM," *IEEE Transactions on Magnetics*, Vol. 40, No. 2, 2004, pp. 961–964.

[35]Mur, G., "Absorbing Boundary Conditions for the Finite-Difference Approximation of the Time-Domain Electromagnetic-Field Equations," *IEEE Transactions on Electromagnetic Compatibility*, Vol. EMC-23, No. 4, 1981, pp. 377–382.

[36]Sturrock, P. A., *Plasma Physics: An Introduction to the Theory of Astrophysical, Geophysical, and Laboratory Plasmas*, Cambridge University Press, New York, 1994.

[37]Choudhuri, A. R., *The Physics of Fluids and Plasmas: An Introduction for Astrophysicists*, Cambridge University Press, New York, 1998.

	Inflow ($v_e^\perp < 0$)	Outflow ($v_e^\perp > 0$)
Subsonic ($|v_e^\perp| < a_e$)	extrapolate n_e $v_e^\perp = k_r - \gamma_E \Gamma_i^+ / n_e$ $\mathbf{v}_e^\parallel = 0$ $T_e = \mathrm{avg}(T_{ea}, T_{es})$	extrapolate n_e $v_e^\perp = k_r - \gamma_E \Gamma_i^+ / n_e$ extrapolate $\mathbf{v}_e^\parallel$ $T_e = \mathrm{avg}(T_{ea}, T_{es})$
Supersonic ($|v_e^\perp| \geq a_e$)	$n_e = \gamma_E \Gamma_i^+ / a_e$ $v_e^\perp = -a_e$ $\mathbf{v}_e^\parallel = 0$ $T_e = T_{es}$	extrapolate n_e extrapolate $\mathbf{v}_e$ extrapolate T_e

(a) Electrons, five-moment model.

Inflow ($v_i^\perp < 0$)	Outflow ($v_i^\perp > 0$)
extrapolate n_i	extrapolate n_i
$v_i^\perp = 0$	extrapolate $\mathbf{v}_i$
extrapolate $\mathbf{v}_i^\parallel$	extrapolate T_i
$T_i = T_\infty$	

(b) Ions, five-moment model.

Inflow/Outflow
$n_e v_e^\perp = n_e k_r - \gamma_E n_i v_i^+$
$T_e = \mathrm{avg}(T_{ea}, T_{es})$

(c) Electrons, two-moment model.

Inflow ($v_i^\perp < 0$)	Outflow ($v_i^\perp > 0$)
$v_i^\perp = 0$	extrapolate n_i
$T_i = T_\infty$	extrapolate T_i

(d) Ions, two-moment model.

Figure 1. Electrode boundary conditions for charged particles in the DC discharge test case.
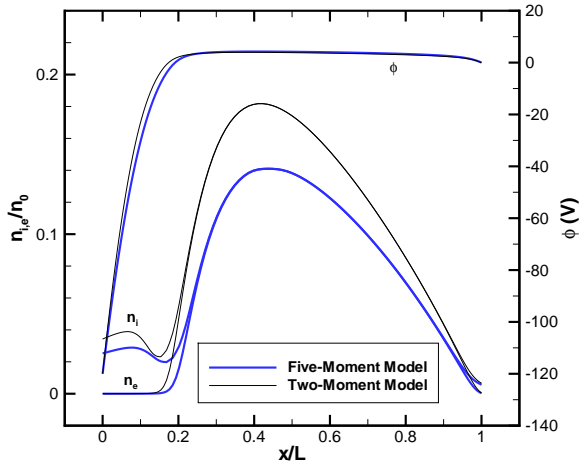
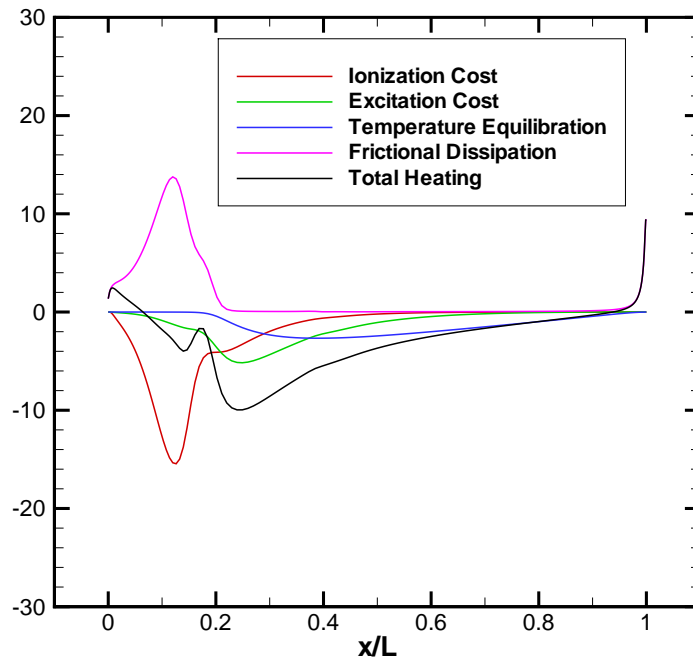(a) Number densities and potential.
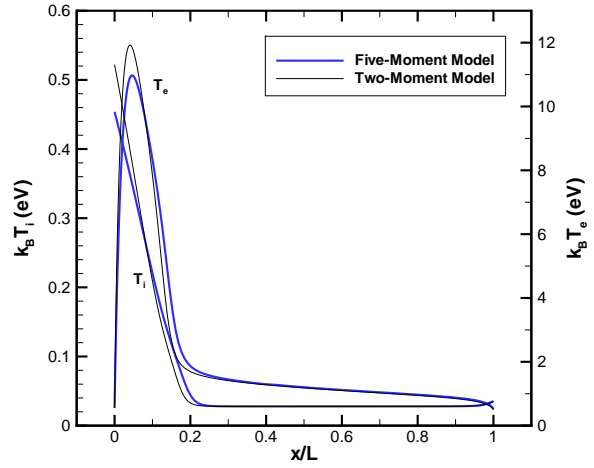
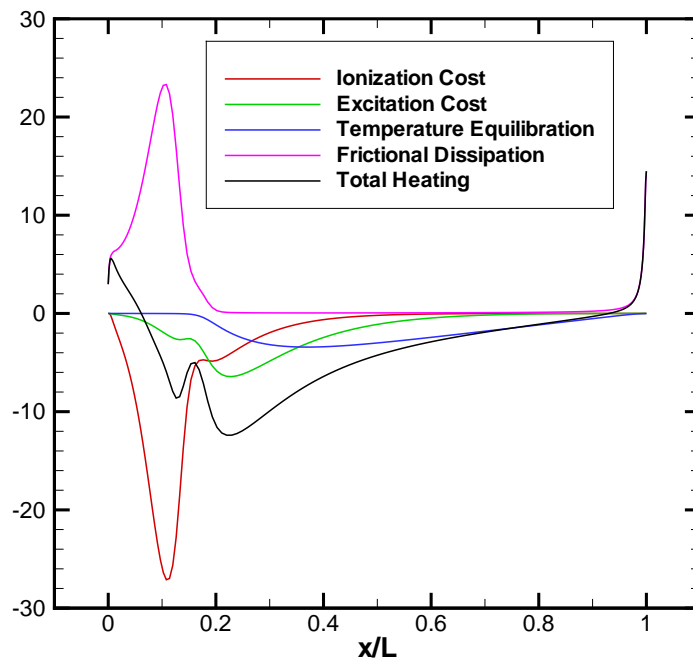(b) Temperatures.
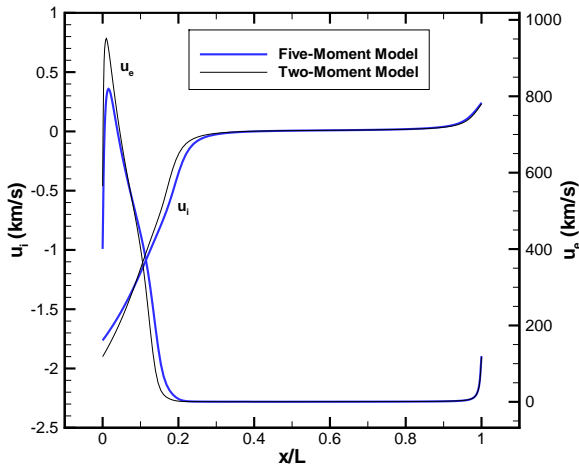
(c) Velocities.
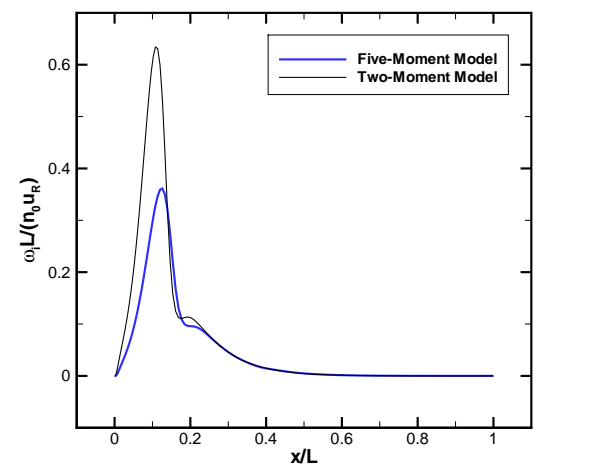
(d) Ionization rates.

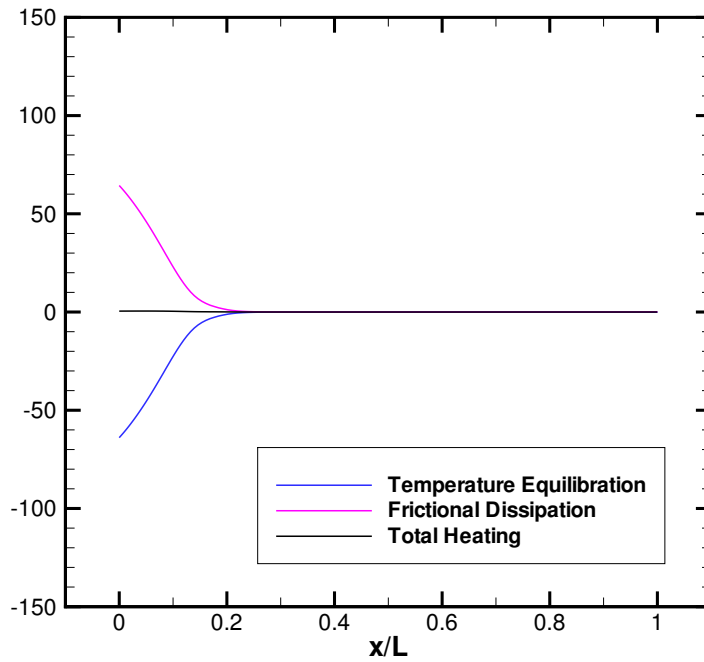Figure 2. Comparison of two-moment and five-moment models for one-dimensional DC discharge.
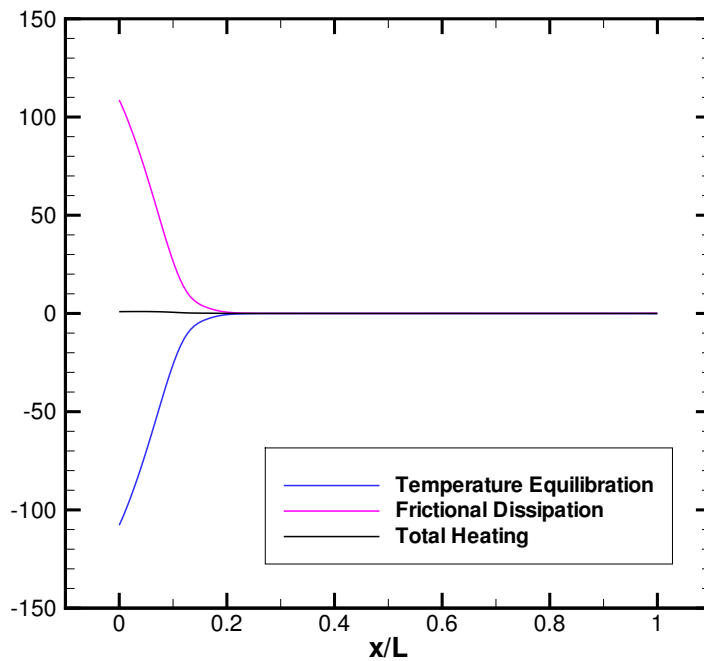
(a) Five-moment model.

(b) Two-moment model.

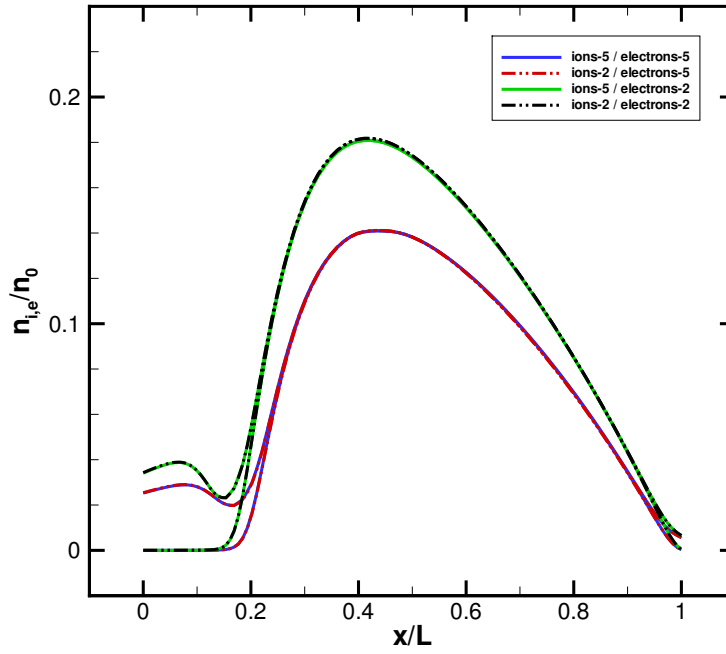**Figure 3. Electron heating terms for one-dimensional DC discharge.**

(a) Five-moment model.

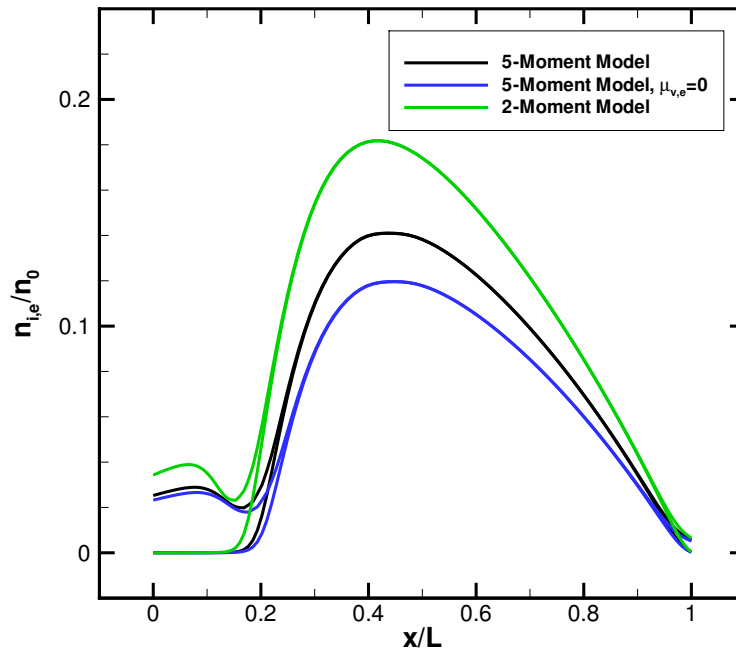(b) Two-moment model.

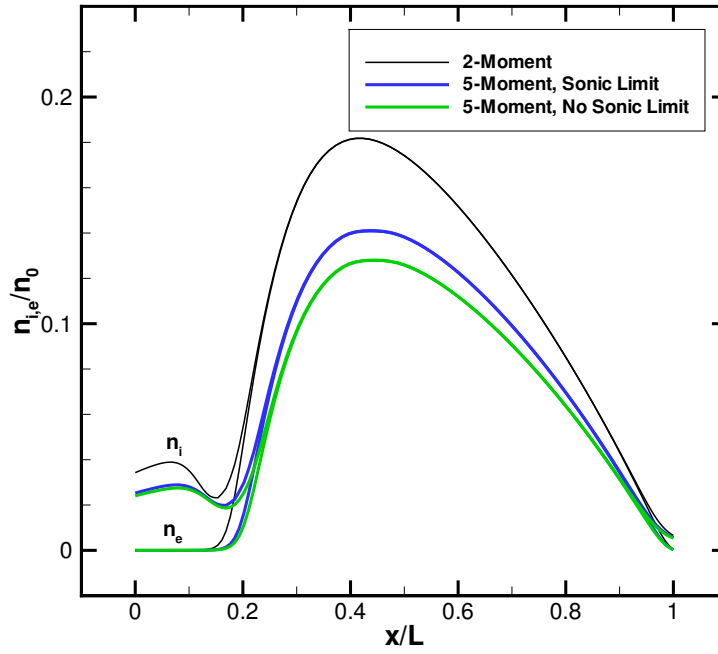**Figure 4. Ion heating terms for one-dimensional DC discharge.**

(a) Comparison of various combinations of two- and five-moment models.

(b) Effect of electron viscosity.

Figure 5. Physical model sensitivity for one-dimensional DC discharge.

(a) Number density.
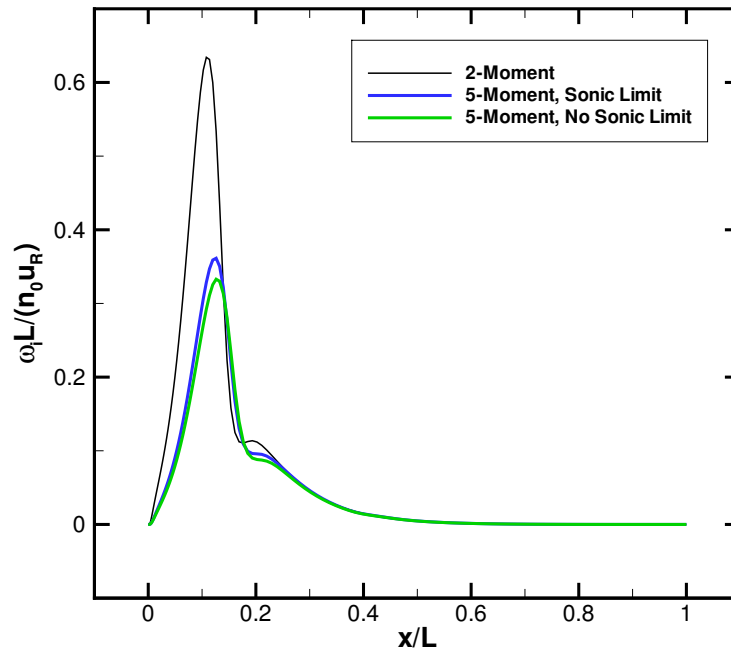
(b) Ionization rate.

Figure 6. Effect of boundary conditions on one-dimensional DC discharge.
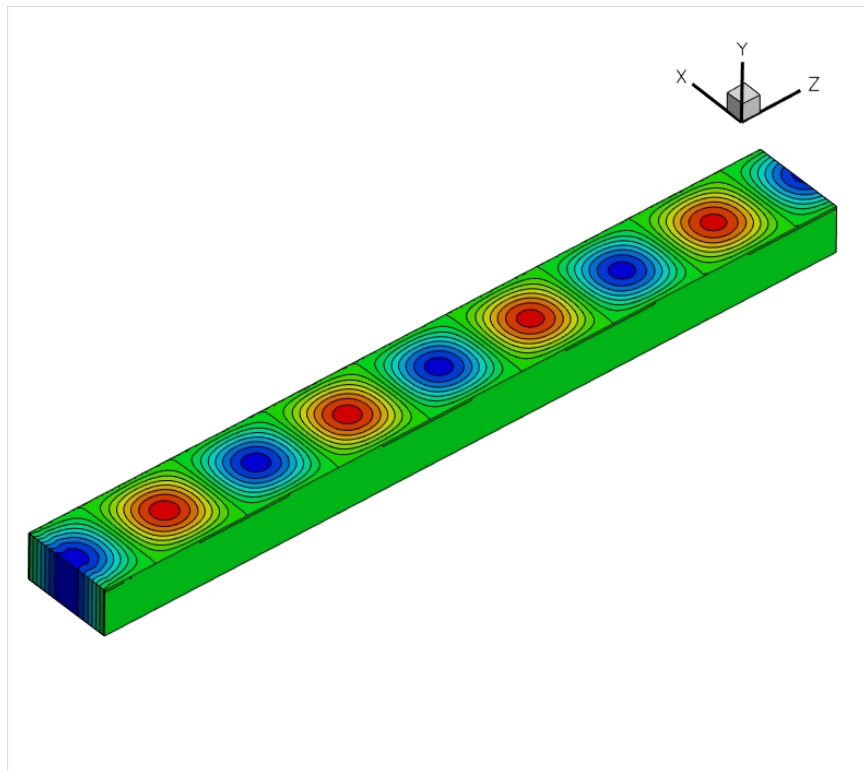
(a) Surface electric field, E_y contours.
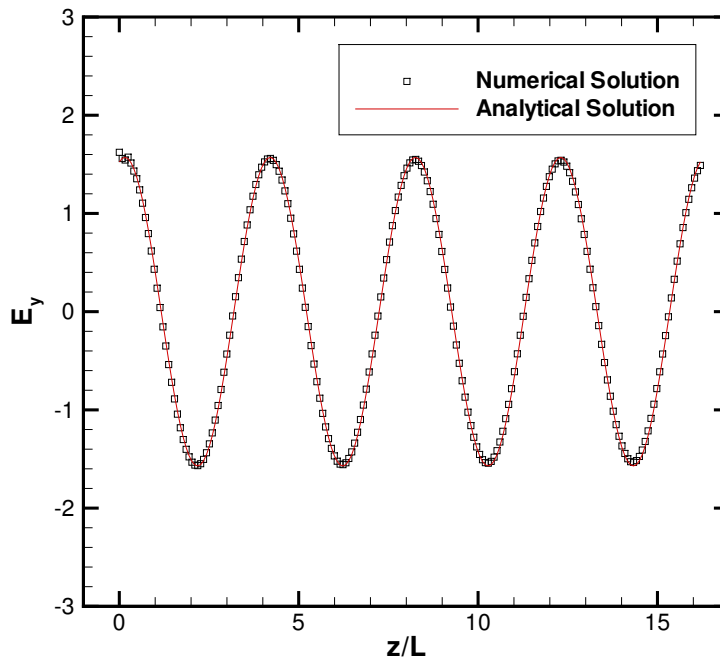
(b) Centerline electric field (L = 43 mm).

Figure 7. Waveguide with 43 mm by 86 mm cross-section driven at 2.45 GHz.
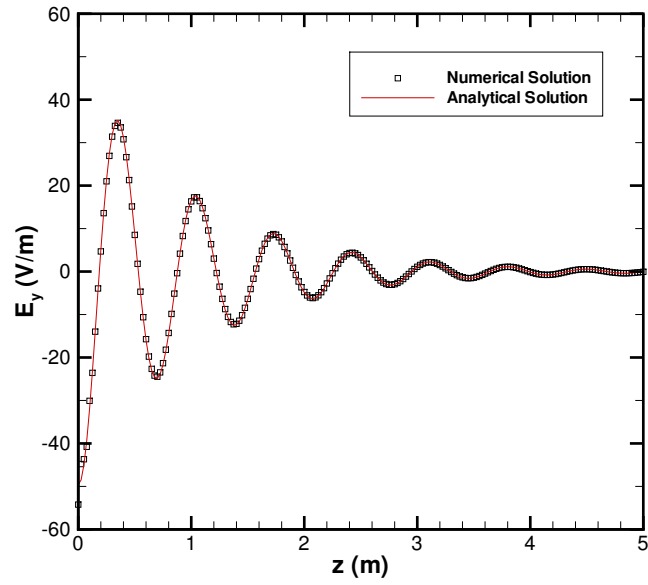
(a) Frequency 434 MHz.
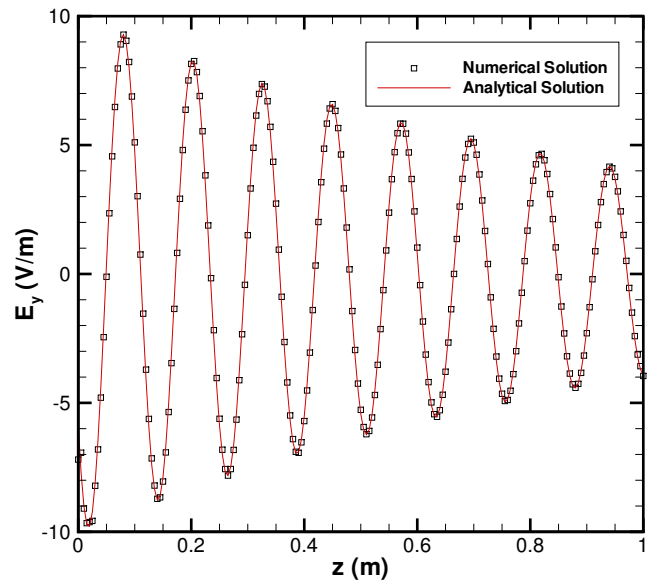
(b) Frequency 2.45 GHz.

Figure 8. Transverse electromagnetic waves in plasma. Plasma frequency 9.0 GHz; collision frequency 53 GHz.

Appendix C

Air Plasma Chemical Kinetics for Pulsed Electrical Discharges

**42nd AIAA Plasmadynamics and Lasers Conference
 in conjunction with the
 18th Internati**
27 - 30 June 2011, Honolulu, Hawaii

AIAA 2011-3104

High-Speed Flow Control
with Electrical Discharges

Jonathan Poggie[*] and Nicholas J. Bisek[†]

Air Force Research Laboratory, Wright-Patterson AFB, Ohio 45433-7512 USA

Igor V. Adamovich[‡] and Munetake Nishihara[§]

The Ohio State University, Columbus, Ohio 43210 USA

Numerical calculations were carried out to examine the physics of the operation of nanosecond-pulse, single dielectric barrier discharges for high-speed flow control. Conditions were selected to be representative of the stagnation region of a Mach 5 cylinder flow that was the subject of recent experiments. A four-species formulation was employed, including neutrals, ions, electrons, and a representative excited molecular species. The following models were employed to predict particle motion: a drift-diffusion formulation for the charged particles, a diffusion equation for the excited molecules, and a five-moment fluid formulation for the neutrals. The Poisson equation was solved for the electric potential. During a 20 kV Gaussian input pulse lasting approximately 120 ns, an average energy density of about 40 J/m^3 was stored in excited molecular states. Quenching reactions released this stored energy within about 10 μs, converting it into translational energy of the neutrals and forming weak shock waves. The maximum neutral gas temperature rise predicted by the model was about 40 K.

I. Introduction

Interest in plasma-based flow control dates to the mid-1950s, when magnetohydrodynamic reentry heat shields were first investigated.[1,2] Activity in the research area waned in the 1970s, with some work on drag reduction using corona discharges appearing in the 1980s.[3] A resurgence in the field took place in the 1990s, with the introduction of dielectric barrier discharge (DBD) actuators,[4] a revisit of reentry magnetohydrodynamics,[5] and the disclosure of the AJAX hypersonic vehicle concept.[6] In the fifteen years since this resurgence, plasma-based flow control techniques have been a topic of ongoing research, motivated by the possibility of extremely rapid actuation, a low-profile configuration, and the ability to operate in hostile environments.[7–17]

In the high-speed regime, plasma-based flow control devices have had the drawbacks of either excessive weight[18] or insufficient control authority.[4] Pulsed discharge devices, based on either arc[19] or glow discharges,[20] seem to be a promising way around these difficulties. Nanosecond-scale pulsed glow discharges are efficient generators of both ions and electronically excited molecules because of the extremely high instantaneous reduced electric field.[21]

The generation of shock waves by volumetric heat release in pulsed discharges was observed and explained in the 1970s in the context of gas laser technology.[22,23] Early computations by Aleksandrov et al.[23] assumed that all the power dissipated in the discharge immediately went into heating the neutral gas. Analogous calculations have been carried out recently for two dimensions by Unfer and Boeuf.[24] Popov,[25] however, has emphasized a two-stage heating mechanism in which electronically excited molecular states are generated by electron impact, and then the stored energy is converted to neutral gas heating through quenching reactions.

---

[*]Team Leader, High-Speed Flow Research Group, Computational Aerophysics Branch. Associate Fellow AIAA.
[†]Research Aerospace Engineer, High-Speed Flow Research Group, Computational Aerophysics Branch. Member AIAA.
[‡]Professor, Nonequilibrium Thermodynamics Laboratories, Dept. of Mechanical Engineering. Associate Fellow AIAA.
[§]Postdoctoral Researcher, Nonequilibrium Thermodynamics Laboratories, Dept. of Mechanical Engineering.

In recent experiments,[17, 26] control of a Mach 5 cylinder flow was demonstrated using a pulsed surface dielectric barrier discharge. Typical pulse durations were on the order of 100 ns long and 20 kV in amplitude. Phase-locked schlieren images detected the formation of shock waves near the actuator surface. These waves propagated upstream in the shock-layer flow, altering the shape of the bow shock, and increasing the shock standoff by up to 25%. Given the close relationship between shock standoff and gradients at the stagnation point,[9] this system might be able to alter heat transfer rates at the nose of blunt body flows. Further, the system is promising for general high-speed flow control applications.

We have begun to formulate a high-fidelity physical model of the energy transfer process in the pulsed surface dielectric barrier discharge. (In a companion project, we are exploring the fluid mechanics of the experiment using a gasdynamics code with a phenomenological volumetric energy deposition model.[27]) In particular, we have developed a simplified model for the transfer in the discharge of electrical energy into excited neutral molecules, and its subsequent relaxation into translational energy of the neutrals.

II. Physical Model

A simplified physical model of a nanosecond-pulse air discharge was devised to represent the storage of discharge energy in excited molecular states, and its subsequent relaxation into translational energy. A four-species formulation was employed, including neutrals, ions, electrons, and excited neutral molecules. The following models were employed to predict particle motion: a drift-diffusion formulation for the charged particles, a diffusion equation for the excited molecules, and a five-moment fluid formulation for the neutrals. The Poisson equation was solved for the electric potential. A detailed description of the overall physical model is given below.

For computational efficiency, the calculations were carried out in two stages. The first stage encompassed the period in which an external waveform was applied to the electrodes. For this stage, the full physical model was employed. Shortly after the external potential was turned off, electromagnetic effects and charged particle motion became negligible. In this second stage of the problem, we solved only for the neutrals and excited molecules.

A. Governing Equations

The following drift-diffusion formulation was used for the ions, electrons, and excited molecules:

$$
\begin{aligned}
\frac{\partial n_i}{\partial t} + \nabla \cdot (n_i \mathbf{v}_n + n_i \mu_i \mathbf{E} - D_i \nabla n_i) &= \alpha \Gamma_e - \beta n_i n_e \\
\frac{\partial n_e}{\partial t} + \nabla \cdot (n_e \mathbf{v}_n - n_e \mu_e \mathbf{E} - D_e \nabla n_e) &= \alpha \Gamma_e - \beta n_i n_e \\
\frac{\partial n_x}{\partial t} + \nabla \cdot (n_x \mathbf{v}_n - D_x \nabla n_x) &= \eta_h \dot{q}/\epsilon_x - k_r n_x n_n
\end{aligned}
\tag{1}
$$

Here the electric field is $\mathbf{E} = -\nabla \phi$, where ϕ is the electric potential. The subscripts i, e, x, and n indicate, respectively, the ions, electrons, excited molecules, and neutrals. For each species-s, the number density is n_s, the mobility is μ_s, the diffusion coefficient is D_s, and the laboratory-frame velocity is $\mathbf{v}_s$. The magnitude of the electron flux in the reference frame of the neutrals is given by:

$$
\Gamma_e = n_e |\mathbf{v}_e - \mathbf{v}_n| = |-n_e \mu_e \mathbf{E} - D_e \nabla n_e|
\tag{2}
$$

The ionization coefficient is α and the recombination coefficient is β. The local rate of energy dissipation in the discharge is:

$$
\dot{q} = \mathbf{E}' \cdot \mathbf{j}' = \mathbf{E} \cdot [e n_i (\mathbf{v}_i - \mathbf{v}_n) - e n_e (\mathbf{v}_e - \mathbf{v}_n)]
\tag{3}
$$

where the primes indicate that the quantity is evaluated in the reference frame moving with the neutrals. The coefficient η_h represents the fraction of dissipated energy rapidly converted into molecular excitation, the quantity ϵ_x is the excitation energy of the excited molecules, and k_r is the corresponding relaxation coefficient.

A five-moment, fluid-dynamic model was used for the neutral background gas:

$$\frac{\partial}{\partial t}(m_n n_n) + \nabla \cdot (m_n n_n \mathbf{v}_n) = m_n \omega_n$$

$$\frac{\partial}{\partial t}(m_n n_n \mathbf{v}_n) + \nabla \cdot (m_n n_n \mathbf{v}_n \mathbf{v}_n + p_n \mathbf{I}) = \nabla \cdot \tau_n + \mathbf{A}_n^E + \mathbf{A}_n^I \tag{4}$$

$$\frac{\partial}{\partial t}(m_n n_n \mathcal{E}_n) + \nabla \cdot (m_n n_n \mathbf{v}_n \mathcal{E}_n + p_n \mathbf{v}_n) = \nabla \cdot (\tau_n \cdot \mathbf{v}_n - \mathbf{Q}_n) + M_n^E + M_n^I$$

Here m_n is the mass per particle, $p_n = n_n k_B T_n$ is the pressure, k_B is the Boltzmann constant, T_n is the temperature, $\mathcal{E}_n = k_B T/[m_n(\gamma_n - 1)] + v_n^2/2$ is the total energy per unit volume, and γ_n is the adiabatic exponent. The viscous stress and heat flux are as follows:

$$\tau_n = \mu_{vn}\left[(\nabla \mathbf{v}_n) + (\nabla \mathbf{v}_n)^T - \tfrac{2}{3}\nabla \cdot \mathbf{v}_n \mathbf{I}\right]$$
$$\mathbf{Q}_n = -k_n \nabla T_n \tag{5}$$

where μ_{vn} is the viscosity and k_n is thermal conductivity. The elastic collision terms[28, 29] for the neutrals are:

$$\mathbf{A}_n^E = \sum_{s=i,e,x} n_s m_{sn} \nu_{sn}(\mathbf{v}_s - \mathbf{v}_n)$$

$$M_n^E = \sum_{s=i,e,x} n_s \frac{m_{sn}\nu_{sn}}{m_s + m_n}\left[3k_B(T_s - T_n) + (\mathbf{v}_s - \mathbf{v}_n)\cdot(m_s \mathbf{v}_s + m_n \mathbf{v}_n)\right] \tag{6}$$

where $m_{sn} = m_s m_n/(m_s + m_n)$ is the reduced mass and ν_{sn} is the collision rate. The inelastic collision terms for the neutrals are:

$$\omega_n = -\alpha \Gamma_e + \beta n_i n_e - \eta_h \dot{q}/\epsilon_x + k_r n_x n_n$$
$$\mathbf{A}_n^I = \omega_n m_n \mathbf{v}_n \tag{7}$$
$$M_n^I = \omega_n m_n \mathcal{E}_n + k_r n_x n_n \epsilon_x$$

The Poisson equation is employed to compute the electric potential:

$$\nabla^2 \phi = -e(n_i - n_e)/\epsilon_0 \tag{8}$$

B. Gas Properties

The properties of the neutral particles were taken to be representative average values corresponding to air: $m_n = k_B/R_n$, where $R_n = 287$ m^2/(s$^2\cdot$K) and $\gamma_n = 1.4$. Correlations for the transport properties of air were taken from the Sutherland-law formulas of Ref. 30.

The charged particle properties were based on those employed in Ref. 13 to represent nitrogen. The ion and electron mobilities were taken to be $\mu_i = 2.75\,(760\,\text{Torr})/p^*$ cm^2/(V·s) and $\mu_e = 400\,(760\,\text{Torr})/p^*$ cm^2/(V·s), where $p^* = p\,(300\,\text{K})/T$. The corresponding diffusion coefficients were found from $D_s = \mu_s k_B T_s/e$, with $T_i = T_n$ and $k_B T_e = 1$ eV. The collision rates in Eq. (6) were derived from the mobilities as follows: $m_{sn}\nu_{sn} = e/\mu_s$.

The diffusion coefficient for the excited neutrals was determined by assuming the following Schmidt number: $\text{Sc}_x = \mu_{vn}/(\rho_n D_x) = 0.77$. This is a reasonable estimate for self-diffusion in a diatomic gas.[31] The corresponding collision rates were $m_{xn}\nu_{xn} = k_B T_x/D_x$, with $T_x = T_n$.

The ionization coefficient was:

$$\alpha/p^* = \begin{cases} \dfrac{900}{E/p^*}\exp\left[-\dfrac{315}{E/p^*}\right], & E/p^* \leq 100\,\text{V}/(\text{cm Torr}) \\[2ex] 12\exp\left[-\dfrac{342}{E/p^*}\right], & 100 < E/p^* \leq 800\,\text{V}/(\text{cm Torr}) \\[2ex] 12\exp\left[-\dfrac{342}{800}\right], & E/p^* > 800\,\text{V}/(\text{cm Torr}) \end{cases}$$

Here p^* is in Torr, α in cm^{-1}, and E in V/cm. The recombination coefficient was $\beta = 2\times10^{-7}\sqrt{300/T_e}$ cm^3/s, where $T_e = 11600$ K.

In order to obtain a lower bound on the neutral gas heating rate, values for the excitation reactions were taken to represent $N_2(A^3\Sigma)$, an excited species that relaxes relatively slowly. The recombination coefficient was taken to be $k_r = 5 \times 10^{-13}$ cm$^3/s$ and the excitation energy $\epsilon_x = 6.3$ eV. The fraction of energy going into molecular excitation $\eta_h(E/N)$ was evaluated using a point Boltzmann equation solution; the results are shown in Fig. 1.

C.   Boundary Conditions

Standard no-slip boundary conditions with a constant temperature wall were employed for the neutral particles. The number density of the excited molecules was set to a small value on the boundaries (1.0×10^8 m^{-3}).

Standard boundary conditions were employed for the charged particles. First, the conditions at the wall were determined by setting the normal derivative to zero. Then, if the provisional ion flow was away from the boundary, the ion flux was set to zero. The electron number density was determined through a balance between the kinetic flux to the wall and secondary emission. For certain cases, these boundary conditions led to numerical instability at the exposed electrode boundary. When this occurred, the simplified boundary conditions described in Ref. 32 were employed.

For a bare electrode the potential was specified as zero (grounded). An alternative boundary condition was employed for an electrode with a dielectric coating. The dielectric layer was assumed to be sufficiently thin that a linear potential profile (uniform electric field $\mathbf{E}_d$) was a good approximation. The electric field inside the dielectric was related to the electric field $\mathbf{E}$ at the surface through the relation $\epsilon_0\mathbf{E} - \epsilon_r\epsilon_0\mathbf{E}_d = \sigma\mathbf{n}$, where σ is the surface charge density and $\mathbf{n}$ is the unit normal vector pointing into the computational domain. The surface charge was determined by integrating $\partial\sigma/\partial t = -\mathbf{j} \cdot \mathbf{n}$ for each surface point, using a time-marching scheme analogous to that of the main governing equations.

III.   Numerical Methods

The calculations were carried out using the Air Force Research Laboratory code HOPS (Higher Order Plasma Solver).[33–36] The code includes several physical models and numerical schemes. Here, the physical model consisting of Eqs. (1), (4), and (8) was solved using an implicit, second-order, upwind formulation. All the equations were solved in a nondimensional form that has been described in previous papers.[33–36]

Time integration of the conservation equations (1) and (4) was carried out using a second-order implicit scheme, based on a three-point backward difference of the time terms. The formulation is similar to the standard technique of Beam and Warming,[37] but adapted to a multi-fluid formulation with different models for particle motion.

Approximate factoring and quasi-Newton subiterations were employed. The implicit terms were linearized in the standard 'thin layer' manner. The implicit terms were evaluated with second-order spatial accuracy, yielding a block tridiagonal system of equations for each factor. The species were loosely coupled, limiting the rank of the flux Jacobian matrices to the order of the moment model. Each factor was solved in turn using a standard block tridiagonal solver, and the change in the solution vector of conserved variables was driven to zero by the subiteration procedure at each time step.

For the five-moment model employed for the neutrals, the Roe scheme[38, 39] was employed for the inviscid fluxes. For the one- and two-moment models, a simple upwinding scheme was employed, based on the convection-drift velocity. This is similar to the approach of Surzhikov and Shang.[32] Stability was enforced using the minmod limiter in the MUSCL formalism.[40]

The Poisson equation (8) was solved at the end of each sub-iteration in the implicit time-marching scheme. An approximately factored implicit scheme was employed, adapted from the approach described by Holst.[41] The formulation of the implicit scheme was analogous to that of the conservation equations, with linearization of the implicit terms, approximate factoring, and an iterative procedure that drives the change in the solution to zero. The spatial derivatives were evaluated using second-order central differences, and the system was solved using the Thomas tridiagonal algorithm.[42]

IV. Results

Schematics of the Mach 5 cylinder flow experiment[17, 26] are shown in Fig. 2. Figure 2a shows a diagram of the cylinder model mounted in the wind tunnel, and Figs. 2b-c illustrate the construction of the test article. The hollow cylinder model was made of fused quartz, with a 6 mm outside diameter and a 2 mm thick wall. A thin copper exposed electrode (12 mm × 1.5 mm) was affixed to the surface of the cylinder, with a second copper electrode mounted inside (a 3 mm diameter tube, 0.35 mm thick and 10 mm long).

A combination of positive and negative polarity pulses to the two electrodes produced a potential difference of around 20 kV, lasting on the order of 100 ns. The effects of the energy release in the resulting discharge were captured using schlieren photography. Selected side-view schlieren images are shown in Fig. 3. Weak shock waves are seen to form near the edge of the exposed electrode, and propagate upstream in the shock-layer flow on a time scale on the order of microseconds. When they reach the bow shock, they alter its shape, and increase the shock standoff by up to 25%.

In the experiments, typical freestream conditions for the neutral gas were a speed of 715 m/s, a pressure of 159.5 Pa, and a temperature of 56 K. Sample calculations are presented here for a one-dimensional discharge under conditions representative of the stagnation region of the cylinder flow experiment. The corresponding stagnation conditions, computed using the Rayleigh supersonic Pitot formula[43] were 4.74 kPa and 310.3 K. For each case in the calculations discussed below, the initial, uniform state of the neutral gas was set to these stagnation values.

The configuration considered here is illustrated in Fig. 4a. The problem is one-dimensional. In the simulations, the right electrode was grounded and the left electrode, which was coated by a thin dielectric layer, was powered with the following input signal:

$$V_s = -V_0 \exp\left[-(t/\tau - 4)^2\right] \tag{9}$$

For the present calculations, we assumed $V_0 = 20$ kV and $\tau = 15$ ns.

The discharge gap was taken to be 10 mm. The initial number density of charged particles was taken to be 10^{13} m^{-3}, the initial number density of excited molecules was 10^{11} m^{-3}, and the initial electric field was zero. The dielectric coating was assumed to be 2 mm thick, with a relative dielectric constant of $\epsilon_r = 3.8$, chosen to be representative of fused quartz. The secondary emission coefficient was $\gamma_{\text{sem}} = 0.05$.

As mentioned earlier, the calculations were carried out in two phases. The first stage of the calculations encompassed the first 400 ns of the discharge, and employed the full physical model discussed above: Eqs. (1), (4), and (8). Since electromagnetic effects and charged particle motion became negligible after the input pulse died away (~ 120 ns), in the second stage of the computations (0.4 μs to 100.4 μs), only the behavior of the neutrals and excited molecules was modeled: Eqs. (1)c and (4). This approach resulted in a substantial savings in computational cost, allowing the time-step to be increased by a factor of about 10^4.

Results obtained in these two stages are illustrated in Fig. 4b. The plot shows the energy density of the excited molecular species, averaged over the discharge gap. The red line indicates the Stage 1 computations with the full model, and the blue line the Stage 2 computations with the reduced model. Close inspection of the figure indicates that the difference in energy deposition rate predicted by the two models at the 400 ns switch-over is extremely small.

Figure 5 shows results from a grid resolution study of this problem. Calculations were carried out on uniform grids of 401, 801, and 1601 points. The minimum mesh spacings for the respective cases were 25 μm, 12.5 μm, and 6.25 μm. For each case, the time step was 0.25 ps for the Stage 1 computations, and 5 ns for Stage 2.

Figure 5a shows a close-up view of the electron number density distribution near the left electrode at the 60 ns mark (Stage 1) for each of the grids. For this case, the computations appear to be approaching grid convergence for a mesh of 801 points.

Analogous results of the Stage 2 calculations are shown in Fig. 5b. This plot shows the neutral gas velocity profile at 10.4 μs. The wave generated near the left electrode appears to be well-resolved on all the grids, but the corresponding wave on the right appears to diminish with grid refinement. This result is being investigated in ongoing work. The remainder of the discussion will focus on the finest grid case, with 1601 points.

Figure 6 presents the properties of the electric circuit as a function of time. The input voltage (blue line) and the corresponding voltage on the dielectric surface (red line) are shown in Fig. 6a. The two potentials differ because of charge accumulation on the dielectric surface. The 20 kV negative Gaussian pulse used as

American Institute of Aeronautics and Astronautics

100

an input waveform results in a maximum negative potential on the dielectric surface of about 7 kV at 46 ns, and a positive peak of around 2 kV which appears later at about 73 ns.

The current density $\mathbf{j}$ and dissipated power $\mathbf{E}\cdot\mathbf{j}$, averaged across the domain, are shown in Fig. 6b. Three major peaks are seen in the plots, at about 46 ns, 54 ns, and 73 ns, and appear to be associated with the maximum of dV_s/dt. The average current is initially negative, flowing toward the left electrode, but changes sign at about 62 ns. Afterwards there is significant current flow in the opposite direction. The current and power dissipation approach zero as the input waveform decays.

The accumulation of surface charge on the dielectric plays an important role in limiting the electric field and current in the discharge. The surface charge on the left electrode is shown as a function of time in Fig. 7a, along with the current density at the same location. Current flow toward the electrode (negative values of $\mathbf{j}$) results in accumulation of positive charge on the dielectric. The current at the left boundary changes sign at about 65 ns, and begins draining the accumulated surface charge. For large times, both current and surface change approach zero.

Both the surface charge on the dielectric and the space charge in the electrode sheath act to reduce the electric fields in the discharge gap. Figure 7b illustrates this effect. The blue line indicates the electric field that would be present if perfect neutrality prevailed. This field $E = V_s/(L + d/\epsilon_r)$ reflects the capacitance of the dielectric layer and an empty discharge gap. For comparison, the electric field at a representative location in the plasma ($x = 8$ mm) is indicated by the red line. Initially, the two curves coincide closely, but after about 45 ns, the plasma field is substantially diminished over the reference field because of unbalanced charge.

The evolution of the electric field is illustrated in Fig. 8. Figure 8a shows, as a function of time, the fields in the plasma (black line) and at the left boundary (red line) and right boundary (blue line). Figure 8b shows the distribution of the reduced electric field across the domain for selected times. Initially the electric field is fairly uniform. Then a brief, intense, negative peak in the electric field at the left boundary occurs, centered at about 54 ns. The reduced electric field briefly exceeds 10^4 Td (10^{-17} V·m^2) during this phase. (Comparable reduced electric fields were reported in Ref. 44.) Later, a corresponding positive peak occurs at the right electrode, centered around 73 ns. It is interesting to note the sign change in the plasma field around 61 ns (see Fig. 7b), and that a period occurs in which the electric field is directed toward the boundary on both sides (dual cathode regime[21]).

Energy storage and release are examined in detail in Figs. 9-10. Figure 9 shows the net rate of energy deposition, per unit volume, in excited molecular states:

$$P = \eta_h \mathbf{E}\cdot\mathbf{j} - k_r n_n n_x \epsilon_x \tag{10}$$

This is the source term in an equation for the internal energy formed by multiplying Eq. (1c) by the excitation energy per molecule ϵ_x. Results for the energy deposition phase (Fig. 9a) closely mirror the behavior of the electric field. Peak energy deposition occurs in brief, intense peaks close to the electrodes. Energy release occurs in the same regions, over longer time scales (Fig. 9b).

Figure 10 shows the corresponding averages over the discharge gap as a function of time. (See also Fig. 4b.) Comparing to Fig. 6b, we see that the energy deposition (blue curve) closely tracks the dissipated electric power. The stored energy (red curve) peaks and begins to decline even before the end of the input waveform. Once the input pulse is over, the stored energy undergoes an exponential decay, with most of the energy disappearing within 10 μs.

Profiles through the discharge for different times in the Stage 1 computations are shown in Fig. 11. At early stages in the pulse (Fig. 11a, 44 ns), the cathode sheath begins to form, but the electric field is essentially uniform (linear potential distribution). Even for this low field, excited molecules have been generated over the initial level, in particular in the plasma away from the left electrode sheath. At later times (Fig. 11b-c, 45-46 ns), rapid change occurs in the left electrode sheath. The electric field becomes much higher there than in the plasma, and substantial ionization and excitation occur. There is a corresponding reduction in the sheath thickness.

By 54 ns (Fig. 11d), the electric field at the left electrode has reached its maximum value, and around 73 ns (Fig. 11e), a corresponding process occurs at the right electrode.

After the decay of the input waveform, some additional excitation occurs, particularly near the right electrode, which behaves like a cathode as the ionization generated by the pulse leaks out of the domain. At the end of Stage 1 (Fig. 11f, 400 ns), we are left with large concentrations of excited molecules near both electrodes, and a negligible electric field.

Selected profiles through the discharge for the Phase 2 calculations are shown in Fig. 12. Without excitation, the number density rapidly relaxes, and the peaks in the distribution are essentially gone within about 10 μs (Fig. 12a). The corresponding energy release generates weak shocks (acoustic waves) that travel toward the center of the domain from the vicinity of the electrodes (Figs. 12b-d). At later stages in the computation (not shown) multiple reflections of these waves occur.

The maximum neutral gas temperature rise is about 40 K, maximum velocities are about 10 m/s, and maximum pressure rise is about 0.2 kPa. It is interesting to note that although energy release continues to occur throughout the computation (note the final temperature distribution), the contribution to gas motion only comes from the portion of energy released faster than the characteristic time for an acoustic wave to traverse the domain.

V. Summary and Conclusions

Numerical calculations were carried out to examine the physics of the operation of nanosecond-pulse, single dielectric barrier discharges for high-speed flow control. Conditions were selected to be representative of the stagnation region of a Mach 5 cylinder flow that was the subject of recent experiments.[17,26] A four-species formulation was employed, including neutrals, ions, electrons, and a representative excited molecular species. The following models were employed to predict particle motion: a drift-diffusion formulation for the charged particles, a diffusion equation for the excited molecules, and a five-moment fluid formulation for the neutrals. The Poisson equation was solved for the electric potential. During a 20 kV Gaussian input pulse lasting approximately 120 ns, an average energy density of about 40 J/m^3 was stored in excited molecular states. Quenching reactions released this stored energy within about 10 μs, converting it into translational energy of the neutrals and forming weak shock waves. The maximum neutral gas temperature rise predicted by the model was about 40 K.

This work represents a first step towards detailed modeling of the nanosecond-pulse dielectric barrier discharge actuator. Despite the idealizations in the model, the computations predict the same order of magnitude of effect that was observed experimentally. In ongoing work, we are extending the model to include about ten species and carrying out a detailed study of the boundary conditions. The nanosecond-pulse dielectric barrier discharge actuators show promise for high-speed flow control, and accurate numerical modeling will contribute the optimization of these devices.

Acknowledgments

References

[1]Kantrowitz, A. R., "A Survey of Physical Phenomena Occurring in Flight at Extreme Speeds," *Proceedings of the Conference on High-Speed Aeronautics*, edited by A. Ferri, N. J. Hoff, and P. A. Libby, Polytechnic Institute of Brooklyn, New York, 1955, pp. 335–339.

[2]Resler, E. L. and Sears, W. R., "The Prospects for Magneto-Aerodynamics," *Journal of the Aeronautical Sciences*, Vol. 25, No. 4, 1958, pp. 235–245,258.

[3]Malik, M., Weinstein, L., and Hussaini, M. Y., "Ion Wind Drag Reduction," AIAA Paper 83-0231, January 1983.

[4]Roth, J. R., Sherman, D. M., and Wilkinson, S. P., "Electrohydrodynamic Flow Control with a Glow-Discharge Surface Plasma," *AIAA Journal*, Vol. 38, No. 7, 2000, pp. 1166–1172.

[5]Palmer, G., "Magnetic Field Effects on the Computed Flow over a Mars Return Aerobrake," *Journal of Thermophysics and Heat Transfer*, Vol. 7, No. 2, 1993, pp. 294–301.

[6]Gurijanov, E. P. and Harsha, P. T., "AJAX: New Directions in Hypersonic Technology," AIAA Paper 96-4609, November 1996.

[7]Adamovich, I. V., Subramaniam, V. V., Rich, J. W., and Macheret, S. O., "Phenomenological Analysis of Shock-Wave Propagation in Weakly Ionized Plasmas," *AIAA Journal*, Vol. 36, No. 5, 1998, pp. 816–822.

[8]Poggie, J., "Modeling the Propagation of a Shock Wave Through a Glow Discharge," *AIAA Journal*, Vol. 38, No. 8, 2000, pp. 1411–1418.

[9]Poggie, J. and Gaitonde, D. V., "Magnetic Control of Flow Past a Blunt Body: Numerical Validation and Exploration," *Physics of Fluids*, Vol. 14, No. 5, 2002, pp. 1720–1731.

[10]Gaitonde, D. V. and Poggie, J., "Implicit Technique for Three-Dimensional Turbulent Magnetoaerodynamics," *AIAA Journal*, Vol. 41, No. 11, 2003, pp. 2179–2191.

[11]Adamovich, I. V., Lempert, W. R., Nishihara, M., Rich, J. W., and Utkin, Y. G., "Repetitively Pulsed Nonequilibrium Plasmas for Magnetohydrodynamic Flow Control and Plasma-Assisted Combustion," *Journal of Propulsion and Power*, Vol. 24, No. 6, 2008, pp. 1198–1215.

[12]Poggie, J., "Numerical Simulation of Direct Current Glow Discharges for High-Speed Flow Control," *Journal of Propulsion and Power*, Vol. 24, No. 5, 2008, pp. 916–922.

[13]Adamovich, I. V., Nishihara, M., Choi, I., Uddi, M., and Lempert, W. R., "Energy Coupling to the Plasma in Repetitive Nanosecond Pulse Discharges," *Physics of Plasmas*, Vol. 16, Art. 113505, 2009.

[14]Bisek, N., Boyd, I., and Poggie, J., "Numerical Study of Plasma-Assisted Aerodynamic Control for Hypersonic Vehicles," *Journal of Spacecraft and Rockets*, Vol. 46, No. 3, 2009, pp. 568–576.

[15]Bisek, N., Boyd, I., and Poggie, J., "Numerical Study of Magnetoaerodynamic Flow Around a Hemisphere," *Journal of Spacecraft and Rockets*, Vol. 47, No. 5, 2010, pp. 816–827.

[16]Poggie, J., Tilmann, C. P., Flick, P. M., Silkey, J. S., Osborne, B. A., Ervin, G., Maric, D., Mangalam, S., and Mangalam, A., "Closed-Loop Stall Control System," *Journal of Aircraft*, Vol. 47, No. 5, 2010, pp. 1747–1755.

[17]Nishihara, M., Takashima, K., Rich, J. W., and Adamovich, I. V., "Mach 5 Bow Shock Control by a Nanosecond Pulse Surface DBD," AIAA Paper 2011-1144, January 2011.

[18]Romig, M. F., "The Influence of Electric and Magnetic Fields on Heat Transfer to Electrically Conducting Fluids," *Advances in Heat Transfer*, edited by T. F. Irvine and J. P. Hartnett, Vol. 1, Academic Press, New York, 1964, pp. 267–354.

[19]Samimy, M., Adamovich, I., Webb, B., Kastner, J., Hileman, J., Keshav, S., and Palm, P., "Development and Characterization of Plasma Actuators for High Speed Jet Control," *Experiments in Fluids*, Vol. 37, No. 4, 2004, pp. 577–588.

[20]Roupassov, D. V., Nikipelov, A. A., Nudnova, M. M., and Starikovskii, A. Y., "Flow Separation Control by Plasma Actuator with Nanosecond Pulsed-Periodic Discharge," *AIAA Journal*, Vol. 47, No. 1, 2009, pp. 168–185.

[21]Macheret, S. O., Shneider, M. N., and Miles, R. B., "Modeling of Air Plasma Generation by Repetitive High-Voltage Nanosecond Pulses," *IEEE Transactions on Plasma Science*, Vol. 30, No. 3, 2002, pp. 1301–1314.

[22]Pugh, E. R., Wallace, J., Jacob, J. H., Northam, D. B., and Daugherty, J. D., "Optical Quality of Pulsed Electron-Beam Sustained Lasers," *Applied Optics*, Vol. 13, No. 11, 1974, pp. 2512–2517.

[23]Aleksandrov, V. V., Koterov, V. N., Pustovalov, V. V., Soroka, A. M., and Suchkov, A. F., "Space-Time Evolution of the Cathode Layer in Electron-Beam-Controlled Lasers," *Soviet Journal of Quantum Electronics*, Vol. 8, No. 1, 1978, pp. 59–63.

[24]Unfer, T. and Boeuf, J. P., "Modelling of a Nanosecond Surface Discharge Actuator," *Journal of Physics D: Applied Physics*, Vol. 42, Art. 194017, 2009.

[25]Popov, N. A., "Investigation of the Mechanism for Rapid Heating of Nitrogen and Air in Gas Discharges," *Plasma Physics Reports*, Vol. 27, No. 10, 2001, pp. 886–896.

[26]Nishihara, M., Takashima, K., Rich, J. W., and Adamovich, I. V., "Mach 5 Bow Shock Control by a Nanosecond Pulse Surface Dielectric Barrier Discharge," *Physics of Fluids*, 2011, accepted for publication.

[27]Nishihara, M., Adamovich, I., Bisek, N., and Poggie, J., "Computational and Experimental Analysis of Mach 5 Air Flow over a Cylinder with Nanosecond Pulse Discharge," AIAA Paper, January 2012, submitted to the AIAA Aerospace Sciences Meeting.

[28]Burgers, J. M., *Flow Equations for Composite Gases*, Academic Press, New York, 1969.

[29]Golant, V. E., Zhilinsky, A. P., and Sakharov, I. E., *Fundamentals of Plasma Physics*, J. Wiley, New York, 1980, Trans. K. Z. Vedeneyeva and V. F. Agranat.

[30]White, F. M., *Viscous Fluid Flow*, McGraw-Hill, New York, 2nd ed., 1991.

[31]Olejniczak, J. and Candler, G. V., "Vibrational Energy Conservation with Vibration-Dissociation Coupling: General Theory and Numerical Studies," *Physics of Fluids*, Vol. 7, No. 7, 1995, pp. 1764–1774.

[32]Surzhikov, S. T. and Shang, J. S., "Two-Component Plasma Model for Two-Dimensional Glow Discharge in Magnetic Field," *Journal of Computational Physics*, Vol. 199, 2004, pp. 437–464.

[33]Poggie, J., "High-Order Compact Difference Methods for Glow Discharge Modeling," AIAA Paper 2009-1047, January 2009.

[34]Poggie, J., "Compact Difference Methods for Discharge Modeling in Aerodynamics," AIAA Paper 2009-3908, June 2009.

[35]Poggie, J., "Role of Charged Particle Inertia in Pulsed Electrical Discharges," AIAA Paper 2010-1195, 2010.

[36]Poggie, J., "High-Order Numerical Methods for Electrical Discharge Modeling," AIAA Paper 2010-4632, 2011.

[37]Beam, R. and Warming, R., "An Implicit Factored Scheme for the Compressible Navier-Stokes Equations," *AIAA Journal*, Vol. 16, No. 4, 1978, pp. 393–402.

[38]Morrison, J., "Flux Difference Split Scheme for Turbulent Transport Equations," AIAA Paper 90-5251, October 1990.

[39]Gaitonde, D. and Shang, J. S., "Accuracy of Flux-Split Algorithms in High-Speed Viscous Flows," *AIAA Journal*, Vol. 31, No. 7, 1993, pp. 1215–1221.

[40]Anderson, W. K., Thomas, J. L., and van Leer, B., "A Comparison of Finite Volume Flux Vector Splittings for the Euler Equations," AIAA Paper 85-0122, January 1985.

[41]Holst, T. L., "Transonic Flow Computations Using Nonlinear Potential Methods," *Progress in Aerospace Sciences*, Vol. 36, 2000, pp. 1–61.

[42]Cheney, W. and Kincaid, D., *Numerical Mathematics and Computing*, Brooks/Cole Publishing, Pacific Grove, California, 3rd ed., 1994.

[43]Liepmann, H. W. and Roshko, A., *Elements of Gasdynamics*, J. Wiley, New York, 1957.

[44]Macheret, S. O., Shneider, M. N., and Murray, R. C., "Ionization in Strong Electric Fields and Dynamics of Nanosecond-Pulse Plasmas," *Physics of Plasmas*, Vol. 13, Art. 023502, 2006.
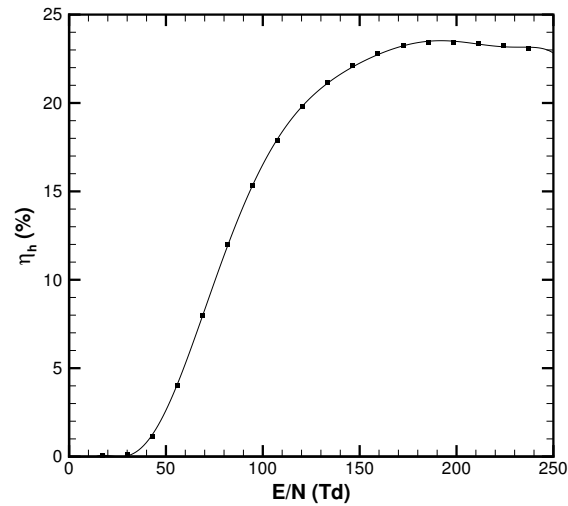
Figure 1. Fraction of discharge energy going into excitation as a function of reduced electric field: points from Boltzmann solution along with eighth-order polynomial fit.
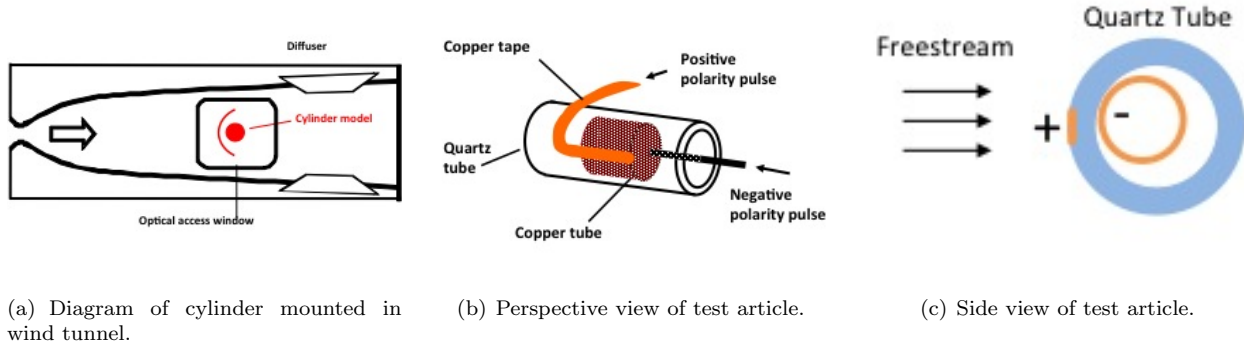

(a) Diagram of cylinder mounted in wind tunnel.

(b) Perspective view of test article.

(c) Side view of test article.

Figure 2. Configuration of Mach 5 cylinder flow experiment.[26]

(a) Time: 1 μs.　　　(b) Time: 2 μs.　　　(c) Time: 3 μs.　　　(d) Time: 4 μs.
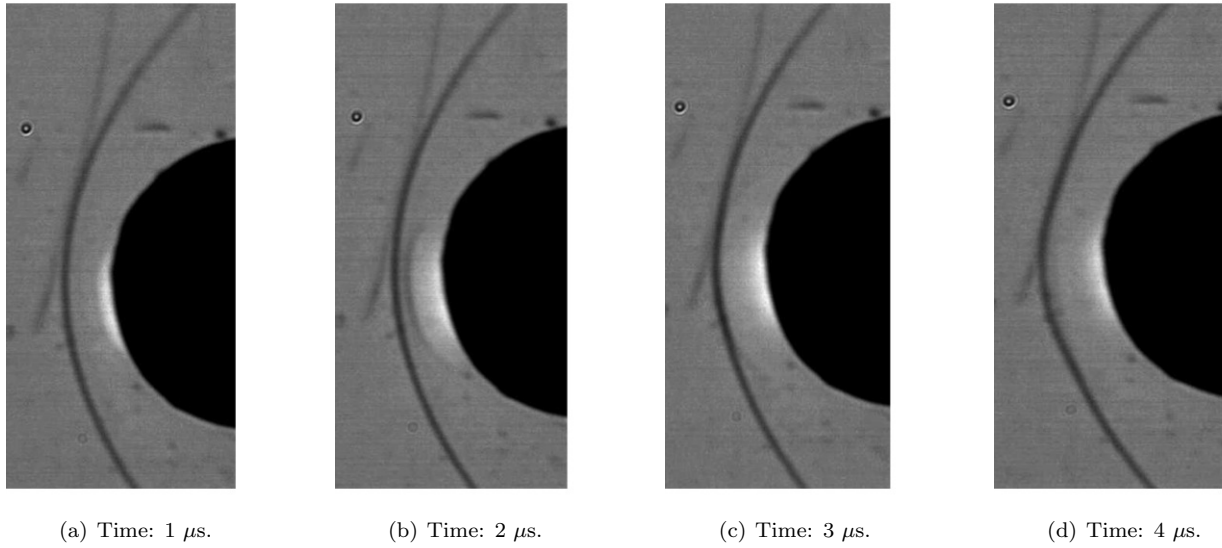
Figure 3. Side-view schlieren images of Mach 5 cylinder flow perturbed by pulsed discharge.

(a) Diagram of computational domain.

(b) Two-stage computational strategy: energy density for excited molecules, averaged across discharge gap.
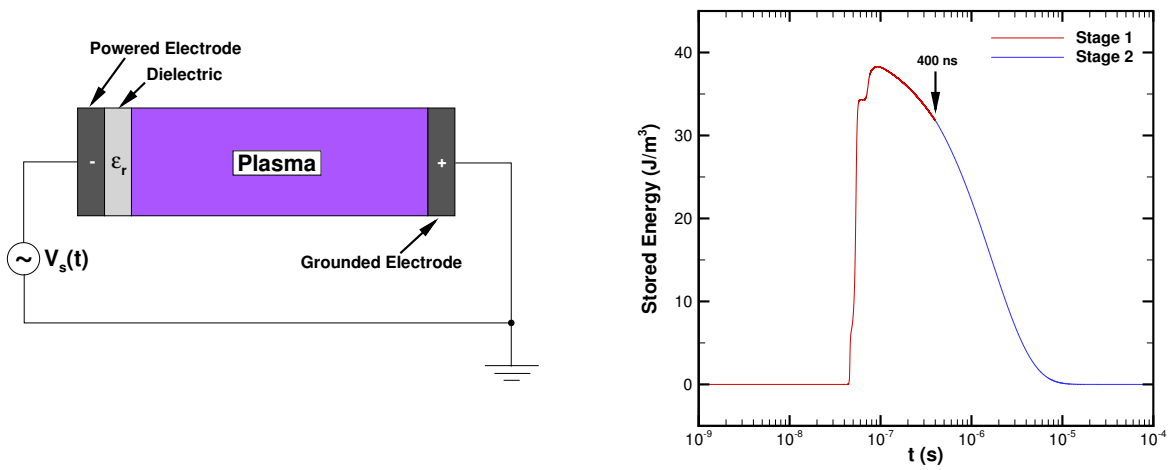
Figure 4. Configuration for one-dimensional discharge problem.
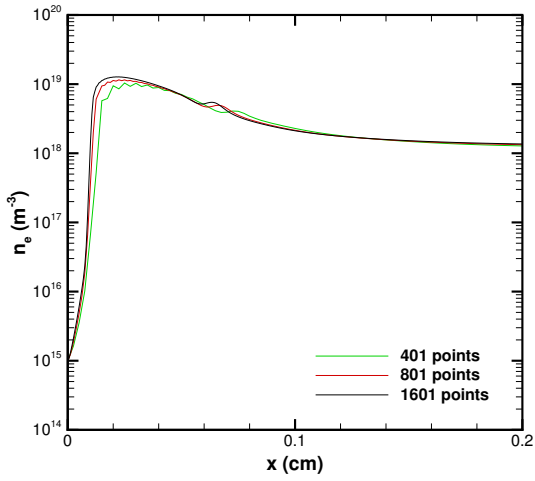
(a) Electron number density profile at 60 ns.
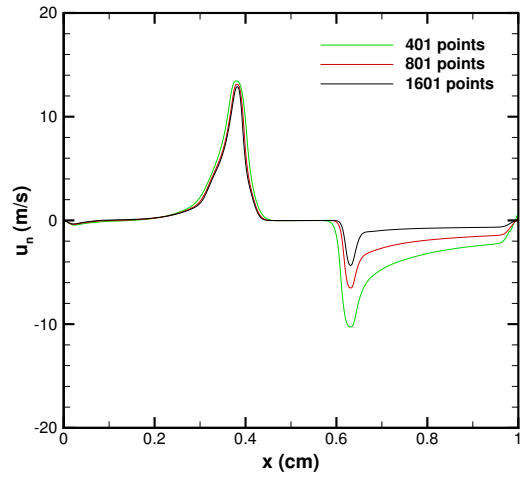
(b) Neutral gas velocity profile at 10.4 μs.

Figure 5. Grid resolution study of one-dimensional discharge problem.
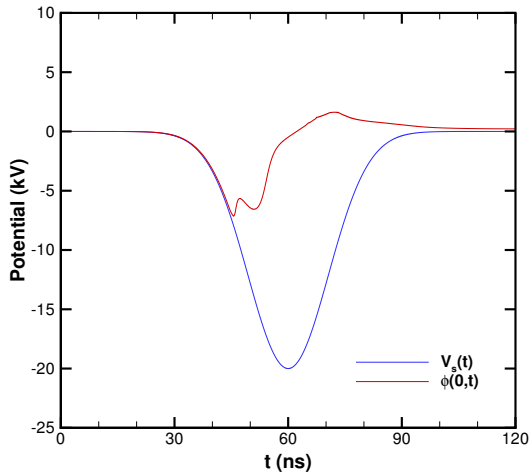
(a) Applied potential and potential at left electrode.
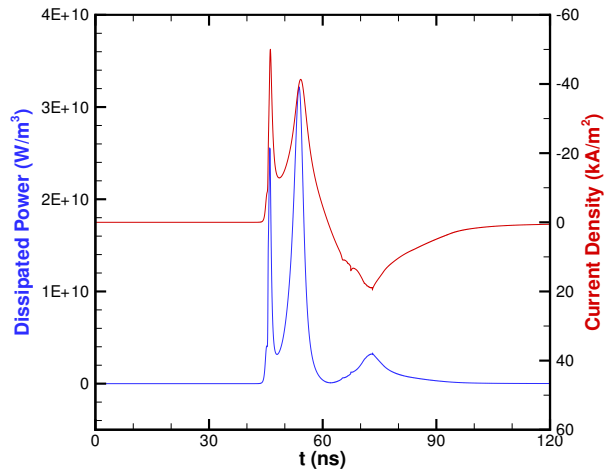
(b) Current density $\mathbf{j}$ and dissipated power density $\mathbf{E} \cdot \mathbf{j}$, both averaged across gap.

Figure 6. Properties of electrical circuit.
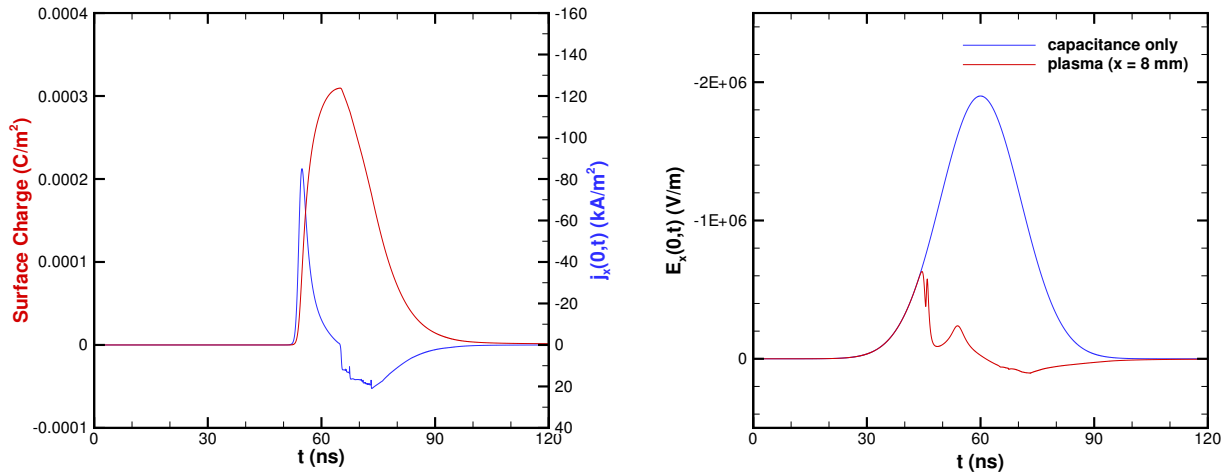
(a) Current and surface charge at left boundary.

(b) Effect of surface and space charge on plasma electric field.

Figure 7. Effect of surface and space charge.
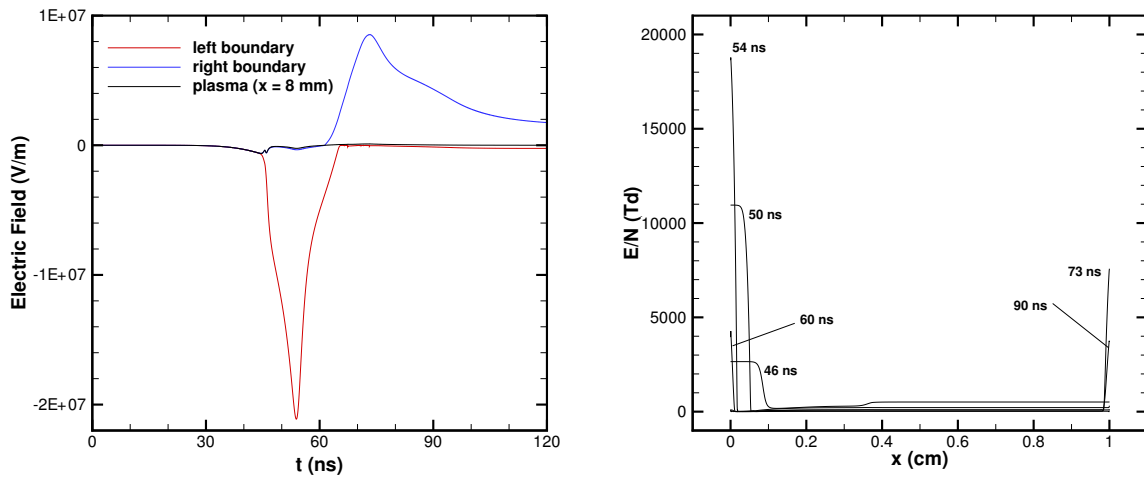
(a) Electric field in plasma and at left and right boundaries.

(b) Reduced electric field distribution.

Figure 8. Variation of electric field in space and time.
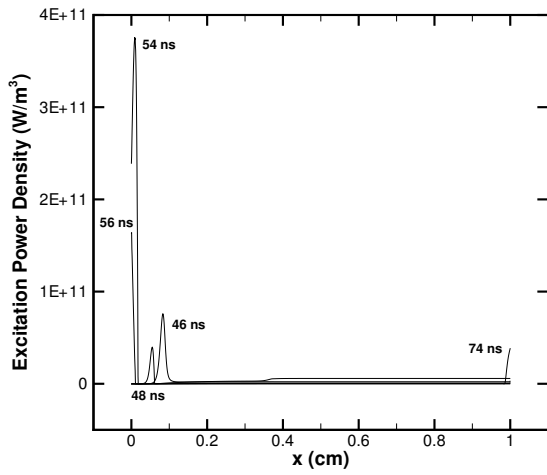
(a) Energy storage phase.
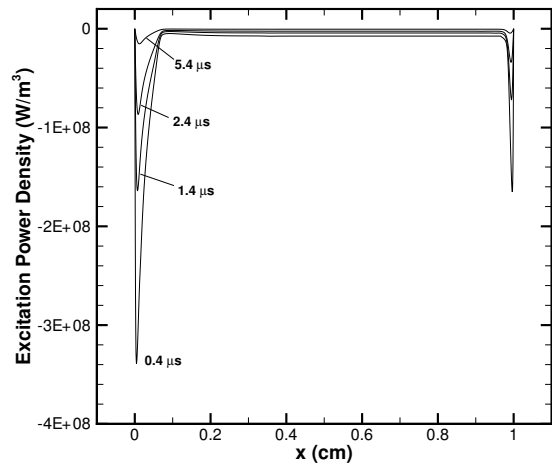
(b) Energy release phase.

Figure 9. Spatial variation of power density for storage and release of energy in excited molecules.
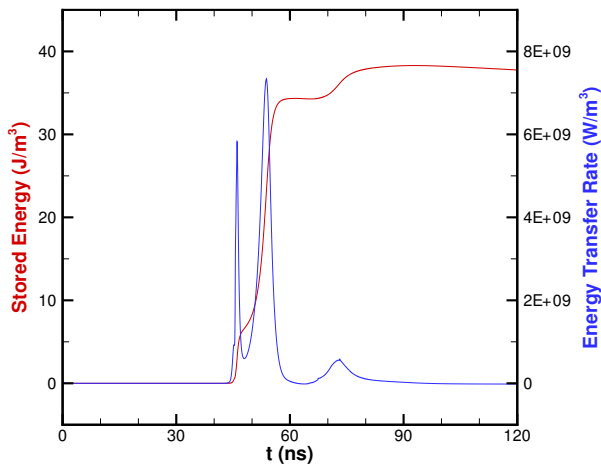
(a) Energy storage phase.
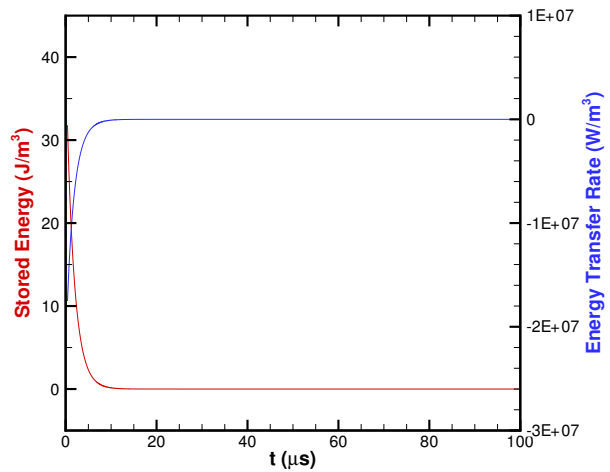
(b) Energy release phase.

Figure 10. Energy storage and release; quantities averaged across discharge gap.
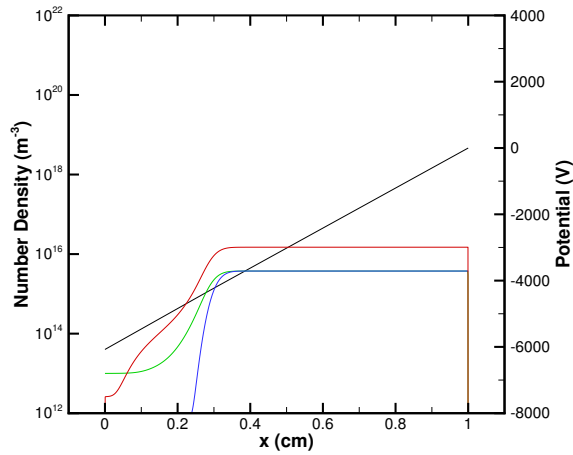
(a) Time: 44 ns.
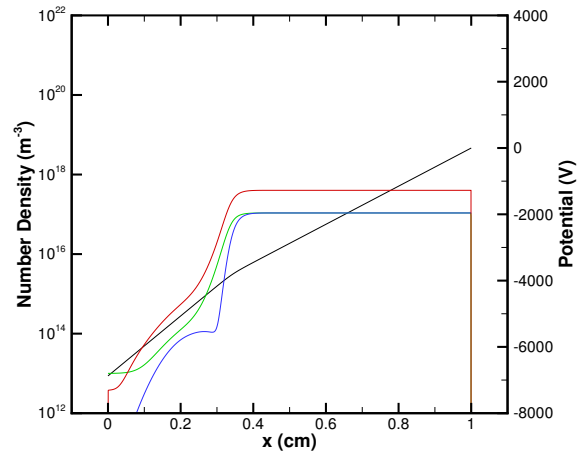
(b) Time: 45 ns.
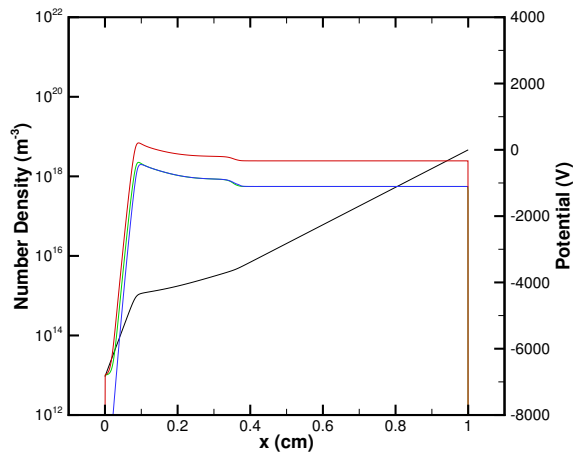
(c) Time: 46 ns.
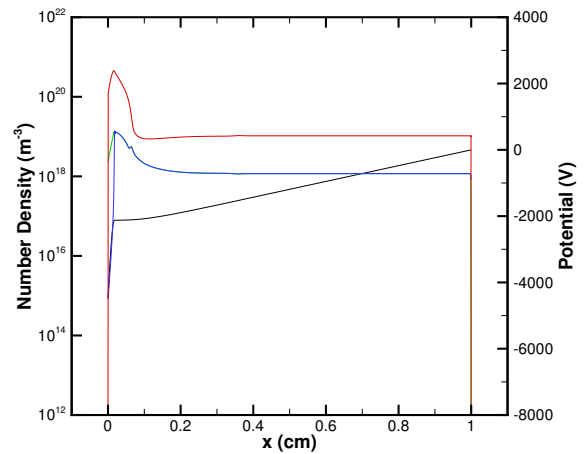
(d) Time: 54 ns.
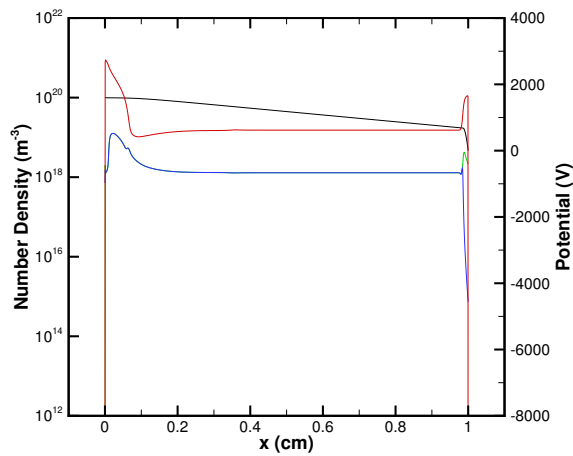
(e) Time: 73 ns.
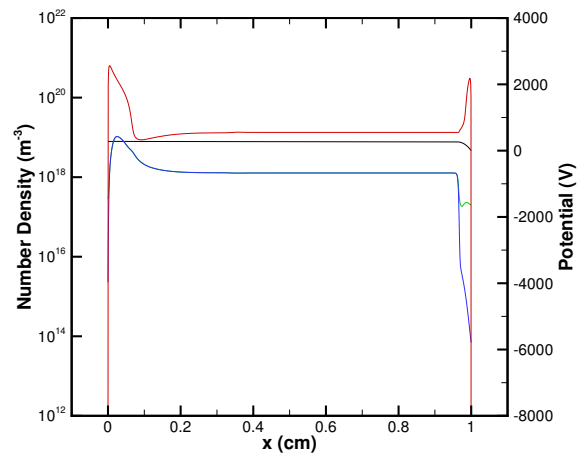
(f) Time: 400 ns.

Figure 11. Discharge profiles for energy storage phase. Line key: black − electric potential; red − number density of excited molecules; green − number density of ions; blue − number density of electrons.
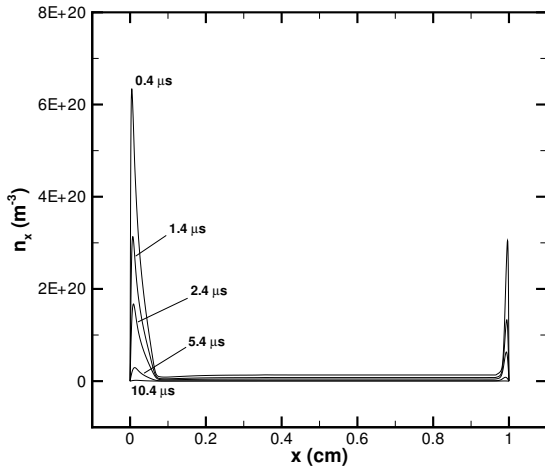
(a) Number density of excited molecules.
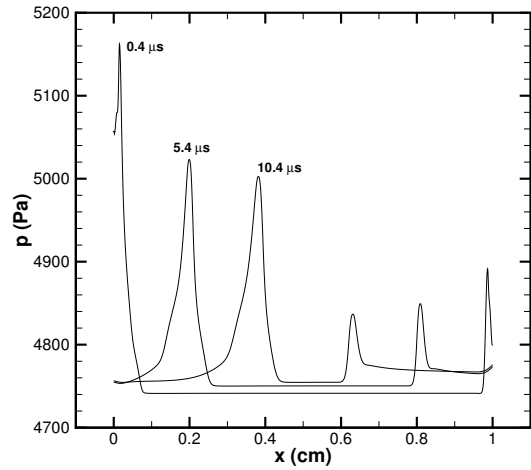
(b) Neutral gas pressure.
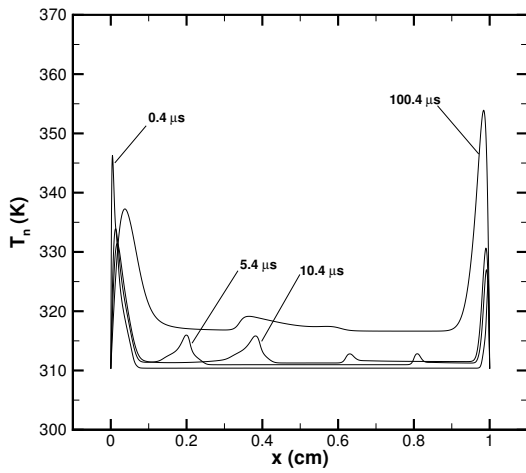
(c) Neutral gas temperature.
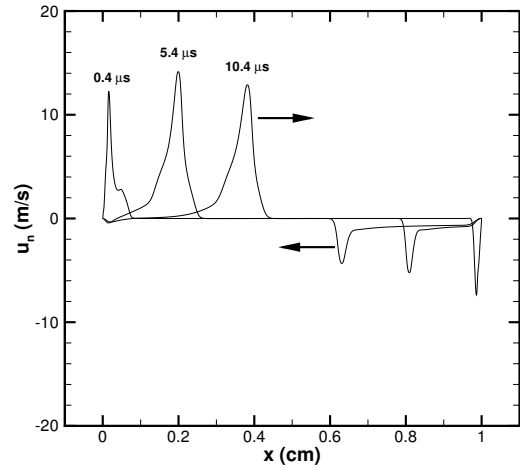
(d) Neutral gas velocity.

Figure 12. Discharge profiles for energy release phase.

50th AIAA Aerospace Sciences Meeting including the New Horizons Forum and Aerospace Exposition
09 - 12 January 2012, Nashville, Tennessee

AIAA 2012-1025

Numerical Simulation
of Nanosecond-Pulse Electrical Discharges

Jonathan Poggie[*] and Nicholas J. Bisek[†]

Air Force Research Laboratory, Wright-Patterson AFB, Ohio 45433-7512 USA

Igor V. Adamovich[‡] and Munetake Nishihara[§]

The Ohio State University, Columbus, Ohio 43210 USA

Numerical calculations were carried out to examine the physics of the operation of a nanosecond-pulse, single dielectric barrier discharge in a configuration with planar symmetry. This simplified configuration was chosen as a vehicle to develop a physics-based nanosecond discharge model, including realistic air plasma chemistry and compressible bulk gas flow. First, a reduced plasma kinetic model (15 species and 42 processes) was developed by carrying out a sensitivity analysis of zero-dimensional plasma computations with an extended chemical kinetic model (46 species and 395 processes). Transient, one-dimensional discharge computations were then carried out using the reduced kinetic model, incorporating a drift-diffusion formulation for each species, a self-consistent computation of the electric potential using the Poisson equation, and a mass-averaged gas dynamic formulation for the bulk gas motion. Discharge parameters (temperature, pressure, and input waveform) were selected to be representative of recent experiments on bow shock control with a nanosecond discharge in a Mach 5 cylinder flow. The computational results qualitatively reproduce many of the features observed in the experiments, including the rapid thermalization of the input electrical energy and the consequent formation of a weak shock wave. At breakdown, input electrical energy is rapidly transformed (over roughly 1 ns) into ionization products, dissociation products, and electronically excited particles, with subsequent thermalization over a relatively longer time-scale (roughly 10 μs). The motivation for this work is modeling nanosecond-pulse, dielectric barrier discharges for applications in high-speed flow control. The effectiveness of such devices as flow control actuators depends crucially on the rapid thermalization of the input electrical energy, and in particular on the rate of quenching of excited electronic states of nitrogen molecules and oxygen atoms and on the rate of electron-ion recombination.

I.   Introduction

Interest in plasma-based flow control dates to the mid-1950s, when magnetohydrodynamic reentry heat shields were first investigated.[1,2] Activity in the research area waned in the 1970s, with some work on drag reduction using corona discharges appearing in the 1980s.[3] A resurgence in the field took place in the 1990s, with the introduction of dielectric barrier discharge (DBD) actuators,[4] a revisit of reentry magnetohydrodynamics,[5] and the disclosure of the AJAX hypersonic vehicle concept.[6] In the fifteen years since this resurgence, plasma-based flow control techniques have been a topic of ongoing research, motivated by the possibility of extremely rapid actuation, a low-profile configuration, and the ability to operate in hostile environments.[7–17]

In the high-speed regime, plasma-based flow control devices have suffered the drawbacks of either excessive weight[18] or insufficient control authority.[4] Pulsed discharge devices, based on either arc[19] or glow discharges,[20] seem to be a promising way around these difficulties. Nanosecond-scale pulsed glow discharges

---

[*]Team Leader, High-Speed Flow Research Group, Computational Aerophysics Branch. Associate Fellow AIAA.
[†]Research Aerospace Engineer, High-Speed Flow Research Group, Computational Aerophysics Branch. Member AIAA.
[‡]Professor, Nonequilibrium Thermodynamics Laboratories, Dept. of Mechanical Engineering. Associate Fellow AIAA.
[§]Postdoctoral Researcher, Nonequilibrium Thermodynamics Laboratories, Dept. of Mechanical Engineering. Member AIAA.

are efficient generators of both ions and electronically excited molecules because of the extremely high instantaneous reduced electric field.[21]

The generation of shock waves by volumetric heat release in pulsed discharges was observed and explained in the 1970s in the context of gas laser technology.[22,23] Early computations by Aleksandrov et al.[23] assumed that all the power dissipated in the discharge immediately went into heating the neutral gas. Popov,[25] however, has emphasized a two-stage heating mechanism in which product species and electronically excited species are generated by electron impact, and then the stored chemical energy is converted to thermal energy through quenching reactions. Two-dimensional calculations have been carried out recently by Unfer and Boeuf,[24] assuming instant thermalization of 30% of the dissipated power going into electronic excitation.

In recent experiments,[17,26] control of a Mach 5 cylinder flow was demonstrated using a pulsed surface dielectric barrier discharge. Schematics of the experiment are shown in Fig. 1. Figure 1a shows a diagram of the model mounted in the wind tunnel, and Figs. 1b-c illustrate the actuator configuration on the cylinder.

The hollow cylinder model was made of fused quartz, with a 6 mm outside diameter and a 2 mm thick wall. A thin copper exposed electrode (12 mm × 1.5 mm × 0.1 mm) was affixed to the surface of the cylinder, with a second copper electrode mounted inside (a 3 mm diameter tube, 0.35 mm thick and 10 mm long). DuPont[TM] Kapton[®] polyimide film was placed over the ends of the exposed electrode, leaving a 10 mm span exposed to the flow.

A combination of positive and negative polarity pulses to the two electrodes produced a potential difference of about 27 kV, lasting on the order of 5 ns (pulse full-width at half maximum). The effects of the energy release in the resulting discharge were captured using phase-locked schlieren imaging. Side-view schlieren images are shown in Fig. 2 for several time-delays after the discharge. A weak shock wave is seen to form near the edge of the exposed electrode, and propagate upstream in the shock-layer flow on a time scale on the order of microseconds. When it reaches the bow shock, the shock shape is altered, and the shock standoff increases by up to 25%. Given the close relationship between shock standoff and gradients at the stagnation point,[9] this system might be able to alter heat transfer rates at the nose of blunt body flows. Further, the system is promising for general high-speed flow control applications, for example control of supersonic inlet flows.[27]

We have begun to formulate a high-fidelity physical model of the energy transfer process in the pulsed surface dielectric barrier discharge.[28] For simplicity in the present work, we have focused on a planar geometry, where experimental evidence exists that a nearly one-dimensional discharge can occur at relatively low pressures.[29] (In a companion project, we are exploring the three-dimensional fluid mechanics of the experiment using a gasdynamics code with a phenomenological volumetric energy deposition model.[30]) Using coupled modeling of the plasma and compressible flow in a one-dimensional geometry, we plan to study the dominant physical effects, including energy thermalization kinetics and compression wave formation and propagation.

To this end, a reduced plasma kinetic model (15 species and 42 processes) was developed first by carrying out a sensitivity analysis of a zero-dimensional plasma computation with an extended chemical kinetic model (46 species and 395 processes). Transient, one-dimensional discharge computations were then carried out using the reduced kinetic model, incorporating a drift-diffusion formulation for each species, a self-consistent computation of the electric potential using the Poisson equation, and a mass-averaged gas dynamic formulation for the bulk gas motion.

II.   Development of Reduced Kinetic Model

To obtain the reduced kinetic model, we applied a sensitivity analysis to a detailed, transient, zero-dimensional air plasma model used in previous work.[31] The reduced model was developed to identify the dominant species and reactions affecting the energy balance and the rate of thermalization in the discharge, and to minimize the computational cost of the transient, one-dimensional calculations that will be presented in Sec. III.

The full air plasma model is based on the model developed by Kossyi et al.[32] It incorporates a set of ordinary differential equations for number densities of neutral species N, N_2, O, O_2, O_3, NO, NO_2, N_2O, NO_3, charged species e^-, N^+, N_2^+, N_3^+, N_4^+, O^+, O_2^+, O_4^+, NO^+, NO_2^+, N_2O^+, $N_2O_2^+$, N_2NO^+, O_2NO^+, $NONO^+$, O^-, O_2^-, O_3^-, NO^-, NO_2^-, NO_3^-, N_2O^-, and excited species $N_2(A^3\Sigma)$, $N_2(B^3\Pi)$, $N_2(C^3\Pi)$, $N_2(a'^1\Sigma)$, $O_2(a^1\Delta)$, $O_2(b^1\Sigma)$, $O_2(c^1\Sigma)$, $N(^2D)$, $N(^2P)$, $O(^1D)$ produced in the plasma, as well as an energy equation for predicting the time evolution of gas temperature. This set of equations is coupled with a steady,

two-term expansion of the Boltzmann equation for the electron energy distribution function (EEDF) of the plasma electrons.[33] These calculations employ experimental cross sections of electron impact electronic excitation, dissociation, ionization, and dissociative attachment processes.[34, 35] The rate coefficients of these electron impact processes, as functions of the reduced electric field E/N, are derived from the Boltzmann solutions by averaging the cross sections over the EEDF. The model also incorporates chemical reactions of ground state species and excited electronic species, electron-ion recombination and ion-ion neutralization processes, ion-molecule reactions, and electron attachment and detachment processes. The rate coefficients of these processes are taken from Kossyi et al.[32] The air plasma processes and the kinetic rates used are listed in a previous paper.[31]

In the zero-dimensional modeling calculations using the full air plasma kinetic model, the time-resolved reduced electric field (i.e. the pulse voltage waveform) was one of the inputs for the model. The voltage waveform was approximated as a pulse with Gaussian form, $U(t) = U_{\text{peak}} \exp[-(t - t_0)^2/\tau^2]$, where U_{peak} is the peak voltage, t_0 is the moment when the voltage peaks, and $\tau = 3$ ns is the pulse width parameter. The pulse width parameter was chosen to fit the experimental voltage pulse duration produced by a nanosecond pulse generator (FID GmbH, FPG 60-100MC4) with pulse full-width half-maximum of 5 ns.[26]

The pulse peak voltage was considered an adjustable parameter, and varied to produce discharge pulse energy loading of 50-100 meV/molecule. At these conditions, if all discharge input energy were thermalized, the resultant temperature rise in the discharge would be $\Delta T \sim 165$-330 K (thermalization of 1 meV/molecule input energy corresponds to $\Delta T = 3.32$ K). However, recent kinetic modeling calculations and experiments[25, 36, 37] suggest that approximately 30% of the input energy is thermalized rapidly after a discharge pulse with a peak reduced electric field of $(E/N)_{\text{peak}} = 200$-900 Td (1 Td $= 10^{-17}$ V-cm^2), during collisional quenching of electronically excited species.

Calculations and experiments by Aleksandrov et al.[38] suggest that in nanosecond pulse discharges at atmospheric pressure at very high values of the reduced electric field, $E/N \sim 1000$ Td, the rapidly thermalized energy fraction increases up to about 50%, due to contributions of ion-molecule reactions, electron-ion recombination, and ion-ion recombination. The time scale for the rapid energy thermalization ranges from a few microseconds at $p \sim 0.01$ atm[37] to below one microsecond at $p \sim 1$ bar.[38] This effect would limit the temperature rise due to rapid energy thermalization after the discharge pulse to $\Delta T \sim 50$-100 K. This is consistent with the temperature rise measured in a single-pulse nanosecond surface dielectric barrier discharge (SDBD) in dry air at $p \sim 30$ Torr using the FID pulse generator, $\Delta T = 40 \pm 30$ K[26] and in a single-pulse nanosecond SDBD in room air using a custom-designed nanosecond pulse generator, $\Delta T = 80 \pm 50$ K.[39]

In the present paper, our primary objective is to study the effect of rapid energy thermalization on compression wave formation in the discharge, for a time scale after the discharge pulse shorter than the acoustic time $\tau_{\text{acoustic}} = L/a$. (Here L is the characteristic size of the plasma and a is the local speed of sound.) Strong compression waves generated by nanosecond-pulse discharges can be used for high-speed flow control. Nanosecond-gate, broadband ICCD images of nanosecond-pulse surface dielectric barrier discharges[17, 26] have shown that the thickness of the near-surface plasma layer at atmospheric pressure is of the order of 100 μm, which corresponds to an acoustic time of $\tau_{\text{acoustic}} \sim 0.3$ μs. Thus, nanosecond-pulse discharge energy thermalization on a shorter time scale at atmospheric pressure would result in strong compression wave formation, as detected in experiments.[17, 20, 39, 40]

Transient, zero-dimensional calculations have been conducted for a single-pulse discharge in dry air at pressures ranging from 30 Torr to 760 Torr, initially at room temperature. Since peak reduced electric field in these calculations varied from $(E/N)_{\text{peak}} \sim 600$ Td (at $p = 30$ Torr) to $(E/N)_{\text{peak}} \sim 200$ Td (at $p = 760$ Torr), vibrational excitation by electron impact was neglected. For $E/N > 200$ Td, discharge energy fraction loaded into the vibrational energy mode of nitrogen does not exceed 10%. Heat transfer from the gas heated in the discharge was also neglected. Using sensitivity analysis, a reduced kinetic model incorporating 15 species (N$_2$, O$_2$, O, O$_3$, NO, N, O(^{1}D), N$_2$(A$^3\Sigma$), N$_2$(B$^3\Pi$), N$_2$(a$'^1\Sigma$), N$_2$(C$^3\Pi$), e$^-$, N$_2^+$, O$^+$, O$_2^+$) and 42 processes was obtained from the full air plasma model including 46 species and 395 processes (see Tables 1-2). Since, at the high peak reduced-electric-fields involved here, the rate of electron impact ionization greatly exceeds the rate of electron attachment, processes involving negative ions do not affect the energy balance. During the sensitivity analysis, the main criterion used was the effect of individual processes on time-dependent energy fraction thermalized after the discharge pulse. The results of calculations for $p = 30$ Torr are summarized in Figs. 3-6, and for $p = 760$ Torr in Figs. 7-10.

From Fig. 3, it can be seen that at $p = 30$ Torr, peak reduced electric field and peak ionization fraction are approximately $(E/N)_{\text{peak}} = 580$ Td and $(ne/N)_{\text{peak}} = 8 \times 10^{-4}$ ($n_e = 7.7 \times 10^{14}$ cm^{-3}), respectively.

Figure 4 shows that energy fraction thermalized during the first 10 μs after the pulse is approximately 31%. Comparing Figs. 4 and 5 demonstrates that the energy thermalization on this time scale is primarily due to collisional quenching of $N_2(A^3\Sigma)$, $N_2(B^3\Pi)$, $N_2(a'^1\Sigma)$, $N_2(C^3\Pi)$, and $O(^1D)$, as well as electron-ion recombination. Further energy thermalization, on a much longer time scale of 10 μs to 100 ms, occurs primarily in reactions of nitrogen and oxygen atoms with oxygen molecules, $N + O_2 \rightarrow NO + O$ and $O + O_2 + M \rightarrow O_3 + M$, resulting in nitric oxide and ozone formation, as well as in reaction $O + O_3 \rightarrow O_2 + O_2$. Figure 4 also demonstrates the accuracy of the reduced kinetic model as compared to the full model.

The results obtained at $p = 760$ Torr are shown in Figs. 7-10. In this case, both peak reduced electric field and peak ionization fraction are lower, $(E/N)_{peak} = 200$ Td and $(ne/N)_{peak} = 2 \times 10^{-4}$ ($n_e = 4.9 \times 10^{15}$ cm^{-3}), respectively (see Fig. 7). From Fig. 8, it can be seen that energy fraction thermalized within 1 μs after the pulse is approximately 23%. Again, energy thermalization on this time scale is due to collisional quenching of $N_2(A^3\Sigma)$, $N_2(B^3\Pi)$, $N_2(a'^1\Sigma)$, $N_2(C^3\Pi)$, and $O(^1D)$ (compare Figs. 8 and 9), followed by an additional 25% of input energy thermalized on a long time scale, 1-300 μs after the pulse, in chemical reactions of nitric oxide and ozone formation. The reduced kinetic model obtained based on the modeling results at $p = 30$ Torr remains accurate (see Fig. 8).

The rest of the zero-dimensional modeling calculations were consistent with the low-pressure and the high-pressure cases shown in Figs. 3-10. For the entire pressure range tested, $p = 30 - 760$ Torr, the rapidly thermalized discharge energy fraction was in the range of 25-30%. The time scale for rapid energy thermalization, predicted by the model, varies from 2-3 μs at $p = 30$ Torr to 0.2-0.3 μs at $p = 760$ Torr (e.g., see Figs. 4 and 8). Thus, rapid heating after a discharge pulse coupling 100 meV/molecule to dry air would result in localized heating by 80-100 K.

Rate coefficients of electron impact processes incorporated into the reduced kinetic model, predicted by the Boltzmann equation solver and approximated as functions of the reduced electric field, are listed in Table 2. These rates, as well as rate coefficients of chemical reactions, excited electronic species quenching, and electron-ion recombination, have been used in the coupled electric discharge / compressible flow model to predict heating and compression wave formation in a nanosecond-pulse discharge in a geometry with planar symmetry.

III.   Discharge Computations

The 15-species reduced kinetic model was applied to transient, one-dimensional discharge computations. The following models were employed to predict particle motion: a drift-diffusion formulation for the charged particles, a diffusion equation for the neutrals, and a mass-averaged fluid formulation for the bulk gas. The Poisson equation was solved for the electric potential. A detailed description of the overall physical model is given below.

For computational efficiency, the calculations were carried out in two stages. The first stage encompassed the period in which an external waveform was applied to the electrodes. For this stage, the full physical model was employed. Shortly after the external potential was turned off, electromagnetic effects and charged particle motion became negligible. In this second stage of the problem, we set the electric field to zero, and imposed neutrality by setting the electron number density to an appropriate value.

A.   Governing Equations

A drift-diffusion formulation was used for the charged particles:

$$\frac{\partial n_s}{\partial t} + \nabla \cdot (n_s\mathbf{w} \pm n_s\mu_s\mathbf{E} - D_s\nabla n_s) = \omega_s \tag{1}$$

and a diffusion formulation was used for the neutrals:

$$\frac{\partial n_s}{\partial t} + \nabla \cdot (n_s\mathbf{w} - D_s\nabla n_s) = \omega_s \tag{2}$$

Here the electric field is $\mathbf{E} = -\nabla\phi$, where ϕ is the electric potential. The subscript s indicates the species number. For each species-s, the number density is n_s, the mobility is μ_s, the diffusion coefficient is D_s, and the rate of production in reactions is ω_s. The bulk fluid velocity is $\mathbf{w}$.

A mass-averaged fluid dynamic formulation was used to model the motion of the gas as a whole:

$$\frac{\partial \rho}{\partial t} + \nabla \cdot (\rho \mathbf{w}) = 0$$

$$\frac{\partial}{\partial t}(\rho \mathbf{w}) + \nabla \cdot (\rho \mathbf{w}\mathbf{w} + p\mathbf{I}) = \nabla \cdot \tau + \zeta \mathbf{E} \qquad (3)$$

$$\frac{\partial}{\partial t}[\rho(\epsilon + w^2/2)] + \nabla \cdot [\rho \mathbf{w}(\epsilon + w^2/2) + p\mathbf{w}] = \nabla \cdot (\tau \cdot \mathbf{w} - \mathbf{Q}) + \mathbf{E} \cdot \mathbf{j}$$

Here ρ is the mass density, p is the pressure, τ is the viscous stress tensor, ζ is the space charge, $\mathbf{j}$ is the total electric current, ϵ is the internal energy, $\mathbf{Q}$ is the heat flux. It useful to also define the dissipated power $P = \mathbf{E} \cdot \mathbf{J}$, where $\mathbf{J} = \mathbf{j} - \zeta \mathbf{w}$.

The relationship between the species properties and the overall properties are as follows:

$$\rho = \sum_s m_s n_s \qquad p = \sum_s p_s$$

$$\rho \epsilon = \sum_s m_s n_s \epsilon_s \quad \rho \mathbf{w} = \sum_s m_s n_s \mathbf{v}_s \qquad (4)$$

$$\zeta = \sum_s q_s n_s \qquad \mathbf{j} = \sum_s q_s n_s \mathbf{v}_s$$

where the mass per particle is m_s, the charge per particle is q_s, the partial pressure is $p_s = n_s k_B T$, and the species internal energy is $\epsilon_s = h_s^0 + C_{v,s}T$. Further, the laboratory-frame species velocity is $\mathbf{v}_s = \mathbf{w} \pm \mu_s \mathbf{E} - (D_s \nabla n_s)/n_s$.

The viscous stress and heat flux are as follows:

$$\tau = \mu_v \left[(\nabla \mathbf{w}) + (\nabla \mathbf{w})^T - \tfrac{2}{3}\nabla \cdot \mathbf{w}\mathbf{I} \right]$$

$$\mathbf{Q} = -k\nabla T + \sum_s \rho_s \mathbf{U}_s h_s \qquad (5)$$

where μ_v is the viscosity, k is thermal conductivity, $\mathbf{U}_s = \mathbf{v}_s - \mathbf{w}$ is the diffusion velocity, and $h_s = \epsilon_s + p_s/\rho_s$ is the species enthalpy.

Given the very high diffusion velocities in the cathode layer of a nanosecond-pulse discharge, careful consideration must be made of the validity of a formulation based on the mass-averaged global conservation laws. The mass averaged formulation assumes, for example, that the species internal energy is the same for the mass-averaged reference frame as for the species reference frame. In the Appendix, we show that the formulation used here is valid as long as the kinetic energy associated with diffusion is small compared to the mixture internal energy. For the present work, this ratio is at most $\frac{1}{2}n_s m_s U_s^2/(\rho \epsilon) \sim 10^{-3}$, so the model is well justified.

The Poisson equation is employed to compute the electric potential:

$$\nabla^2 \phi = -\zeta/\epsilon_0 \qquad (6)$$

where ϵ_0 is the permittivity of free space.

B. Gas Properties and Boundary Conditions

The 15-species, 42-process formulation described previously was employed, including neutrals, ions, electrons, and electronically-excited species (Tables 1-2). Data for mobility and diffusion coefficient for each species of heavy particle were take from the literature.[13, 41–43] Correlations of electron temperature and electron mobility with reduced electric field (Fig. 11) were developed from the Boltzmann equation solutions described in Sec. II. The viscosity and thermal conductivity of the bulk gas were based on standard correlations for air.[44]

A one-dimensional computational domain was employed to represent a single dielectric barrier discharge (Fig. 12). No-slip boundary conditions with a constant temperature wall were employed for the bulk gas. A zero wall-normal derivative was imposed for the neutral species.

Standard boundary conditions were employed for the charged particles. First, the conditions at the wall were determined by setting the normal derivative to zero. Then, if the provisional ion flow was away from

the boundary, the ion flux was set to zero. The electron number density was determined through a balance between the kinetic flux to the wall and secondary emission. For certain cases, these boundary conditions led to numerical instability at the exposed electrode boundary (anode). When this occurred, the simplified boundary conditions described in Ref. 45 were employed.

For the bare electrode the potential was specified as zero (grounded). An alternative boundary condition was employed for the powered electrode with a dielectric coating (see also Ref. 46). The dielectric layer was assumed to be sufficiently thin that a linear potential profile (uniform electric field $\mathbf{E}_d$) was a good approximation. The electric field inside the dielectric was related to the electric field $\mathbf{E}$ at the surface through the relation $\epsilon_0\mathbf{E} - \epsilon_r\epsilon_0\mathbf{E}_d = \sigma\mathbf{n}$, where σ is the surface charge density and $\mathbf{n}$ is the unit normal vector pointing into the computational domain. The surface charge was determined by integrating $\partial\sigma/\partial t = -\mathbf{j}\cdot\mathbf{n}$ for each surface point, using a time-marching scheme analogous to that of the main governing equations.

C.   Numerical Methods

The calculations were carried out using the Air Force Research Laboratory code HOPS (Higher Order Plasma Solver).[47–50] The code includes several physical models and numerical schemes. Here, the physical model consisting of Eqs. (1)-(3) and (6) was solved using an implicit, second-order, upwind formulation. All the equations were solved in a nondimensional form that has been described in previous papers.[47–50]

Time integration of the conservation equations (1)-(3) was carried out using a second-order implicit scheme, based on a three-point backward difference of the time terms. The formulation is similar to the standard technique of Beam and Warming,[51] but adapted to a multi-fluid formulation with different models for particle motion.

Approximate factoring and quasi-Newton subiterations were employed. The implicit terms were linearized in the standard 'thin layer' manner. The implicit terms were evaluated with second-order spatial accuracy, yielding a block tridiagonal system of equations for each factor. The species were loosely coupled, limiting the rank of the flux Jacobian matrices to the order of the moment model (one for the drift-diffusion formulation, five for the overall conservation equations). Each factor was solved in turn using a standard block tridiagonal solver, and the change in the solution vector of conserved variables was driven to zero by the subiteration procedure at each time step. Three applications of the flow solver per time-step were employed for the present work.

For the mass-averaged fluid model employed for the bulk gas, the Roe scheme[52,53] was employed for the inviscid fluxes. For the drift-diffusion model, a simple upwinding scheme was employed, based on the convection-drift velocity. This is similar to the approach of Surzhikov and Shang.[45] In both formulations, stability was enforced using the minmod limiter in the MUSCL formalism.[54]

The Poisson equation (6) was solved at the end of each sub-iteration in the implicit time-marching scheme. (Using this strategy with the subiteration procedure gives about the same improvement in stable time-step as methods based on the linearization of the right-hand-side of the Poisson equation.[55]) An approximately factored implicit scheme was employed, adapted from the approach described by Holst.[56] The formulation of the implicit scheme was analogous to that of the conservation equations, with linearization of the implicit terms, approximate factoring, and an iterative procedure that drives the change in the solution to zero. The spatial derivatives were evaluated using second-order central differences, and the system was solved using the Thomas tridiagonal algorithm.[57]

As mentioned earlier, the calculations were carried out in two phases. The first stage of the calculations encompassed the first 100 ns of the discharge, and employed the full physical model discussed above, Eqs. (1)-(3) and (6). Since electromagnetic effects and charged particle motion became negligible after the input pulse died away (after about 24 ns), in the second stage of the computations (0.1 μs to 100.1 μs), the electric field was set to zero and neutrality was enforced by appropriately setting the electron number density. This approach resulted in a substantial savings in computational cost.

For the calculations presented here, a uniform grid of 1001 points across the gap was employed. Grid resolution studies presented in a previous paper[28] indicate that this level of grid resolution is sufficient for this problem. The time step used for the Phase 1 calculations was 1 ps, and the time-step for Phase 2 was 5 ns.

D. Results

In the experiments illustrated in Figs. 1-2, typical freestream conditions for the neutral gas were a speed of 715 m/s, a pressure of 159.5 Pa, and a temperature of 56 K. Sample calculations are presented here for a one-dimensional discharge under conditions representative of the stagnation region of the cylinder flow experiment. The corresponding stagnation conditions, computed using the Rayleigh supersonic Pitot formula[58] were 4.74 kPa (36 Torr) and 310.3 K. For each case in the calculations discussed below, the initial, uniform state of the neutral gas was set to these stagnation values.

The configuration considered here is illustrated in Fig. 12. The problem is one-dimensional. In the simulations, the right electrode was grounded and the left electrode, which was coated with a thin dielectric layer, was powered with the input signal $V_s = -V_0 \exp\left[-(t-t_0)^2/\tau^2\right]$. For the present calculations, we assumed $V_0 = 20$ kV, $\tau = 3$ ns, and $t_0 = 12$ ns.

The discharge gap was taken to be 10 mm. The initial mole fraction of the electrons and each of the neutral minor species was taken to be 1×10^{-10}. The mole fraction for each ion species was equal, and set so that the space charge was zero. The initial electric field was zero. The dielectric coating was assumed to be 2 mm thick, with a relative dielectric constant of $\epsilon_r = 3.8$, chosen to be representative of fused quartz. The secondary emission coefficient was $\gamma_{\mathrm{sem}} = 0.05$.

A previous paper[13] presented an analytical model of nanosecond-pulse dielectric barrier discharges, in which an electron-free sheath region was coupled to a uniform, quasi-neutral plasma region. The model provided closed-form expressions for the discharge properties, and displayed good agreement with experiment. We employ this model here to provide a basic check of the correctness of our computer code, and to introduce the general features of the nanosecond-pulse discharge in one dimension. Figure 13 compares the discharge properties in the plasma predicted by this analytical model and by the one-dimensional computations. Note that $t_0 = 100$ ns for the analytical model, but $t_0 = 12$ ns for the numerical computations.

Figures 13a-b show the applied electric field (field in the absence of plasma), the computed field, and the ionization fraction. Some quantitative differences are present, but the general shape of the curves is in agreement. Because of the shielding effect of space charge in the cathode sheath and surface charge accumulation on the dielectric, the field in the plasma is less than the applied field. The one-dimensional computations predict a peak electric field at 9.4 ns, before the input pulse maximum at 12 ns, followed by a smaller peak of opposite sign at 14.5 ns. The peak electron mole fraction reaches about 2×10^{-6}.

Figures 13c-d show the reduced electric field E/N, the dissipated power $\mathbf{E}\cdot\mathbf{J}$, and the increase in gas energy density $\Delta(\rho\epsilon)$ (including chemical and thermal energy). Again, the results are qualitatively consistent between the two models, with moderate quantitative differences.

For the one-dimensional numerical computations, the peak reduced electric field is about 750 Td. Peak dissipated power (1.0×10^{11} W/m^3) occurs as the reduced electric field in the plasma is rapidly falling, but before the peak in the applied electric field. The analytical model predicts a total energy transferred to the gas of about 0.70 meV/molecule, whereas the numerical computations predict about one-third of this value (0.2 meV/molecule or 38 J/m^3). This difference is primarily due to the use of different expressions for the ionization rate coefficient as a function of reduced electric field in the analytical model and the present numerical computations. If the same expressions for ionization rate are used in the analytical model and the numerical simulations, the agreement for the predicted pulse energy coupled to the plasma improves considerably (see Ref. 13).

Recall that for the corresponding zero-dimensional computations discussed in Sec. II (Figs. 3-6), a discharge energy loading on the order of 100 meV/molecule was required to replicate the experimental results, with about 30 meV/molecule thermalized with 0.1 ms. In the present one-dimensional calculations, we obtained a discharge energy loading of about 0.2 meV/molecule in the plasma. The plasma electric field is comparable for the two the formulations (580 Td for zero-dimensional vs. 750 Td for one-dimensional), but the ionization fraction in the plasma is two orders of magnitude higher for the zero-dimensional calculations (8×10^{-4} vs. 2×10^{-6}).

The discrepancy between the predictions of the two models occurs because of plasma self-shielding in the one-dimensional calculations. This effect rapidly reduces the electric field in the plasma and limits the peak electron density. The results demonstrate that using zero-dimensional plasma kinetic modeling, with an imposed voltage waveform, is not appropriate even in a simple, symmetric configuration, since it greatly overestimates both peak electron density and energy coupled to the plasma.

Figure 14 shows discharge profiles at several stages in the computations. The species are grouped: the profiles of the total number densities of all ions (N$_2^+$, O$_2^+$, and O$^+$), electrons (e$^-$), excited neutrals

($N_2(A^3\Sigma)$, $N_2(B^3\Pi)$, $N_2(a'^1\Sigma)$, $N_2(C^3\Pi)$, and $O(^1D)$), and ground-state neutrals (O, O_3, NO, N) are shown. The concentrations of N_2 and O_2 remain almost constant, and are omitted. The onset of breakdown and appearance of the peak reduced electric field are illustrated in Figs. 14a-b (9-10 ns). The sheath forms rapidly at the left (covered) electrode, is about 1 mm thick, and carries most of the potential drop across the gap. Most of the production of new species occurs near the sheath edge and in the plasma. At later stages in the computation (Fig. 14c, 14 ns), the electric field reverses sign in the plasma (see also Ref. 21), with an accompanying local maximum in time of the field magnitude. At the end of first state of the calculations (Fig. 14d, 100 ns), quasi-neutrality prevails in the domain, and the electric field is negligible. Since diffusion has not had time to act, a number of local maxima are present in the species number density profiles. These appear to reflect the motions of the sheath edge.

Figure 15 shows the time-history in the plasma ($x = 8$ mm) of the mole fraction of each of the species except N_2 and O_2, which remain essentially constant. Results are shown for both the Phase 1 computations (0–0.1 μs, space charge included) and Phase 2 computations (0.1 μs–100.1 μs, zero electric field and neutrality imposed). The concentrations of charged and excited particles increase suddenly when the electric field becomes strong, and decrease gradually after the input waveform ends. The longest-lived species are O_2^+ and $N_2(A^3\Sigma)$. The radicals N and O appear at breakdown, whereas NO and O_3 increase gradually after the end of the input waveform.

We see from Fig. 15 that breakdown results in the rapid formation of new species, which gradually recombine over a longer time scale. Figure 16 addresses the accompanying energy redistribution. For a station in the quasi-neutral plasma ($x = 8$ mm), the distribution of chemical energy over different groups of species is shown in Fig. 16a, and the distribution between chemical and thermal energy is shown in Fig. 16b. Corresponding plots for a station near the sheath edge ($x = 1$ mm), are shown in Figs. 16c-d.

Through the dissipative power term $\mathbf{E} \cdot \mathbf{J}$, breakdown converts part of the input electric energy into chemical energy of new species over a time scale of about 1 ns, then recombination reactions convert the stored chemical energy to thermal energy over roughly a 10 μs time scale. Initially, most of the chemical energy is stored in charged particles and excited neutrals. With time, this energy thermalizes through electron-ion recombination and collisional quenching of electronically excited species. At the same time additional energy goes into neutral species in the ground electronic states (N, O, NO, and O_3), tending to reduce the efficiency of the device in rapidly converting electrical energy to heat.

In the plasma, most of the input energy is initially stored in chemical energy, whereas near the sheath edge this fraction is relatively small. In ongoing work, we are investigating how nonlocal effects and the uncertainty in reaction rates in this region of very high reduced electric field influence this result.

The oscillations in internal energy seen in Fig. 16c for times of 10-20 ns are related to the rapid motion of the sheath edge during that time interval. (See Fig. 14.)

Also shown in Figs. 16b and 16d is a comparison of the time-integral of the input power density $\int_0^t \mathbf{E} \cdot \mathbf{J} \, d\hat{t}$ to the change in total internal energy. For the plasma region, these are seen to agree almost exactly, indicating that the heating is essentially a zero-dimensional phenomenon: spatial gradient terms like convection and heat conduction act over much longer time scales. For the sheath region, however, fluid motion is seen to begin to carry away thermal energy within 100 ns.

The acoustic time scale mentioned previously is nicely illustrated in Figs. 16b and 16d: after several microseconds, acoustic waves form due to the rapid heating, creating the spikes apparent in the plots. Only energy that is released as heat on a time scale shorter than the acoustic time can contribute to the formation of these waves.

The acoustic waves are more apparent in Fig. 17, which shows the heating and gas motion induced by the discharge. The majority of the heating occurs near the edge of the cathode sheath, forming weak waves that travel across the domain. For example, consider the velocity profiles in Fig. 17b, and note the wave structure. Two waves, traveling in opposite directions, appear near $x = 1$ mm for the 0.1 μs profile (red curve). After 4.1 μs (green curve), the left-running wave has reflected off the left boundary and trails the other compression wave. Note also the growth in wave strength between these two times; the waves are driven by exothermic reactions in a manner analogous to a detonation.

For this case, the waves are relatively weak, with a peak gas velocity of about 3 m/s and peak temperature rise of about 11 K. The stationary background gas experiences less than a 1 K temperature rise over the time covered in the simulation. For an air temperature of 310.8 K, the speed of sound is about 353 m/s. Estimating the wave speed by measuring displacements in Fig. 17a, we find 355 m/s, which is very slightly supersonic.

Substantially supersonic wave speeds (up to 480 m/s) have been observed experimentally.[20] In ongoing work, we are attempting to replicate this stronger gasdynamic interaction by altering the simulation conditions to increase the coupled energy density.

IV. Summary and Conclusions

Numerical calculations were carried out to examine the physics of the operation of a nanosecond-pulse, single dielectric barrier discharge in a configuration with planar symmetry. This simplified configuration was chosen as a vehicle to develop a physics-based nanosecond discharge model, including realistic air plasma chemistry and compressible bulk gas flow. Discharge parameters (temperature, pressure, and input waveform) were selected to be representative of recent experiments on bow shock control with a nanosecond discharge in a Mach 5 cylinder flow.

First, a reduced plasma kinetic model (15 species and 42 processes) was developed by carrying out a sensitivity analysis of zero-dimensional plasma computations with an extended chemical kinetic model (46 species and 395 processes). Transient, one-dimensional discharge computations were then carried out using the reduced kinetic model, incorporating a drift-diffusion formulation for each species, a self-consistent computation of the electric potential using the Poisson equation, and a mass-averaged gas dynamic formulation for the bulk gas motion.

A grid converged solution and reasonable comparison to a validated analytical model indicate that the computations reflect an accurate solution of the mathematical model. The computational results qualitatively reproduce many of the features observed in experiments, including the rapid thermalization of the input electrical energy and the consequent formation of a weak shock wave. The results illustrate how input electrical energy is rapidly transformed (over roughly 1 ns) at breakdown into ionization products, dissociation products, and electronically excited particles, and how thermalization occurs over a relatively longer time-scale (roughly 10 μs).

The motivation for the present work is modeling nanosecond-pulse, dielectric barrier discharges for applications in high-speed flow control. The effectiveness of such devices as flow control actuators depends crucially on the rapid thermalization of the input electrical energy, and in particular on the rate of quenching of excited electronic states of nitrogen molecules and oxygen atoms and on the rate of electron-ion recombination.

Future work will include using the coupled nanosecond discharge / compressible flow model developed in the present work for simulation of surface nanosecond pulse discharges. The main difference of the present approach from other recent studies of nanosecond pulse discharges in air[24] is that the present model incorporates the kinetics of energy storage and thermalization.

In addition, various flow control applications will be explored. One option under consideration is replacing the cylinder model with a blunt oblique shock generator, and examining whether the nanosecond discharge can affect an impinging shock / boundary layer interaction. There is a strong motivation to control such interactions for supersonic engine inlet applications.[27]

Appendix: Mass-Averaged Conservation Equations

The present paper employs a mass-averaged formulation of the conservation laws for the gas as a whole, Eq. (3). Here we present a brief derivation of the mass-averaged formulation from the conservation laws for individual species, and discuss the range of applicability of the conventional mass-averaged formulation for our applications. (See also Ref. 59.)

A derivation of the conservation laws for the individual species, as moments of the Boltzmann equation, was presented in a previous paper,[49] and is also addressed elsewhere.[60–62] Briefly, the moment equations are obtained by multiplying the Boltzmann equation by a conserved quantity, and integrating over all velocity space. Considering a quantity $\phi(\mathbf{u})$ associated with each particle of species-s, an average value is defined as $\langle\phi\rangle_s(\mathbf{x}, t) = \int \phi(\mathbf{u}) f_s(\mathbf{x}, \mathbf{u}, t)\, d^3u$, where where $\mathbf{u}$ is the particle velocity, f_s is the distribution function, and the integral is over all velocity space. The resulting the mass, momentum, and energy conservation equations

for species-s are:

$$\frac{\partial \rho_s}{\partial t} + \nabla\cdot(\rho_s \mathbf{v}_s) = S_s$$

$$\frac{\partial}{\partial t}(\rho_s \mathbf{v}_s) + \nabla\cdot(\rho_s \mathbf{v}_s \mathbf{v}_s + p_s \mathbf{I}) = \nabla\cdot\tau_s + \rho_s \mathbf{g} + \zeta_s(\mathbf{E} + \mathbf{v}_s \times \mathbf{B}) + \mathbf{A}_s \tag{7}$$

$$\frac{\partial}{\partial t}\left[\rho_s\left(\epsilon_s + \tfrac{1}{2}v_s^2\right)\right] + \nabla\cdot\left[\rho_s \mathbf{v}_s\left(\epsilon_s + \tfrac{1}{2}v_s^2\right) + p_s \mathbf{v}_s\right] =$$
$$\nabla\cdot[\tau_s\cdot\mathbf{v}_s - \mathbf{Q}_s] + \rho_s \mathbf{v}_s\cdot\mathbf{g} + \zeta_s \mathbf{v}_s\cdot\mathbf{E} + M_s$$

where the mass density has been defined as $\rho_s = n_s m_s$ and the charge density as $\zeta_s = n_s q_s$. The mean velocity is defined as $\mathbf{v}_s = \langle\mathbf{u}\rangle_s$ and the peculiar velocity as $\mathbf{V}_s = \mathbf{u} - \mathbf{v}_s$. The source terms S_s, $\mathbf{A}_s$, and M_s represent the exchange between species of particle identity, momentum, and energy in collisions. Also defined are the:

$$\text{Kinetic pressure: } p_s = \tfrac{1}{3}n_s m_s\langle V_s^2\rangle_s$$
$$\text{Thermal energy: } \epsilon_s = \epsilon_{\text{int},s} + \tfrac{1}{2}\langle V_s^2\rangle_s$$
$$\text{Viscous stress: } \tau_s = -n_s m_s[\langle\mathbf{V}_s\mathbf{V}_s\rangle_s - \tfrac{1}{3}\langle V_s^2\rangle_s\mathbf{I}] \tag{8}$$
$$\text{Heat flux: } \mathbf{Q}_s = \mathbf{Q}_{\text{int},s} + \tfrac{1}{2}n_s m_s\langle\mathbf{V}_s V_s^2\rangle_s$$

The terms $\epsilon_{\text{int},s}$ and $\mathbf{Q}_{\text{int},s}$ represent internal molecular energy and the transfer of such energy by diffusion (e.g., see Ref. 62).

The conservation of mass, momentum, and total energy in collisions requires that the sum over all species of each of the corresponding collision source terms is zero: $\sum_s S_s = 0$, $\sum_s \mathbf{A}_s = 0$, $\sum_s M_s = 0$. These properties can be used to relate the species conservation laws (7) to the conservation laws for the gas as a whole.

The overall density is defined as $\rho = \sum_s \rho_s$. Consider the alternative peculiar velocity $\mathbf{W} = \mathbf{u} - \mathbf{w}$, where $\mathbf{w} = \sum_s \rho_s \mathbf{v}_s/\rho$ is the mass-weighted average velocity. The species diffusion velocity is defined as $\mathbf{U}_s = \langle\mathbf{W}\rangle_s = \mathbf{v}_s - \mathbf{w}$. (Note that $\mathbf{W} = \mathbf{U}_s + \mathbf{V}_s$.) In the mass-average reference frame, the moment terms, analogous to Eq. (8), are:

$$\tilde{p}_s = \tfrac{1}{3}\rho_s\langle W^2\rangle_s = p_s + \tfrac{1}{3}\rho_s U_s^2$$
$$\tilde{\epsilon}_s = \epsilon_{\text{int},s} + \tfrac{1}{2}\langle W^2\rangle_s = \epsilon_s + \tfrac{1}{2}U_s^2$$
$$\tilde{\tau}_s = -\rho_s[\langle\mathbf{W}\mathbf{W}\rangle_s - \tfrac{1}{3}\langle W^2\rangle_s\mathbf{I}] = \tau_s - \rho_s[\mathbf{U}_s\mathbf{U}_s - \tfrac{1}{3}U_s^2\mathbf{I}] \tag{9}$$
$$\tilde{\mathbf{Q}}_s = \mathbf{Q}_{\text{int},s} + \tfrac{1}{2}\rho_s\langle\mathbf{W} W^2\rangle_s$$
$$= \mathbf{Q}_s + [\rho_s(h_s + \tfrac{1}{2}U_s^2)\mathbf{I} - \tau_s]\cdot\mathbf{U}_s$$

where $h_s = \epsilon_s + p_s/\rho_s$ is the species enthalpy. Introducing (9) into (7), the following conservation equations are obtained:

$$\frac{\partial \rho_s}{\partial t} + \nabla\cdot(\rho_s \mathbf{w} + \rho_s \mathbf{U}_s) = S_s$$

$$\frac{\partial}{\partial t}(\rho_s \mathbf{w} + \rho_s \mathbf{U}_s) + \nabla\cdot(\rho_s \mathbf{w}\mathbf{w} + \mathbf{w}\rho_s \mathbf{U}_s + \rho_s \mathbf{U}_s \mathbf{w} + \tilde{p}_s \mathbf{I}) =$$
$$\nabla\cdot\tilde{\tau}_s + \rho_s \mathbf{g} + \zeta_s \mathbf{E} + (\zeta_s \mathbf{w} + \zeta_s \mathbf{U}_s) \times \mathbf{B} + \mathbf{A}_s \tag{10}$$

$$\frac{\partial}{\partial t}\left[\rho_s\left(\tilde{\epsilon}_s + \tfrac{1}{2}w^2\right) + \rho_s \mathbf{U}_s\cdot\mathbf{w}\right]$$
$$+\nabla\cdot\left[\rho_s \mathbf{w}\left(\tilde{\epsilon}_s + \tfrac{1}{2}w^2\right) + \rho_s \mathbf{U}_s\cdot\mathbf{w}\mathbf{w} + \rho_s \mathbf{U}_s\tfrac{1}{2}w^2 + \tilde{p}_s \mathbf{w}\right] =$$
$$\nabla\cdot\left[\tilde{\tau}_s\cdot\mathbf{w} - \tilde{\mathbf{Q}}_s\right] + (\rho_s \mathbf{w} + \rho_s \mathbf{U}_s)\cdot\mathbf{g} + \mathbf{E}\cdot(\zeta_s \mathbf{w} + \zeta_s \mathbf{U}_s) + M_s$$

Define the following overall properties:

$$\epsilon = \sum_s \rho_s\tilde{\epsilon}_s/\rho \quad \zeta = \sum_s \zeta_s \quad \mathbf{J} = \sum_s \zeta_s \mathbf{U}_s$$
$$p = \sum_s \tilde{p}_s \qquad \tau = \sum_s \tilde{\tau}_s \quad \mathbf{Q} = \sum_s \tilde{\mathbf{Q}}_s \tag{11}$$

The terms in (11) are, respectively, the net thermal energy, space charge, conduction current, pressure, viscous stress, and heat flux. The total electrical current is $\mathbf{j} = \zeta\mathbf{w} + \mathbf{J}$. Using these new definitions, and summing (10) over all species, the global conservation laws for mass, momentum, and total energy are obtained:

$$\frac{\partial \rho}{\partial t} + \nabla\cdot(\rho\mathbf{w}) = 0$$

$$\frac{\partial}{\partial t}(\rho\mathbf{w}) + \nabla\cdot(\rho\mathbf{w}\mathbf{w} + p\mathbf{I}) = \nabla\cdot\tau + \rho\mathbf{g} + \zeta\mathbf{E} + \mathbf{j}\times\mathbf{B} \tag{12}$$

$$\frac{\partial}{\partial t}\left[\rho(\epsilon + \tfrac{1}{2}w^2)\right] + \nabla\cdot\left[\rho\mathbf{w}(\epsilon + \tfrac{1}{2}w^2) + p\mathbf{w}\right] =$$
$$\nabla\cdot[\tau\cdot\mathbf{w} - \mathbf{Q}] + \rho\mathbf{w}\cdot\mathbf{g} + \mathbf{E}\cdot\mathbf{j}$$

where all the collision source terms have summed to zero. This is a slightly generalized form of Eq. (3).

Note the appearance in Eq. (9) of the diffusion velocity terms that arise from the change of reference frame from that of the species velocity to that of the mass-averaged velocity. If terms of order U_s^2 are neglected, all the quantities except the heat flux are the same in the mass-averaged reference frame as in the species reference frame. For the heat flux we have $\tilde{\mathbf{Q}}_s \approx \mathbf{Q}_s + \rho_s\mathbf{U}_s h_s$, so that the total heat flux becomes $\mathbf{Q} = \sum_s \mathbf{Q}_s + \sum_s \rho_s\mathbf{U}_s h_s$ in this approximation, which is the form used in Eq. (5).

The error introduced by this approximation in the summations of Eq. (11) is small if $\frac{1}{2}\rho_s U_s^2 \ll \rho\epsilon$, in other words for either small diffusion velocities or small mass fractions. This is a good approximation for a weakly-ionized gas, because the neutral particles have high number density but small diffusion velocities, whereas the charged particles have high diffusion velocities but low number densities.

A check of representative values of $\frac{1}{2}\rho_s U_s^2/(\rho\epsilon)$ at a time (10 ns) close the the peak in electric field magnitude in the present calculations illustrates this point. In the numerical solution, this parameter for both ions and electrons has value of about 1×10^{-6} in the plasma. Values for the electrons drop off in the sheath, but the values for the ions peak near the sheath edge, with a maximum of about 2×10^{-3} for N_2^+. Thus the mass-averaged formulation should be accurate for the present calculations, but a careful check is warranted if calculations are carried out for lower density discharges.

Acknowledgments

References

[1]Kantrowitz, A. R., "A Survey of Physical Phenomena Occurring in Flight at Extreme Speeds," *Proceedings of the Conference on High-Speed Aeronautics*, edited by A. Ferri, N. J. Hoff, and P. A. Libby, Polytechnic Institute of Brooklyn, New York, 1955, pp. 335–339.

[2]Resler, E. L. and Sears, W. R., "The Prospects for Magneto-Aerodynamics," *Journal of the Aeronautical Sciences*, Vol. 25, No. 4, 1958, pp. 235–245,258.

[3]Malik, M., Weinstein, L., and Hussaini, M. Y., "Ion Wind Drag Reduction," AIAA Paper 83-0231.

[4]Roth, J. R., Sherman, D. M., and Wilkinson, S. P., "Electrohydrodynamic Flow Control with a Glow-Discharge Surface Plasma," *AIAA Journal*, Vol. 38, No. 7, 2000, pp. 1166–1172.

[5]Palmer, G., "Magnetic Field Effects on the Computed Flow over a Mars Return Aerobrake," *Journal of Thermophysics and Heat Transfer*, Vol. 7, No. 2, 1993, pp. 294–301.

[6]Gurijanov, E. P. and Harsha, P. T., "AJAX: New Directions in Hypersonic Technology," AIAA Paper 96-4609.

[7]Adamovich, I. V., Subramaniam, V. V., Rich, J. W., and Macheret, S. O., "Phenomenological Analysis of Shock-Wave Propagation in Weakly Ionized Plasmas," *AIAA Journal*, Vol. 36, No. 5, 1998, pp. 816–822.

[8]Poggie, J., "Modeling the Propagation of a Shock Wave Through a Glow Discharge," *AIAA Journal*, Vol. 38, No. 8, 2000, pp. 1411–1418.

[9]Poggie, J. and Gaitonde, D. V., "Magnetic Control of Flow Past a Blunt Body: Numerical Validation and Exploration," *Physics of Fluids*, Vol. 14, No. 5, 2002, pp. 1720–1731.

[10]Gaitonde, D. V. and Poggie, J., "Implicit Technique for Three-Dimensional Turbulent Magnetoaerodynamics," *AIAA Journal*, Vol. 41, No. 11, 2003, pp. 2179–2191.

[11]Adamovich, I. V., Lempert, W. R., Nishihara, M., Rich, J. W., and Utkin, Y. G., "Repetitively Pulsed Nonequilibrium Plasmas for Magnetohydrodynamic Flow Control and Plasma-Assisted Combustion," *Journal of Propulsion and Power*, Vol. 24, No. 6, 2008, pp. 1198–1215.

[12]Poggie, J., "Numerical Simulation of Direct Current Glow Discharges for High-Speed Flow Control," *Journal of Propulsion and Power*, Vol. 24, No. 5, 2008, pp. 916–922.

[13]Adamovich, I. V., Nishihara, M., Choi, I., Uddi, M., and Lempert, W. R., "Energy Coupling to the Plasma in Repetative Nanosecond Pulse Discharges," *Physics of Plasmas*, Vol. 16, 2009, Art. 113505.

[14]Bisek, N., Boyd, I., and Poggie, J., "Numerical Study of Plasma-Assisted Aerodynamic Control for Hypersonic Vehicles," *Journal of Spacecraft and Rockets*, Vol. 46, No. 3, 2009, pp. 568–576.

[15]Bisek, N., Boyd, I., and Poggie, J., "Numerical Study of Magnetoaerodynamic Flow Around a Hemisphere," *Journal of Spacecraft and Rockets*, Vol. 47, No. 5, 2010, pp. 816–827.

[16]Poggie, J., Tilmann, C. P., Flick, P. M., Silkey, J. S., Osborne, B. A., Ervin, G., Maric, D., Mangalam, S., and Mangalam, A., "Closed-Loop Stall Control System," *Journal of Aircraft*, Vol. 47, No. 5, 2010, pp. 1747–1755.

[17]Nishihara, M., Takashima, K., Rich, J. W., and Adamovich, I. V., "Mach 5 Bow Shock Control by a Nanosecond Pulse Surface DBD," AIAA Paper 2011-1144.

[18]Romig, M. F., "The Influence of Electric and Magnetic Fields on Heat Transfer to Electrically Conducting Fluids," *Advances in Heat Transfer*, edited by T. F. Irvine and J. P. Hartnett, Vol. 1, Academic Press, New York, 1964, pp. 267–354.

[19]Samimy, M., Adamovich, I., Webb, B., Kastner, J., Hileman, J., Keshav, S., and Palm, P., "Development and Characterization of Plasma Actuators for High Speed Jet Control," *Experiments in Fluids*, Vol. 37, No. 4, 2004, pp. 577–588.

[20]Roupassov, D. V., Nikipelov, A. A., Nudnova, M. M., and Starikovskii, A. Y., "Flow Separation Control by Plasma Actuator with Nanosecond Pulsed-Periodic Discharge," *AIAA Journal*, Vol. 47, No. 1, 2009, pp. 168–185.

[21]Macheret, S. O., Shneider, M. N., and Miles, R. B., "Modeling of Air Plasma Generation by Repetitive High-Voltage Nanosecond Pulses," *IEEE Transactions on Plasma Science*, Vol. 30, No. 3, 2002, pp. 1301–1314.

[22]Pugh, E. R., Wallace, J., Jacob, J. H., Northam, D. B., and Daugherty, J. D., "Optical Quality of Pulsed Electron-Beam Sustained Lasers," *Applied Optics*, Vol. 13, No. 11, 1974, pp. 2512–2517.

[23]Aleksandrov, V. V., Koterov, V. N., Pustovalov, V. V., Soroka, A. M., and Suchkov, A. F., "Space-Time Evolution of the Cathode Layer in Electron-Beam-Controlled Lasers," *Soviet Journal of Quantum Electronics*, Vol. 8, No. 1, 1978, pp. 59–63.

[24]Unfer, T. and Boeuf, J. P., "Modelling of a Nanosecond Surface Discharge Actuator," *Journal of Physics D: Applied Physics*, Vol. 42, 2009, Art. 194017.

[25]Popov, N. A., "Investigation of the Mechanism for Rapid Heating of Nitrogen and Air in Gas Discharges," *Plasma Physics Reports*, Vol. 27, No. 10, 2001, pp. 886–896.

[26]Nishihara, M., Takashima, K., Rich, J. W., and Adamovich, I. V., "Mach 5 Bow Shock Control by a Nanosecond Pulse Surface Dielectric Barrier Discharge," *Physics of Fluids*, Vol. 23, 2011, Art. 066101.

[27]Lee, S., Goettke, M. K., Loth, E., Tinapple, J., and Benek, J., "Microramps Upstream of an Oblique-Shock / Boundary-Layer Interaction," *AIAA Journal*, Vol. 48, No. 1, 2010, pp. 104–118.

[28]Poggie, J., Bisek, N. J., Adamovich, I. V., and Nishihara, M., "High-Speed Flow Control with Electrical Discharges," AIAA Paper 2011-3104.

[29]Kirpichnikov, A. A. and Starikovskii, A. Y., "Nanosecond Pulse Discharge – Always Uniform?" *IEEE Transactions on Plasma Science*, Vol. 36, No. 4, 2008, pp. 898–899.

[30]Bisek, N., Poggie, J., Nishihara, M., and Adamovich, I., "Computational and Experimental Analysis of Mach 5 Air Flow over a Cylinder with Nanosecond Pulse Discharge," AIAA Paper, January 2012, submitted to the AIAA Aerospace Sciences Meeting.

[31]Uddi, M., Jiang, N., Adamovich, I. V., and Lempert, W. R., "Nitric Oxide Density Measurements in Air and Air/Fuel Nanosecond Pulse Discharges by Laser Induced Fluorescence," *Journal of Physics D: Applied Physics*, Vol. 42, 2009, Art. 075205.

[32]Kossyi, I. A., Kostinsky, A. Y., Matveyev, A. A., and Silakov, V. P., "Kinetic Scheme of the Nonequilibrium Discharge in Nitrogen-Oxygen Mixtures," *Plasma Sources Science and Technology*, Vol. 1, 1992, pp. 207–220.

[33]Huxley, L. G. H. and Crompton, R. W., *The Diffusion and Drift of Electrons in Gases*, Wiley, New York, 1974.

[34]Itikawa, Y., Hayashi, M., Ichimura, A., Onda, K., Sakimoto, K., Takayanagi, K., Nakamura, M., Nishimura, M., and Takayanagi, T., "Cross Sections for Collisions of Electrons and Photons with Nitrogen Molecules," *J. Phys. Chem. Ref. Data*, Vol. 16, 1986, pp. 985–1010.

[35]Itikawa, Y., Ichimura, A., Onda, K., Sakimoto, K., Takayanagi, K., Hatano, Y., Hayashi, M., Nishimura, H., and Tsurubichi, S., "Cross Sections for Collisions of Electrons and Photons with Oxygen Molecules," *J. Phys. Chem. Ref. Data*, Vol. 18, 1989, pp. 23–42.

[36]Popov, N. A., "Fast Gas Heating in a Nitrogen-Oxygen Discharge Plasma: I. Kinetic Mechanism," *Journal of Physics D: Applied Physics*, Vol. 44, 2011, Art. 285201.

[37]Mintoussov, E. I., Pendleton, S. J., Gerbault, F. G., Popov, N. A., and Starikovskaia, S. M., "Fast Gas Heating in Nitrogen-Oxygen Discharge Plasma: II. Energy Exchange in the Afterglow of a Volume Nanosecond Discharge at Moderate Pressures," *Journal of Physics D: Applied Physics*, Vol. 44, 2011, Art. 285202.

[38]Aleksandrov, N. L., Kindysheva, S. V., Nudnova, M. M., and Starikovskiy, A. Y., "Mechanism of Ultra-Fast Heating in a Non-Equilibrium Weakly Ionized Air Discharge Plasma in High Electric Fields," *Journal of Physics D: Applied Physics*, Vol. 43, 2010, Art. 255201.

[39]Takashima (Udagawa), K., Zuzeek, Y., Lempert, W. R., and Adamovich, I. V., "Characterization of Surface Dielectric Barrier Discharge Plasma Sustained by Repetitive Nanosecond Pulses," *Plasma Sources Science and Technology*, Vol. 20, 2011, Art. 055009.

[40]Little, J., Takashima, K., Nishihara, M., Adamovich, I., and Samimy, M., "Separation Control with Nanosecond Pulse Driven Dielectric Barrier Discharge Plasma Actuators," *AIAA Journal*, 2011, Accepted for publication.

[41]Viehland, L. A. and Mason, E. A., "Transport Properties of Gaseous Ions over a Wide Energy Range, IV," *Atomic Data and Nuclear Data Tables*, Vol. 60, 1995, pp. 37–95.

[42]Nelson, D., Benhenni, M., Eichwald, O., and Yousfi, M., "Ion Swarm Data for Electrical Discharge Modeling in Air and Flue Gas Mixtures," *Journal of Applied Physics*, Vol. 94, No. 1, 2003, pp. 96–103.

[43]Mahadevan, S. and Raja, L., "Simulations of Direct-Current Air Glow Discharges at Pressures 1 Torr: Discharge Model Validation," *Journal of Applied Physics*, Vol. 107, 2010, Art. 093304.

[44]White, F. M., *Viscous Fluid Flow*, McGraw-Hill, New York, 2nd ed., 1991.

[45]Surzhikov, S. T. and Shang, J. S., "Two-Component Plasma Model for Two-Dimensional Glow Discharge in Magnetic Field," *Journal of Computational Physics*, Vol. 199, 2004, pp. 437–464.

[46]Deconinck, T., Mahadevan, S., and Raja, L. L., "Simulation of Direct-Current Surface Plasma Discharge Phenomena in High-Speed Flow Actuation," *IEEE Transactions on Plasma Science*, Vol. 35, No. 5, 2007, pp. 1301–1311.

[47]Poggie, J., "High-Order Compact Difference Methods for Glow Discharge Modeling," AIAA Paper 2009-1047.

[48]Poggie, J., "Compact Difference Methods for Discharge Modeling in Aerodynamics," AIAA Paper 2009-3908.

[49]Poggie, J., "Role of Charged Particle Inertia in Pulsed Electrical Discharges," AIAA Paper 2010-1195.

[50]Poggie, J., "High-Order Numerical Methods for Electrical Discharge Modeling," AIAA Paper 2010-4632.

[51]Beam, R. and Warming, R., "An Implicit Factored Scheme for the Compressible Navier-Stokes Equations," *AIAA Journal*, Vol. 16, No. 4, 1978, pp. 393–402.

[52]Morrison, J., "Flux Difference Split Scheme for Turbulent Transport Equations," AIAA Paper 90-5251.

[53]Gaitonde, D. and Shang, J. S., "Accuracy of Flux-Split Algorithms in High-Speed Viscous Flows," *AIAA Journal*, Vol. 31, No. 7, 1993, pp. 1215–1221.

[54]Anderson, W. K., Thomas, J. L., and van Leer, B., "A Comparison of Finite Volume Flux Vector Splittings for the Euler Equations," AIAA Paper 85-0122.

[55]Ventzek, P. L. G., Hoekstra, R. J., and Kushner, M. J., "Two-Dimensional Modeling of High Plasma Density Inductively Coupled Sources for Materials Processing," *Journal of Vacuum Science and Technology B*, Vol. 12, No. 1, 1994, pp. 461–477.

[56]Holst, T. L., "Transonic Flow Computations Using Nonlinear Potential Methods," *Progress in Aerospace Sciences*, Vol. 36, 2000, pp. 1–61.

[57]Cheney, W. and Kincaid, D., *Numerical Mathematics and Computing*, Brooks/Cole Publishing, Pacific Grove, California, 3rd ed., 1994.

[58]Liepmann, H. W. and Roshko, A., *Elements of Gasdynamics*, J. Wiley, New York, 1957.

[59]Nachbar, W., Williams, F., and Penner, S. S., "The Conservation Equations for Independent Coexistent Continua and for Multicomponent Reacting Gas Mixtures," *Quarterly Journal of Applied Mathematics*, Vol. 17, No. 1, 1959, pp. 43–54.

[60]Chapman, S. and Cowling, T. G., *The Mathematical Theory of Non-Uniform Gases*, Cambridge University Press, 2nd ed., 1952.

[61]Seshadri, S. R., *Fundamentals of Plasma Physics*, Elsevier, New York, 1973.

[62]Olejniczak, J. and Candler, G. V., "Vibrational Energy Conservation with Vibration-Dissociation Coupling: General Theory and Numerical Studies," *Physics of Fluids*, Vol. 7, No. 7, 1995, pp. 1764–1774.

No.	Species	h^0 (eV/particle)
1	N_2	0
2	O_2	0
3	O	2.58
4	O_3	1.48
5	NO	0.93
6	N	4.90
7	$O(^1D)$	2.0
8	$N_2(A^3\Sigma)$	6.17
9	$N_2(B^3\Pi)$	7.35
10	$N_2(a'^1\Sigma)$	8.40
11	$N_2(C^3\Pi)$	11.0
12	e^-	0
13	N_2^+	16.36
14	O^+	16.26
15	O_2^+	12.70

Table 1. Species incorporated in kinetic model.

No.	Reaction	Rate Expression	Coefficients
1	$N_2 + e^- \rightarrow N_2^+ + e^- + e^-$	$\log_{10} k = A + B/(E/N)$	-7.76, -37.0 (-7.17, -61.1)
2	$O_2 + e^- \rightarrow O_2^+ + e^- + e^-$	$\log_{10} k = A + B/(E/N)$	-8.34, -30.7 (-7.42, -71.0)
3	$O_2 + e^- \rightarrow O + O^+ + e^- + e^-$	$\log_{10} k = A + B/(E/N)$	-7.94, -32.2 (-7.78, -35.2)
4	$N_2 + e^- \rightarrow N_2(A^3\Sigma) + e^-$	$\log_{10} k = A + B/(E/N)$	-8.57, -11.3 (-9.06, 15.3)
5	$N_2 + e^- \rightarrow N_2(B^3\Pi) + e^-$	$\log_{10} k = A + B/(E/N)$	-7.97, -13.2 (-8.14, -3.42)
6	$N_2 + e^- \rightarrow N_2(C^3\Pi) + e^-$	$\log_{10} k = A + B/(E/N)$	-7.82, -22.0 (-7.45, -37.0)
7	$N_2 + e^- \rightarrow N_2(a'^1\Sigma) + e^-$	$\log_{10} k = A + B/(E/N)$	-8.15, -15.8 (-8.12, -15.6)
8	$N_2 + e^- \rightarrow N + N + e^-$	$\log_{10} k = A + B/(E/N)$	-7.96, -22.7 (-7.34, -50.2)
9	$O_2 + e^- \rightarrow O + O + e^-$	$\log_{10} k = A + B/(E/N)$	-8.31, -8.40 (-8.63, 7.10)
10	$O_2 + e^- \rightarrow O + O(^1D) + e^-$	$\log_{10} k = A + B/(E/N)$	-7.86, -17.2 (-7.42, -37.1)
11	$N + O_2 \rightarrow NO + O$	$k = AT^n \exp(-E_a/T)$	0.110E-13, 1.00, 3150.
12	$N + NO \rightarrow N_2 + O$	$k = AT^n$	0.105E-11, 0.50
13	$O + O_3 \rightarrow O_2 + O_2$	$k = A \exp(-E_a/T)$	0.200E-10, 2300.
14	$O + O + N_2 \rightarrow O_2 + N_2$	$k = A \exp(-E_a/T)$	0.276E-33, -720.
15	$O + O + O_2 \rightarrow O_2 + O_2$	$k = AT^n$	0.245E-30, -0.63
16	$O + O_2 + N_2 \rightarrow O_3 + N_2$	$k = AT^n$	0.558E-28, -2.00
17	$O + O_2 + O_2 \rightarrow O_3 + O_2$	$k = AT^n$	0.861E-30, -1.25
18	$N_2(A^3\Sigma) + O_2 \rightarrow N_2 + O + O$	$k = 0.170E-11$	
19	$N_2(A^3\Sigma) + O_2 \rightarrow N_2 + O_2$	$k = 0.750E-12$	
20	$N_2(A^3\Sigma) + O \rightarrow N_2 + O(^1D)$	$k = 0.300E-10$	
21	$N_2(A^3\Sigma) + N_2(A^3\Sigma) \rightarrow N_2 + N_2(B^3\Pi)$	$k = 0.770E-10$	
22	$N_2(A^3\Sigma) + N_2(A^3\Sigma) \rightarrow N_2 + N_2(C^3\Pi)$	$k = 0.160E-09$	
23	$N_2(B^3\Pi) + N_2 \rightarrow N_2(A^3\Sigma) + N_2$	$k = 0.300E-10$	
24	$N_2(B^3\Pi) \rightarrow N_2(A^3\Sigma)$	$k = 0.150E+06$	
25	$N_2(B^3\Pi) + O_2 \rightarrow N_2 + O + O$	$k = 0.300E-09$	
26	$N_2(a'^1\Sigma) + N_2 \rightarrow N_2 + N_2$	$k = 0.200E-12$	
27	$N_2(a'^1\Sigma) + O_2 \rightarrow N_2 + O + O(^1D)$	$k = 0.281E-10$	
28	$N_2(C^3\Pi) + N_2 \rightarrow N_2(B^3\Pi) + N_2$	$k = 0.100E-10$	
29	$N_2(C^3\Pi) \rightarrow N_2(B^3\Pi)$	$k = 0.300E+08$	
30	$N_2(C^3\Pi) + O_2 \rightarrow N_2(A^3\Sigma) + O + O$	$k = 0.301E-09$	
31	$O(^1D) + N_2 \rightarrow O + N_2$	$k = 0.257E-10$	
32	$O(^1D) + O_2 \rightarrow O + O_2$	$k = 0.400E-10$	
33	$O^+ + O_2 \rightarrow O_2^+ + O$	$k = 0.199E-10$	
34	$N_2^+ + O_2 \rightarrow N_2 + O_2^+$	$k = 0.600E-10$	
35	$N_2^+ + e^- \rightarrow N + N$	$k = AT_e^n$	0.831E-05, -0.50
36	$O_2^+ + e^- \rightarrow O + O$	$k = AT_e^n$	0.599E-04, -1.00
37	$N_2^+ + e^- + e^- \rightarrow N_2 + e^-$	$k = AT_e^n$	0.140E-07, -4.50
38	$O_2^+ + e^- + e^- \rightarrow O_2 + e^-$	$k = AT_e^n$	0.140E-07, -4.50
39	$O^+ + e^- + e^- \rightarrow O + e^-$	$k = AT_e^n$	0.140E-07, -4.50
40	$N_2^+ + e^- + M \rightarrow N_2 + M$	$k = AT_e^n$	0.312E-22, -1.50
41	$O_2^+ + e^- + M \rightarrow O_2 + M$	$k = AT_e^n$	0.312E-22, -1.50
42	$O^+ + e^- + M \rightarrow O + M$	$k = AT_e^n$	0.312E-22, -1.50

Table 2. Reaction mechanism. Units consistent with number densities in cm^{-3}, and temperatures in K, reduced electric field in 1×10^{-16} V cm^2 (10 Td), one-body rates in s^{-1}, two-body rates in cm^3/s, and three-body rates in cm^6/s. Values in parentheses are alternative curve fits for $E/N > 50 \times 10^{-16}$ V cm^2 ($E/N > 500$ Td).
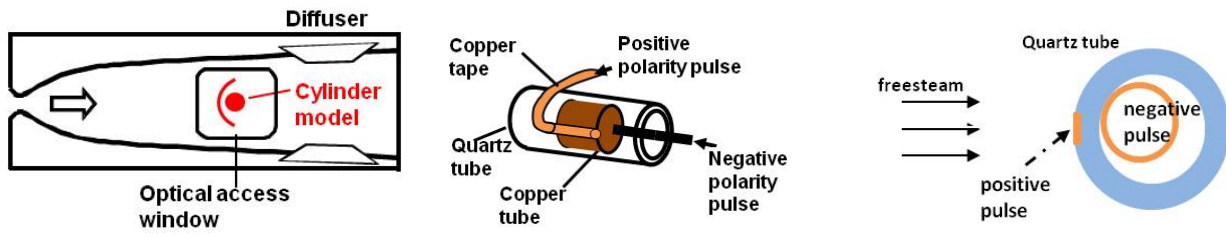
(a) Diagram of cylinder mounted in wind tunnel.

(b) Perspective view of cylinder model.

(c) Side view of cylinder model.

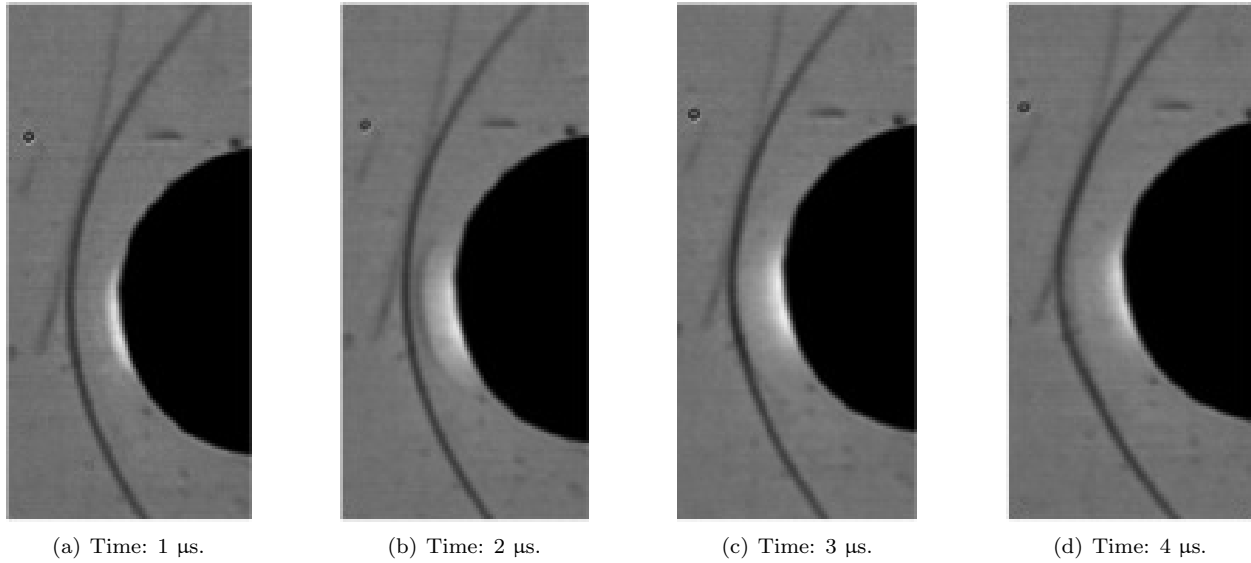**Figure 1. Configuration of Mach 5 cylinder flow experiment.**

(a) Time: 1 µs.

(b) Time: 2 µs.

(c) Time: 3 µs.

(d) Time: 4 µs.

Figure 2. Side-view schlieren images of Mach 5 cylinder flow perturbed by pulsed discharge.
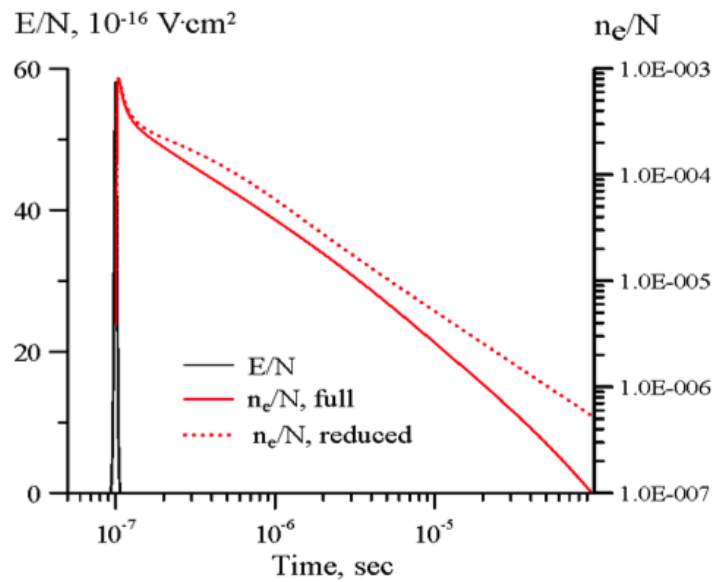
Figure 3. Reduced electric field during the pulse; ionization fraction predicted by the full and reduced air plasma models. Conditions: $p = 30$ **Torr,** $T_0 = 300$ **K, discharge energy loading 100 meV/molecule.**
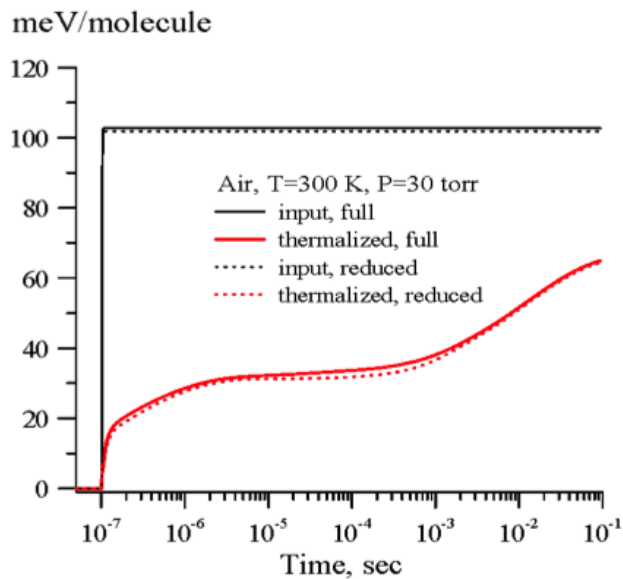
Figure 4. Input pulse energy and energy thermalized after the pulse predicted by the full and reduced air plasma models at the conditions of Fig. 3 ($p = 30$ **Torr,** $T_0 = 300$ **K, 100 meV/molecule).**

(a) Full kinetic model.

(b) Reduced kinetic model.
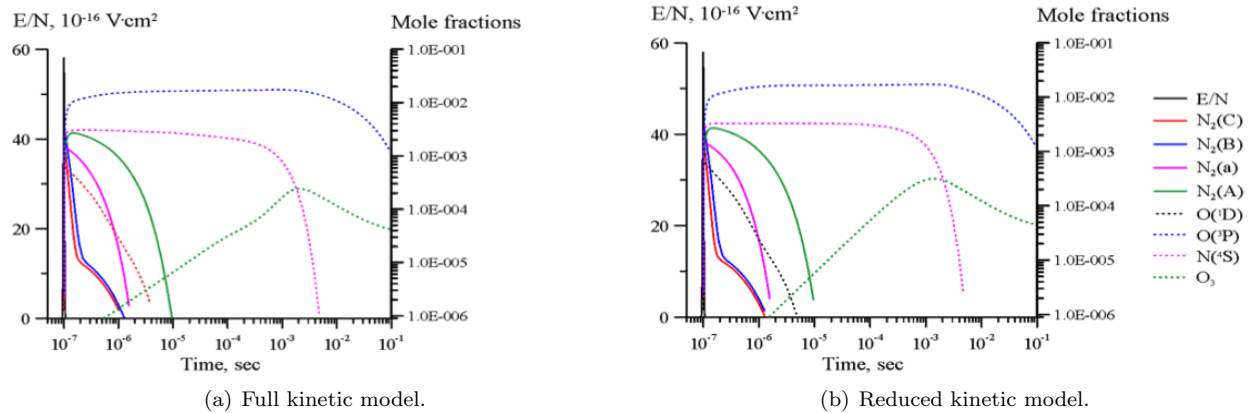
Figure 5. Mole fractions of dominant neutral species at the conditions of Fig. 3 ($p = 30$ Torr, $T_0 = 300$ K, 100 meV/molecule).

(a) Full kinetic model.

(b) Reduced kinetic model.
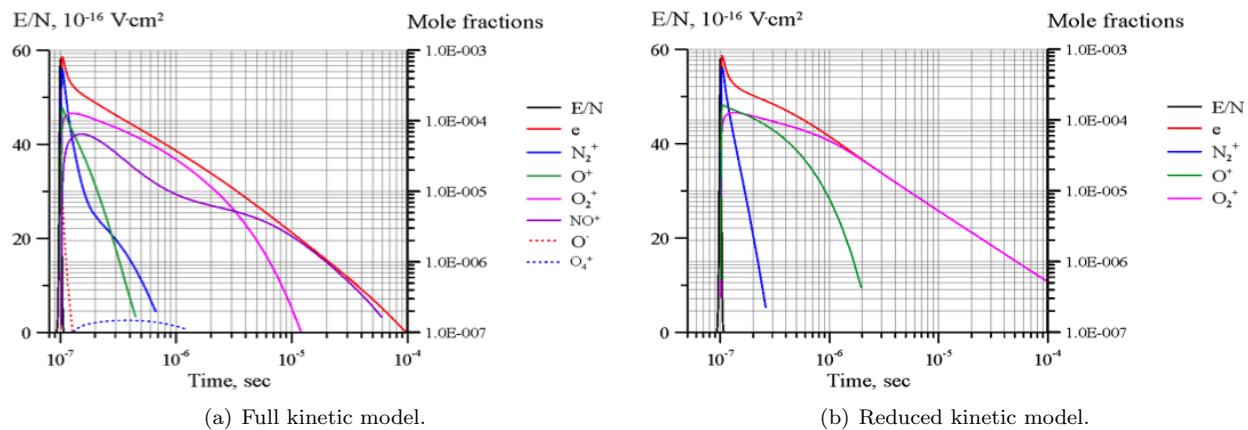
Figure 6. Mole fractions of dominant charged species at the conditions of Fig. 3 ($p = 30$ Torr, $T_0 = 300$ K, 100 meV/molecule).
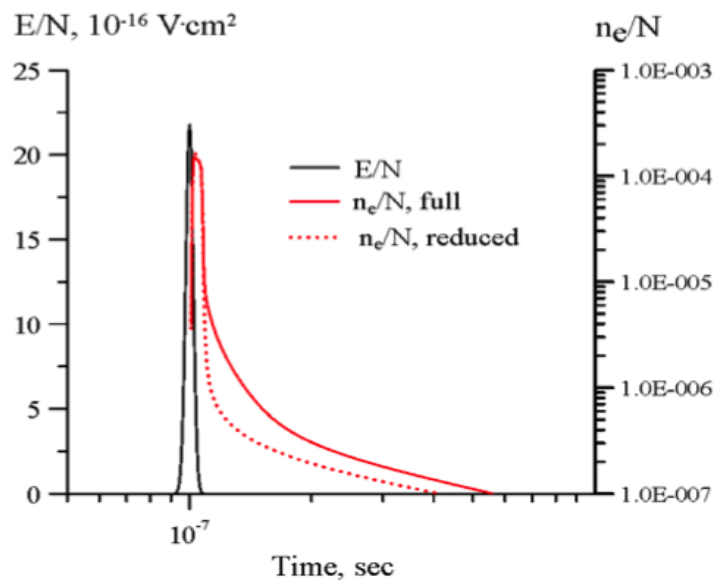
Figure 7. Reduced electric field during the pulse; ionization fraction predicted by the full and reduced air plasma models. Conditions: $p = 760$ **Torr,** $T_0 = 300$ **K, discharge energy loading 130 meV/molecule.**
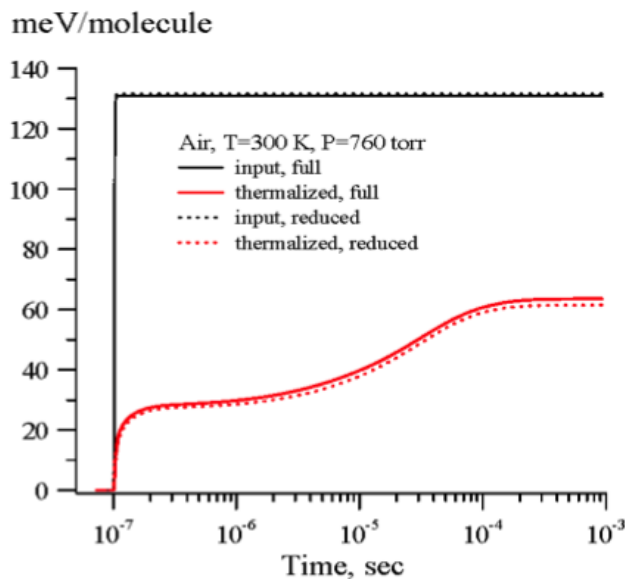
Figure 8. Input pulse energy and energy thermalized after the pulse predicted by the full and reduced air plasma models at the conditions of Fig. 7 ($p = 760$ **Torr,** $T_0 = 300$ **K, 130 meV/molecule).**

(a) Full kinetic model.   (b) Reduced kinetic model.
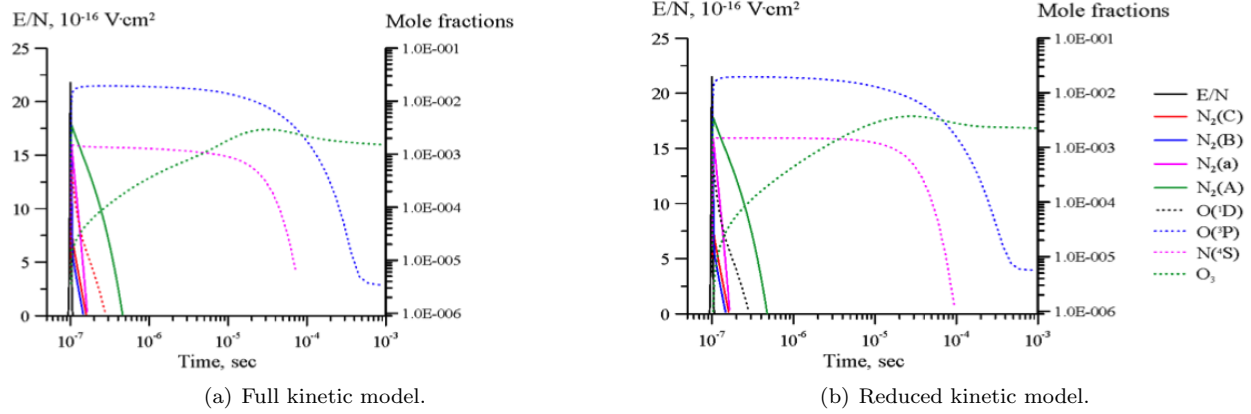
Figure 9. **Mole fractions of dominant neutral species at the conditions of Fig. 7** ($p = 760$ **Torr,** $T_0 = 300$ **K,** **130 meV/molecule**)**.**

(a) Full kinetic model.   (b) Reduced kinetic model.
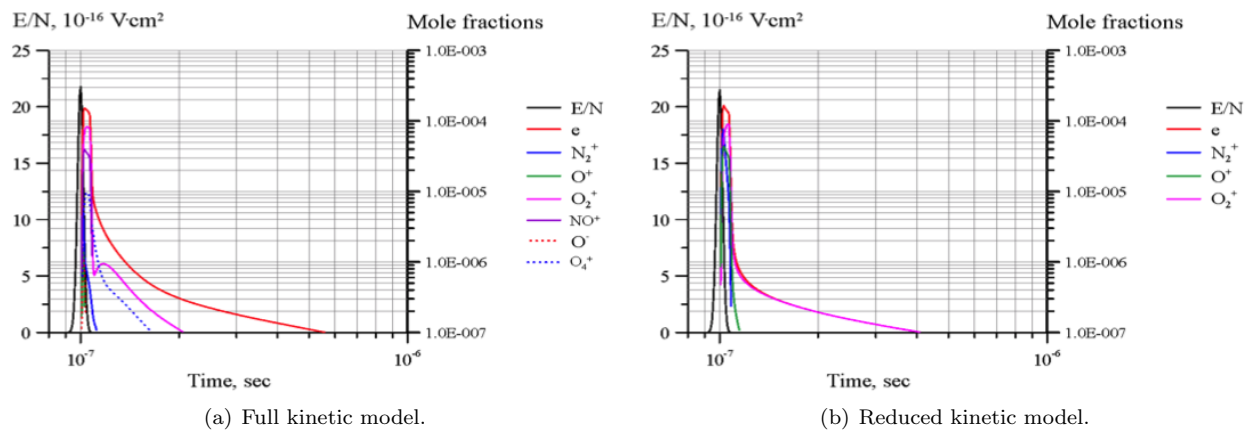
Figure 10. **Mole fractions of dominant charged species at the conditions of Fig. 7** ($p = 760$ **Torr,** $T_0 = 300$ **K,** **130 meV/molecule**)**.**

(a) Electron temperature.

(b) Electron mobility at atmospheric pressure ($N = 2.4 \times 10^{19}$ cm^{-3}).
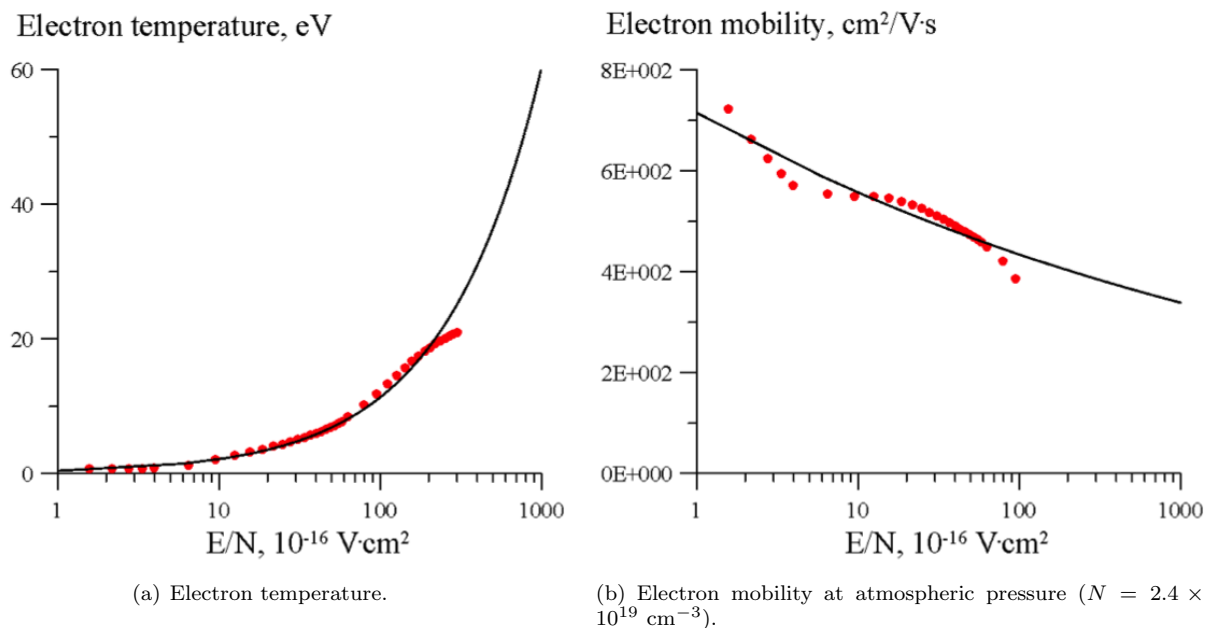
Figure 11.   Electron properties as a function of reduced electric field.   Lines: curve fits; points: data from Boltzmann equation solutions.
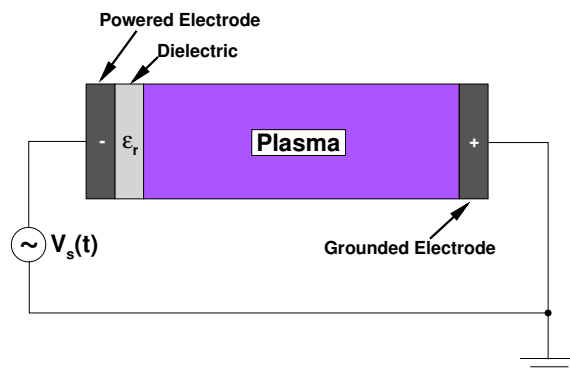
Figure 12.   Diagram of computational domain.
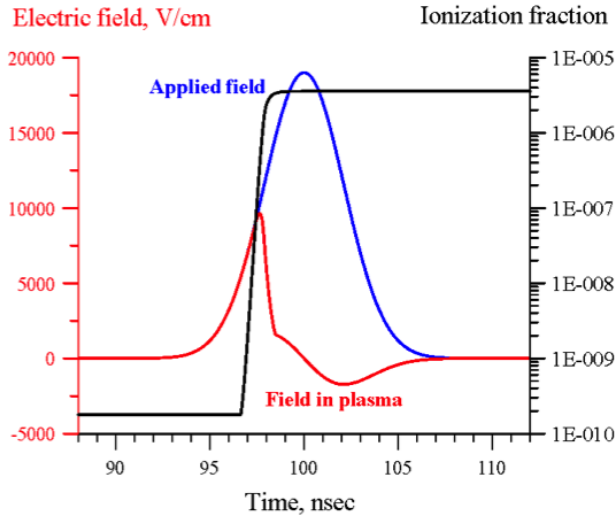
(a) Electric field and ionization fraction, analytical model.
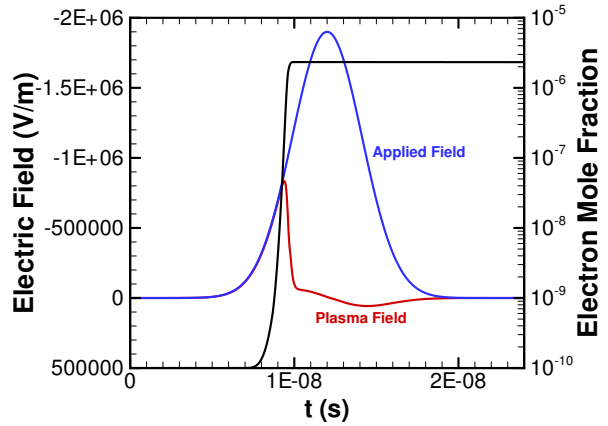
(b) Electric field and ionization fraction, 1-D computations ($x = 8$ mm).
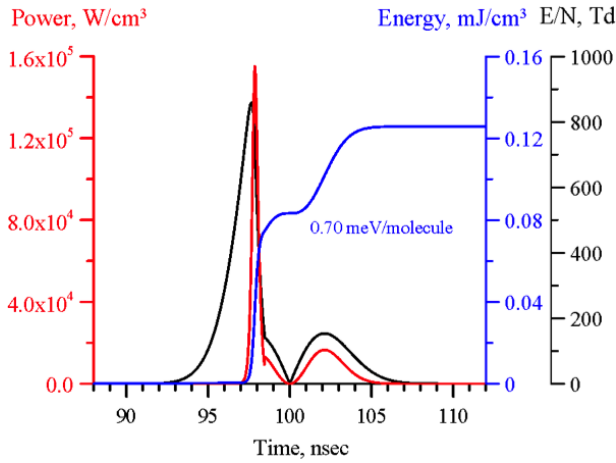
(c) Reduced electric field, power, and thermalized energy, analytical model.
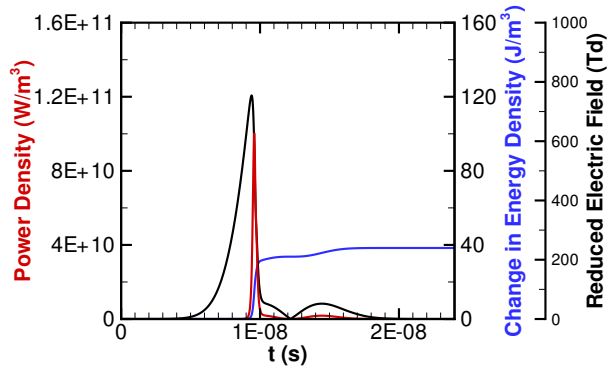
(d) Reduced electric field E/N, dissipated power $\mathbf{E} \cdot \mathbf{J}$, and change in internal energy $\Delta(\rho\epsilon)$, 1-D computations ($x = 8$ mm).

Figure 13. Comparison of analytical model[13] to one-dimensional computations for a station in the quasi-neutral plasma.
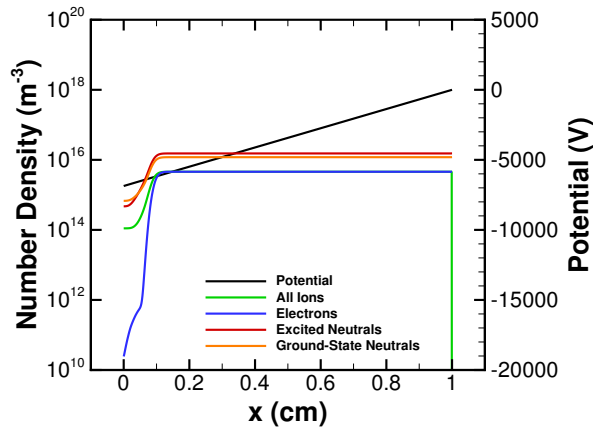
(a) Time: 9 ns.
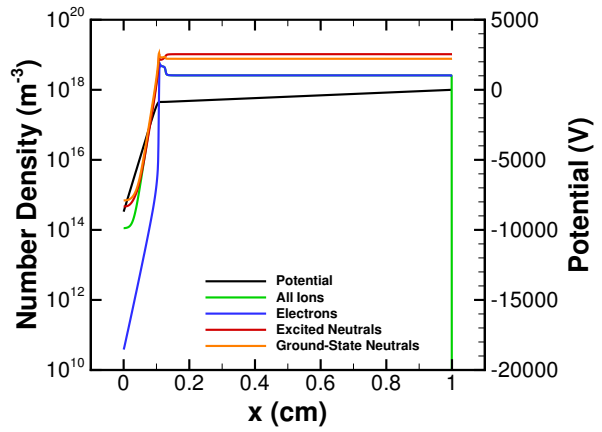
(b) Time: 10 ns.
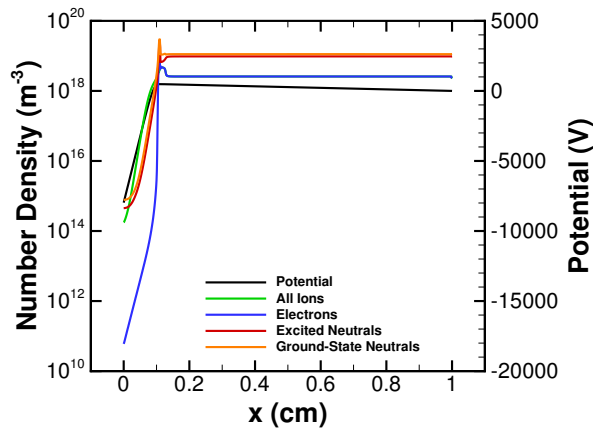
(c) Time: 14 ns.
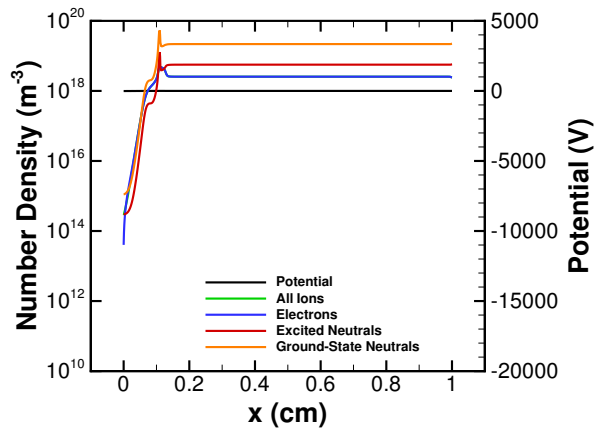
(d) Time: 100 ns.

Figure 14. Discharge profiles predicted by the numerical computations. Ions: N_2^+ , O_2^+, and O^+; electrons: e^-; excited neutrals: $N_2(A^3\Sigma)$, $N_2(B^3\Pi)$, $N_2(a'^1\Sigma)$, $N_2(C^3\Pi)$, and $O(^1D)$; ground-state neutrals: O, O_3, NO, N.
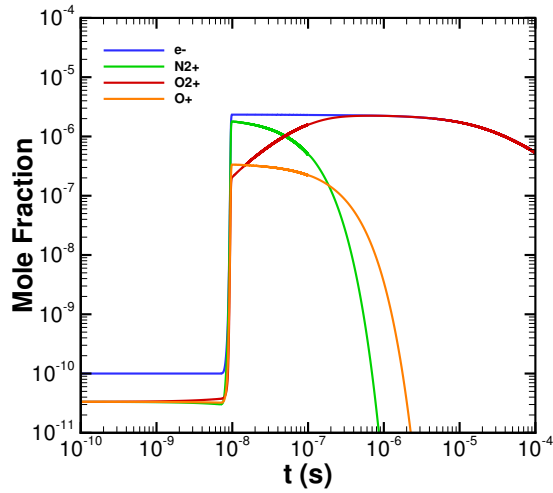
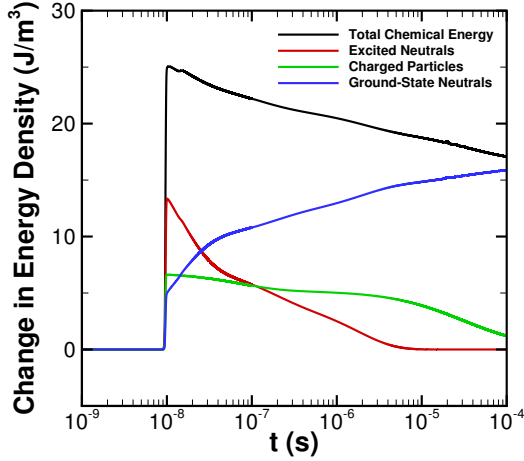(a) Charged particles: N_2^+, O_2^+, O^+, and e^-.
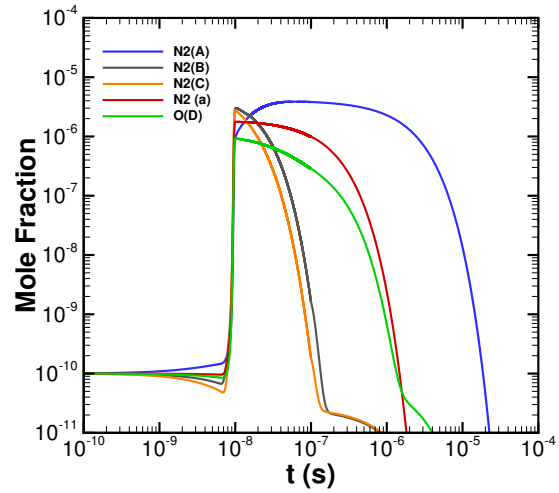
(b) Electronically excited neutrals: $N_2(A^3\Sigma)$, $N_2(B^3\Pi)$, $N_2(a'^1\Sigma)$, $N_2(C^3\Pi)$, and $O(^1D)$.
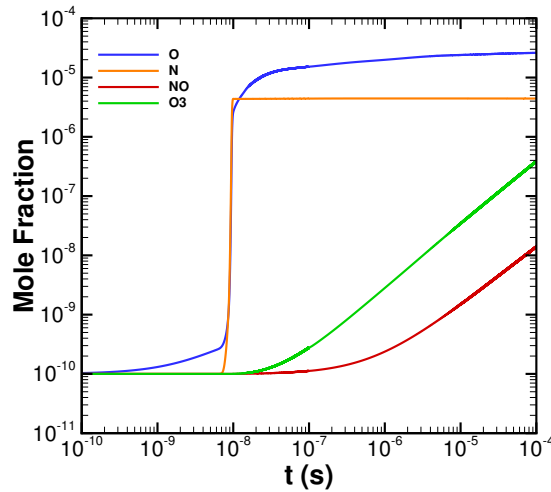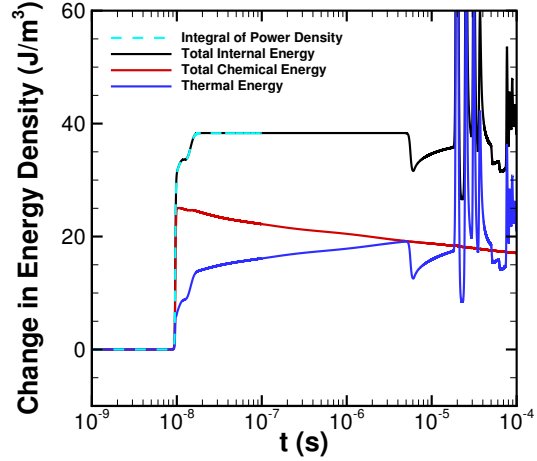

(c) Ground-state neutrals: O, O_3, NO, N.

Figure 15. Time history of species mole fraction in the plasma ($x = 8$ mm). The calculations switch from the full model to the neutral, zero-field model at 1×10^{-7}s.
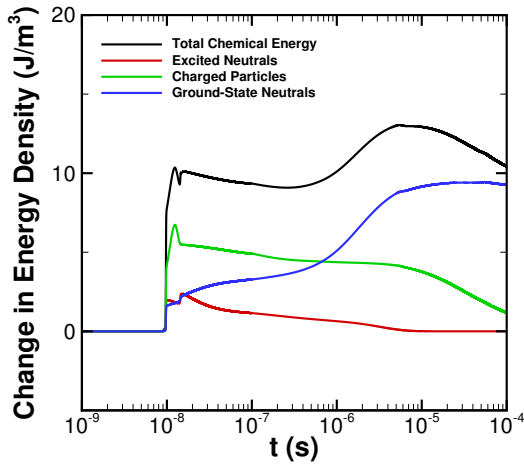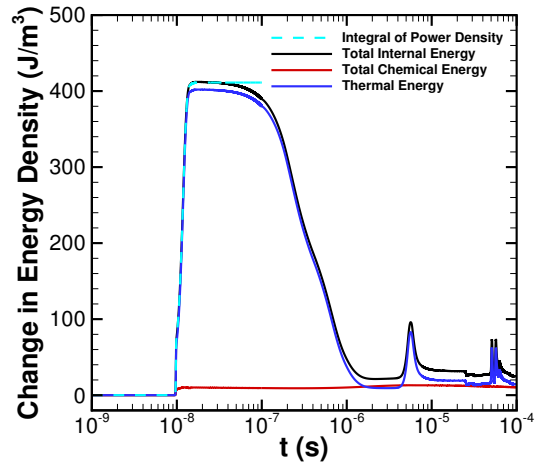
(a) Distribution of chemical energy density over different groups of species. (Plasma, $x = 8$ mm.)

(b) Distribution of energy between chemical and thermal modes. (Plasma, $x = 8$ mm.) Spikes in thermal energy correspond to acoustic wave motion.

(c) Distribution of chemical energy density over different groups of species. (Sheath, $x = 1$ mm.)

(d) Distribution of energy between chemical and thermal modes. (Sheath, $x = 1$ mm.) Spikes in thermal energy correspond to acoustic wave motion.

Figure 16. Distribution of energy in the plasma and in the sheath. Charged particles: N_2^+, O_2^+, O^+, and e^-; excited neutrals: $N_2(A^3\Sigma)$, $N_2(B^3\Pi)$, $N_2(a'^1\Sigma)$, $N_2(C^3\Pi)$, and $O(^1D)$; ground-state neutrals: O, O_3, NO, N; change in energy density $\Delta(\rho\epsilon)$, integrated power $\int_0^t \mathbf{E}\cdot\mathbf{J}\,d\hat{t}$. The calculations switch from the full model to the neutral, zero-field model model at 1×10^{-7}s.
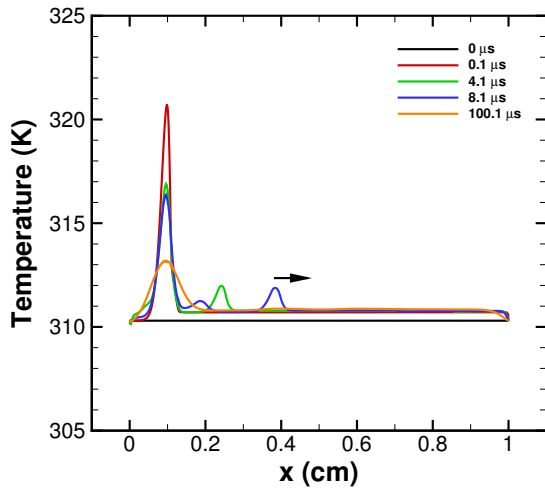
(a) Temperature.
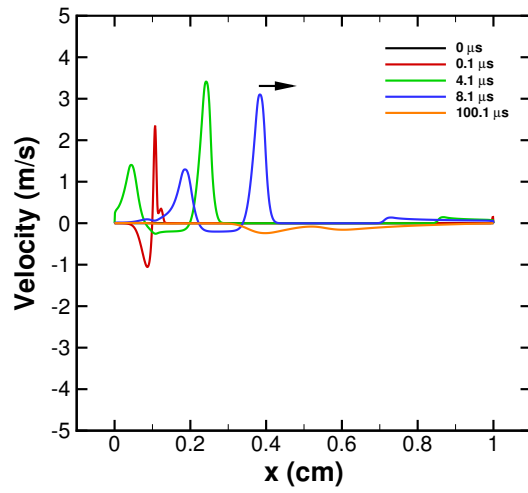
(b) Velocity.

Figure 17. Profiles of the properties of the bulk gas for selected times in the simulation. Arrows indicate the direction of wave motion.

Appendix D

Fluid Dynamics and Three-Dimensionality in Pulsed Discharge Experiments

50th AIAA Aerospace Sciences Meeting including the New Horizons Forum and Aerospace Exposition
09 - 12 January 2012, Nashville, Tennessee

AIAA 2012-0186

Computational and Experimental Analysis of Mach 5 Air Flow over a Cylinder with a Nanosecond Pulse Discharge

Nicholas J. Bisek,[*] Jonathan Poggie[†]

Air Force Research Laboratory, Wright-Patterson AFB, OH, 45433-7512, USA

and

Munetake Nishihara [‡] Igor Adamovich,[§]

The Ohio State University, Columbus, OH 43210, USA

A computational study is performed for Mach 5 air flow over a cylinder with a dielectric barrier discharge actuator set into the cylinder surface. The actuator is pulsed at nanosecond time scales, which rapidly adds energy to the flow, thereby creating a shock wave that travels away from the pulse source. As the shock wave travels upstream, it interacts with the standing bow-shock and momentarily increases the bow-shock standoff distance. This phenomenon is also observed in phase-locked schlieren photography captured during the experiment. The focus of this paper is to reproduce flow phenomena observed in the experiment using high-fidelity computations in order to provide additional insight into the shock-shock interaction, the effect the dielectric barrier discharge pulse has on the surface properties of the cylinder, and develop a reduced-order phenomenological model representative of the nanosecond pulse discharge system. Experimental and high-fidelity modeling studies of the nanosecond pulse dielectric barrier discharge plasma actuators are known to operate with relatively low temperatures. This work explores the possibility that the induced compression wave is generated by rapid thermalization of the discharge which results in a local temperature rise occurring on longer time scales. Two-dimensional simulations are performed and provide many useful details about the discharge event while comparing with many measurements captured by the experiment. However, the simulations indicate the experiment experiences significant three-dimensional effects, thus requiring a three-dimensional simulation of the entire experiment to accurately capture the complex cylinder/tunnel-sidewall interaction and replicate the resultant flow. Three-dimensional results of the discharge event reveal the discharge pulse produces a compression wave that interacts with the standing bow-shock and that the momentary increase in the bow-shock standoff distance is not due to the interaction the three-dimensional compression wave has with the cylinder/tunnel-sidewall boundary layer.

Nomenclature

a, b, c	= equatorial radii of an ellipsoid, [m]
c_p	= coefficient of pressure, $\frac{p-p_\infty}{1/2\,\rho_\infty\,u^2}$
c_h	= nondimensional heating coefficient, $\frac{q_w}{1/2\,\rho_\infty\,u^3}$
M	= Mach number
p	= pressure, [Pa]
R	= gas constant, [J/kg-K]
q	= heat flux, [W/m²]

---

[*]Research Aerospace Engineer, High-Speed Flow Research Group, Computational Aerophysics Branch. Member AIAA.
[†]Team Lead, High-Speed Flow Research Group, Computational Aerophysics Branch. Associate Fellow AIAA.
[‡]Postdoctoral Researcher, Nonequilibrium Thermodynamics Laboratories, Dept. of Mechanical Engineering, Member AIAA.
[§]Professor, Nonequilibrium Thermodynamics Laboratories, Dept. of Mechanical Engineering, Associate Fellow AIAA.

Q	= total energy input by actuator, [W]
T	= temperature, [K]
u, v, w	= streamwise, transverse, and spanwise velocity components, [m/s]
U	= velocity magnitude, [m/s]
x, y, z	= streamwise, transverse, and spanwise coordinates
α	= accommodation coefficient for partial slip wall boundary conditions
γ	= specific heat ratio, (1.4 for air)
ε	= emissivity
θ	= angle along cylinder surface, $\tan^{-1}\left(\frac{y - y_{cy}}{x - x_{cy}}\right)$
λ	= mean free-path, $\frac{\mu}{\rho}\sqrt{\frac{\pi}{2R\,T}}$, [m]
μ	= kinetic viscosity, [kg/m-s]
ρ	= density, [kg/m^3]
σ_0	= Stefan-Boltzmann constant, $5.6704 \cdot 10^{-8}$ J/m^2-s-K^4
τ	= duration of the energy deposition pulse, [s]

Subscript

c	= center of ellipsoid
cy	= center of the cylinder
g	= gas
ve	= vibrational-electron-electronic
w	= wall
0	= stagnation
∞	= freestream

I. Introduction

A recent experimental study of a nanosecond pulse Dielectric Barrier Discharge (DBD) in a Mach 5 flow demonstrated the feasibility of plasma-based supersonic flow control.[1] A bow-shock perturbation on a microsecond time scale was detected in phase-locked schlieren visualization. Compression wave generation due to a rapid localized heating from the DBD propagates upstream from the cylinder surface and interacts with the standing bow-shock. This interaction temporarily increases the shock standoff distance. This series of events can be repeated at time spacing up to 10 µs (100 kHz). Previous demonstration of the nanosecond pulse DBD includes separated flow reattachment[2] up to Mach = 0.85, characterization of compression wave propagation in a quiescent air,[3] and visualization of large-scale, spanwise vortex over the airfoil[4] at M = 0.3.

The flow control mechanism (rapid heating) in these experiments[2,4] appears consistent with a Localized Arc Filament Plasma Actuator (LAFPA).[5–7] The main idea of this approach is forcing the flow with a high amplitude, high bandwidth perturbation, at a frequency approaching one of the flow instability frequencies, thereby triggering subsequent growth. Previous flow-control studies using LAFPA actuators in atmospheric pressure jet flows[5–7] (M = 0.9-2.0), demonstrated significant localized heating and repetitive shock-wave formation by the plasma, large-scale coherent structure generation, and mixing enhancement. This effect was achieved at a low actuator power ($\sim$ 10 W per actuator), at forcing frequencies near the jet column instability frequency (preferred mode). This low power budget contrasts with previous bow shock control studies, typically on the order of 10 kW, using pulsed DC discharge,[8] pulsed microwave discharge,[9] and laser optical breakdown.[10,11]

In this paper, the demonstrated effect will be reproduced using the LeMANS code,[12,13] developed at University of Michigan.[14,15] LeMANS was previously used for hypersonic flow-control by energy deposition,[12] therefore rapid energy coupling by the nanosecond pulse DBD is modeled in the same phenomenological approach. It is assumed that the phenomenological model prediction replicates the thermal effect of the DBD. Various important parameters, such as temperature distribution, pressure and heat coefficients are not available in the experiment. Thus, this modeling study is meant to reveal details about the flow perturbation mechanism, and afford an evaluation of its validity for practical applications, such as flow control at hypersonic inlet, isolator, and engine exhaust, while concurrent work by Poggie *et al.*[16] focuses on high-fidelity modeling of only the dielectric barrier discharge in order to identify the relevant energy transfer processes and develop a reduced-order model of the DBD.

The nonequilibrium plasma wind tunnel used in the experiment was initially manufactured to study

nonequilibrium hypersonic flows and develop optical diagnostics that can be portable to and perform measurements at national ground hypersonic test facilities. Owing to this purpose, the freestream velocity and temperature have been measured. Results from previous measurements of the freestream velocity and temperature are used for freestream uncertainty quantification.

The work uses LeMANS to compute flow around a 5 mm cylinder and a 6 mm cylinder using two-dimensional computations to compare with existing experiments. While the 5 mm cylinder simulation results match the experiment, the 6 mm cylinder simulation results over-predict the bow-shock location. The nanosecond DBD experiment used the 6 mm cylinder, so a parametric study exploring the uncertainties associated with the freestream, wall boundary, and thermo-chemical nonequilibrium flow conditions is conducted to quantify their effects on the standing bow-shock location. The study revealed that none of the parameters explained the discrepancy in bow-shock location. Nonetheless, the two-dimensional simulations allow the large design-space to be explored with minimal computational cost, including results from the phenomenological energy deposition modeling of the discharge event. The energy deposition modeling results are able to replicate the DBD discharge induced compression wave speed and resultant perturbed bow-shock shape and qualitatively match phase-locked schlieren images.

In order to explain the bow-shock standoff discrepancy, a three-dimensional computation of the full tunnel is computed and found to agree well with all available experimental measurements. The results show that cylinder/tunnel sidewall interaction produces a significant pressure drop along the cylinder span, which draws the standing bow-shock closer to the cylinder. In addition, a three-dimensional simulation with the phenomenological energy deposition model representing the discharge event is able to reproduce many of the features observed in the phase-locked schlieren images of the experiment.

II.   Experimental Facilities

A schematic of a small-scale Mach 5 nonequilibrium wind tunnel is shown in Fig. 1 (also used in Ref. 17, 18). The wind tunnel was operated using dry air supplied from high-pressure cylinders, at plenum pressures of $p_0 = 370$ Torr (0.5 atm), and the mass flow rate of 7 g/s. The steady state run time at the constant static pressure in the supersonic test section is up to 10 seconds. The flow expands through an aerodynamically contoured Mach 5 nozzle, with the throat height of 1.6 mm. Top and bottom walls of the supersonic test section after the nozzle exit each diverge at a $1.5°$ angle to provide boundary layer relief. Rectangular optical access windows, made of UV-grade fused silica, are flush mounted in all four walls in the supersonic test section, providing ample optical access for schlieren photography, emission spectroscopy, Planar Laser Induced Fluorescence (PLIF) visualization / thermometry,[17,18] and NO_2 Molecular Tagging Velocimetry (MTV)[19] diagnostics, as well as currently on-going vibrational temperature measurement by picosecond Coherent Anti-Stokes Raman Scattering (CARS) system.[20]
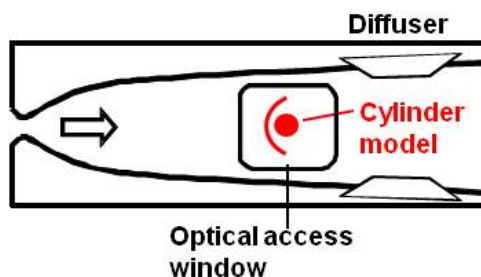
Figure 1. Schematic of the Mach 5 wind tunnel with a cylinder model installed in the test section.

The dimensions of a quartz cylinder model used to generate a bow-shock and also used as a DBD actuator is 4 cm long, 6 mm outer diameter, and 4 mm inner diameter. The model is located 14.5 cm downstream of the throat (3.5 cm downstream of the end of nozzle contour), where the flow cross sectional area is 4 cm x 4.6 cm. The ends of the model are embedded in the optical access windows in the side walls of the test section. The baseline shock standoff distance (without nanosecond pulse discharge), measured in the schlieren photography is 1.2 mm, with the spanwise length of about 1 cm, which is 25% of the test section width. The spanwise extent of the bow-shock is limited by the boundary layer growth on the sidewalls of the test section.[17]

The test section static pressure, $p_\infty = 1.2$ Torr (160 Pa), was measured using a wall pressure tap in the side wall at the end of the nozzle, and 4 cm upstream of the cylinder model. The pressure is assumed to be constant through the sidewall boundary, a valid assumption for a laminar boundary layer (no experimental measurements taken thus far have indicated the wall boundary layer is turbulent). The flow Mach number inferred from the plenum pressure and freestream static pressure is $M_\infty = 4.6$, while the total pressure measured at the flow stagnation point (downstream of the bow-shock) was $p = 36$ Torr, which corresponds to a freestream Mach number of $M_\infty = 4.8$, using one-dimensional normal shock relations and assuming the static pressure is constant across the side-wall boundary layer.

Figure 2 shows a cartoon of the electrode configuration for the bow-shock perturbation by the nanosecond pulse DBD. One actuator electrode is composed of a 1 cm long, 3 mm diameter copper tube with a tube wall thickness of 0.35 mm, and is immersed inside the quartz tube. Since the tube's inside diameter is 4 mm, the actuator electrode is positioned to contact the quartz surface near the upstream side, as seen in Fig. 9. The other electrode consists of a strip of adhesive copper tape 1.5 mm wide and 12 mm long, attached to the outside surface of the quartz tube model. The two electrodes overlap over a spanwise distance of 10 mm, centered behind the core flow bow-shock, with the ends of the tape covered by non-conducting Kapton® tape. Output pulse voltage and current were measured during each run. Measured peak voltage and current are 27 kV and 70 A, respectively, coupling between 4-7 mJ/pulse.
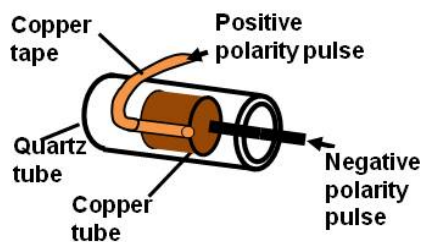

Figure 2. Diagram of the cylinder model with a nanosecond pulse surface DBD plasma actuator.

Time evolution of the shock generated by the NanoSecond Dielectric Barrier Discharge (NSDBD), as well as its interaction with the bow shock was recorded using a phase-locked schlieren system.[3] It was shown that a discharge pulse generates a compression wave that propagates upstream and locally 'pushes' the bow-shock away from the cylinder. This perturbed region bends away from the flow stagnation line, convects downstream, and eventually returns the shock envelop to the baseline shock shape about 20 μs later. Image sets for this microsecond-scale shock-shock interaction were taken both for a 'single pulse' mode (pulse repetition rate of 200 Hz), and 'double pulse' mode (two pulses separated by a 10 microsecond delay, which corresponds to a pulse repetition rate of 100 kHz). This study will primarily use on the 'single pulse' mode, so each discharge pulse acts on the baseline bow-shock. Additional details about the NSDBD process are available in Ref. 1.

A.   Freestream flow parameters

The facility is able to achieve Mach 5 flows using a blow-down wind tunnel. While it is not possible to exactly characterize the test section for each experiment run, through various proven approaches, the inputs necessary for a computational simulation can be determined. As shown in previous work,[17] the test section has an inviscid core that composes about 25% of the cross-section area. Since the cylinder test model is essentially two-dimensional and only composes a fraction of the core flow, it is reasonable to assume that the freestream flow is uniform and the resultant flow-field will be two-dimensional. This assumption is justified by looking at Fig. 3, a top-down view of phase-locked schlieren image at $p_0 = 370$ Torr dry air (baseline condition), with the standoff distance $\Delta S = 1.2$ mm.

Freestream velocity was measured $u_\infty = 719 \pm 6$ m/s in the NO_2 MTV.[19] In this measurement, a small amount of NO_2 ($\sim 1\%$ mole fraction), was seeded in the main nitrogen flow at the plenum pressure, $p_0 = 370$ Torr. A pulse-burst laser system[21] generated two simultaneous outputs: one for the photo-dissociation of NO_2 into NO and O at 355 nm to tag a line in the flow, the other tuned at 226 nm for interrogation of the line progression by NO PLIF imaging. The NO fluorescence intensity distributions were fitted by a Gaussian curve, and it was found that the average velocity is 719 m/s with absolute statistical error of $\sigma = 5.8$ m/s.
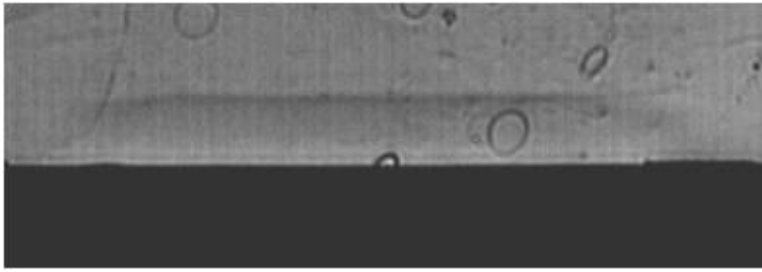
Figure 3. Phase-locked schlieren image (top-down view) in dry air at $p_0 = 370$ Torr at baseline condition (without discharge). Flow direction is top to bottom in the figure.

The NO PLIF thermometry was used for temperature measurement behind the Mach 5 bow-shock in Ref. 18. A sheet of laser was tuned to pump a rotational transition of J = 5.5 or J = 16.5 on the NO(X,v' = $0 \rightarrow$A,v'' = 0) band. The pair of these lines was selected because the ratio of absorption strength is linear at around $T_0 = 300$ K. In one of preliminary experiments, sheet laser wavelengths were tuned to excite the J = 5.5 and J = 9.5 rotational states in order to probe lower temperatures in the freestream. Only a few of experiments have been carried out thus far with some uncertainty in the results. But, the results tend to fall within a temperature range of about $T_\infty = 50-60$ K, which appears consistent with a freestream temperature obtained by considering the freestream pressure ratio, $T_\infty = 56$ K. Freestream temperatures calculated from the isentropic relation, using the freestream velocity measured in the NO_2 MTV measurement, are $T_\infty = 78$ K, 60 K, and 50 K for Mach numbers of M = 4, 4.55, and 5, respectively. The freestream temperature for M = 4.55 is also close to this isentropic flow temperature.

As previously mentioned, the test section static pressure, $p_\infty = 1.2$ Torr (160 Pa), was measured using a wall pressure tap in the side wall at the end of the nozzle, and 4 cm upstream of the cylinder model. The precision on the pressure gauge is 0.1 Torr, so its uncertainty is ±0.05 Torr (±6.67 Pa). The freestream density is inferred using the ideal gas relation ($p = \rho$ R T). For this work, the freestream dry air is composed of 78% nitrogen (N_2), and 22% oxygen (O_2), by density. Table 1 lists the nominal freestream conditions and uncertainty bounds. The effect of the uncertainties will be addressed in a later section.

Table 1. Freestream conditions and uncertainty bounds for Mach 5 air flow around a cylinder.

Parameter	Value
u_∞, [m/s]	719 ± 6
T_∞, [K]	56 ± 5
ρ_∞, [kg/m^3]	0.009924 ± 0.0013
p_∞, [Pa]	160 ± 6.7
M_∞	4.76 ± 0.25

III. Numerical Method

Flow-field results are obtained using Computational Fluid Dynamics (CFD) to solve the Navier-Stokes equations. The CFD computations are executed using the Michigan Aerothermodynamic Navier-Stokes (Le-MANS), code developed at the University of Michigan.[14, 15] LeMANS is a general 2D/axisymmetric/3D, parallel, unstructured finite-volume CFD code and has been used previously in numerous studies of hypersonic flows.[12–15] LeMANS may be employed with any of three thermodynamic models: perfect gas, equilibrium, and nonequilibrium thermochemistry. LeMANS employs a two-temperature model to account for thermal nonequilibrium and a standard finite-rate chemistry model for nonequilibrium chemistry. The two temperature model assumes that a single temperature, T, accounts for the translational and rotational energy modes of all species while the vibrational and electronic energy modes are accounted for by a separate temperature, T_{ve}. The simulations are performed using second-order accurate spatial discretization and carry double precision arithmetic throughout.

LeMANS is primarily used for steady-state simulations, but is capable of computing time accurate scenarios with first-order temporal accuracy. However, numerical error associated the low temporal accuracy is minimized by enforcing a sub-nanosecond time step (Δt $\leq$ 1 ns).

The nanosecond DBD discharge used in the experiment is effectively a thermal actuator. As such, a phenomenological model of dissipative heating is used to represent it. This model is accounted for in the Navier-Stokes equations by the addition of a source term, S, to the right side of total energy equation,

without any energy being directly deposited into the vibrational-electron-electric energy equation when the simulation is performed assuming thermodynamic nonequilibrium. Deposition of all the energy into the translational mode is a strong assumption, but is adequate for the purpose of this study since it is assumed the compression wave generated by the DBD is due to a rapid transfer of energy into the translation energy mode, an observation seen in previous work by Popov.[22]

The shape and location of the actuator are modeled with contours of constant S having an ellipsoidal shape. This approach has been used successfully in previous numerical investigations.[12] The strength (total energy), deposited into the flow uses exponential decay from the centroid of the energy deposition pattern, which for two-dimensional simulations is:

$$
\begin{aligned}
S &= \frac{Q}{\pi\,a\,b}\,\exp\left(-\left(\frac{\hat{x}}{a}\right)^2 - \left(\frac{\hat{y}}{b}\right)^2\right) \\
\hat{x} &= (x - x_{\mathrm{c}}) \\
\hat{y} &= (y - y_{\mathrm{c}})
\end{aligned}
\tag{1}
$$

where variables a and b are the equatorial radii (along the x and y axes). Coordinates $(x_{\mathrm{c}}, y_{\mathrm{c}})$ represent the centroid of the ellipsoid. Note that Q represents the total power deposited in the flow and $\iint_{-\infty}^{\infty} S\,dx\,dy = Q$.

A. Grid Independence

Figure 4 shows a structured mesh for a two-dimensional computational domain around a 6 mm diameter cylinder. Flow direction is left to right, and the stagnation point is located at $x = 0.003$ m. Only the first $90°$ of the cylinder surface is computed in this section to minimize computational cost and because measurements behind the cylinder, such as the wake or shear layer structure, were not captured in the experiment. Note full cylinder computations are discussed in subsequent sections. The meshes were developed such that clustering in the radial direction occurs at both the cylinder surface and at the bow-shock, while the mesh in the azimuthal direction is distributed to provide orthogonality of the cells at the bow-shock.
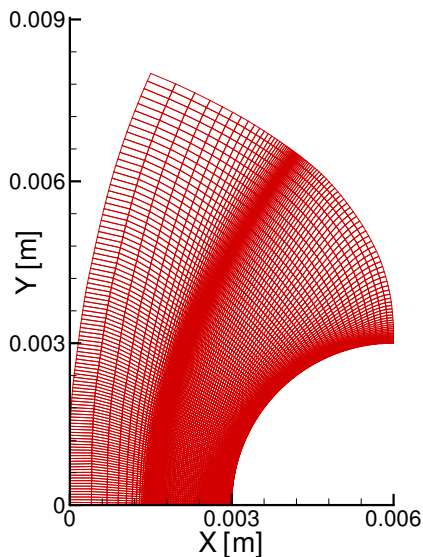
Figure 4. Shock-fitted grid for Mach 5 air flow around a cylinder. (100×100)

Three doubly refined grids: 50×50 (coarse), 100×100 (medium), and 200×200 (fine), were used for the grid independence study. Input parameters were taken from the nominal conditions listed in Table 1; $u_\infty = 719$ m/s, $T_\infty = 56$ K, and $\rho_\infty = 0.009924$ kg/m³. Since the input parameters correspond to the baseline scenario (i.e., steady-state), the solution is advanced until the root-mean-square residual error approaches machine-precision and remains unchanged for subsequent time steps, as seen in Fig. 5. As the mesh number increases, the number of iterations required for the convergence also increases due to the reduction in the time step required to maintain stability, which is calculated based on the smallest cells

size used in the computational domain. In addition, a maximum time step of $\Delta t = 1$ μs is enforced for all steady-state simulations performed in this paper.
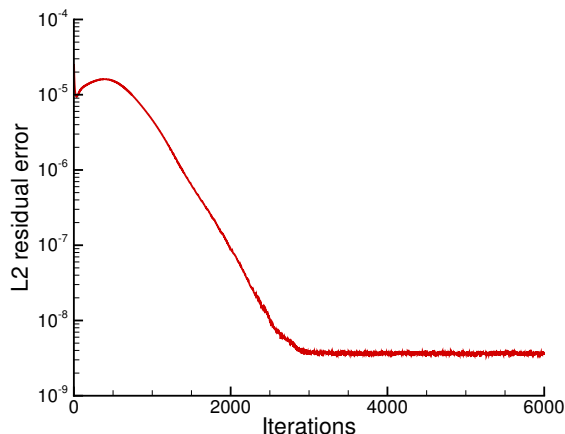

Figure 5. Root-mean-square residual error for the nominal baseline case with the medium grid.

Figure 6 compares the temperature contours from the fine grid (top) and medium grid (bottom). The distributions are nearly identical, except at the bow-shock, where the shock appears more smeared for the medium grid. While the shock thickness decreases with increasing mesh number, the standoff distance (defined as the distance between the stagnation point and the location of maximum density gradient), remains the same ($\Delta S = 1.55$ mm), for all three grids.
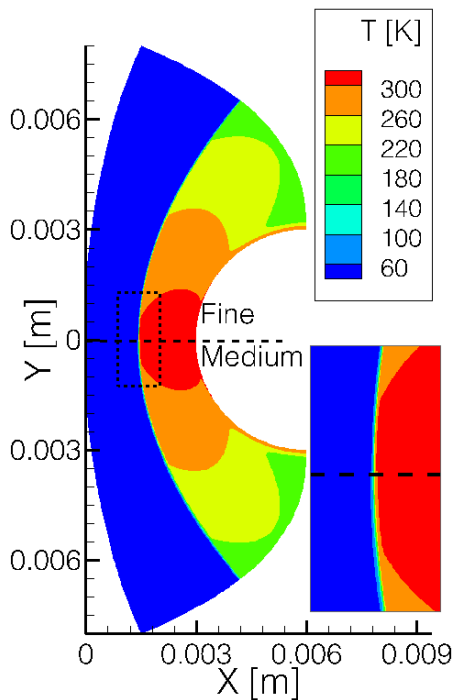
Figure 6. Temperature contours for Mach 5 air flow over a cylinder with fine grid (top) and medium grid (bottom).

Figure 7 plots pressure coefficient, c_p, and nondimensional heating coefficient, c_h, along the cylinder surface for all three grids. Coordinates along the cylinder are converted into the degree angle, θ, with $\theta = 0°$ located at the stagnation point. The pressure coefficient is nearly identical for all three grids, while the nondimensional heating coefficient exhibits an offset for the coarse grid. Both the pressure and

nondimensional heating coefficients achieved on the fine grid replicate those from the medium grid. Therefore, the medium grid (100×100), is considered grid-independent and will be used in the remaining two-dimensional baseline simulations, unless otherwise noted.
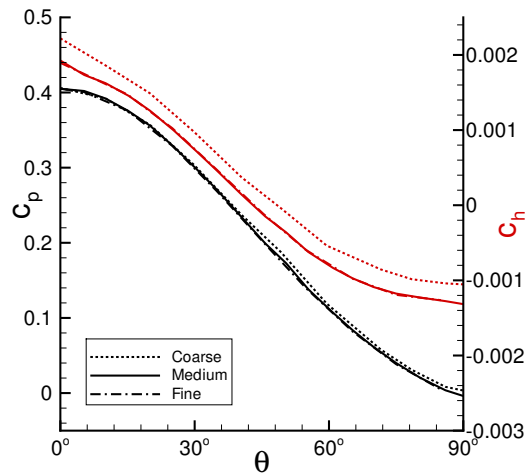

Figure 7. Pressure and nondimensional heat coefficient along the cylinder surface for various grids.

The temperature distribution is compared with a schlieren image of a bow-shock ahead of 6 mm diameter cylinder in Fig. 8(a). The experiment's bow-shock standoff distance of $\Delta S = 1.2$ mm is 20% smaller than the computed standoff distance of $\Delta S = 1.55$ mm. Also displayed in the figure is an empirical relation for the shock envelop developed by Billig *et al.*,[23, 24] which was developed by comparing schlieren images from many shock tube experiments and has dependencies on Mach number and cylinder radius. Billig's empirical relationship to determine the bow-shock standoff location on the stagnation line is specified later in Eq. (3). For a Mach number of M = 4.8 and the radius of 3 mm, Billig's empirical standoff distance $\Delta S = 1.42$ mm is much closer to the LeMANS computed standoff distance and shows a good agreement with the shock profile as well.

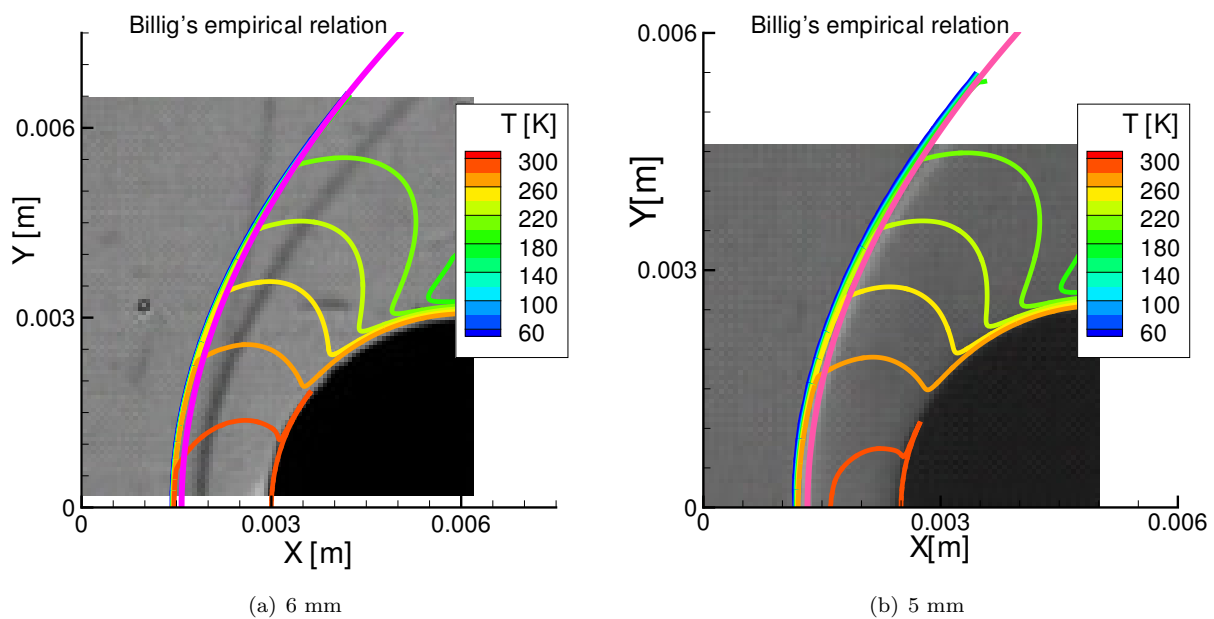(a) 6 mm   (b) 5 mm

Figure 8. Contour lines of temperature for Mach 5 air flow over a cylinder for two cylinder diameters. The figures include schlieren images from the experiment and Billig's empirical formula of the shock envelope.[24]

The discrepancy in the bow-shock standoff location between the computation and the experiment suggests there may be inappropriate assumptions made in the simulation or there are three-dimensional effects in the experiment that cannot be replicated by the two-dimensional computation. To help assess the validity of the two-dimensional computational results, a computation was performed for a 5 mm diameter cylinder scenario, which was also performed experimentally (although the nanosecond DBD was not employed for this experimental setup). As seen in Fig. 8(b), the 5 mm cylinder experimental results are in much better agreement with the computations and Billig's empirical relationship. These results suggest that the differences in standoff distance observed in the 6 mm diameter cylinder scenario are mostly likely attributed to a three-dimensional effect found in the experiment or greater uncertainty in freestream and wall boundary conditions. The following subsections explore the effects associated with tunnel and boundary conditions using the two-dimensional simulations since exploration of the full three-dimensional simulation requires a significant increase in computational cost.

B. Wall Boundary Conditions

One uncertainty about the experiment is the temperature of the cylinder surface. Since the cylinder is initially at room temperature, one assumption is that the cylinder surface is at a constant isothermal condition. However, given the experiment's long run time (10 seconds), the cylinder should cool to adiabatic conditions (i.e., no heat transfer to the surface). Another common approach in CFD is to assume the surface is in radiative equilibrium. This assumption is modeled by using the Stefan-Boltzmann Law:

$$q_w = \varepsilon \, \sigma_0 \, \mathrm{T}_w^4 \tag{2}$$

where q_w is the heat transfer to the wall, ε is the emissivity of the body, and σ_0 is the Stefan-Boltzmann constant. Assuming the body (i.e., cylinder surface), can be treated as a 'black body', its emissivity is unity ($\varepsilon = 1$). However, Fig. 9 shows the cylinder is composed of quartz (a dielectric), which has an emissivity[25] of $\varepsilon = 0.93$, except for the exposed electrode, which has an emissivity[26] of $\varepsilon = 0.02$. Preliminary simulations accounting for the actual thickness of the exposed electrode (0.1 mm), extruded from the quartz surface did not significantly alter the resultant flow-field, so the remaining simulations assume the cylinder surface has a continuous radius of 3 mm (i.e., the exposed electrode is incorporated into the cylinder surface). Table 2 tabulates the four scenarios considered for the wall boundary condition study. Each steady-state scenario uses the shock-fitted grid-independent mesh and nominal freestream conditions listed in Table 1, without the nanosecond discharge event (i.e., baseline scenario).
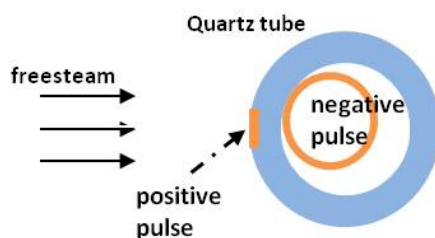

Figure 9. Side-view cartoon of the experimental setup of the cylinder.

Table 2. Wall boundary condition scenarios investigated for Mach 5 air flow over a cylinder.

Scenario	Details
Adiabatic	$q_w = 0$
Isothermal	$\mathrm{T}_w = 300$ K
Fully Radiative	$\varepsilon = 1$
Mixed Emissivity	$\varepsilon_{\mathrm{quartz}} = 0.93$ $\varepsilon_{\mathrm{copper}} = 0.02$

Figures 10(a) and 10(b) show the surface temperature distribution and the nondimensional heating coefficient, along the surface for each of the scenarios. As seen in Fig. 10(a), the adiabatic solution is very similar to the radiative boundary condition scenarios, whereas the nondimensional heating coefficient is very similar for the isothermal and radiative boundary conditions.
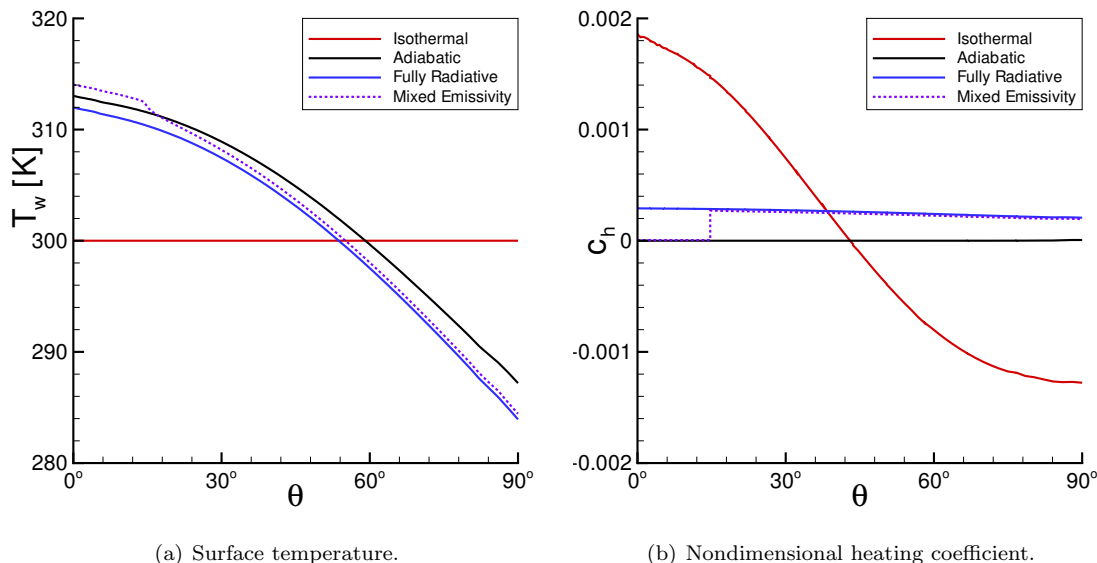

(a) Surface temperature.

(b) Nondimensional heating coefficient.

Figure 10. Distributions along the surface of a cylinder in Mach 5 air with various wall boundary conditions.

Table 3 tabulates the shock standoff distance, which is determined by identifying the peak density gradient in streamwise direction (i.e., along the x−axis). While the surface profiles seen in Figs. 10(a) and 10(b) exhibit differences, the shock standoff distance is not influenced by the wall boundary condition selected. This occurs because the boundary layer that develops on the cylinder surface is quite small, and since the adiabatic wall boundary condition only significantly influences the boundary layer thickness, the shock standoff distance is not influenced by the boundary condition enforced. The effect of

Table 3. Shock standoff distance for various wall boundary scenarios.

Scenario	Shock Standoff
Adiabatic	1.55 mm
Isothermal	1.55 mm
Fully Radiative	1.55 mm
Mixed Emissivity	1.55 mm

wall boundary conditions is expected to be more pronounced at higher temperatures, such as during the nanosecond discharge event, where the gas temperature near the stagnation point reaches 2000 K on a microsecond time scale.

C.   Thermo-Chemical Nonequilibrium

The freestream conditions are quite cold (see Table 1),. As such, it is unlikely that a significant amount of thermal-chemical nonequilibrium is present in the flow. For completeness, with regards to chemical nonequilibrium, simulations were run using a one-species perfect gas, and a five-species gas (N_2, O_2, NO, N, and O), using Park's 1990 data sets. Since the latter of the two scenarios requires LeMANS to carry 5 conservation equations for the mass, the computational resources required to obtain a solution also increases. As anticipated, the simulation results show no appreciable differences between the one-species perfect gas and the five-species finite-rate chemistry simulations. For completeness, two simulations are also conducted allowing for thermal nonequilibrium of the vibrational temperature. The Landau-Teller model[27] is used to account for energy exchange between the vibrational-electronic and the translational-rotational energy modes.

Typically, rates of vibration-translation energy transfer in a nitrogen-oxygen system are very low,[28] and therefore vibrational temperature at the plenum T_{ve}=300 K is assumed frozen in the freestream. For this thermo-chemical nonequilibrium case, translational and vibrational temperature distributions are compared in Fig. 11(a). For comparison, Fig. 11(b) displays translational and vibrational temperature distributions

at the freestream vibrational temperature, T_{ve}=240 K, which corresponds to a scenario where thermal equilibrium exists up to the nozzle throat, at which point it freezes and remains frozen downstream into the test section.
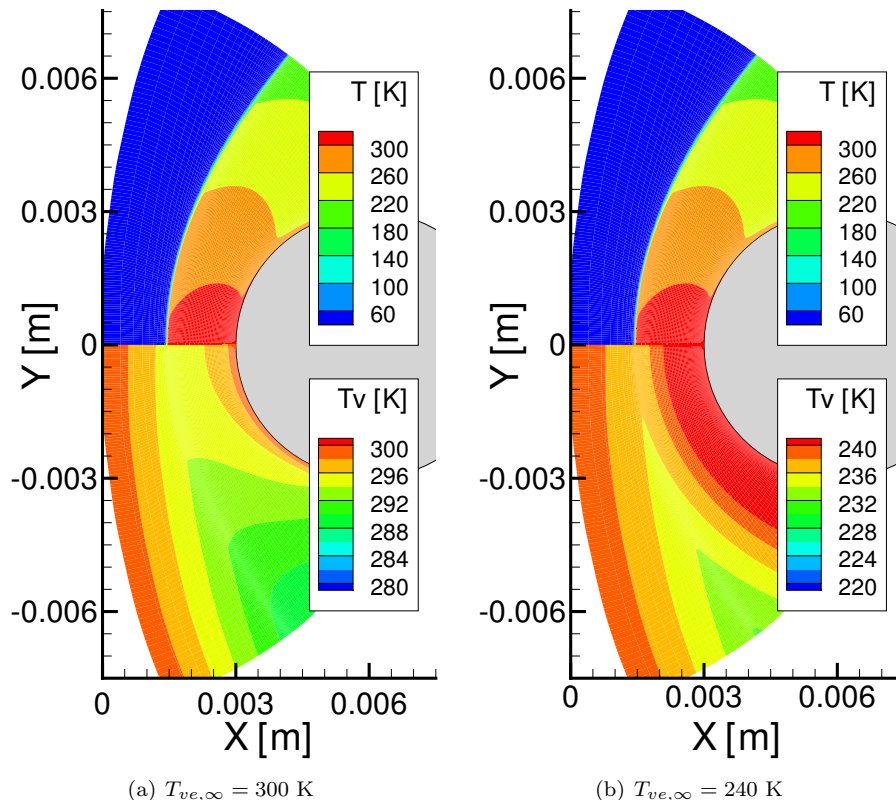

(a) $T_{ve,\infty} = 300$ K   (b) $T_{ve,\infty} = 240$ K

Figure 11. Translational and vibrational temperature contours for Mach 5 air flow over a 6mm cylinder.

As seen in the figures, the vibrational temperatures are essentially frozen across the shock. Also, no noticeable differences in the standoff distance or wall properties are observed in either scenario. Therefore, the thermal nonequilibrium effects are ignored for the remainder of the baseline calculations. However, finite-rate chemistry is included in the energy deposition scenarios due to the rapid rise in local temperature during the discharge event.

D.   Freestream Uncertainty Quantification

The freestream conditions observed in the wind tunnel have uncertainty associated with them. As such, it is important to quantify the effect these uncertainties have of flow properties of interest, such as standoff distance, as they may explain the discrepancy observed for the 6 mm diameter scenario. LeMANS requires the freestream density, temperature, and velocity as input parameters. These three variables determine the possible scenarios that need to be simulated to quantify the uncertainty in baseline shock standoff distance associated with the nominal freestream conditions. Table 4 lists the various runs with the parameter combinations. The simulations were performed assuming thermal-chemical equilibrium and the isothermal wall boundary condition, $T_w = 300$ K.

Results of standoff distance are summarized in Fig. 12, which plots standoff distance versus Mach number. The points are denoted by color to indicate the Reynolds number (based on cylinder radius). As seen in the figure, the standoff distance decreases with increasing Reynolds number. The general trend of these points appears to be consistent with Billig's empirical formula for cylinder flow.[24]

$$\frac{\Delta S}{r} = 0.386 \, \exp\left(\frac{4.67}{M^2}\right) \tag{3}$$

Table 4. Input parameters for uncertainty quantification of freestream conditions for Mach 5 air flow over a cylinder.

Run	u_∞, [m/s]	T_∞, [K]	ρ_∞, [kg/m^3]	Re_∞/L [m^{-1}]	Mach
1	713	50	0.008876	$1.97 \cdot 10^6$	5.02
2	713	50	0.011578	$2.57 \cdot 10^6$	5.02
3	713	60	0.008876	$1.59 \cdot 10^6$	4.59
4	713	60	0.011578	$2.07 \cdot 10^6$	4.59
5	725	50	0.008876	$2.0 \cdot 10^6$	5.11
6	725	50	0.011578	$2.61 \cdot 10^6$	5.11
7	725	60	0.008876	$1.62 \cdot 10^6$	4.66
8	725	60	0.011578	$2.11 \cdot 10^6$	4.66

where ΔS is the shock standoff distance, r is the cylinder radius, and M is the upstream Mach number. The similarity between Eq. (3) and the solutions in Fig. 12 exists because expansion of Eq. (3) generates the quadratic dependence of the standoff distance over a small range of Mach numbers, while the quadratic curve fit for the solution points in Fig. 12 yields a similar dependence on the Mach number, ΔS [mm] $= 0.103\,M^2 - 1.151\,M + 4.688$.
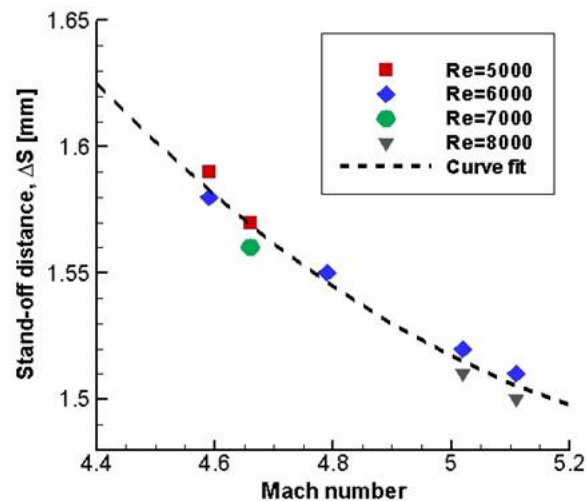

Figure 12. Standoff distance versus Mach number for various scenarios of air flow over a 6 mm cylinder.

Comparing the maximum and minimum computed standoff distances to the nominal scenario shows the uncertainty in standoff distance due to uncertainty in freestream conditions is $\pm3\%$, which is essentially negligible for the energy deposition scenario since the maximum standoff distance increase was 25%.[1] As such, the nominal freestream conditions listed in Table 1 are employed for the remaining two-dimensional simulations.

E. Partial Slip Walls

Since the experiment was performed in a very cold, low pressure wind tunnel, it is possible that part of the cylinder experiences velocity slip along its surface due to the transition of flow into to the free molecular regime. To check for partial velocity slip, the gradient length Knudsen number developed by Boyd *et al.*,[29] is computed from the nominal baseline steady-state solution using Eq. (4):

$$\mathrm{Kn_{GL}} = \frac{\lambda}{Q}\left|\frac{\partial Q}{\partial l}\right| \qquad (4)$$

where λ is the mean free-path, Q is any primitive quantity (U, T, p, or ρ), and the derivative is taken in the direction of the maximum gradient. Note when computing the velocity magnitude Knudsen number gradient, the gradient is normalized by the local velocity magnitude, except when the velocity is zero. During these situations, the gradient is normalized by the local speed of sound. The Navier-Stokes equations breakdown when the flow transitions from continuum to free molecular flow, which is assumed when $\mathrm{Kn_{GL}} > 0.05$.[30] However, using partial slip wall boundary conditions where $\mathrm{Kn_{GL}} > 0.05$ will extend the range of validity of the Navier-Stokes solver being employed.

Figure 13 shows contours for the gradient length Knudsen number for the nominal baseline scenario (using the grid shown in Fig. 25). As seen in Fig. 13, the flow experiences continuum breakdown in the vicinity of the shock and along the top and leeward side of the cylinder. Continuum breakdown within the shock is anticipated due to the strong flow discontinuity, though breakdown of the governing equations in this region does not adversely affect the post-shock flow conditions because the Rankine-Hugoniot condition is preserved through the shock. However, continuum breakdown observed on the cylinder surface is problematic as it indicates that the LeMANS solver should not be used in that region without modifying the surface boundary conditions to account for the slight deviation from the continuum assumption made when deriving the Navier-Stokes equations used in LeMANS.
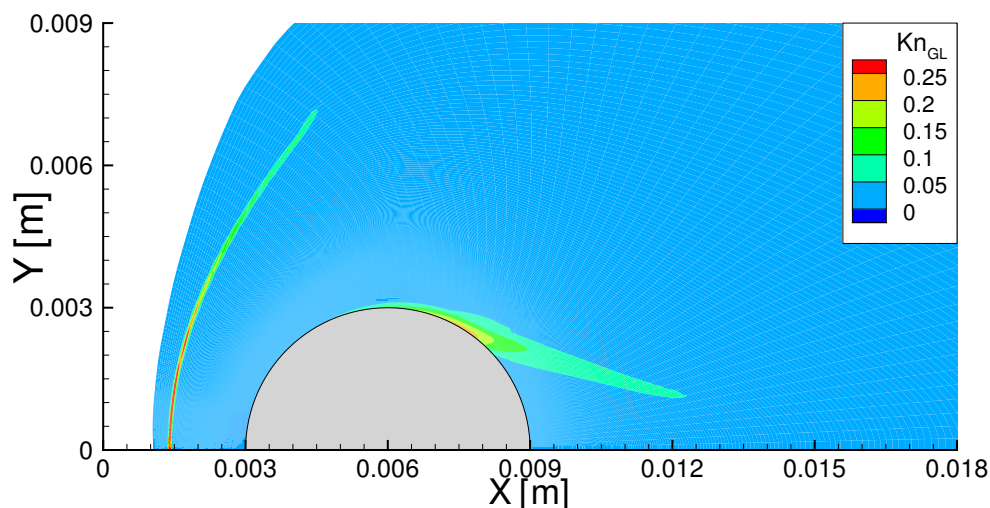

Figure 13. Contours of the gradient length Knudsen number for Mach 5 air flow over a cylinder.

In order to quantify the effects of continuum breakdown on the shock structure, a partial slip wall model is employed using Maxwell's slip condition, as described in Refs. 30, 31. Maxwell's slip condition was derived for a flat plate. It modifies the surface's tangential velocity, and, subsequently, provides a temperature jump. Equations (5) and (6) show the modifications to the surface velocity and temperature:

$$U_w = A \left(\frac{2 - \alpha}{\alpha} \right) \lambda \left. \frac{\partial u_x}{\partial n} \right|_n \tag{5}$$

$$\mathrm{T}_w = \mathrm{T}_g - \left(\frac{2 - \alpha}{\alpha} \right) \lambda \left. \frac{\partial \mathrm{T}}{\partial n} \right|_n \tag{6}$$

where λ is the mean free-path, T_w-T_g is the temperature jump, α is the accommodation coefficient, and A is a constant based on the scenario being considered. For simplicity in this work, both A and α are set to unity, as it is unclear what they should before hand for a good nonequilibrium solution for the flow considered. The derivative is computed normal to the wall surface and u_x is the velocity in the streamwise direction (along the wall surface).

In order to validate the partial slip boundary used, a nonequilibrium solution is computed using the Direct Simulation Monte Carlo (DSMC), code: HAP, developed by Burt et $al.$[32] Figure 14 shows the surface velocity and temperature jump for both the DSMC and LeMANS with Maxwell's slip condition. While the DSMC solution exhibits a large amount of scatter (due to a minimal sample of particles used in the simulation and an insufficient number of samples collected to further reduce the variance), the solution

confirms that the flow experiences surface velocity slip and a small temperature jump as the flow moves over the top and along the leeward side of the cylinder. In addition, the DSMC results provide direction for the proper adjustments to A and α in the partial slip boundary conditions. However, the values selected provide reasonable adjustments to the wall boundary conditions and are considered sufficient to quantify the effect a partial slip wall has on the bow-shock location.
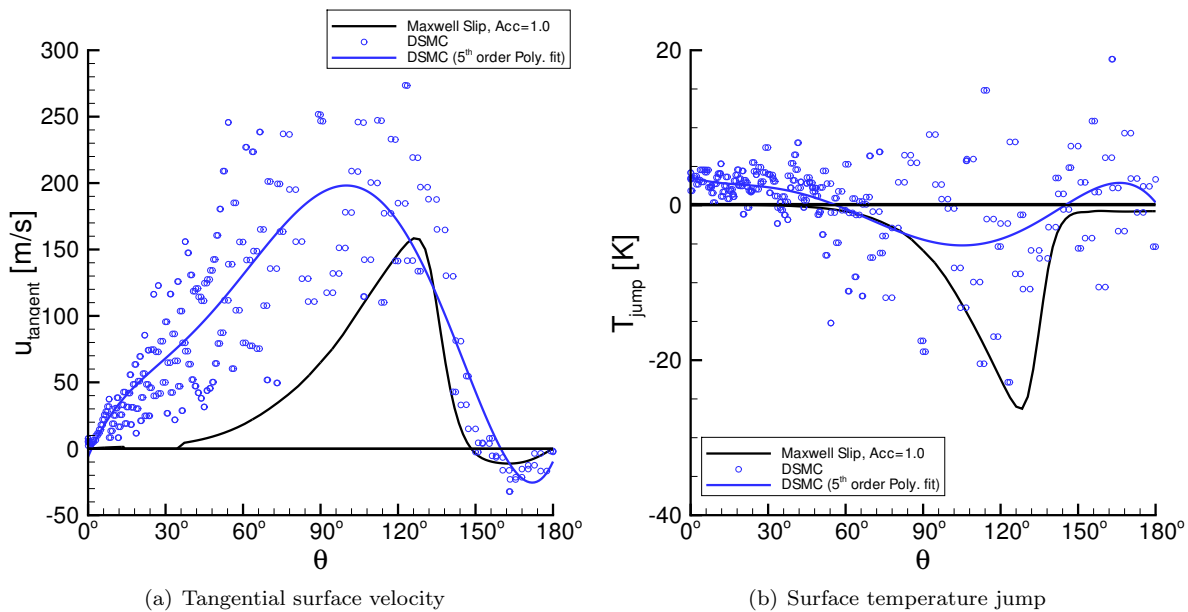

(a) Tangential surface velocity

(b) Surface temperature jump

Figure 14. Surface properties for Mach 5 air flow over a cylinder from a DSMC simulation and LeMANS using a simple Maxwell wall slip condition.

While the surface does experience partial velocity slip, which changes the size and flow properties of the recirculating wake region, the bow-shock standoff is not influenced by the change in wall boundary conditions, as seen in Fig. 15. As such, continuum breakdown along the top and leeward side of the cylinder does not explain the observed discrepancy in bow-shock standoff distance and is neglected in the remaining simulations.
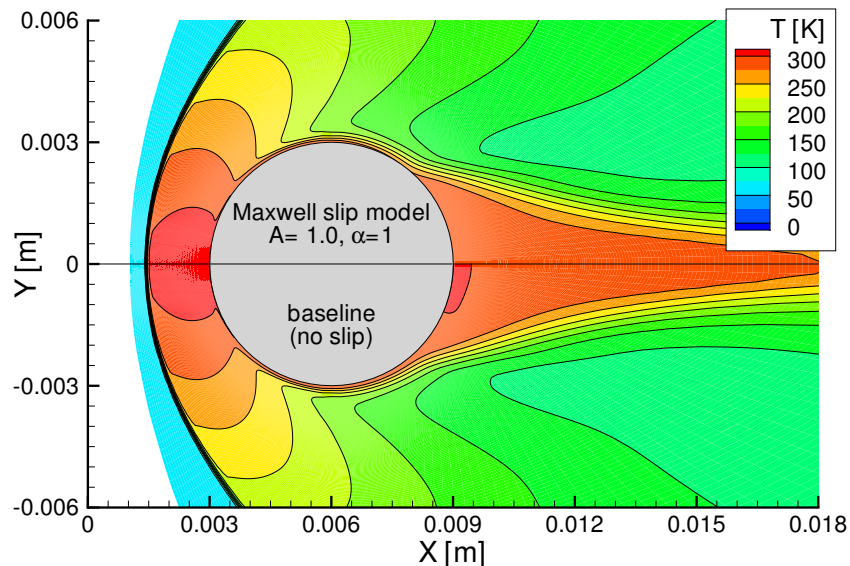

Figure 15. Temperature contours for Mach 5 air flow over a cylinder with and without partial velocity slip and temperature jump wall boundary condition.

As seen in the previous subsections, uncertainty in the computed shock standoff distance due to freestream conditions, boundary conditions, and thermochemical effects is relatively small and does not account for the discrepancy in shock standoff seen in the experiment. While the difference in shock standoff distance in the baseline flow is important for replicating and quantifying the effects of the discharge event, the next section uses the two-dimensional approach to qualitatively explore the nanosecond DBD discharge effect and subsequent perturbation on the flow. These computations are performed to develop sufficient grid and time-step bounds for the discharge simulations, and to develop and optimize the shape of the deposition model before transitioning to three-dimensional simulations.

IV.   2D Energy Deposition

The nanosecond DBD event performed in the experiment results in rapid thermalization of the electrical energy in the surrounding air, which produces a compression wave that interacts with the cylinder bow-shock. Since the thermal efficiency of the DBD is not exactly known, one of the critical parameters in the reduced-order model used in the CFD modeling of event is the rate of energy thermalization, which is controlled by the parameter Q in Eq. (1).

Figure 16 shows a grid used in the energy deposition simulation. The grid points are spaced uniformly both in the x and θ directions to reduce the spatial error due to the propagation of the bow-shock perturbed by the compression wave formed during the discharge event. Three doubly refined grids have been used to study the effect of grid resolution on the numerical solution, 201×101 points (coarse), 401×201 points (medium) and 801×401 points (fine). For the coarse grid, the cell size is $1 \cdot 10^{-5}$ m $\times 2.3 \cdot 10^{-5}$ m. The computational domain length in the streamwise direction extends 2 mm from the stagnation point of the cylinder (see Fig. 16), which allows the shock standoff distance to increase by up to 30% from the steady-state baseline solution standoff distance without being influenced by the domain inlet.

The spatial profile of energy deposition by the discharge used in the calculations is set in Eq. (1). The size of the energy deposition region was determined from the size of the plasma visible emission in the experiment, and approximated as an ellipse with axes of $a = 0.1$ mm and $b = 0.3$ mm, with the center of the ellipse located at the stagnation point (for the coordinate system used in the computations $x_c = 3.0$ mm and $y_c = 0.0$ mm), and Gaussian distribution of power density. Thus, approximately 67% of the input power is deposited for $x \leq a$ and $y \leq b$, and 95% of power is deposited for $x \leq 2a$ and $y \leq 2b$. The temporal profile of energy deposition is modeled as a step function. Due to the difference between baseline shock standoff distance predicted by the CFD model and the experimental value ($\Delta S = 1.55$ mm versus $\Delta S = 1.2$ mm), obtaining agreement with all experimentally measured parameters, i.e. compression wave speed of $U_c = 370$ m/s, perturbed bow-shock propagation velocity of $U_s = 92$ m/s, and shock standoff distance increase of 25%, is problematic. Since the compression wave is expanding radially as it travels, its strength decreases significantly with distance traveled before interacting with the bow-shock. As a result, a stronger wave will need to be generated in the computational exercise in order to produce a perturbed bow-shock with dynamics similar to those observed in the experiment.

Figure 16. Grid used for the energy deposition simulation (201×101).

To ensure spatial and temporal independence during the discharge event and subsequent flow interaction, simulations were conducted using an energy deposition pulse $\tau = 800$ ns long, with total power deposited $Q = 3$ kW, and a fixed computational time step $\Delta t = 0.5$ ns. These parameters were selected for the grid independence study because the deposition energy represents a high thermal efficiency scenario and the resultant flow perturbation is significant.
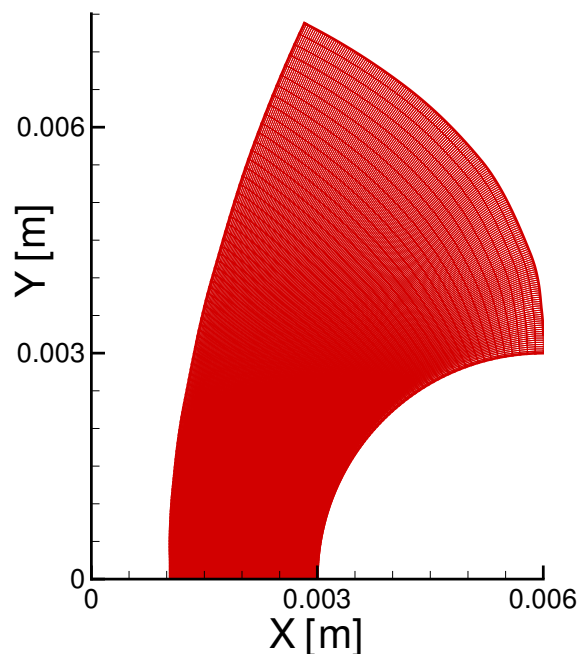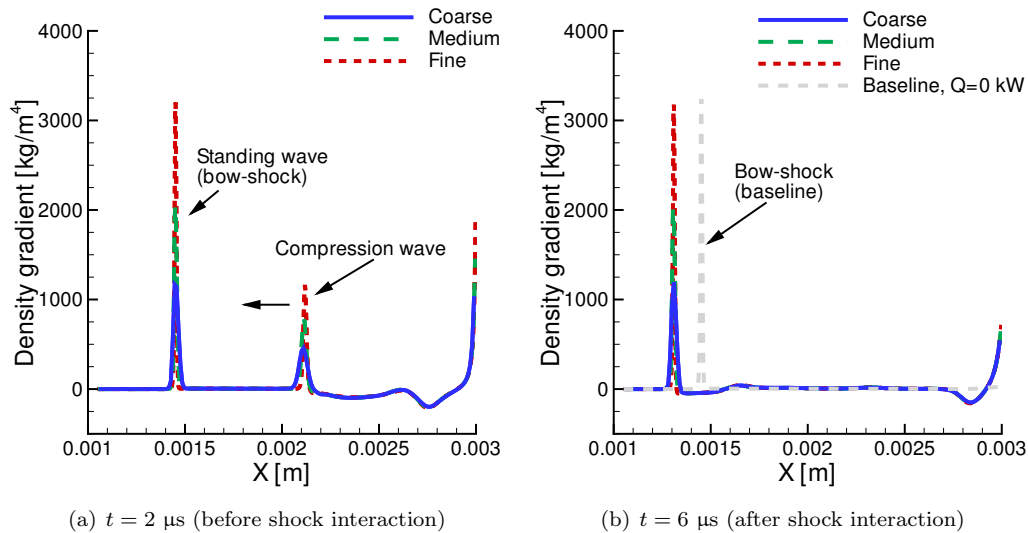
Figure 17(a) plots density gradient distributions at $t = 2$ μs after the beginning of the energy deposition pulse, obtained using three different grids and a time step of $\Delta t = 0.5$ ns. The density gradient was calculated using a 3-point central difference. The bow-shock and the propagating compression wave front are located at $x = 0.00145$ m and $x = 0.0021$ m, respectively. It can be seen that the magnitude of the density gradient increases approximately linearly with increasing grid resolution. Similarly, the magnitude of the peak density gradient is also observed in Fig. 17(b), which shows density gradient distributions of the perturbed bow-shock at $t = 6$ μs after the beginning of the energy deposition pulse. These results indicate that the medium grid has sufficient resolution to adequately capture the discharge event and resultant shock-shock interaction.

(a) $t = 2$ μs (before shock interaction)

(b) $t = 6$ μs (after shock interaction)

Figure 17. Density gradient distributions for the perturbed bow-shock obtained using three different grids at various times after the energy deposition pulse. Flow direction is left to right.

Figures 18(a) and 18(b) show distributions of wall pressure and nondimensional heat transfer coefficients on the cylinder model at $t = 2$ μs after the discharge pulse, calculated for the three different grids. It can be seen that with pulsed energy deposition, peak wall pressure is reached off stagnation line, approximately at $\theta = 20°$ (see Fig. 18(a)). Pulse energy deposition also results in significant heat transfer increase near the stagnation line (see Fig. 18(b)). These results indicate that all three grids provide sufficient resolution to obtain accurate estimates of the cylinder surface properties.

(a) Pressure coefficient

(b) Nondimensional heat transfer coefficient
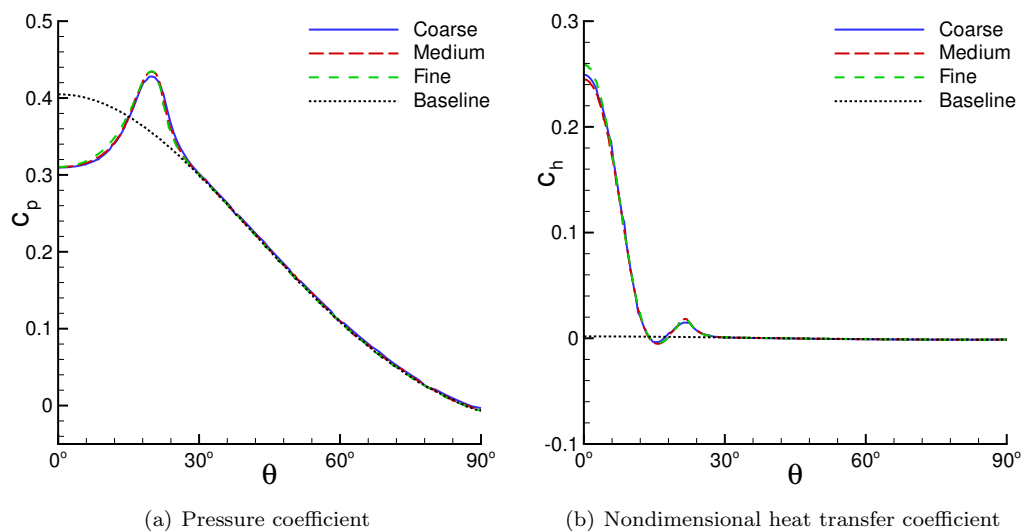
Figure 18. Surface distributions at $t = 2$ μs after energy deposition pulse for various grids.

Figure 19 plots compression wave speed and perturbed bow-shock velocity from simulations for three fixed time steps: $\Delta t = 5$ ns, 1 ns, and 0.5 ns on the three different grids. To calculate the compression wave speed, the location of the density peak was sampled every 400 ns at $t = 1 - 3$ µs after the beginning of the energy deposition pulse. After the compression wave reached the standing bow-shock (approximately 4 µs after the beginning of the energy deposition pulse), the location of the density peak was sampled every 400 ns at $t = 4 - 6$ µs after the beginning of the energy deposition pulse to determine the perturbed bow-shock speed. From Fig. 19, it can be seen that the calculated compression wave speed and perturbed bow-shock speed depend on grid resolution when the computation time step is $\Delta t = 5$ ns, but fully converges when the time step is reduced to $\Delta t = 0.5$ ns. Based on these results, a fixed time step of $\Delta t = 0.5$ ns and the medium grid (401×201), provide sufficient temporal and spatial independence and is used for all subsequent two-dimensional simulations.

Figure 20 shows dependence of compression wave propagation velocity on deposited pulse energy for input powers of $Q = 1$, 2, and 3 kW. Since the energy is deposited uniformly in time, the duration of energy deposition pulse is varied as follows: 400ns $\leq \tau \leq$ 3200 ns for $Q = 1$ kW, 200ns $\leq \tau \leq$ 1600 ns for $Q = 2$ kW, and 200ns $\leq \tau \leq$ 1200 ns for $Q = 3$ kW, respectively. Fig. 20 also denotes the speed of sound evaluated using the post-shock temperature averaged along the stagnation line (T= 307 K, $C_s = 351$ m/s).
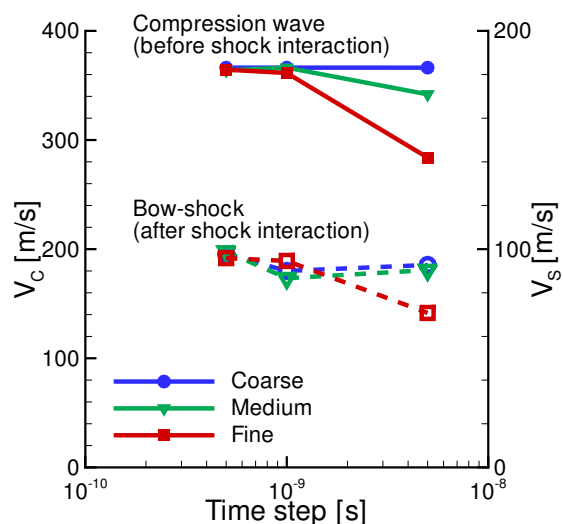

Figure 19. Compression wave propagation velocity (closed symbols) and perturbed bow-shock velocity (open symbols) vs. time step for the three grids used.
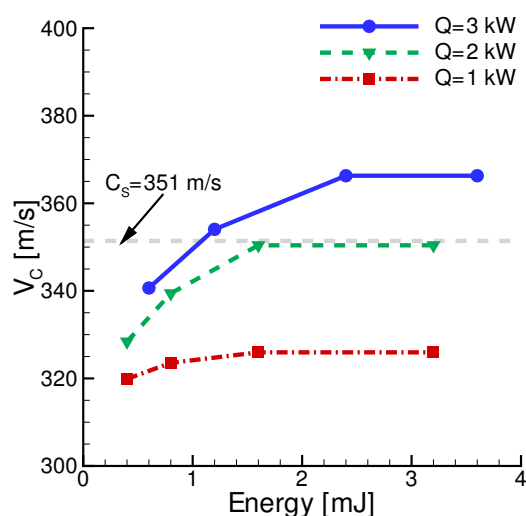
Figure 20. Compression wave speed dependence on input power and energy added (i.e. duration of energy deposition pulse).

As seen in Fig. 20, input power of $Q =1$ kW and 2 kW produce a compression wave speed that increases with total pulse energy until an energy of 1.6 mJ, whereas the input power of $Q = 3$ kW achieves a compression wave speed that increases up to pulse energy 2.4 mJ. This is due to the fact that the smaller values of Q fail to produce a supersonic compression wave, which limits the amount of energy that can be used to increase the wave speed. Since the compression wave is supersonic in the experiment (see Fig. 21), a value of $Q \geq 3$ kW seems most appropriate to investigate the discharge effect and subsequent flow perturbation. In addition, selection of an input power of $Q = 3$ kW for $\tau = 800$ ns, corresponds to a pulse energy of 2.4 mJ, which is consistent with about 30% the experiment's coupled pulse energy 'quickly' thermalizing. The thermal efficiency assumed here is consistent with a study by Popov.[22]

Figure 22(a) shows density distributions along the stagnation streamline, calculated for pulse duration of $\tau = 1200$ ns ($Q = 3$ kW), at $t = 200$ ns, 400 ns, 800 ns, and 1200 ns after the beginning of the energy deposition. As seen in the figure, the region of fluid displacement (i.e. density reduction near the stagnation point) expands up to $t = 800$ ns, which results in density increase to the left of the energy deposition region. At $t \geq 800$ ns, the density in the energy deposition region no longer decreases, thus limiting mass displacement due to energy deposition and, consequently, compression wave speed. After this limit is reached, additional energy input no longer contributes to increasing the compression wave speed. As a result, the compression wave speed remains constant for pulse deposition durations greater than 800 ns (for $Q = 3$ kW).
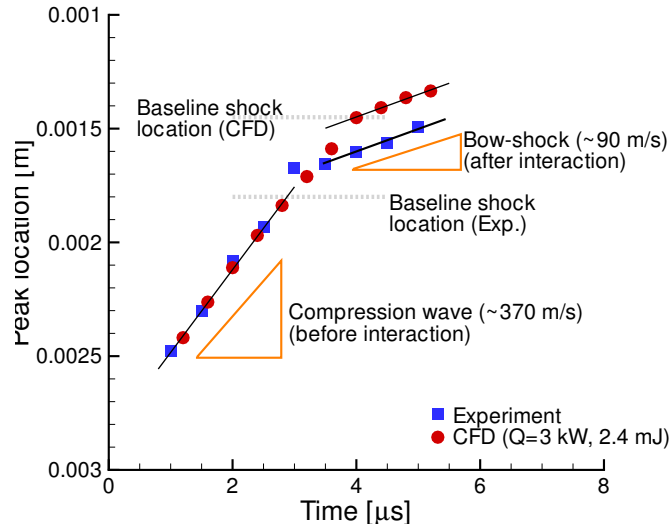
Figure 21. Comparison of predicted peak density gradient location with the experiment (phase-locked schlieren). $(401 \times 201, \Delta\mathbf{t} = 0.5 \text{ ns}, Q = 3 \text{ kW}, \tau = 800 \text{ ns})$

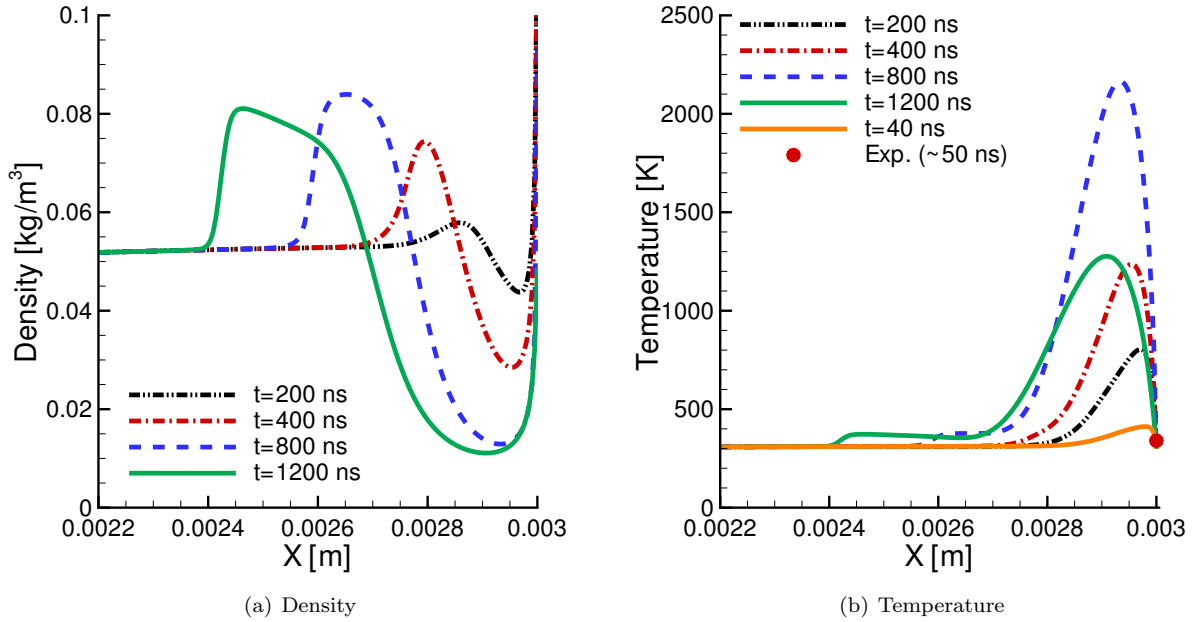**Figure 22. Stagnation streamline distributions at different delays after the start of the energy deposition pulse** $(Q = 3 \text{ kW}, \tau = 800 \text{ ns})$, for Mach 5 air over a cylinder.

Using a total input power of $Q = 3$ kW and energy deposition pulse duration of $\tau = 800$ ns yields the maximum compression wave speed for its total input power while providing a wave speed that is slightly greater than the experiment's measured wave speed. As such, this scenario provides the best agreement for both compression wave velocity and perturbed bow-shock propagation velocity along the stagnation line, as shown in Fig. 21. The total energy deposited for this scenario amounts to 2.4 mJ/pulse (for the full geometry), which means the nanosecond DBD pulse would have to have a thermal efficiency of over 30%. However this conclusion can be confusing since the baseline bow-shock location is 1.55 mm from the cylinder in the computation and only 1.2 mm for the experiment. Since the shock is located farther from the cylinder, the energy deposited in the simulation must be exaggerated in order to create a compression wave with sufficient speed and strength such that its interaction with the standing bow-shock produces a

resultant combined wave that has the same velocity as the experiment.

Figure 22(b) plots temperature distributions at the same delays as Fig. 22(a). In these calculations, temperature at the stagnation point is fixed at T = 300 K (isothermal wall). However, the peak temperature increases during the energy deposition process and reaches maximum at $t = 800$ ns, T = 2160 K. This peak temperature value is much higher than the temperature measured in the experiment using N_2 second positive bands emission spectra, T = 340 ± 30 K. However, it is well known that N_2 second positive system emission decays over a few tens of nanoseconds after the discharge pulse. Note that temperature in the energy deposition region predicted at $t = 40$ ns more reasonably matches the experiment, with a peak temperature of T = 410 K. In addition, the average temperature along the stagnation line (within the shock layer) during the first 40 ns of the energy deposition pulse computation is T = 355 K.

Confirmation of the post-shock temperature 50 nanoseconds after the discharge event suggests that the significant temperature rise seen later in the computation could actually be occurring in the experiment or that the strong temperature rise is merely an artifact of the phenomenological deposition modeling processing including the shape, distribution, and duration of the deposition. Verifying the this requires taking additional temperature measurements during the experiment at much longer time delays after the discharge pulse ($t = 1$ μs), a challenge still being pursued, though the recent picosecond CARS results[33] may produce a method for obtaining the necessary measurements.

Figure 23(a) plots wall pressure coefficient distributions for several time delays after the energy deposition pulse. It can be seen that the initial pressure rise due to energy deposition is followed by a rarefaction wave. At $t = 1.2$ μs and 2.0 μs, the rarefaction wave reduces the wall pressure coefficient below baseline value for the first 15° along the cylinder surface. The wall pressure perturbation is subsequently reduced and approaches baseline profile approximately at $t = 4$ μs, which has been excluded from figure as it overlaps the baseline solution.
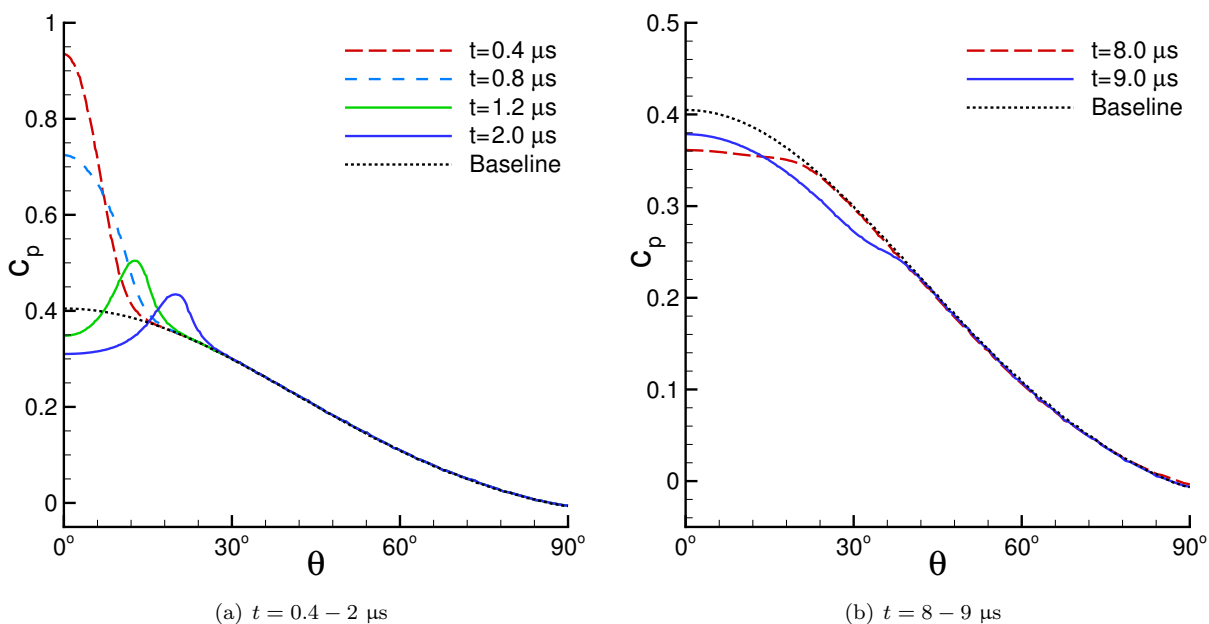

(a) $t = 0.4 - 2$ μs

(b) $t = 8 - 9$ μs

Figure 23. Surface pressure coefficient for different time delays after beginning of energy deposition pulse

Figure 23(b) shows wall pressure coefficient distributions at $t = 8$ μs and 9 μs, displaying a second wall pressure 'dip' near the stagnation line. The second pressure reduction is due to a rarefaction wave, which reflects off the perturbed bow-shock and returns back to the cylinder. The movement of the rarefaction wave is also visible in Fig. 24, which plots pressure distributions along the stagnation streamline for different time delays after the pulse.

To determine the drag on the cylinder, the computational domain is extended to include the recirculating wake region, as shown in Fig. 25. The grid used for these calculations is 401 × 401 points, with the grid resolution for 0° < θ < 90° being the same as the medium resolution grid discussed previously.

Figure 26(a) shows time evolution of total drag (i.e., the sum of pressure drag and shear drag over the
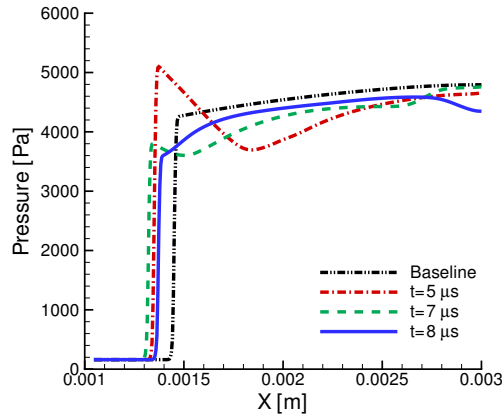
Figure 24. Pressure distributions along the stagnation streamline at $t = 5$ μs, 7 μs, and 8 μs delays after the energy deposition pulse.

cylinder surface). The total drag for the baseline steady-state scenario is D = 2.4 N. Note that shear drag accounts for 1% of the drag due to the low temperatures observed in the experiment. The drag reaches a maximum D = 3.04 N (26% increase from the baseline), at $t = 400$ ns, and a minimum D = 2.27 N (5% decrease from the baseline) at $t = 8.5$ μs. Following the interaction with the rarefaction wave on the cylinder, the drag recovers the baseline value around $t = 15$ μs after the discharge event.
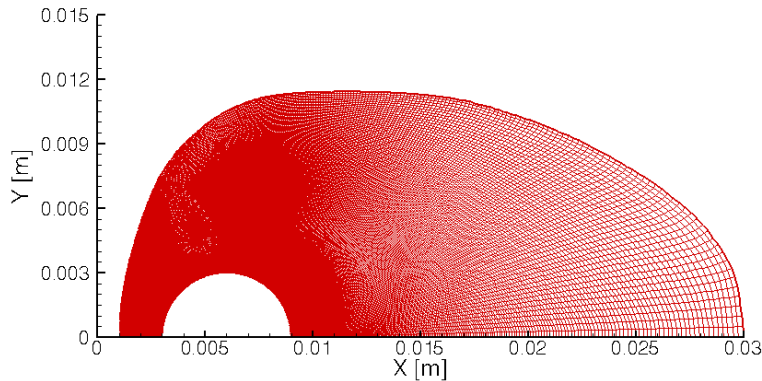
Figure 25. Computational domain used for drag calculations (401×401).

To evaluate the effect of energy deposition on drag reduction, the time-averaged change in total drag is shown in Fig. 26(b). As seen in the figure, the drag increases up to 20% at $t = 1$ μs, and then monotonically decreases to -1% at $t = 11$ μs, and remains unchanged thereafter. Figure 26(b) show that the nanosecond DBD discharge provides a slight reduction in total drag over the lifetime of the discharge event. However, the drag reduction comes with a substantial increase to the heat load on the cylinder.

To test if there is a continued reduction in drag by repetitive discharge events, three additional scenarios are considered. The first repeats the energy deposition at $t = 15$ μs (i.e, the discharge event begins after the previous discharge event cycle). This would be consistent with an operational frequency of 67 kHz. The results essentially replicate those previously presented for a single pulse effect, which suggests the 1% drag reduction on the cylinder could be sustained if the DBD was pulsed at this frequency. In the second scenario, the second discharge event begins when the total drag is at its lowest ($t = 8.5$ μs after the discharge event), which corresponds to an operational frequency of 110 kHz. The third scenario starts the second discharge event at $t = 11$ μs, which corresponds to the lowest time-averaged drag, or an operating frequency of 90 kHz.

Figure 27 shows the total drag time histories for repetitive discharges. As seen in the figure, neither of the higher frequency repetitive energy deposition scenarios resulted in an improvement to the total drag reduction. This occurs because the temperature in the energy deposition region is slightly hotter during
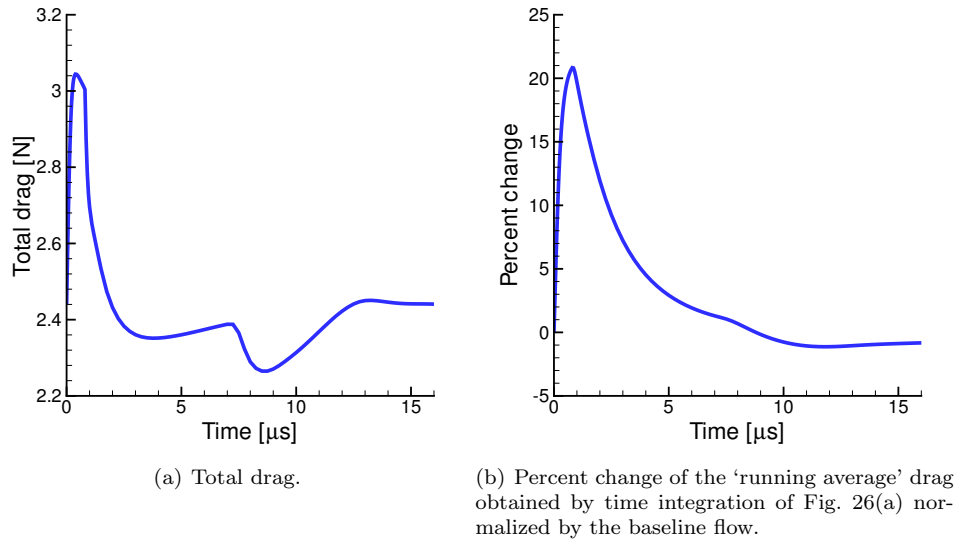
(a) Total drag.

(b) Percent change of the 'running average' drag obtained by time integration of Fig. 26(a) normalized by the baseline flow.

Figure 26. Time evolution of drag on the cylinder, calculated using the grid show in Fig. 25.

the second discharge (for the two higher frequency scenarios), since the flow has less time to cool down between discharge events. As a result, the energy deposited during the second pulse has a diminished effect in generating the subsequent compression wave, so its interaction with bow-shock is also reduced. These results suggest that it is best to operate the nanosecond DBD actuator at 67 kHz when it is being used for continuous operation since the total power requirements are the lowest, and it is still able to maintain the 1% reduction in running average total drag over the discharge cycle.
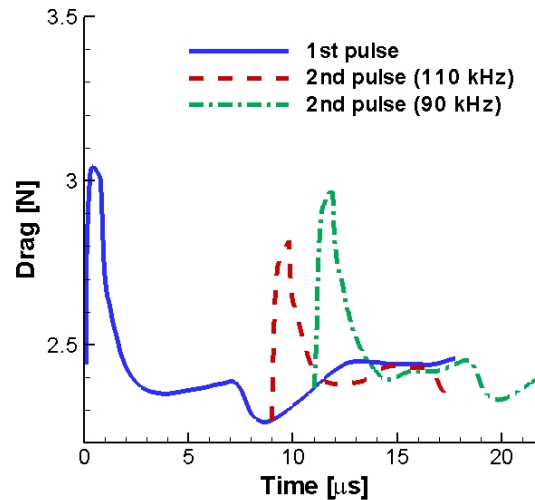

Figure 27. Time evolution of the total drag on the cylinder, with a second energy deposition pulse generated at $t = 9\mu$s (110 kHz) and $t = 11$ μs (90 kHz).

As a final exploration using two-dimensional simulations, a simulation is performed with an input power $Q = 35$ kW over $\tau = 200$ ns (7 mJ/pulse for a whole cylinder, though the computation was performed using the 1/4 cylinder domain). This simulation was conducted in order to obtain a compression wave with sufficient speed such that the shock-shock interaction occurred in the same time as the experiment. In Fig. 28, simulation results are shown at the same time moments as the experimental phase-locked schlieren images. The figure shows many similarities between the bow-shock perturbation from the experiment and the computation.
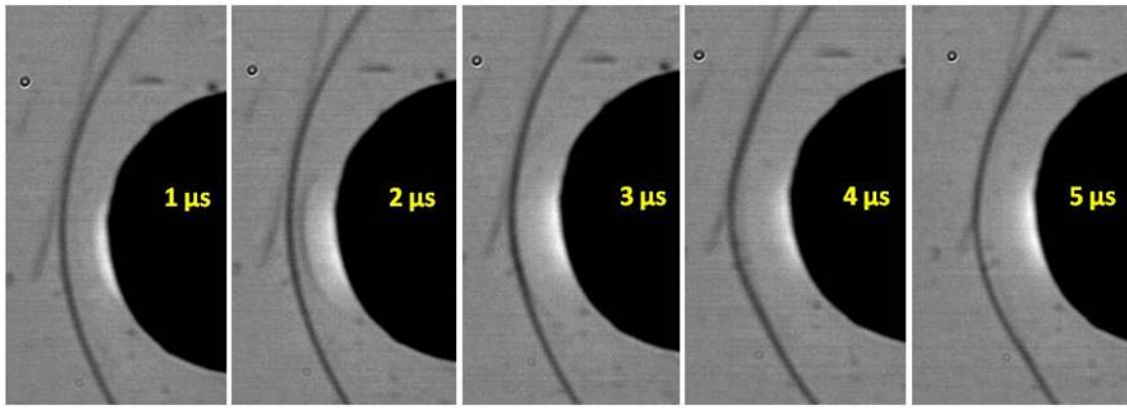
(a) Phase-locked schlieren images
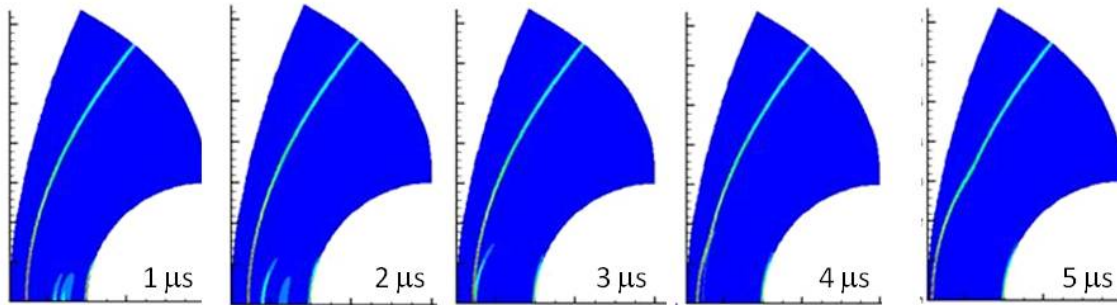
(b) CFD generated density gradient distributions

Figure 28. Temporal evolutions of the bow-shock (a) schlieren photography (experiment) and (b) density gradient distribution in the streamwise direction (CFD).

As seen in the Fig. 28, the generated compression wave propagates upstream and reaches the bow-shock at $t = 3$ μs. The interaction results in a 25% increase in the shock location from the baseline standoff distance, which is consistent with the results observed in the experiment's schlieren images. Note in this simulation, higher power input was required for the compression wave to reach the bow-shock at $t = 3$ μs, while compensating for a 30% difference in the bow-shock standoff distance. It would require a significantly smaller amount of deposition energy for a compression wave to travel 1.2 mm in the same amount of time.

V. 3D Simulations

As previously discussed, the two-dimensional nominal baseline simulation predicts a bow-shock standoff distance that is significantly larger than that observed in the experiment. Several two-dimensional simulations were performed to quantify the uncertainty of the freestream and boundary conditions, along with thermochemical nonequilibrium flow effects. However, the results did not explain the observed discrepancy in shock location. As such, a simulation of the entire tunnel (including the nozzle and the region downstream of the test section), is performed in order to replicate the experiment's shock standoff distance and identify the reason for the discrepancy in bow-shock location. Details about the tunnel were previously mentioned in Section II. Note Fig. 29 provides an outline of the computational domain used in the simulation. Only 1/4 of the tunnel is simulated because the tunnel is assumed to be symmetric in both the spanwise and transverse directions. The nozzle throat conditions used in the simulation are listed in Table 5.

**Table 5. Input conditions for the Mach 5 wind tunnel at the nozzle throat.**

Parameter	Value
u^*, [m/s]	318
T^*, [K]	250
ρ^*, [kg/m^3]	0.3609
p^*, [Pa]	26,020
Mach*	1.0
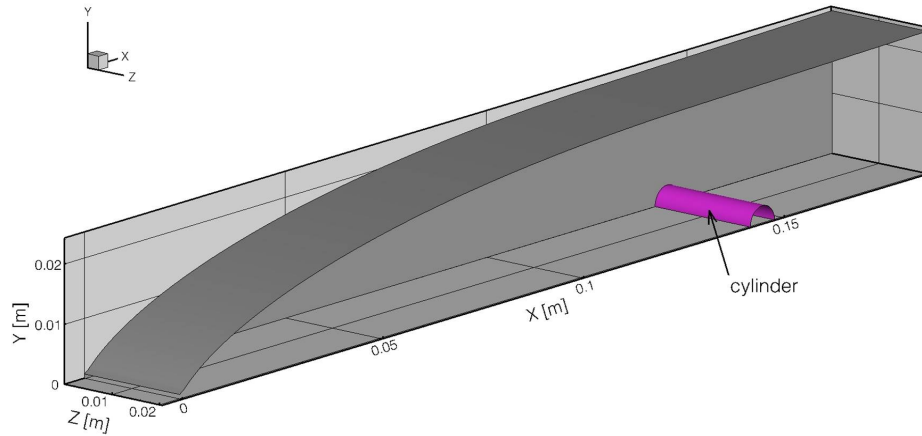
Figure 29. The computational domain for the entire tunnel. The gray surface depicts the tunnel while the pink surface illustrates the location of the cylinder test article. Only $1/4$ of the geometry is simulated.

Using the lessons learned from the two-dimensional simulations, a grid was developed for the tunnel using 4 computational blocks. Each block is composed of structured cells. The grid spacing is such that grid clustering occurs near all surfaces. The computational block surrounding the cylinder geometry is identical to the grid-independent 'medium' grid used for the two-dimensional analysis. In total, the three-dimensional computational domain contains 15 M cells and was run using 512 processors. For the baseline simulation (i.e., without the discharge event), implicit time integration was employed with a time step-size varying from $\Delta t = 0.1$ ns to $\Delta t = 2$ μs.

No slip, isothermal walls ($T_w = 300$ K), are assumed for all surfaces and a non-reflective first-order extrapolation is used at the domain exit plane. The simulation is started from quiescent air, except for the input conditions listed in Table 5. As a result, the simulation required about 20 milliseconds ($\sim 30,000$ iterations), for the wall boundary layer and cylinder bow-shock structure to develop and achieve a quasi steady-state in the inviscid region. Figure 30 shows a Mach 1.25 iso-surface of the flow, which is colored by temperature. This iso-surface level was selected as it illustrates the substantial growth of the sidewall boundary layer as the flow expands in the tunnel. It is also easy to see that the top wall boundary does not grow as dramatically due to the 1.5° divergence of the top wall. In addition, the figure shows the bow-shock standoff distance is 1.23 mm from the cylinder (as seen in the zoomed box), which matches the experiment's measurement of the shock location.
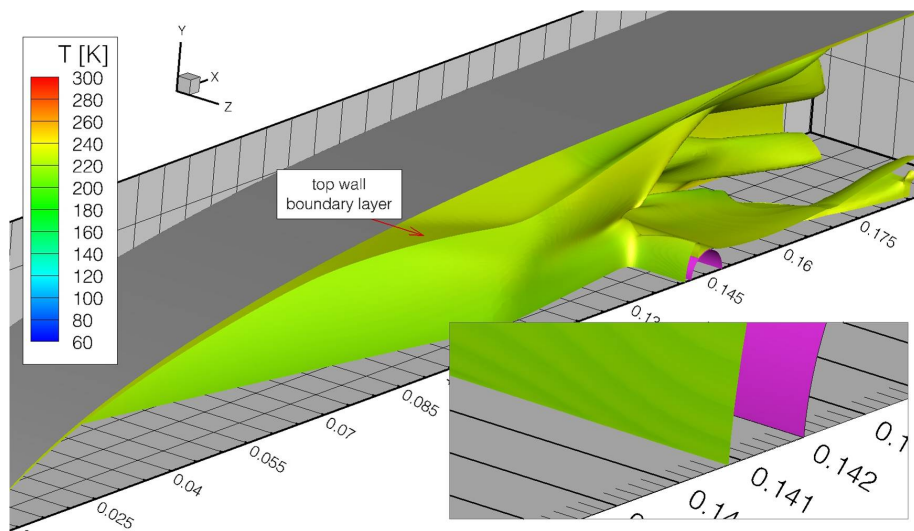

Figure 30. Mach 1.25 iso-contour colored by temperature at $t = 19$ ms. The pink surface indicates the cylinder for the $1/4$ geometry simulation of air expanding in a Mach 5 wind tunnel.

Figure 31 shows the phase-locked schlieren images from the experiment, which have been overlaid with the computational solutions. The schlieren images in the experiment were taken with a knife-edge set in the streamwise direction. To replicate this, the computational schlieren result is computed in the same direction (i.e., spanwise average of the derivative of density in the x-direction). Accounting for the thickness and location of the Kapton® tape placed on the cylinder, it can be seen that the computational shock standoff distance matches the experimental quite well.

(a) Side view　　　　　　　　(b) Top-down view
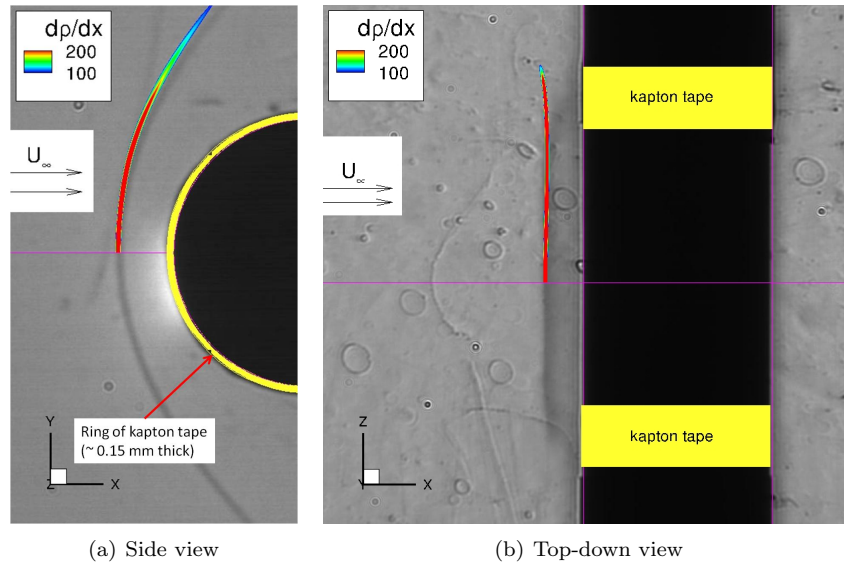
Figure 31. Schlieren images from the experiment, along with the computational density gradient in the x-direction at t = 40 ms.

Aside from schlieren visualization, the only other validation available from the experiment is the surface pressure tap located on sidewall of the tunnel, 4 cm upstream of the cylinder. Figure 32 plots the pressure on the tunnel sidewall. The computed pressure at the location of the pressure tap is $p_w = 1.1$ Torr, which is slightly lower than the experimental value of $p_w = 1.2$ Torr. However, given the precision of the experimental measurement (± 0.05 Torr), and the uncertainties associated with the tunnel conditions, the computational results are consider to be in very good agreement with the experimental measurement.
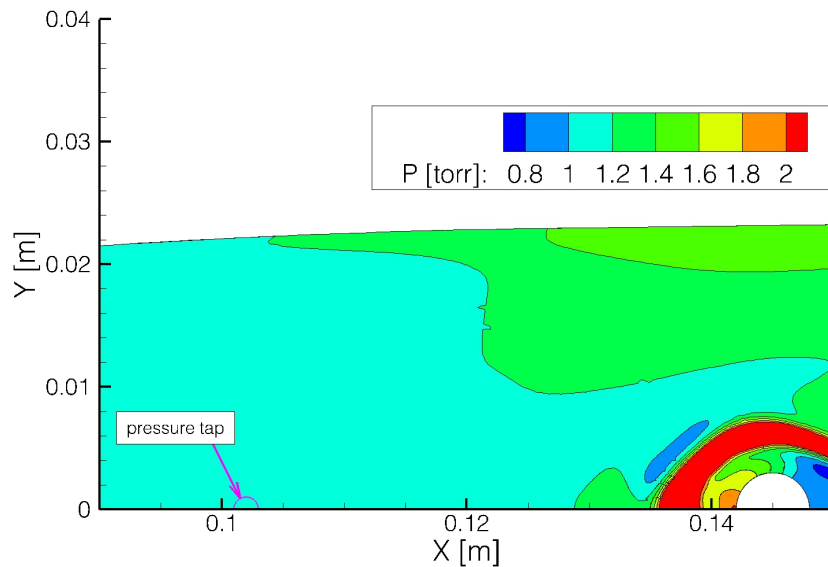
Figure 32. Pressure contours along the sidewall the Mach 5 wind tunnel with a 6 mm cylinder in the test section. Flow direction is left to right. ($t = 20$ ms)

In addition to the location of the bow-shock, Fig. 30 also illustrates the complexity of the flow-field, including a reflected Mach wave downstream of the cylinder wake along the flow spanwise centerline. In particular, the interaction between the cylinder and sidewall results in a complex wake region that oscillates at a low frequency (30 Hz). The low frequency oscillation of the boundary layer is due to interaction between the sidewall and the cylinder body, and is a characteristic of wall/blunt-body experiments, where a lambda shock structure forms at the edge of the inviscid region and the boundary layer. The oscillation in the wake region of the cylinder/side-wall interaction can be seen in Fig. 33, which shows the Mach 1.25 iso-surface, but viewed looking upstream. Oscillations at the shock/boundary layer junction were also observed in schlieren images from the experiment.

As seen in Fig. 34, the pressure is essentially uniform in the boundary layer, but rapidly changes in the inviscid region (decreasing when the Mach number is increasing and increasing where the Mach number is decreasing). As such, the assumptions made to originally estimate the tunnel's flow conditions were appropriate (i.e., constant static pressure through the boundary layer), but the approach did not account for the rapid increase in boundary layer thickness so far upstream of the test article. As a result, the inviscid flow just upstream of the cylinder's bow-shock is Mach 4 (rather than Mach 5). According to Billig's empirical formulation, the decrease in freestream Mach number should further increase the shock standoff distance, but due to the complex flow structures from the cylinder/side-wall junction, the bow-shock remains close to the geometry.

(a) $t = 10$ ms

(b) $t = 20$ ms

(c) $t = 30$ ms

(d) $t = 40$ ms
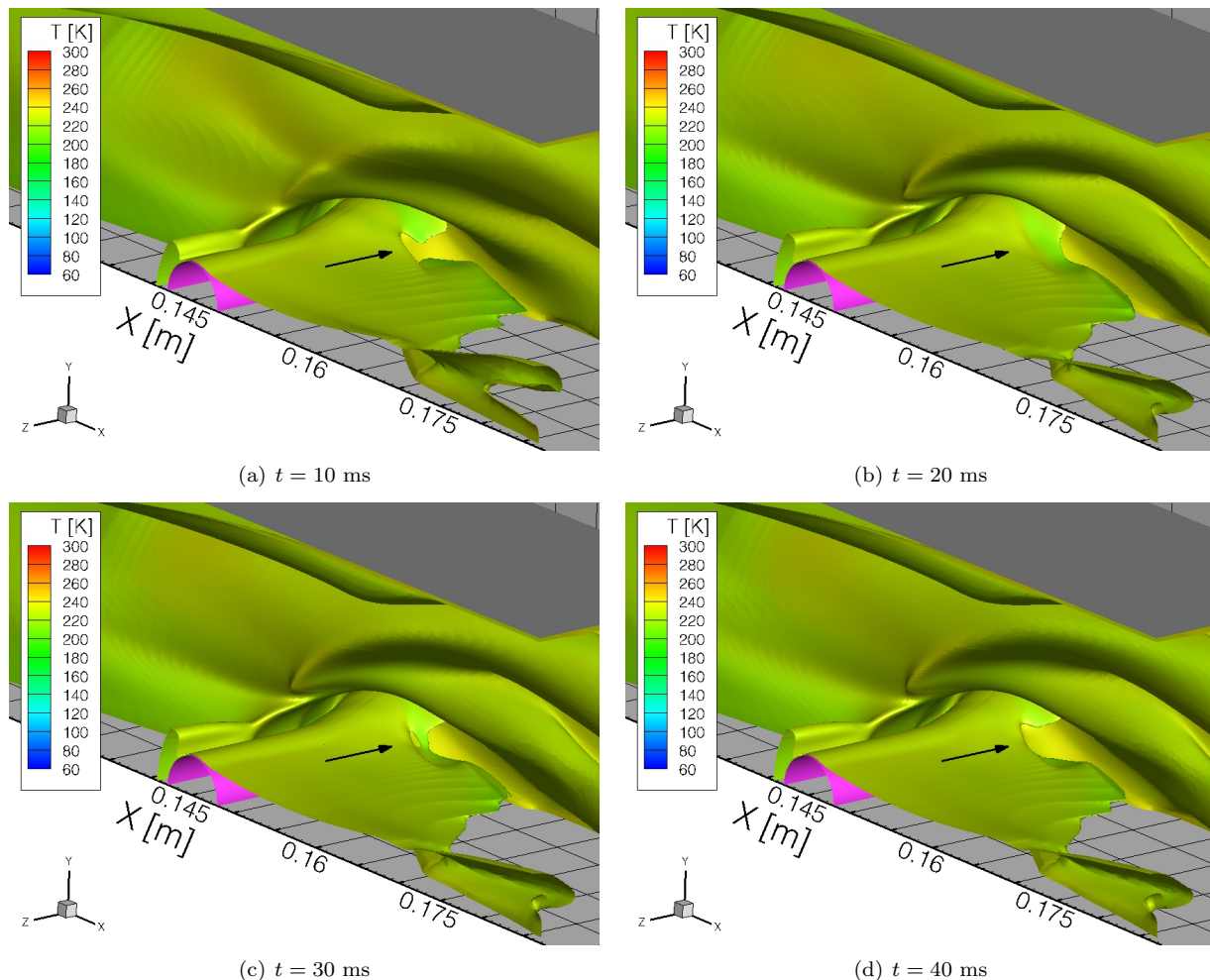
Figure 33. Mach 1.25 iso-surface colored by temperature for Mach 5 air in a wind tunnel. The cylinder/side-wall junction results in a complex wake flow that 'breathes' over a 30 ms cycle (~ 30 Hz).

As the flow accelerates through the nozzle, the pressure in the inviscid core drops, but due to the thick boundary layer far upstream of the test section, the inviscid core flow eventually contracts and slows slightly.

The decrease in Mach number coincides with an increase in static pressure within the inviscid core. As a result, there is a higher post bow-shock pressure and a larger spanwise pressure gradient in that region. Figure 34 shows Mach number and pressure contours along the transverse symmetry plane upstream of the test section.
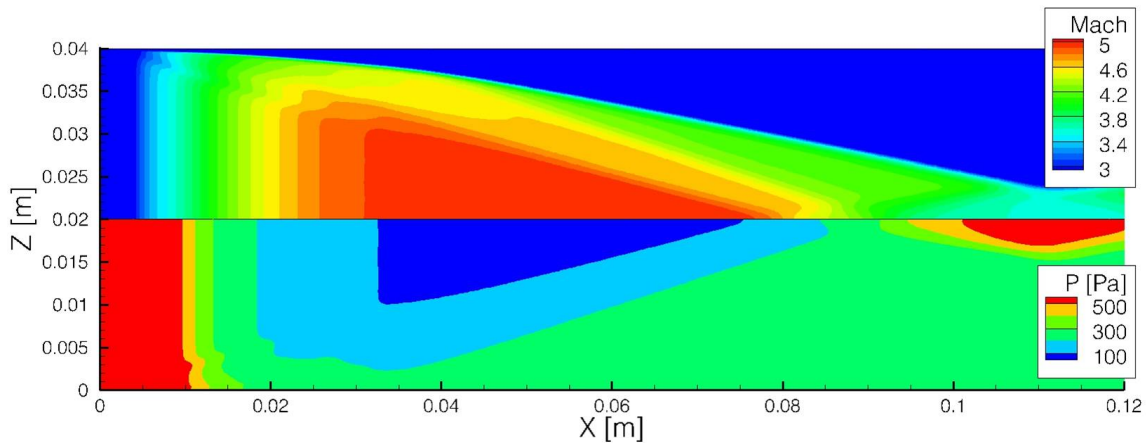

Figure 34. Top-down view of Mach and pressure contours along the transverse symmetry plane ($y = 0$), for air flow in a Mach 5 wind tunnel.

Figure 35 shows a slice of pressure contours along the transverse symmetry plane near the cylinder. As seen in the figure, there is a very large pressure drop in the spanwise direction just after the bow-shock. This pressure drop is due to the low pressure present in the boundary layer, and is further strengthened due to the strong interaction between the cylinder with the sidewall.
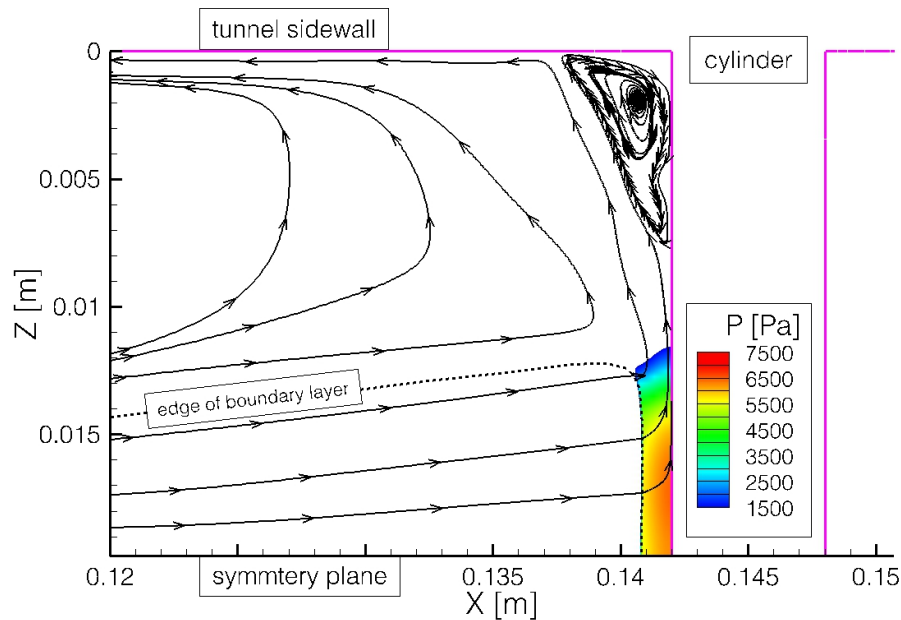

Figure 35. Top-down view of pressure contours along the transverse symmetry plane ($y = 0$), for air flow in a Mach 5 wind tunnel. The figure also includes streamlines of velocity. Note contours $p < 1500$ Pa have been excluded.

The large pressure gradient causes the inviscid core flow to turn into the spanwise direction after it goes through the bow-shock. While the post-shock flow escaping into the boundary layer is subsonic, it still has a large velocity and, as such, a large portion of the mass flow is no longer two-dimensional. As a result of the three-dimensionality of the flow, the bow-shock location is much closer to the cylinder than would be expected in a two-dimensional flow.

A. Energy Deposition

Once the three-dimensional baseline simulation results were completed, as simulation of the discharge event was computed using the same phenomenological discharge model as the two-dimensional results, except the model was extended for three-dimensions:

$$S = \frac{Q}{\pi^{3/2}\,a\,b\,c}\ \exp\left(-\left(\frac{\hat{x}}{a}\right)^2 - \left(\frac{\hat{y}}{b}\right)^2 - \left(\frac{\hat{z}}{c}\right)^2\right)$$
$$\hat{x} = (x - x_{\rm c})$$
$$\hat{y} = (y - y_{\rm c})$$ (7)
$$\hat{z} = (z - z_{\rm c})$$

where the center of the ellipsoid is set to the stagnation point of the cylinder along both symmetry planes (so half the ellipsoidal volume is inside the cylinder, and is excluded from the computational domain). For the wind tunnel geometry shown previously, the values are $x = 14.2$ cm, $y = 0$, $z = 2.0$ cm. The equatorial radii of the ellipsoidal deposition are consistent with the two-dimensional simulations, and the polar radius, c, is half the width of the exposed electrode ($a = 0.1$ mm, $b = 0.3$ mm, $c = 5$ mm). Note $\iiint_{-\infty}^{\infty} S\,dx\,dy\,dz = Q$

The simulation was carried out assuming a total power deposition $Q = 5$ kW for 100 ns (for 1/4 the geometry), at a time step of $\Delta t = 0.5$ ns to ensure temporal independence based on the two-dimensional simulations. The power deposited amounts to a total energy deposition of 2 mJ/pulse, (i.e., a thermal efficiency of over 25%). While the computational representation of the discharge event results in a relatively high thermal efficiency, the value of Q was selected to ensure a supersonic compression wave was generated.

The simulation is run for 15 µs using a $\Delta t = 0.5$ ns time-step (i.e., 30,000 iterations) to capture the evolution of the compression wave/bow-shock interaction. Figure 36 shows the Mach 1.25 iso-surfaces colored by temperature at $t = 4.1$ µs after the deposition event.
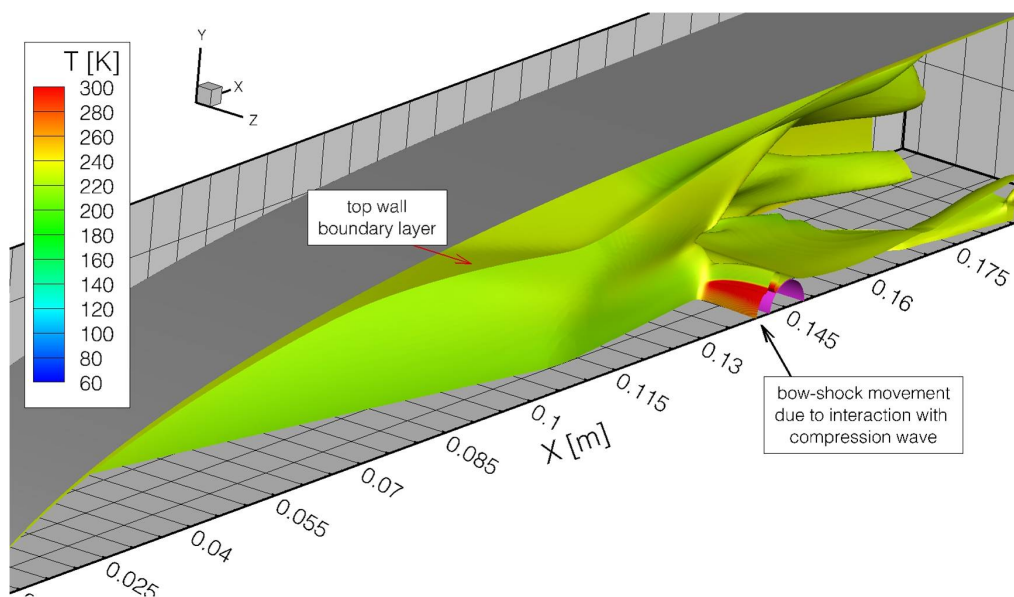
Figure 36. Mach 1.25 iso-contour colored by temperature for air in a Mach 5 wind tunnel $t = 4.1$ µs after a discharge event. The compression wave pushes the bow-shock outward, as seen in the red region.

Consistent with the two-dimensional results, the power deposited by the phenomenological model was sufficiently high to generate a supersonic compression, which traveled upstream and interacts with the standing bow-shock. However, either the energy was deposited over too small an area, and/or too much energy was deposited, because the compression wave speed was slightly faster than the experimental value and, thus, started interacting with the bow-shock before the time observed experimentally with the phase-locked schlieren images. Further evolution of the flow shows the resultant compression wave/bow-shock structure extending out more than 2.2 mm from the cylinder (along the centerline), which is a 85% increase in the shock standoff distance. This increase is much higher than that observed in the experiment (25%). In addition, the shape of the perturbed shock does not completely match the shape in schlieren images. These

164

results suggest that both the shape and amount of energy deposited in the phenomenological deposition model need to be adjusted in order to fully replicate the experiment using three-dimensional simulations.

The extra computations needed to fine tune the three-dimensional phenomenological energy deposition model are beyond the current resources dedicated for this work. Future studies will further refine the reduced-order model, though given the high computational cost associated with the three-dimensional simulations, it may be more feasible to experimentally explore the nanosecond DBD on a 5 mm diameter cylinder since the two-dimensional computations and two-dimensional empirical correlation are in much better agreement with the experiment.

While the three-dimensional computation results do not replicate the exact behavior observed in the experiment, the solutions do show that the compression wave's interaction with the bow-shock is directly responsible for the bow-shock movement and that the movement is not the result of a portion of the compression wave interacting the with flow in the cylinder/side-wall junction, since the flow remains quasi-steady in that region during the entire 15 μs discharge cycle.

VI.   Conclusions

A computational study of Mach 5 air flow around a 6 mm cylinder with a nanosecond DBD discharge was replicated using high-fidelity numerical simulations in order to better understand the resulting flow perturbation and the impact the discharge event has on the flow and the cylinder surface. The shock standoff distance for the 6 mm cylinder scenario was found to be 20% smaller in the experiments than the predictions of the empirical correlation and computations. However, the computed shock standoff distance for a 5 mm cylinder agreed well with the empirical correlation and experiment. In order to determine the cause of the shock location discrepancy, the tunnel's uncertainty in freestream conditions were estimated, and computations performed. The freestream differences resulted in a variation of the bow-shock standoff distance of about ±3%. In addition, the effects due to wall boundary conditions, including partial slip walls, as well as thermo-chemical nonequilibrium were found to provide an insignificant change in the bow-shock location. Therefore, the observed discrepancy is attributed to the interaction at the junction of the cylinder and sidewall which results in a complex, quasi-steady boundary layer. This complex flow acts to lower the post-shock pressure thereby drawing the bow-shock closer to the cylinder. This was verified with a three-dimensional simulation of the entire wind tunnel, which was able to computationally replicate the bow-shock structure seen in the schlieren photography, predict the width of the tunnel's inviscid core, and match static pressure with the experiment's sidewall pressure tap.

The effect of the nanosecond pulse surface dielectric barrier discharge on a Mach 5 flow over a cylinder model was modeled using two-dimensional compressible Navier-Stokes flow code, LeMANS, which incorporated a phenomenological thermal energy deposition model. In spite of a difference between the baseline bow-shock standoff distance measured in the experiments and that predicted by the CFD model, other experimentally measured parameters such as compression wave speed and perturbed bow-shock speed, as well as the time evolution of the perturbed bow-shock shape were replicated using the model. Distributions of wall pressure and heat transfer coefficient, as well as total drag on the model have also been calculated and show that the cylinder experiences a small reduction in total drag (1%), over a discharge event cycle of 15 μs, though the cylinder is subjected to a large increase in peak heating during the first microsecond of the discharge cycle.
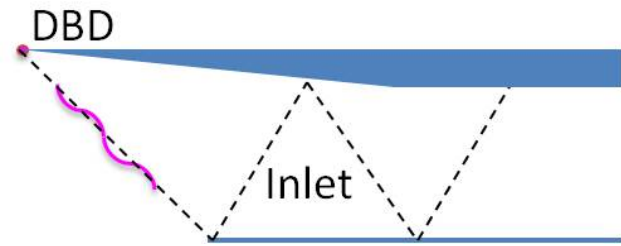
A three-dimensional simulation was also computed to replicate the discharge event from the baseline flow conditions. While these results do not agree as well with the experiment's phase-locked schlieren images as the two-dimensional results, the resultant flow field indicates that the cylinder/sidewall junction is not immediately influenced by the discharge event and therefore is not responsible for the increase in bow-shock standoff distance due to the nanosecond DBD pulse. In addition, the behavior of the shock perturbation is independent of the form of energy input (due to the short pulse duration), so the resultant flow is being accurately simulated.

While the nanosecond DBD actuator simulated in this work is not very effective at improving the cylinder surface conditions (i.e., it creates a large increase in heat load on the cylinder surface with only a minor decrease to total drag), the device is very effective at moving a strong standing shock. This technology could prove very useful in supersonic inlets and isolators found in RAM jet and SCRAM jet engines, where engine 'un-start' continues to be a technical challenge. One example of engine 'un-start' is the upstream movement of the shock-train within the inlet which leads to unfavorable conditions in the combustor. If 'un-start' of
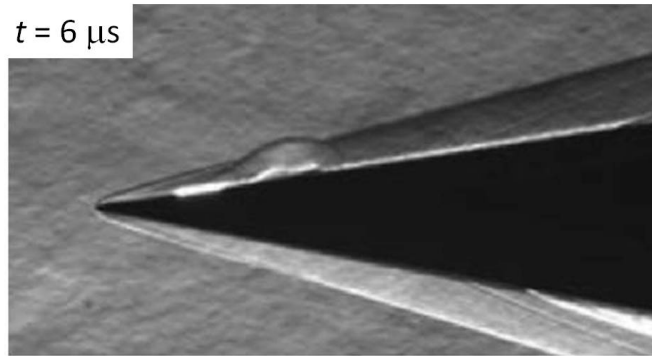
the shock-train could be sensed in the inlet, a nanosecond DBD device could be rapidly fired to move the shock-train back to its nominal location.

From this work, it appears these devices would be best situated in subsonic regions of the flow (i.e., in the sub-sonic region of a separation bubble or in the subsonic region downstream of a bow-shock), where a supersonic compression wave could more easily be generated. Figure 37 illustrates the concept of placing a nanosecond DBD actuator at the leading edge of a supersonic inlet flow-path. As seen in the figure, the DBD induced bow-shock perturbation travels along the standing shock, effectively moving the subsequent shock-train.

Figure 37. Schematic illustrating a shock train perturbation due to nanosecond DBD actuator locating at the leading edge of a supersonic inlet.

This concept already has received some attention. In 2008, Gnemmi *et al.* successfully applied the concept of shock perturbation on external flows by using a short duration arc discharge,[34] as seen in Fig. 38. In their work, the surface discharge created a shock-wave perturbation on one side of a cone, which was used to generate a steering moment. Future work may explore using nanosecond DBD discharges for an internal flow-path to achieve similar shock control.

$t = 6$ μs

Figure 38. Evolution of arc-discharge generated disturbance on the surface of a supersonic cone, taken from Ref. 34.

In addition to exploration of the controlling shock boundary-layer interactions using nanosecond DBD actuators for internal flow paths, it is also necessary to improve the fidelity of the phenomenological energy deposition model. To this end, future work will incorporate the recent work by Poggie *et al.*,[16] which more accurately models the energy transfer processes in a pulsed surface dielectric barrier discharge.

Acknowledgments

References

[1]Nishihara, M., Takashima, K., Rich, J. W., and Adamovich, I. V., "Mach 5 Bow Shock Control by a Nanosecond Pulse Surface Dielectric Barrier Discharge," *Physics of Fluids*, Vol. 23, No. 6, 2011, pp. 066101.

[2]Roupassov, D. V., Nikipelov, A. A., Nudnova, M. M., and Starikovskii, A. Y., "Flow Seperation Control by Plasma

Actuator with Nanosecond Pulsed-Periodic Discharge," *AIAA Journal*, Vol. 47, No. 1, January 2009, pp. 168–185.

[3]Takashima, K., Zuzeek, Y., Lempert, W. R., and Adamovich, I. V., "Characterization of a surface dielectric barrier discharge plasma sustained by repetitive nanosecond pulses," *Plasma Sources Science and Technology*, Vol. 20, No. 5, 2011, pp. 055009.

[4]Little, J., Takashima, K., Nishihara, M., Adamovich, I., and Samimy, M., "High Lift Airfoil Leading Edge Separation Control with Nanosecond Pulse Driven DBD Plasma Actuators," AIAA Paper 2010-4256, 2010, submitted for publication in AIAA Journal.

[5]Samimy, M., Adamovich, I., Webb, B., Kastner, J., Hileman, J., Keshav, S., and Palm, P., "Development and Characterization of Plasma Actuators for High Speed Jet Control," *Experiments in Fluids*, Vol. 37, No. 4, March 2004, pp. 577–588.

[6]Utkin, Y. G., Keshav, S., Kim, J.-H., Kastner, J., Adamovich, I. V., and Samimy, M., "Development and use of localized arc filament plasma actuators for high-speed flow control," *Journal of Physics D*, Vol. 40, No. 3, February 2007, pp. 685–695.

[7]Adamovich, I. V., Choi, I., Jiang, N., Kim, J.-H., Keshav, S., Lempert, W., Mintusov, E., Nishihara, M., Samimy, M., and Uddi, M., "Plasma Assisted Ignition and High-Speed Flow Control: Non-Thermal and Thermal Effects," *Plasma Sources Science and Technology*, Vol. 18, No. 3, 2009, pp. 034018.

[8]Myrabo, L. N., Raizer, Y. P., Schneider, M. N., and Bracken, R., "Reduction of Drag and Energy Consumption during Energy Release Preceding a Blunt Body in Supersonic Flow," *High Temperature*, Vol. 42, No. 6, 2004, pp. 901–910.

[9]Lashkov, V., Mashek, I., Anisimov, Y., Ivanov, V., Kolesnichenko, Y., Ryvkin, M., and Gorynya, A., "Gas Dynamic Effect of Microwave Energy Discharge on Supersonic Cone Shaped Bodies," AIAA Paper 2004-0671, 2004.

[10]Adelgren, R. G., Yan, H., Elliott, G. S., Knight, D. D., Beutner, T. J., and Zheltovodov, A. A., "Control of Edney IV Interaction by Pulsed Laser Energy Deposition," *AIAA Journal*, Vol. 43, No. 2, 2005, pp. 256–269.

[11]Sasoh, A., Sekiya, Y., Sakai, T., Kim, J.-H., and Matsuda, A., "Supersonic Drag Reduction with Repetitive Laser Pulses Through a Blunt Body," *AIAA Journal*, Vol. 48, No. 12, December 2010, pp. 2811–2817.

[12]Bisek, N. J., Boyd, I. D., and Poggie, J., "Numerical Study of Plasma-Assisted Aerodynamic Control for Hypersonic Vehicles," *Journal of Spacecraft and Rockets*, Vol. 46, No. 3, May-June 2009.

[13]Bisek, N. J., Boyd, I. D., and Poggie, J., "Numerical Study of Magnetoaerodynamic Flow Around a Hemisphere," *Journal of Spacecraft and Rockets*, Vol. 47, No. 5, September-October 2010.

[14]Scalabrin, L. C. and Boyd, I. D., "Development of an Unstructured Navier-Stokes Solver For Hypersonic Nonequilibrium Aerothermodynamics," AIAA Paper 2005-5203, 2005.

[15]Scalabrin, L. C. and Boyd, I. D., "Numerical Simulation of Weakly Ionized Hypersonic Flow for Reentry Configurations," AIAA Paper 2006-3773, 2006.

[16]Poggie, J., Bisek, N. J., Adamovich, I., and Nishihara, M., "High-Speed Flow Control with Nanosecond-Pulse Electrical Discharges," AIAA Paper, January 2012, submitted to the AIAA Aerospace Sciences Meeting, 2012.

[17]Nishihara, M., Takashima, K., Jiang, N., Lempert, W., Adamovich, I. V., and Rich, J. W., "Development of a Mach 5 Nonequilibrium Wind Tunnel," AIAA Paper 2010-1567, 2010.

[18]Nishihara, M., Takashima, K., Jiang, N., Lempert, W., Adamovich, I. V., and Rich, J. W., "Nonequilibirum Flow Characterization in a Mach 5 Wind Tunnel," AIAA Paper 2010-4515, 2010.

[19]Jiang, N., Nishihara, M., and Lempert, W. R., "Quantitative NO2 Molecular Tagging Velocimetry at 500 kHz Frame Rate," *Applied Physics Letters*, Vol. 97, No. 22, 2010, pp. 221103.

[20]Montello, A., Nishihara, M., Rich, J. W., Adamovich, I. V., and Lempert, W., "Picosecond CARS Measurements of Vibrational Distribution Functions in a Nonequilibrium Mach 5 Flow," AIAA Paper 2011-1322, 2011.

[21]Jiang, N., Webster, M., and Lempert, W. R., "New Advances in Generation of High Repetition Rate Burst Mode Laser Output," *Applied Optics*, Vol. 48, No. 4, 2009, pp. B23–B31.

[22]Popov, N., "Investigation of the Mechanism for Rapid Heating of Nitrogen and Air in Gas Discharges," *Plasma Physics Reports*, Vol. 27, No. 10, 2001, pp. 886–896.

[23]Ambrosio, A. and Wortman, A., "Stagnation Point Shock Detachement Distance for Flow Around Spheres and Cylinders," *ARS Journal*, Vol. 33, No. 2, 1962, pp. 281.

[24]Billig, F. S., "Shock-Wave Shapes around Spherical- and Cylindrical-Nosed Bodies," *Journal of Spacecraft*, Vol. 4, No. 6, 1967.

[25]White, F. M., *Heat Transfer*, 1984, Addison-Wesley Publishing Company.

[26]Marks, L. S., *Mechanical Engineers Handbook*, 1941, McGraw-Hill Book Company.

[27]23. Vincenti, W. G. and Kruger, C. H., *Introduction to Physical Gas Dynamics*, 2002, Krieger Publishing Company.

[28]Gordiets, B. and Ricard, A., "Production of N, O and NO in N_2-O_2 flowing discharges," *Plasma Sources Science and Technology*, Vol. 2, No. 3, 1993, pp. 158–163.

[29]Boyd, I. D., Chen, G., and Candler, G. V., "Predicting Failure of the Continuum Fluid Equations in Transitional Hypersonic Flows," *Physics of Fluids*, Vol. 7, No. 1, 1995.

[30]Lofthouse, A., *Nonequilibrium Hypersonic Aerothermodynamics Using the Direct Simulation Monte Carlo an Navier-Stokes Models*, 2008, PhD thesis, Department of Aerospace Engineering, University of Michigan.

[31]Lockerby, D. A., Reese, J. M., Emerson, D. R., and Barber, R. W., "Velocity Boundary Conditions at Solid Walls in Rarefied Gas Calculations," *Physical Review E*, Vol. 70, 2004, pp. 017303.

[32]Burt, J. M., Josyula, E., and Boyd, I. D., "A Novel Cartesian Implementation of the Direct Simulation Monte Carlo Method," AIAA Paper 2011-632, 2011.

[33]Montello, A., Nishihara, M., Rich, J., Adamovich, I., and Lempert, W., "Unstable-Resonator Spatially Enhanced Detection Picosecond CARS Measurements of Vibrational Distribution Functions in and Around a Bow Shock in a Highly Non-equilibrium Mach 5 Flow," AIAA Paper, January 2012, submitted to the AIAA Aerospace Sciences Meeting, 2012.

[34]Gnemmi, P., Charon, R., Duperoux, J.-P., and A., G., "Feasibility Study for Steering a Supersonic Projectile by a Plasma Actuator," *AIAA Journal*, Vol. 46, No. 6, June 2008, pp. 1308–1317.

List of Acronyms, Abbreviations, and Sympols

Acronym/ Abbreviation	Description
AFRL	Air Force Research Laboratory
AFRL/RB	Air Vehicles Directorate
AFRL/RBAC	Compuational Aerophysics Branch
AFOSR	Air Force Office of Scientific Research
AFOSR/RSL	Mathematics, Information, and Life Sciences Directorate
AJAX	Russian acronym for hypersonic plasma technology demonstrator
CSIRF	Chief Scientist Innovative Research Fund
DBD	Dielectric barrier discharge
DoD	Department of Defense
DSMC	Direct Simulation Monte Carlo
DSRC	DoD Supercomputing Resource Center
ERDC	US Army Engineer Research and Development Center
eV	Electron-volts
HPC	High-Performance Computing
LeMANS	Michigan Aerothermodynamic Navier-Stokes code
MHD	Magnetohydrodynamics
OSU	The Ohio State University
TE	Transverse electric field

List of Acronyms, Abbreviations, and Sympols (continued)

Symbol	Description
a, b	Constants
E	Electric field
L	Reference length scale
n	Number density
Re	Reynolds number
t	Time
T	Temperature
u, v, w	Velocity components
x, y, z	Spatial coordinates
α	Constant
Δx	Computational mesh spacing
ϕ	Generic dependent variable
ρ	Density

Subscripts	Description
e	Electrons
i	Ions
n	Neutral